Ph.D. Thesis

Ultrashort Pulsed Laser-Induced Chemistry: Methodology, Instrumentation, and Analysis

Marcus Straw
Faculty of Science, University of Technology, Sydney
Supervisor: Prof. Matthew Phillips

Submitted in fulfilment of the requirements of the degree of
Doctor of Philosophy at the Faculty of Science,
University of Technology, Sydney

October 15, 2013

Certificate of Original Authorship

I certify that the work in this thesis has not previously been submitted for a degree nor has it been submitted as part of requirements for a degree. I also certify that the thesis has been written by me. Any and all help that I have received in my research work has been acknowledged. Finally, I certify that all information sources and literature used are indicated in the thesis.

Marcus Straw

Acknowledgements

The work presented in this dissertation was carried out under the supervision of Prof. Matthew Phillips, at the Microstructural Unit, Faculty of Science, University of Technology, Sydney, New South Wales, Australia. The work was performed within the Advanced Technology Group, Beam Technology R&D, FEI Company, Hillsboro, OR, U.S.A. I sincerely wish to thank Prof. Phillips for his guidance and support. I would also like to thank FEI Company for material support, Dr. Michael Lysaght for his support and flexibility, and Prof. Milos Toth for his review of my work and ongoing support throughout this process.

All work presented in the pages that follow was planned, coordinated, and managed exclusively by the author. As with any large project however, some degree of collaboration was required to achieve all that was achieved. I would like to take a moment here to explicitly acknowledge the work of those who contributed.

The instrumentation (see Figure 3.1) and experiments discussed in Chapter 3 were built and performed extensively by the author with the exception of the experiment using electron beam induced etching to illustrate the temperature dependence of surface adsorption (see Section 3.5.1). This experiment was suggested by Prof. Milos Toth and he did the EBIE work. The atomic force microscope line profiles shown in Figure 3.5 were collected by Dr. Steven Randolph.

The instrumentation (see Figure 4.1) and experiments detailed in Chapter 4 were likewise exclusively the work of the author with but two exceptions. First, the analysis of intensity data leading to the plot shown in Figure 4.5 was done by Dr. Jorge Filevich. Second, the author received a great deal of assistance from Dr. Steven Randolph setting up and learning to operate the quadrupole mass spectrometer portion of the instrumentation shown in Figure 4.10. Dr. Randolph was also instrumental in refining the subsequent experiments done to characterise the

by-products of the laser-induced plasma-mediated chemical reactions.

The development of the TripleBeam system has a long and storied history. It's hard to say definitively, but it is quite possible that the concept was first conceived by Dr. Mark Utlaut over a decade prior to the author's initial efforts. Dr. Utlaut was certainly the first to propose the idea within FEI Company and it is at FEI's world headquarters in Hillsboro, Oregon, USA that the earliest and the majority of the instrument's development has taken place. The first two prototypes of the tool were designed, built, and characterised almost exclusively by the author. The third and most current version has been a collaborative effort. The author's colleagues Mark Emerson, Dr. Steven Randolph, Dr. Jorge Filevich, and Dr. Aurélien Botman, as well as the author himself, all contributed variously to development of the LabView UI, alignment procedures, stage programming, beam stabilisation, contamination mitigation, optics, and beam delivery and control. In addition, elements of the most current design, particularly with regard to the laser injection port and the stage mount, were developed in collaboration with Dr. Tresa Pollock's group at the University of California, Santa Barbara in Santa Barbara, California, USA. This collaboration is discussed in more detail in Sections 5.6 and 5.7.

While the data collection and the segmentation work required to produce the three dimensional reconstruction of the geological sample presented in Section refsec:Gap was done solely by the author, the effort to quantify UPL-induced damage presented in the same section was a collaborative effort. Laser processing of tungsten carbide cobalt was done largely by Dr. Steven Randolph, while silicon processing was performed by the author. Transmission electron microscope and scanning transmission electron microscope analysis of these samples were performed by other FEI colleagues both in the U.S. and in Holland. Dr. Randolph also performed the electron backscatter diffraction analysis of UPL processed, single crystal copper discussed at the end of this section. Finally, the instrumentation, experiments, and analysis presented in Chapter 6 are the result of the collaborative efforts of the author and Dr. Randolph, and Dr. Randolph's contributions were considerable.

In addition to their critical technical support, I would like to offer special thanks to Dr. Steven Randolph, Dr. Mark Utlaut, Dr. Jorge Filevich, Dr. Milos Toth, and Dr. Aurélien Botman for the many, many useful discussions in which we engaged throughout this project's course.

Abstract

This dissertation explores the science and application of ultrashort pulsed lasers to locally induced chemical reactions having high spatial resolution. Chemical reactions driven in the gas phase by micro- to millimetre-scale plasmas formed when ultrashort pulsed laser ablation is performed in reactive gas atmospheres are studied via scanning electron microscopy, time-resolved optical emission spectroscopy, spatially resolved fast photography, plasma diagnostics, and mass spectrometry. Surface reactions resulting in metal deposition are explored via energy dispersive X-ray spectroscopy, electron backscatter diffraction, transmission electron microscopy, atomic force microscopy, and the use of a complex scientific instrument known as the TripleBeam designed and developed over the course of the project, and described in detail in this dissertation.

With wide scientific and industrial potential as both an experimental platform and a nanofabrication tool, the design and development of the TripleBeam instrument was initially motivated by the need to speed industrial processes currently employing focused ion beams. To that end, gas-phase ultrashort pulsed laser-induced chemistry was explored as a means of protecting sensitive components inside the instrument from material removed during in situ laser ablation. For this reason, reactions resulting in the transformation of solids to gas-phase compounds are targeted. However, a demonstration of the technique as a means for the fabrication of novel nanoparticles is also given.

Ultrashort pulsed laser-induced surface chemistries were explored with the hope of improving deposition rates and the purity of deposits made via electron and ion beam-induced processes. A previously unreported technique is presented in which electron-beam induced depositions provide templates for laser induced deposition, enabling both higher deposition rates and sub-diffraction limited pattern resolution.

With a rich potential application space driven by fundamental physics, ultrashort pulsed laser-induced chemistry can be seen as both an end in itself and as a means for exploring the complex interaction of light and matter. The work detailed in this dissertation produced methodologies, instrumentation, and analysis relevant to both the fundamental physics and the application of ultrashort pulsed-laser induced chemistry.

Contents

Certificate of Original Authorship i

Acknowledgements ii

Abstract iv

List of Figures ix

List of Tables xiii

List of Symbols and Abbreviations xiv

1 Introduction **1**

1.1 Ultrashort Laser Pulses and Their Interaction with Matter 1

1.2 Thesis Structure 5

2 Pulsed Laser-Induced Processes in Various Ambient Environments **9**

2.1 Introduction 9

2.2 Ablation 10

2.3 Deposition 24

3 Ultrashort Pulsed Laser Ablation in Reactive Gas Atmospheres **27**

3.1 Introduction and Background 27

3.2 Model System 29

3.3 Instrumentation 30

3.4 Evidence of UPL Driven Chemistry 31

3.5 The Feasibility of a Surface Reaction: A Simple Analysis 35

3.5.1 The Temperature Dependence of Surface Adsorption and a Brief Foray into EBIE . . . 39
3.6 Other Substrate/Precursor Systems Explored . . . 42
3.7 Summary and Conclusions . . . 44

4 Gas Phase Chemical Reactions Driven by UPLA-Induced Plasmas 46
4.1 Instrumentation . . . 46
4.2 Procedure and Results . . . 51
4.2.1 Characterisation of the Plasma . . . 61
4.2.2 Reaction By-Products . . . 66
4.3 Conclusions . . . 69

5 TripleBeam Design and Development 71
5.1 Introduction . . . 71
5.2 Overview . . . 71
5.3 Laser . . . 73
5.3.1 Erbium Doped Fibre Oscillator . . . 74
5.3.1.1 Mode-locking . . . 75
5.3.1.2 Group Velocity Dispersion . . . 80
5.3.2 Chirped Pulse Amplification and the Regenerative Amplifier . 82
5.4 DualBeam™ . . . 90
5.4.1 FIB . . . 92
5.4.2 SEM . . . 96
5.5 Analysis Techniques . . . 99
5.5.1 Energy Dispersive X-ray Spectroscopy . . . 100
5.5.2 Electron Backscatter Diffraction . . . 101
5.6 Integration . . . 102
5.6.1 Beam Delivery . . . 105
5.6.2 Beam Control . . . 108
5.6.3 Beam Stability/Auto Alignment . . . 111
5.6.4 Sample Control . . . 115
5.6.5 Contamination Mitigation . . . 117
5.6.6 Ongoing Development Effort . . . 119
5.7 Instrument Characterisation and Validation . . . 119

5.7.1 The Need for 3D and the Gap in Length Scales 120
5.7.2 A Tool for Bridging the Gap 123
5.8 Conclusion 134

6 Laser-Induced Surface Chemistry 135
6.1 Introduction and Background 135
6.1.1 Photolysis 137
6.1.2 Pyrolysis 139
6.2 Instrumentation: A Note on Gas Delivery 144
6.3 Experimental Background 146
6.4 LID: Procedure and Results 148
6.5 EBID Templated LID: Ongoing Efforts 157
6.6 Summary and Future Work 164
6.6.1 Non-Templated LID 164
6.6.2 EBID Templated LID 166

7 Summary and Concluding Remarks 168

Bibliography 175

List of Figures

1.1 A timeline of the complex processes involved in ultrashort pulsed laser ablation 6

2.1 Silicon microstructures formed via ultrashort pulsed laser processing in an SF_6 atmosphere 14

3.1 Experimental arrangement for study of laser ablation in reactive gas atmospheres 32
3.2 100 μm × 100 μm pits machined in SiO_2 33
3.3 100 μm× 100 μm pits machined in N_2 34
3.4 Possible adsorbate mediated scenarios for UPLA driven reaction in the model system. 37
3.5 AFM line profiles of etch pits in SiO_2 generated by XeF_2-mediated EBIE 40
3.6 100 μm× 100 μm pits machined in SiO_2 heated to 150°C 41
3.7 SEM image of nanoparticles generated by laser ablation of SiC in XeF_2 45

4.1 Direct spatio-temporal analysis 47
4.2 Intensified CCD schematic 49
4.3 Time-resolved optical emission spectra of SiO_2 ablated in Xe and XeF_2 52
4.4 Composite, time-resolved CCD images of plasma plume expansion into N_2 and XeF_2 atmospheres 55
4.5 Time-resolved integrated intensity of the 390.55 nm emission from Figure 4.4 58
4.6 Model of plume expansion into a background gas 59

4.7 Modelled versus measured values of plume expansion into N_2 and Xe_2 atmospheres . . . 60
4.8 An example of the Boltzmann plot method used for measuring electron temperature T_e of a plasma . . . 64
4.9 Si ion lines used to measure n_e . . . 65
4.10 Arrangement of the mass spectrometer used to characterise reaction by-products . . . 67
4.11 RGA analysis of by-products produced when the plasma generated during ultrashort pulsed laser ablation of SiO_2 interacts with XeF_2 in the gas phase . . . 68
4.12 The reaction pathway for the formation of fluorinated silicon compounds during UPL ablation of SiO_2 in a XeF_2 atmosphere . . . 70

5.1 The TripleBeam System . . . 72
5.2 Main sub-components of the TripleBeam's laser . . . 74
5.3 Longitudinal modes supported by a laser system . . . 76
5.4 Additive pulse mode-locking schematic . . . 79
5.5 Generalised polarisation APM schematic . . . 80
5.6 Erbium doped fibre oscillator design . . . 82
5.7 Typical grating-based stretcher configuration used in laser amplifiers that employ chirped pulse amplification . . . 84
5.8 A schematic of the energy states of bound electrons in a Ti:Sapphire crystal used as the gain medium in a regenerative laser amplifier . . . 86
5.9 Detailed schematic of the TripleBeam laser's upper level including the Nd:YAG pump laser and the regen cavity . . . 87
5.10 Gain curve resulting from the amplification of a hypothetical pulse illustrating gain saturation . . . 89
5.11 Oscilloscope traces of actual laser pulses transiting a Ti:Sapphire gain medium . . . 89
5.12 Typical grating-based compressor configuration . . . 90
5.13 Evolution of a pulse as it progresses through a chirped pulse amplification laser system . . . 91
5.14 An example of ion channelling . . . 93
5.15 A typical gallium liquid metal ion source . . . 94

5.16 Electron-sample interactions 99
5.17 Atomic orbitals K, L, and M 100
5.18 Electron backscatter diffraction 103
5.19 Kikuchi lines from a copper sample 104
5.20 Schematic of the TripleBeam layout and the general beam path of the laser 106
5.21 Specimen chamber of the TripleBeam system 107
5.22 The laser injection port of the TripleBeam system as mounted on the instrument 108
5.23 Output of the scan field distortion routine used to determine the extent of the scan field as well as the area over which the lens produces a usable spot 109
5.24 A screen-shot of the LabView UI developed to communicate with the laser and the FSM 110
5.25 A simplified slice-and-view routine illustrating how computer control of the laser and FSM are integrated with computer control of the DualBeam 111
5.26 The two-levels of the beam stabilisation system 113
5.27 The actual path the beam takes through the lower level of the beam stabilisation system 114
5.28 The TripleBeam system's custom stage 116
5.29 The effect of detector saturation due to "gentle" ablation being performed during SEM imaging 118
5.30 Geometry used for FIB serial sectioning 122
5.31 A three dimensional reconstruction of a 3.6 million μm^3 geological sample serially sectioned with the laser in 200 nm slices 125
5.32 SEM micrographs of bulk material removal on a WC-Co sample via UPL as performed on the TripleBeam system 126
5.33 An analysis of a laser polished WC-Co sample 127
5.34 Electron diffraction analysis of laser polished WC-Co 128
5.35 TEM analysis of the heat affected zone in UPL machined silicon . . . 129
5.36 EBSD analysis of features laser machined at a range of fluences and with both single and multiple shots per feature 133

6.1 Potential energy versus internuclear distance of a molecular system's vibrational states . . . 138
6.2 Pathways for dissociation of molecules with photo-excited electronic structures . . . 139
6.3 On-stub gas delivery assembly . . . 145
6.4 Deposition rate data used to calibrate the gas field produced by the custom, on stub gas delivery system . . . 146
6.5 Dendritic Pt structures formed via LID of $Pt(PF_3)_4$ . . . 148
6.6 A comparison of EDS analysis of laser-induced platinum deposition on gold to a reference spectrum taken of gold with no laser-induced platinum deposition and a spectrum of platinum deposited on silicon via EBID . . . 151
6.7 A comparison of EDS analysis of laser-induced platinum deposition on black glass to a reference spectrum taken of black glass with no laser-induced platinum deposition and a spectrum of platinum deposited on silicon via EBID . . . 152
6.8 Ultrashort pulsed laser-induced platinum deposits on gold and black glass using $Pt(MeCp)Me_3$ as the precursor . . . 153
6.9 A serpentine pattern of 60 to 70 nm wide Pt lines deposited via EBID templated LID demonstrating the ability to produce sub-diffraction limited features using this technique. . . . 158
6.10 Deposited volume of EBID templated laser-induced deposition as a function of EBID dose . . . 159
6.11 AFM images of EBID templated laser-induced deposition of Pt on gold and SiO_2/Si substrates . . . 160
6.12 AFM images of the morphologies of the deposits on gold and on the SiO_2/Si substrate . . . 163
6.13 AFM images of an EBID templated LID of Pt straddling a gold-SiO_2 interface illustrating the differences in both morphology and deposition rate . . . 164

List of Tables

4.1 Wavelength, energy levels, probability, and transition configurations of Si lines observed during LIBS 53
4.2 Table of XeF^* excimer states, their electronic configurations, radiative transitions, and lifetimes. 54

6.1 Single pulse and steady state sample heating results modelled using different laser fluences and repetition rates 143
6.2 Substrates, laser powers, and results of attempted LID 150

List of Symbols and Abbreviations

α	optical absorption coefficient
$\Delta\tau$	ICCD gate delay
ν	photon frequency
ν_L	laser repetition rate
ϕ	laser fluence
ϕ_{th}	threshold laser fluence at which ablation occurs
τ_e	electron cooling time
τ_i	lattice heating time
τ_p	laser pulse duration
c	the speed of light
h	Planck's constant
k_B	Boltzmann constant
n_e	electron density
T_e	electron temperature
T_i	lattice temperature
v_g	group velocity
v_p	phase velocity

E_p laser pulse energy

a.u. arbitrary units

AFM atomic force microscope

APM additive pulse mode-lock

BSD backscattered electron detector

BSE backscattered electrons

BSS beam stabilisation system

CPA chirped pulse amplification

CW continuous wave

EBID electron beam-induced deposition

EBIE electron beam-induced etching

EBSD electron backscatter diffraction

EBSP electron backscatter pattern

EDS energy dispersive X-ray spectroscopy

ESEM environmental scanning electron microscope

ETD Everhart-Thornley secondary electron detector

FSM fast steering mirror

GIS gas injector system

GVD group velocity dispersion

HAZ heat affected zone

IBID ion beam-induced deposition

IBIE ion beam induced-etching

ICCD intensified charge coupled device

LCE laser chemical etch

LIBS laser-induced breakdown spectroscopy

LID laser-induced deposition

LIP laser injection port

LIPPS laser-induced periodic surface structures

LMIS liquid metal ion source

LTE local thermodynamic equilibrium

MCP microchannel plate

NA numerical aperture

ND neutral density

Nd:YAG neodymium-doped yttrium aluminium garnet laser gain medium

PE primary electrons

PLA pulsed laser ablation

RGA residual gas analyser

SE secondary electrons

SED secondary electron detector

SEM scanning electron microscope

SF_6 sulphur hexafluoride

SHG second harmonic generation

SiO_2 silicon dioxide

TE thermodynamic equilibrium

TEM transmission electron microscope

THG third harmonic generation

Ti:Sapphire titanium doped monocrystalline sapphire (Al_2O_3) laser gain medium

UI user interface

UPL ultrashort pulsed laser

UPLA ultrashort pulsed laser ablation

XeF_2 xenon difluoride

Chapter 1

Introduction

The origins of this project are rooted in the exploration of the varied application space accessible by ultrashort pulsed laser technology. In particular, the work presented in the following pages will probe the physics behind the interaction of light and matter with the intent of understanding how ultrashort pulsed lasers (UPL) can be used to drive chemical reactions, both in the gas-phase and on surfaces. In order to lay the foundation necessary for a cogent discussion of the literature, and ultimately, the practice of ultrashort pulsed laser chemistry, this chapter begins with a general overview of ultrashort pulses, both as solitary entities and in their interaction with matter.

1.1 Ultrashort Laser Pulses and Their Interaction with Matter

Ultrashort laser pulses are among the shortest man made events ever recorded. To put their time scale in perspective, a typical ultrashort laser pulse[1] is to one second as one day is to the age of the universe. The remarkable temporal concentration of optical energy provided by these events and the extreme physics their fleeting interaction with matter induces has led to a significant body of work by hundreds of researchers exploring a wide range of topics and technologies including ultrashort pulse generation, ultrashort pulse propagation, the optics of ultrashort pulses, and

[1] The ultrashort pulses used in the work described in this dissertation have a duration of approximately 200 fs.

the application of ultrashort pulses to the study of ultrafast processes including ultrafast spectroscopy, femtochemistry, and ultrashort pulsed laser ablation.

The typical definition of an ultrashort pulse is one having a duration between 1 fs and 10 ps, though some literature puts the upper bound at 1 ps or less. Functionally, "ultrashort" typically describes the regime entered when the material response to an incident pulse is non-linear, i.e. when it is dominated by the square (or higher order) terms of the electric field. As an example, consider the polynomial expansion of the macroscopic polarisation **P** of a material illuminated by laser pulse having an electric field **E**:

$$\frac{\mathbf{P}}{\epsilon_0} = \chi^{(1)} \cdot \mathbf{E} + \chi^{(2)} \cdot \mathbf{EE} + \chi^{(3)} \cdot \mathbf{EEE} + ... \qquad (1.1)$$

where ϵ_0 is the vacuum permittivity and $\chi^{(n)}$ is the nth order of the electric susceptibility[2]. The second and higher order terms describe the non-linear response of the polarisation and when laser pulses are shorter than about 10 ps, their peak irradiance is large enough to induce non-linear effects.

Due to their fleeting nature, ultrashort pulses can achieve very high peak powers at relatively small pulse energies (recall that power is defined as the derivative of energy with respect to time or $P = dE/dt$). When focused to a spot with an area of a few square microns, ultrashort pulses reach power densities many orders of magnitude larger than the power density of the sun's photosphere.

Typically, light absorption in matter is described in terms of the Beer-Lambert law, which states that light of a particular wavelength is absorbed by a given material as a function of the length of the path the light takes through the material. Mathematically, the Beer-Lambert law is expressed as

$$I = I_0 \exp(-\alpha x) \qquad (1.2)$$

where I is the intensity of the transmitted light, I_0 is the intensity of the incident light, x is the length of the path the light takes through the material, and α is the absorption coefficient. The absorption coefficient is a property of the material and is typically expressed in units of cm^{-1}.

Note that absorption according to Beer-Lambert is independent of the intensity of light. For light of moderate intensities, this is an adequate description. However,

[2] The "·" in this case represents the matrix scalar product.

for light of extreme intensities as in the case of ultrashort pulses, non-linear effects dominate and light is absorbed through other mechanisms such as multi-photon absorption. Absorption as described by Beer-Lambert implies that electrons excited by photon absorption collisionally transfer their energy to the material lattice resulting in sample heating and eventually, melting. The photon flux and thus the electric field required to initiate non-linear absorption can exceed that required to create a solid density plasma. Given sufficiently high laser intensities, the resulting free electrons can diffuse through the material or escape into vacuum as photoelectrons. The remaining ions tend to repel one another explosively in a process typically referred to as coulombic explosion. The resulting material removal event, accompanied by the formation and expansion of a plasma plume, is commonly referred to as ablation.

The precise physical nature of ultrashort pulsed laser ablation and the extent to which it is a thermal process is the focus of much research and debate. It is widely acknowledged that thermal damage concomitant with ultrashort pulsed laser ablation (UPLA) is far less than that resulting from nanosecond pulsed laser ablation. One simple argument commonly put forth to explain this is based on the notion of the thermal diffusion length [1, 2]. The thermal diffusion length L_{th} of a material over the duration of irradiation by a laser pulse having a temporal width τ_p is given by

$$L_{th} = 2\sqrt{D\tau_p} \tag{1.3}$$

where D is the thermal diffusivity (mm^2/s) of a material. To illustrate the argument, consider a 10 ns pulse incident on silicon. Given a thermal diffusivity of 88 mm^2/s for silicon, the thermal diffusion length over the duration of the pulse is approximately 1.9 μm. For a 200 fs pulse however, the thermal diffusion length is only 8.4 nm. Thus, for sufficiently short pulses, the thermal diffusion length is much smaller than the focal size of the laser and the so-called heat affected zone (HAZ) is small relative to the volume of material removed assuming that there is no significant heating of the sample from the laser-induced plasma.

In metals, another commonly cited model to explain the largely a-thermal nature of ultrashort pulsed laser ablation is the so-called two-temperature diffusion model [3, 4] where the spatiotemporal evolution of the electron and lattice temperatures (T_e and T_i, respectively) due to laser heating is given by

$$C_e \frac{\partial T_e}{\partial t} = -\frac{\partial Q(z)}{\partial z} - \gamma(T_e - T_i) + S \tag{1.4}$$

$$C_i \frac{\partial T_i}{\partial t} = \gamma(T_e - T_i) \tag{1.5}$$

where z is the direction normal to the surface, γ is a parameter that characterises the electron-lattice coupling, C_e andC_i are the heat capacities of the electronic and lattice subsystems respectively, and the heat flux $Q(z)$ and the laser heating source S are given by

$$Q(z) = -k_e \frac{\partial T_e}{\partial z} \tag{1.6}$$

$$S = I(t) A \alpha \exp(-\alpha z) \tag{1.7}$$

where k_e is the electron thermal conductivity, $I(t)$ is the laser intensity, A is the surface transmissivity[3], and α is the absorption coefficient. The characteristic time scales for Equations 1.4 through 1.7 are the electron cooling time τ_e

$$\tau_e = \frac{C_e}{\gamma}, \tag{1.8}$$

the lattice heating time τ_i

$$\tau_i = \frac{C_i}{\gamma}, \tag{1.9}$$

and the duration of the laser pulse τ_p. The electron cooling time is typically on the order of 1 to 10 ps. For instance, Schoenlein et al. showed that in gold irradiated with ultrashort pulses, fast electron cooling and the transfer of energy to the lattice takes on the order of 2 to 3 ps [5].

Now consider an ultrashort pulse whose duration is much less than the electron cooling time ($\tau_p << \tau_e$). In this case, both thermal diffusion into the bulk and electron-lattice coupling can be neglected[4] and Equation 1.4 reduces to

[3] $A = 1 - R$ where R is the reflectivity.

[4] Thermal diffusion can be neglected when the diffusion of thermal electrons into the bulk is much less than the optical penetration depth or $D_e \tau_p < \alpha^{-1}$ where $D_e = k_e / C_e$ is the electron thermal diffusivity. Electron-lattice coupling can be neglected because $t = \tau_p << \tau_e$ leads to $C_e T_e / t >> \gamma T_e$.

$$C_e \frac{\partial T_e}{\partial t} = I(t) A \alpha \exp(-\alpha z). \tag{1.10}$$

Solving Equation 1.10 provides an estimate of the electron temperature as a function of the pulse duration such that

$$T_e(\tau_p) \approx \left(\frac{2F_a \alpha}{C_e} \right)^{1/2} \exp(-z/\delta) \tag{1.11}$$

where $F_a = I_0 A \tau_p$ is the absorbed laser fluence ($I(t) = I_0$ is assumed constant) and $\delta = 2/\alpha$ is the laser penetration skin depth.

To summarise the discussion above, the transfer of energy to the lattice through electron cooling results in lattice heating and in just a few picoseconds, the irradiated material transitions from a solid to a dense plasma, followed by explosive expansion. Due to the short time scale involved in this process, thermal conduction into the bulk of the material is insignificant and ultrashort pulsed laser ablation can be said to be a-thermal to a first approximation.

Figure 1.1 shows the timeline of the totality of the complex processes involved in laser ablation, including carrier excitation, thermalisation, carrier recombination, and sample modification. This illustrates the degree to which ultrashort pulsed laser ablation is in general, a complex, multi-step process. The individual processes involved depend very much on the material undergoing ablation. Metals, semiconductors, and dielectrics all respond uniquely to ultrashort pulse illumination and while interesting, the precise details of ultrashort pulsed laser ablation in each material system are beyond the scope of this dissertation. For the interested reader, Shirk et al [2], Lenzner et al. [7], Sundaram et al. [6], and Joglekar et al. [8] all provide good reviews on the topic.

1.2 Thesis Structure

Following the introduction provided here, Chapter 2 gives a comprehensive review of the existing literature on laser-induced processes performed in a variety of atmospheres. The first section of the review covers laser ablation, providing context for Chapters 3 and 4. A great deal of this literature concerns itself with the nature of the material removed during laser ablation, the formation of a plasma plume, and

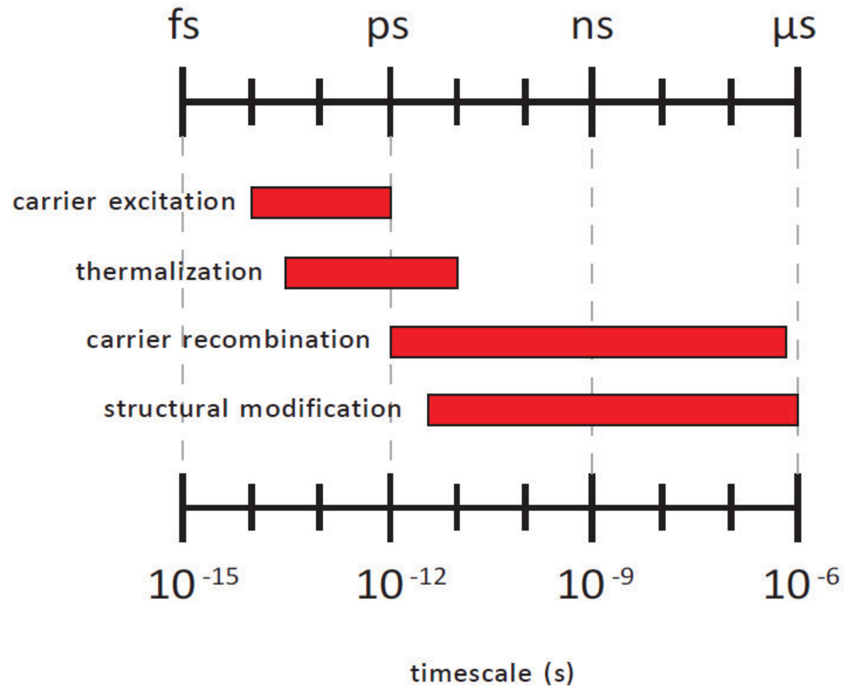

Figure 1.1. Ultrashort pulsed laser ablation is a complex multi-step process involving: (i) carrier excitation via multi-photon absorption, single photon absorption, Zener tunnelling, free carrier absorption (metals), and/or avalanche ionisation; (ii) thermalisation due to carrier-carrier and carrier-phonon scattering; (iii) carrier depletion via radiative, auger, defect, and surface recombination, and diffusion; and (iv) structural modification due to ablation, melting, thermal diffusion, and resolidification [6].

the interaction of the ablated material with the atmosphere in which the ablation is performed. As will be evident, though, very little work has been done studying laser ablation in reactive environments. The second part of Chapter 2 reviews the literature on ultrashort pulsed laser-induced deposition, providing context for Chapter 6.

In Chapters 3 and 4, we extend the current body of literature detailing the effects of background gases on the laser-induced plume of materials ejected during ablation by investigating UPLA in a background gas which has the potential to be reactive. Starting in Chapter 3, we begin by identifying a model system on which experiments are performed. The model system – silicon dioxide (SiO_2) and xenon difluoride (XeF_2) – consists of a substrate and a reactive gas, or precursor, which

have scientific and industrial importance, but do not react with one another spontaneously. The use of a material transparent to visible light is made possible by the non-linear response of the material to the extremely high peak powers produced by ultrashort pulses. After a discussion of the instrumentation used to perform the experiments, experimental evidence of a laser-induced chemical reaction is given, raising the question of whether the reaction occurs in the gas-phase or at the surface. A model is put forth, suggesting that the reaction is a gas-phase one, and experimental evidence is given to support this hypothesis.

While the results presented in Chapter 3 are suggestive, they are by no means conclusive. In Chapter 4, the physical characteristics, components, and dynamics of the plasma plume induced during UPLA of SiO_2 are characterised in both XeF_2 and inert atmospheres. Laser-induced breakdown spectroscopy (LIBS), fast photography, plasma diagnostics, and comparison of the data to existing models all provide further evidence for a gas-phase reaction. Mass spectroscopy is used to identify the reaction by-products and a reaction pathway based on all the experimental evidence is put forth.

Over the course of the work discussed in this dissertation, a complex scientific instrument ideally suited for the investigation of the interaction of light and matter was developed. In Chapter 5, a detailed description of the design and development of this instrument is given. The description begins by outlining the system's major components – an ultrashort pulsed laser system, a focused ion beam, and a scanning electron microscope – and their theories of operation. The chapter then goes on to outline the sub-systems designed in order to integrate these components. Finally, as a brief example of just some of the many potential capabilities of the so-called TripleBeam system, we discuss its application to three dimensional materials characterisation after first providing some background on the technique.

In Chapter 6, we bring the discussion back to the topic at hand by applying the TripleBeam system to the exploration of ultrashort pulsed laser-induced surface chemistry. After a brief discussion of photolytic and pyrolytic dissociation mechanisms, experimental evidence is given of UPL-induced deposition of platinum on a variety of substrates. A dependency of the deposit morphology on the substrate type provides evidence of different dissociation mechanisms, including a surface plasmon-mediated process. Finally, a novel deposition technique is presented in which a thin

template deposited via electron beam-induced deposition is used to spatially define and increase the rate of the the laser-induced deposition.

Chapter 2

Pulsed Laser-Induced Processes in Various Ambient Environments

2.1 Introduction

The development of chirped pulse amplification (CPA) in the mid-1980's by Strickland and Mourou [9] provided an ideal tool for the study of the fundamental physics of the interaction of light and matter. Since then, ultrashort pulsed laser processes have been thoroughly investigated over a wide range of laser parameters (wavelength, pulse duration, repetition rate, fluence, and varying scan parameters) on a wide variety of materials (metals, semiconductors, dielectrics, polymers, oxides, and biological and geological samples), in different environments (ambient, vacuum, and inert atmospheres), and by numerous methods (time-resolved reflectivity, transmission spectroscopy, photoemission spectroscopy, second harmonic generation, and fast photography), and for a number of applications (micromachining, spectroscopy, plasmonic, and femtochemistry). As a result, a vast body of literature exists on UPL-induced phenomena. The particular focus of this dissertation involves (i) laser ablation in reactive gas environments and (ii) the interaction of ultrashort pulses and reactive molecules adsorbed to surfaces. A review of the existing literature relevant to these two topics follows.

2.2 Ablation

Building on earlier work exploring fast phase transitions in optically excited silicon by Shank et al. [10, 11], Downer et al. [12] performed time-resolved pump-probe reflectivity experiments on silicon [111] ablated with ultrashort laser pulses having a duration of 80 fs and a wavelength λ of 620 nm. Prior to excitation of the sample, the beam was divided by a 50% beam splitter and focused into water to generate a white light continuum for use as a probe. Upon photoexitation of the silicon with a 500 mJ/cm^2 laser pulse, an increasingly bright region was observed at the excitation site at time delays of 1 ps and less. Attributing the bright region to the reflection of all wavelengths in the probe continuum by molten silicon, the authors concluded that the sample undergoes melt in the first picosecond after excitation. A dark region appearing after 10 ps, maximising at around 50 ps, and persisting until about 550 ps is attributed to the ejection of an optically dense plume of material from the melted surface. Time-resolved spectral analysis of the transmitted light showed a monotonic increase from blue to red, rather than the discrete absorption lines one would expect if isolated atoms were undergoing state transitions. For this reason, the authors concluded that the ejected plume consisted of small (several hundred angstrom), multi-atom droplets of molten silicon which became atomised several hundred picoseconds later.

In a series of experiments using time-of-flight mass spectroscopy to explore melting and ablation in semiconductors irradiated with ultrashort pulsed lasers, Cavalleri et al. [13] showed that ions and neutral atoms are ejected from silicon and gallium arsenide (GaAs) targets illuminated with 100 to 120 fs pulses having a wavelength of $\lambda = 620$ nm in ultra high vacuum (10^{-10} Torr). The authors used fluences ranging from 50 to 500 mJ/cm^2, explicitly staying well below the threshold for plasma formation, which they place at approximately 1 J/cm^2. Within these fluence limits, they identify three unique fluence ϕ ranges. The very lowest fluences were found to be below the melting threshold, fluences in the middle range were between the melting threshold and the ablation threshold, and the highest fluences were above the ablation threshold. They showed that at fluences below the ablation threshold ($\phi/\phi_{th} < 1$), the rate of change with fluence of particles desorbed through sublimation or photo-induced evaporation (i.e. $dN/d\phi$ where N is the number of particles desorbed) depended heavily on the material under study. Specifically, they found

that the total number of particles produced was lower for silicon than it was for GaAs at the same normalised fluence, but that the yield increased more rapidly for silicon as the applied fluence approached the ablation threshold. At fluences greater than the ablation threshold ($\phi/\phi_{th} > 1$), $dN/d\phi$ was nearly identical for Si and GaAs. They also found that, at the range of fluences over which the experiments were conducted, the ion yield was at least an order of magnitude lower than the neutral yield for both Si and GaAs. For GaAs, the authors observed only single atoms (both ions and neutrals) of gallium, whereas clusters of up to four atoms were observed for arsenic. Arsenic clusters larger than 4 atoms have masses that exceed the limit of those observable by the mass spectrometer employed. Molecules composed of up to six atoms were observed for Si. The ratio of atomic to diatomic silicon (S_1/S_2) was found to be a decreasing function of fluence, with S_1/S_2 being on the order of 100 below threshold, around 28 at ϕ_{th}, and 8 at 1.5 ϕ_{th}.

In a series of pump-probe experiments on crystalline silicon in air, Choi and Grigoropoulos [14] characterised the formation and propagation of the atmospheric shock wave generated during ablation. Capturing time-resolved shadowgraphs, they showed that the shock wave first becomes visible at around 10 to 50 ps after the arrival of the pump pulse. Interestingly, the ablation-induced surface modification was not observable until 28.9 ns after the arrival of the pump pulse. The authors attribute the initial shock wave formation to the presence of energetic electrons having sufficient energy to overcome the work function of silicon, thereby being liberated from the target. Shadowgraphs taken at longer elapsed times revealed a slower shock wave that propagates through the ambient gas, evolving over the course of tens of nanoseconds. Assuming an ideal gas with a constant specific heat and density and a point source release of energy, they estimated the energy released by this shock wave to be between 10% and 17% of the incident laser energy. Using the estimated energy, they then calculated the pressure, temperature, and propagation velocity of the shock wave at a time delay of approximately 20 ns to be 140 to 220 atm, 0.6 to 0.9 eV, and 0.15×10^6 to 0.25×10^6 cm/s respectively (for fluences between 1.0 and 1.5 J/cm^2). After about 100 ns, the shock wave pressure decayed to ambient pressure. The authors make no further claims regarding the composition of the shock wave.

Using a laser source having a titanium doped monocrystalline sapphire (Al_2O_3)

(Ti:Sapphire) gain medium and capable of producing 120 fs pulses at a wavelength of 780 nm, Amoruso et al. [15] ablated silicon targets in vacuum (10^{-7} mbar). The plasma plume generated via ablation with a 0.5 J/cm^2 pulse was viewed through a window in the vacuum chamber. Time-resolved analysis of the light emitted by the plume at a fixed distance from the sample was performed through the use of a fast-gated intensified charged coupled device (ICCD) camera attached to a spectrometer. The authors' analysis suggest that the laser-induced plasma plume is composed of two components. The presence of clear emission lines at time delays less than 100 ns suggest a fast component composed mainly of neutral atoms and ions having velocities of approximately 10^6 cm/s. A structureless broad continuum emission at longer time delays reveals a slow component having velocities of approximately 10^4 cm/s that the authors associate with the formation of nanoparticles. This is considerably slower than the velocity calculated by Choi and Grigoropoulos [14] for the slow component of laser-induced shock waves generated in air. Measured emission from the nanoparticle component was well described by a blackbody radiation model. Tapping mode atomic force microscope (AFM) analysis of nanoparticles deposited on a mica substrate during an ablation event showed a distribution of radii ranging from 5 to 25 nm with a maximum at 7 nm. The authors state that an analysis of the optical emission as a function of fluence showed that reducing the laser fluence eliminated the observable presence of radiative emission lines characteristic of the atomic plume and that only the continuum emission was seen at these low fluences. However, no data is presented supporting the claim. According to the authors, this suggests that nanoparticles do not form in the gas-phase through condensation of the ablative atomic vapour, but are instead the result of "ultrashort melting and consequent expansion into vacuum of the material driven to extremely high temperatures and pressures by the intense fs laser pulse."

In a follow on paper, Amoruso et al. [16] further studied the flux of ions generated during ultrashort pulsed laser ablation of silicon in high vacuum (10^{-7} mbar). Using the same laser as that used in the work discussed above, they performed single shot ablation of silicon over a range of fluences extending from 0.16 J/cm^2 to 0.86 J/cm^2. The ion flux from each ablation experiment was collected by a Langmuir probe located 45 mm from the target. The probe consisted of a 2 mm $\times$ 2 mm square copper plate biased to -20 V. The time-resolved ion current was measured

by monitoring the voltage drop across a load resistor with a digital oscilloscope. The data collected showed the presence of two peaks at laser fluences greater than 0.3 J/cm^2. Making the implicit assumption that both ion components are ejected simultaneously at the moment of irradiation, the authors calculated the mean velocity of the so-called "fast" component to be 5×10^6 to 1×10^7 cm/s. The velocity of the "slow" ion population was calculated to be on the order of 10^6 cm/s. At fluences below 0.3 J/cm^2, only the fast component was observable. While the authors discuss the possible impact on the data of ion-induced secondary electrons at the probe, no data is presented to support their claim that "the fractional yield of secondary electrons produced by high-energy ions...[is] less than 1% and...can be considered negligible." In addition, the authors used a time-gated ICCD equipped spectrometer to show that the fast component is composed exclusively of ions while the the slow component is made up of both ions and neutrals. Measuring the flux of ions as a function of laser fluence and linearly extrapolating this data to zero, the authors go on to claim that the threshold for the generation of the high energy population of ions agrees with the threshold for "non-thermal melting" quoted in other literature, while the threshold for the emission of the low energy population of ions is similar to quoted values for the ablation threshold of silicon.

In a paper published in 1998, Her et al. [17] reported that silicon irradiated with 1 J/cm^2, 100 fs pulses having a wavelength of 800 nm in sulphur hexafluoride (SF_6) or Cl_2 atmospheres (500 Torr) spontaneously form regular arrays of sharp conical spikes topped with small spheres as shown in Figure 2.1. Control experiments performed in vacuum (10^{-4} Torr), N_2, and He (both at 500 Torr) showed that the effect is indeed gas dependent, indicating that a chemical reaction contributes to the spikes' formation. Subsequent work by numerous authors [18, 19, 20, 21, 22] shows that the effect is due to both laser ablation and laser-assisted chemical etching. Specifically, Nayak et al. [21] noted that the early stage development of the spikes is gas-independent and is due to ablation, whereas the later stage morphology occurs only in the presence of reactive gases. While laser-assisted chemical etching is generally considered a surface reaction between the substrate and adsorbed surface molecules, Riedel et al. [19] suggest that "gas-phase collisional, chemical and photochemical processes" may be involved in the etch process. Wen et al. [22] performed transmission electron microscope (TEM) analysis and energy dispersive

X-ray spectroscopy (EDS) on silicon samples processed in this fashion revealing the presence of sulphur dopants concentrated mainly in the outer layer of the tips of the spikes. Nayak et al. [23, 24] also showed that morphologically similar features can be formed on germanium irradiated with ultrashort laser pulses in SF_6 or hydrochloric acid (HCl) atmospheres.

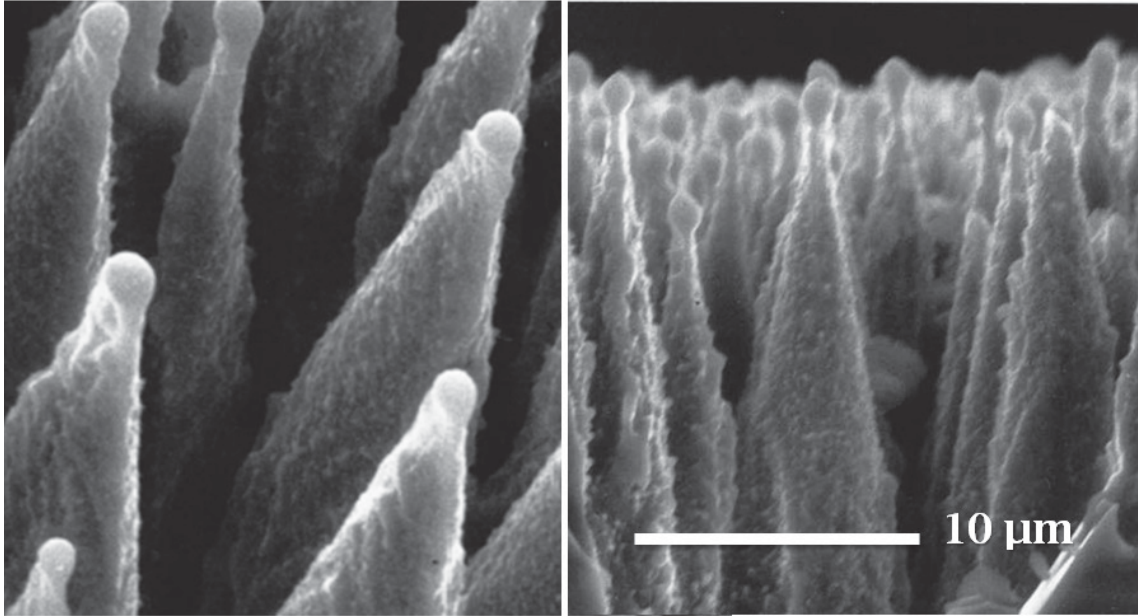

Figure 2.1. Silicon microstructures formed via ultrashort pulsed laser processing in an SF_6 atmosphere. Silicon processed in this fashion is often referred to as "black silicon" due to its enhanced optical absorption over much of the infrared and visible spectrum. Images taken from Her et al. [17].

In two very relevant papers, Issac et al. [25, 26] performed time-resolved Langmuir probe measurements of electron emission during the irradiation of silver targets with 10 ns pulses from a neodymium-doped yttrium aluminium garnet (Nd:YAG) laser (λ = 1.06 μm) in nitrogen, argon, and carbon dioxide atmospheres. The authors showed evidence of two distinct populations of emitted electrons. The distribution of the first population was a sharp one with a temporal width of about 10 ns closely tracking the temporal profile of the laser pulse. The authors referred to these electrons as prompt electrons and measured them to have a maximum temperature of about 60±5 eV. The second distribution was smaller in amplitude and

longer in duration (several μs) and appeared after the laser pulse was no longer incident on the sample. These electrons had a temperature of about 2$\pm$0.5 eV. The authors attributed the first population to photoexcited hot electrons escaping the laser-sample interaction volume before the laser energy is transferred to the lattice through collisions. The second population was attributed to plasma electrons. Time-resolved emission spectroscopy revealed that the laser-induced plasma was preceded by an ionised ambient gas plasma. Monitoring the emission line from ArII at 480.6 nm, they further showed that the density of the prompt electron pulse increased with distance from the sample, suggesting that collisional ionisation of the ambient gas molecules yields additional electrons (i.e. $Ar + e^- \rightarrow Ar^+ + 2e^-$). The electron density peaked at approximately 0.7 cm from the sample surface, attaining a steady-state value of approximately 3.4×10^{17} cm^{-3}. Plotting the probe current against laser intensity, the authors found that the current saturates at approximately 13×10^{10} W cm^{-2}. They suggest that this is due to plasma screening of the laser pulse wherein the optical intensity available at the sample is blocked by the increasingly dense laser-induced plasma.

Albert et al. [27] compared laser-induced plasma plumes generated by nanosecond (τ_p = 10 ns) and femtosecond (τ_p = 80 fs) ablation of titanium in vacuum (10^{-6} mbar). The authors were careful to use fluences calibrated to produce comparable ablation rates in spite of the difference in pulse duration. Using fast photography methods, the authors noted that plumes produced by femtosecond (fs) laser ablation were more spatially confined than those produced by nanosecond (ns) laser ablation. Given the ablation rate calibration, this indicated that the fs-induced plumes had higher densities. Time-resolved optical emission spectroscopy measurements were performed on each plume by imaging a slice of the plume onto the entrance slit of a spectrometer equipped with a fast gated ICCD. These measurements were made at 5 mm from the sample surface allowing the authors to calculate the velocity of the plume. Species temperatures were estimated by assuming that the plasma was in partial local thermal equilibrium and that the electron density was greater than 10^{16} cm^{-3}.

Three distinct plume components were observed for fs ablation versus two plume components for ns ablation. The first fs component had a velocity of 8×10^6 cm/s and was found to be composed entirely of Ti^+ ions. The temperature was estimated to be

50,000 K. This is considerably larger than other UPL-induced plasma temperatures quoted in the literature. The second fs component had a velocity of $2{\times}10^6$ cm/s and composed of Ti neutrals. The third fs component was composed of nanoparticles as evidenced by the observation of a broad continuum emission similar to that seen by Amoruso et al. [15] for silicon ablation using ultrashort pulses. By fitting the spectrum to a black-body radiation model, the temperature of the nanoparticle plume was estimated to be 4800 K . The authors measured the velocity of the nanoparticle plume to be less than 10^5 cm/s.

The faster of the two ns laser-induced plume components that Albert et al. measured was composed of both Ti and Ti^+ species and some higher ionisation states formed during the ns pulse's interaction with the plume. The average velocity of this component was 10^6 cm/s and the temperature was estimated at 10,000 K. While the authors show velocity data for the second ns plume component, they do not reference it in the text and make no mention of its composition. They do, however, compare the third fs plume component – the one comprised of nanoparticles – to "the droplets which are ejected from the target a long time (a few μs) after the nanosecond pulse interaction" stating that no spectral emission from the droplets can be observed. They further conclude that the nanoparticles observed during fs laser ablation form in the gas phase, making the argument that the density of the fs plume is sufficient for them to form through condensation as the plasma expands into the vacuum and cools. No direct evidence is given for this conclusion other than that analysis of the nanoparticles formed by fs ablation are smaller (10 to 100 nm) than those formed by ns ablation and are shown to have oxygen incorporated (1:0.55), presumably from residual oxygen present in the vacuum.

Harilal et al. [28] used a fast-gated ICCD to make time-resolved images of plasma plumes generated via nanosecond laser ablation of aluminium in a range of air pressures from 10^{-6} to 100 Torr. Free expansion of the plume was observed up to pressures of about 10^{-1} Torr. Unlike the results from Albert et al. [27], only one plume was observed in vacuum-like conditions. Above 10^{-1} Torr, separate fast and slow moving plumes were observed. The authors claim that this is also the pressure range at which collisionless expansion of the plume transitions to collisional expansion as supported by the amplification of the emission at these pressure levels. They argue that kinetic energy is transferred to the background gas from the laser-induced

plasma via ion-ion Coulomb scattering, ion-neutral collisions, charge exchange, etc. One result of the interaction is the deceleration of the plume and the appearance of turbulence. Turbulence was maximised in these experiments at around 1 Torr. A model is proposed to account for plume expansion with turbulence (this provides the foundation for the simple model developed by Amoruso et al. [29]). Shock and drag models are included to account for the release of energy into the background gas and the slowing of the plume respectively. Two models were used to calculate the plume length: an adiabatic expansion model and a model using the software package Stopping Range of Ions in Matter (SRIM). Comparison to data shows that SRIM is valid for low pressure regimes only. Time and space resolved laser-induced breakdown spectroscopy showed that the plume is composed of neutrals (Al) and ions (both Al^+ and Al^{++}). These experiments also revealed the splitting of the fast atomic plume. However, they claim that the splitting occurs for Al and Al^+ separately (i.e. there are fast and slow components for each species) as opposed to a fast component comprised of Al^+ and a slow component of Al as proposed by Albert et al. [27]. They estimate the velocities of the fast Al^+ and fast Al plumes at 7.6×10^6 and 6.5×10^6 cm/s (800 and 650 eV) respectively. They also observed enhanced emission from the inner region of the plume. They attribute this to the tendency of the plasma in this region to remain in a more dense state for a longer period of time, thereby undergoing more recombination events than the ions located at the front of the plasma. Gas-phase reactions forming AlO and AlN are mentioned in passing, but no further analysis of this phenomenon is undertaken.

Amoruso et al. [30] ablated nickel and silicon targets in vacuum with laser pulses having durations ranging from 100 to 900 fs in order to study the differences in plume expansion in vacuum and nanoparticle formation. Fast photographic and LIBS analysis again revealed the existence of slow and fast components of the plume. The slow component was found to be composed of nanoparticles and moved with an expansion velocity on the order of 10^4 cm/s. The fast component was further observed to be divided into fast and slow sub-components. The fast-fast plume was made up of ions, while the slow-fast component was made up of neutrals *and* ions. Measurements of the velocity as a function of laser fluence of each component reveal behaviour similar to that observed later by Noel et al. [31]; namely, that the velocity of atoms increases with fluence while the velocity of nanoparticles decreases slightly with fluence for

the range of fluences explored (i.e. up to 0.75 J/cm^2 or "near threshold" – Noel et al. showed that above about 1.0 J/cm^2, the velocities of each are flat with fluence). The authors also observed that the velocities of both the nanoparticle and atomic plumes are independent of pulse duration (i.e. plumes generated with similar fluences have similar velocities independent of pulse duration). This lead them to conclude that laser ablation in the range of fluences explored results in a characteristic dual-plume where the fast component is made of atomic species (ions and neutrals) and the slow component is made of nanoparticles independent of the wavelength or fluence used, or the target material irradiated. Nanoparticle size distributions were measured via AFM. The radii of nickel nanoparticles ranged from a few to 50 nm while the radii of Si nanoparticles ranged from a few to 30 nm. Size distribution was found to be independent of pulse duration (for the range 100 fs to 1 ps) and wavelength (visible to IR). Of particular interest is the authors' assertion that the velocity differences observed between the nanoparticle and atomic plumes suggests that nanoparticles do not form via condensation in the gas phase, contrary to the conclusions drawn by Albert et al. [27]. Instead, they claim that nanoparticles are primarily generated during "the relaxation of the extreme material state created by the intense...pulse."

With the stated goal of studying the mitigation of "ion debris" during laser ablation, Harilal et al. [32] performed nanosecond laser ablation (τ_p = 10 ns pulse at λ = 1064 nm) of tin targets in both vacuum and an argon atmosphere. Spatio-temporal optical emission spectroscopy and fast photography were used to analyse the plume. Ion and electron emissions were analysed with a Faraday cup. Showing relatively good agreement with the work of Amoruso et al., the authors of this study found that the plasma plume was composed a slow component made up of energetic tin neutrals (Sn) and a faster component made up of ions (Sn^+) with respective velocities of $(8\pm0.3)\times10^5$ cm/s (40 eV) and $(1.8\pm0.1)\times10^6$ cm/s (200 eV) in vacuum. Citing earlier work, the authors claim that ions have higher kinetic energy than neutrals due to space charge. They also attribute at least some of the neutrals to the recombination of plasma ions. With the addition of ambient argon, the authors identify three distinct pressure regimes: 1) low pressure (vacuum) characterised by free expansion, 2) intermediate pressures (transition regime) characterised by "strong inter-penetration of the plasma species and background gas that leads to plume splitting and sharpening", and 3) high-pressures where the plume is stopped

and the particles thermalise. Similar to the study by Amoruso et al. of ultrashort pulsed laser ablation of nickel in vacuum [30], they further observe the splitting of the Sn^+ component of the plume into fast and slow sub-components. However, *unlike* Amoruso et al., they only observe this phenomenon with the addition of a background gas (note that Harilal et al. performed nanosecond laser ablation rather than ultrashort pulsed laser ablation). Strangely, they measure the fast Sn^+ component to be faster than the (single) Sn component during free expansion in vacuum ($(3.2\pm0.1)\times10^6$ cm/s (650 eV) – twice as fast or 3 times the energy). No good explanation is given for this. In addition, they observe the ionisation of the ambient argon, also split into fast and slow components. They posit that the fast component may be attributable to the excitation of argon atoms by fast photoelectrons. Using the Faraday cup to measure fast ion velocity, they show much higher values than those measured using optical time-of-flight techniques (4.3×10^6 cm/s). The discussion of this result is somewhat ambiguous and no good explanation is given. One observation not made by the authors, but apparent in their fast photographic data is the difference in the location of the self-emission between the plume observed in 100 mTorr argon and that observed in 300 mTorr argon. The former is more confined to the substrate surface, while the latter is seen increasingly at the front of the plume as it evolves.

Fast photography of ultrashort pulsed laser ablation ($\tau_p = 100$ fs at $\lambda = 800$ nm) of copper and gold targets in vacuum (10^{-4} Pa) by Noel et al. [31] again revealed fast and slow plume components each with different expansion dynamics. In particular, it was observed that the slow component remains in contact with the target surface, while the fast component separates from it. Due to its smaller atomic weight, the expansion velocity of both components was larger for copper than for gold (i.e. lighter particles expand faster). Using spatially resolved LIBS during laser ablation of copper, the authors were able to determine that the slow component is composed of nanoparticles and the fast component of atoms. In addition, they noted the existence of a Cu^+ line that propagated faster than the copper neutral line, suggesting that the atomic plume is itself split into two parts (fast ions and slower neutrals), similar to that seen by other researchers [27, 30, 32]. By showing that the ablation rate (the ablated depth per laser pulse) as a function of fluence is proportional to the integrated plume intensity as a function of fluence for a given delay, the authors

conclude that the temperature of the plume is nearly independent of laser fluence, since “in the case of an optically thin plasma, the plume intensity increases linearly with the number of emitters.” They also compare their ablation rate data to that of Nolte et al. [3] to conclude that ablation rate is independent of pulse duration as long as the pulse duration is much shorter than the electron-lattice relaxation time. The authors then show that the ablation efficiency (the number of ablated atoms per pulse) and the atomisation stage (the ratio between atomised mass and total ablated mass as estimated from intensities) are strongly correlated, with the atomisation stage decreasing with increasing ablation efficiency. They claim that this is due to the fact that total atomisation requires more energy than nanoparticle formation, whereas high ablation efficiency requires large rates of material removal and is the result of the ablation in the thermal regime. From this the reader can infer that the authors discount the notion that nanoparticles form due to condensation in the gas phase (as suggested by Albert et al. [27]) and instead are ejected from the target surface during aggressive ablation. Further notice is taken of the fact that, while ion velocity increases with laser fluence near the ablation threshold and nanoparticle velocity decreases with fluence near threshold, there is only a weak dependence of the velocities of both components on increasing fluence. This suggests that the plasma temperature is independent of laser fluence. Finally, AFM analysis of Cu nanoparticles generated suggest that particles smaller than 7 nm are directly ejected from the substrate, while larger particles are formed by collisions and that by increasing laser fluence, larger particles are formed.

In another paper using fast photography to explore the dynamics of plumes produced by ultrashort pulsed laser ablation ($\tau_p = 300$ fs, $\lambda = 527$ nm) at a fluence ϕ of 0.6 J/cm^2, Amoruso et al. [29] ablated iron substrates in both vacuum and in background gases. The authors again identified two plume components: (i) an early cloud of fast atomic species and (ii) a slower cloud of nanoparticles. Plotting the visible (due to self-emission) plume front position versus time, they estimate the expansion velocity of the atomic component in vacuum (3×10^-6 mbar) to be approximately $(1.6\pm0.1)\times10^4$ m/s. The nanoparticle velocity is estimated to be approximately $(5.2\pm0.2)\times10^2$ m/s at the same pressures. At higher gas pressures, the atomic plume became more hemispherical and self-emission was confined to the plume front. The authors analyse their data using a simple Newtonian model where

they balance the force due to gas pressure with time rate of change of momentum of the plume. For the atomic component, this takes the form

$$\frac{d}{dt}\left[\left(M_a+\frac{2}{3}\pi\rho_g R\left(t\right)^3\right)u_a\left(t\right)\right]=-2\pi R\left(t\right)^2 p_g,\quad \frac{dR}{dt}=u_a\left(t\right) \tag{2.1}$$

where M_a is the mass of the atomic plume, ρ_g is the ambient gas density, p_g is the background gas pressure, R is the radius of the expanding plume front, and u_a is its velocity. The initial conditions are $R\left(0\right)=0$ and $u_a\left(0\right)=u_{a,0}$. The mass of the gas swept away by the expanding plume at a distance R and a time t is given by the term $2/3\pi\rho_g R\left(t\right)^3$. Fitting the model to the data, the authors estimated the mass of the atomic plume, M_a, to be $(1.0 \pm 0.1) \times 10^{-11}$ kg.

For the nanoparticle plume dynamics, they considered a one dimensional (x) case wherein the plume is confined in a forward layer and acts on the ambient gas as a piston of mass M_n and cross-section S such that

$$\frac{d}{dt}\left[\left(\frac{M_n}{S}+\rho_g x\left(t\right)\right)u_n\left(t\right)\right]-p_g,\quad \frac{dx}{dt}=u_n\left(t\right). \tag{2.2}$$

Here the initial conditions are $x\left(0\right)=0$ and $u_n\left(0\right)=u_{n,0}$. Again fitting the model to their data, the authors estimated the mass of the nanoparticle plume component, (M_n) to be $(4.8 \pm 0.6) \times 10^{-11}$ kg. Thus, they posit that the ablated material is made up of $\approx 80\%$ nanoparticles and $\approx 20\%$ atoms.

Using a fast photomultiplier optically coupled to a system for imaging the ablation region, Lehecka et al. [33] studied the duration of light emission from copper and aluminium targets ablated with ultrashort pulses ($\tau_p \approx 200$ fs) in both air and a low pressure atmosphere of approximately 4 Torr. The authors showed that emission from the laser-induced plasma is longer-lived and more intense in air than it is in vacuum. They attribute this to the excitation of the air molecules as the expanding material couples energy to the ambient environment 10 to 1000 ps after the target absorbs the laser pulse. This initial expansion is largely one dimensional. As the expansion continues, it transitions into a three dimensional shockwave at around 1 to 30 ns after excitation. The authors further claim that air heated by this shockwave contributes to the long duration light emission which they observed lasting 100's of nanoseconds. Curiously, other authors [31, 29] have measured emission durations in excess of 10's of microseconds.

With the intent of measuring the kinetic energy of the plasma plume produced by nanosecond laser ablation, the stopping power of a buffer gas, and the cross-section of the interaction between the two, Bleiner et al. [34] performed pump-probe shadowgraphy of laser-induced tin plasmas in argon (at standard temperature and pressure) using a 25 ns pump beam at λ = 308 nm and a 6 ns probe beam at λ = 532 nm. The authors measured the kinetic energy of the the plume to be as high as 1.1 keV at angles normal to sample. Thermalising collisions with the argon buffer gas were found to reduce the plume's kinetic energy and this stopping power was found to be as high as 0.4 eV/mm. However, the stopping power of the gas was found to scale with kinetic energy (i.e. the stopping power is higher with faster particles). A collision cross-section σ of 1.3×10^{-5} barn was calculated at the steady-state.

Rather than focusing on the interaction between ablated material and the atmosphere in which the ablation is performed, Sun and Longtin [35] turned their attention to the effect of ambient gas on the delivery of the laser pulse. Using a Ti:sapphire laser having a pulse duration of 150 fs, they ablated copper targets in various gas atmospheres with the intent of exploring how spot quality (and ultimately feature quality) is altered if processing is done in gases with different breakdown thresholds. The authors' hypothesis was that plasma formation during the delivery of the pulse compromises spot quality via plasma-induced defocusing, self-phase modulation, and filamentation. The authors suggest that processing done in gases with higher breakdown thresholds is less likely to result in the plasma formation they attribute to compromised spot quality. Hence, 3000-shot holes were laser drilled in copper samples with a spot having a diameter of 50 μm. The intensity was quoted as 1.6×10^{14} W/cm^2, but no pulse energy was given. Holes were drilled in air, neon, nitrogen, and helium atmospheres at atmospheric pressure with a flow rate of approximately 25 cc/s for nitrogen, neon, and helium. Helium proved to yield the best results, especially as measured by the amount of debris left at the ablation site. The authors suggest that this is due to "the lower plasma generation in helium, resulting in the smallest resistance to ablated material." The authors also claim that the size of the features made in helium was smaller, but offered only one example to support this claim. It is not clearly the case that this one example is smaller than the rest.

Perrie et al. [36] followed up on Sun and Longtin's paper by machining 500 to

600 μm boxes in aluminium with an identical laser. All processing was done under flowing He ($\approx$ 30 cm^3/sec). One of the parameters the authors used to specify their process was energy deposited per unit area per second (average power density, W/cm^2) given by $\langle$ I $\rangle$ $\approx (\nu_L E_p/d\ s)$ where ν_L is the repetition rate of the laser, E_p is the pulse energy, d is the spot diameter, and s is the scan speed. The authors' conclusions include i) due to its low melting point, high thermal conductivity, and tendency to rapidly oxidise, Al is difficult to micromachine, ii) because it minimises plasma breakdown, reduces oxidation, and removes fine debris, helium is of "major benefit" when micromachining Al, iii) cut quality is improved and the debris produced is made finer with lower fluence and smaller average scanned power densities, and iv) the threshold fluence for Al is $\phi_{th} \approx 400$ mJ/cm^2 for 180 fs pulses at $\lambda = 775$ nm. The scan patterns this group used to do this evaluation are very similar to the ones used in the reactive gas work described in Chapter 3.

In one of the few papers where ablation is performed in a reactive gas, Sajad et al. [37] study the decomposition of SF_6 in the vicinity of laser ablated SiO_2. Focusing a nanosecond excimer laser (τ_p = 8 ns) 3 mm above an SiO_2 sample in an SF_6 atmosphere , Sajad et al. observed modification of the SiO_2 surface. Using Fourier transform infrared spectroscopy (FTIR), they monitored the concentration of SF_6 molecules in the gas chamber during irradiation of the sample, noting a marked decrease in concentration over time. Three different laser gain mediums (producing three different wavelengths) – ArF (193 nm), KrF (248 nm), and XeF (251 nm) – were used to explore the wavelength dependency of the effect. At only the two highest energy wavelengths – namely, 193 and 248 nm – was the effect observed and its rate was significantly increased at 193 nm. The rate of the effect (i.e. the decrease in SF_6 concentration) was observed to increase with increasing laser fluence, but decrease with increasing pressure. Because no dissociation of SF_6 was observed when the laser was focused into the gas without the presence of SiO_2 nearby, the authors conclude that ablation of the SiO_2 in the presence of SF_6 lead to the decomposition of the SF_6. They further note a difference in the induced morphology when ablation was performed in noble gas atmospheres of helium and argon. EDS analysis of the SiO_2 surface after ablation revealed a relatively high fluorine content. It is somewhat unclear from their discussion whether the authors consider the reaction a surface or gas-phase one, but ultimately they characterise the

reaction as one between gas-phase SF_6 molecules and an SiO_2 surface made reactive by laser irradiation such that

$$\mathrm{SiO_2} + h\nu \rightarrow \mathrm{Si}^* + 2\mathrm{O}^* \quad \text{(ablation)} \tag{2.3}$$

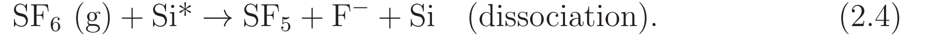

$$\mathrm{SF_6}\ (\mathrm{g}) + \mathrm{Si}^* \rightarrow \mathrm{SF_5} + \mathrm{F}^- + \mathrm{Si} \quad \text{(dissociation).} \tag{2.4}$$

where "*" indicates an excited state. According to the authors, the F^- atoms generated in the dissociation process of Equation 2.4 penetrate into the substrate such that

$$\mathrm{SiO_2(s)} + 2\mathrm{F}^- \rightarrow \mathrm{SiF_2} + \mathrm{O_2} \quad \text{(adsorption)} \tag{2.5}$$

$$\mathrm{SiF_2(ads.)} + \mathrm{SiF_2(ads.)} \rightarrow \mathrm{SiF_4(ads.)} \quad \text{(adsorption)} \tag{2.6}$$

$$\mathrm{SiF_4(ads.)} \rightarrow \mathrm{SiF_4(g)} \quad \text{(volatilisation).} \tag{2.7}$$

Finally, they make the claim that the SF_5 formed via dissociation in Equation 2.4 spontaneously combines in the gas phase to produce S_2F_{10}, which they observed as a "type of white dust, deposited throughout the walls." Oddly, though the authors note the presence of ablation at equivalent fluences in He and Ar atmospheres (rather than just material volatilisation via chemistry), they ignore the possibility of gas phase reactions between ablated silicon and fluorine liberated by the dissociation process detailed in Equation 2.4.

2.3 Deposition

Laser-induced deposition of metals (and more seldom, dielectrics) employing continuous wave (CW) lasers is a mature technology with a significant body of literature. A number of good reviews exist, including those by Rytz-Froidevaux et al. [38], Houle [39], and Herman [40] and a more detailed discussion of the technology is given in Chapter 6. On the topic of ultrashort pulsed laser-induced deposition, however, there is very little in the literature to be found.

Haight et al. [41] deposited sub-diffraction limited chromium lines on a variety of substrates via ultrashort pulsed laser irradiation (τ_p = 120 fs, λ = 400 nm) of said substrate bathed in gaseous chromium hexacarbonyl ($Cr(CO)_6$) delivered at atmospheric pressure. Lines deposited on fused silica were as small as 200 nm wide. Given that the the authors were able to form these deposits on a substrate that does not absorb at the wavelength used, they concluded that the process observed is a photolytic one, relying on the direct absorption of photons by the precursor rather than its dissociation via sample heating. Since the bond energy quoted by the authors to form ground state Cr from $Cr(CO)_6$ is 6.5 eV (no reference given), the authors conclude that the this photolytic process must be a 3-photon one given the wavelength of light used to drive it.

In an attempt to increase the thickness of the deposits, the authors made multiple scans over the initial deposits. This induced significant roughening of the deposits (resulting in decreased reflectivity) as well as the appearance of a "reflective haze" around the deposit. After scanning over the existing deposits with no gas is flowing, they ruled out ablation as the roughening mechanism by confirming that at least a factor of 2 increase in pulse intensity is required for the onset of ablation. Thus they concluded that the roughening must be the result of the change in substrate on which the the deposition is occurring once the initial metal layer is deposited. In fact, they argue that both the roughening and the haze can be attributed to the emission of photoelectrons from the newly formed metal deposits dissociating precursor molecules in the gas-phase, even though they performed their deposition in atmosphere. They provide support this conclusion by showing that the mean free path in air of the photoelectrons having energies from a few eV to greater than 100 eV is on the order of microns. They do little to address the possibility of pyrolytic decomposition of precursor due to absorption in the new substrate.

The authors also performed experiments on smooth evaporated gold substrates, producing lines that were only 100 nm wide and had a threshold for deposition 25% of that required for deposition on fused silica. Acknowledging the fact that excited electrons in molecules adsorbed on insulating substrates cannot tunnel to the conduction band in the same way they do when adsorbed to metal substrates, they point out that the excited state lifetime of an adsorbate on an insulator should be longer than it is on a metal. By itself, this should result in a larger dissociation

cross-section for molecules adsorbed on materials with large band gaps (i.e. the dissociation cross-section should scale with band gap of substrate), making the deposition threshold on insulators lower. Clearly not the case, the authors once again argue for a contribution from photoelectrons, liberated from the metal surface, to a gas-phase dissociation process. In support of this argument, the authors cite low energy electron beam dissociation studies of other organometallics ($(CH_3)_3Al$) adsorbed to semiconductor surfaces that report low cross sections for electron energies similar to those reported for photoelectrons. According to the authors, the fluence of photoelectrons given their experimental conditions is higher than the cross sections reported in the study they cite, yet they make no mention of the method used to measure this fluence. No study of the purity of the deposits was carried out by the authors.

Zhang et al. [42] deposited tungsten nanogratings with sub-100 nm linewidths and sub-wavelength ($\lambda/2$) periods on sapphire (Al_2O_3) samples irradiated with 150 fs pulses (λ = 400 nm, rep rate = 80 MHz) in a tungsten hexacarbonyl ($W(CO)_6$) atmosphere. The orientation of the deposited gratings was always parallel to the polarisation of the electric field of the laser. Various combinations of scan speed and laser power were experimented with, resulting in slight variations in morphology. As with the work of Haight et al., the negligible absorption of 400 nm laser irradiation in sapphire was cited as evidence that dissociation is not due to photoexcited carriers in the substrate, but rather the direct absorption of incident photons. The authors suggest that since the total energy required to form elemental tungsten from $W(CO)_6$ is 11 eV, the process must be a 4-photon one given the wavelength of laser used. However, this neglects the possibility that individual CO ligands might be cleaved by single photons of only 1.83 eV. In fact, the EDS analysis performed by the authors shows the presence of a carbon peak, suggesting that this may indeed be the case. While little discussion of the possible mechanism responsible for the grating structure is provided, the authors do suggest that interference between the incident laser and surface plasmons may explain the periodicity of the features. However, the fact that the substrate is non-metallic and that the orientation of the deposited features is parallel rather than perpendicular as is normally observed in plasmonic phenomena, make this conjecture unlikely.

Chapter 3

Ultrashort Pulsed Laser Ablation in Reactive Gas Atmospheres

3.1 Introduction and Background

As discussed in previous chapters, the scientific community's interest in the complex and fleeting processes that occur during pulsed laser ablation (PLA) has yielded a vast body of literature built up over decades of research. A significant subset of this work explores the dynamics of the material removed during PLA and its interaction with the ambient. To this end, a great deal of research has focused on PLA performed in air [10, 11, 12, 14, 28], while other studies have looked at PLA in vacuum [13, 43, 27, 15, 16]. Still other groups have employed inert gases such as nitrogen, neon, and helium during PLA, showing that their use can help mitigate deleterious plasma-induced effects such as self-phase modulation, spatial defocusing, and plasma-induced variations in refractive index [35, 36, 25, 26]. Inert gases have also been used to mediate the transport of neutral [44] and ionic debris [34, 32, 45] ejected from the ablation site. While non-reactive gases have demonstrated great efficacy in controlling the propagation characteristics of the laser beam and/or the plasma expansion, only a few references exist in which they are explicitly employed to change the chemistry of the material ejected during ablation [37][1].

Since the mid-1980's, numerous researchers have explored the use of reactive

[1] An unintended change in the chemistry of the ablated material is reported by Harilal et al. [28] during nanosecond ablation of aluminium in air.

gases as etch precursors during laser processing [39, 46, 38]. As a result, techniques such as laser-assisted chemical etching (LCE) of silicon [47, 48] and copper [49, 50] are sufficiently mature to have found a number of industrial applications. Slightly more recently, SF_6 has been used in the fabrication of microstructures in silicon [18] and germanium [19], altering the optical absorption characteristics of these important semiconductors. Unlike the process investigated here, both LCE and silicon microstructuring are processes in which no laser-induced plasma plume is formed. While many other substrate/precursor combinations have been investigated, the vast majority of work exploring laser processing in reactive gas atmospheres cites photolytic, pyrolytic, or photochemical dissociation of surface adsorbed precursor molecules as the mechanism by which material is removed.

In contrast to these processes, the work discussed in this chapter and the next examines micro- to millimetre-scale plasma-driven chemical reactions that occur in the gas-phase when UPLA is performed in reactive gas atmospheres. Reactive plasmas, or plasmas "composed of multiple reactive species that continuously transform into each other and that also generate new species as a result of numerous chemical reactions in the ionised gas-phase," have recently been identified as an important nanofabrication tool [51, 52]. The methods typically employed involve the formation of the plasma in the gas-phase using gaseous precursors. The technique reported here is quite different in that the plasma is formed first in a solid substrate via the rapid, localised deposition of energy from an ultrashort laser pulse. The plasma then expands into the reactive gas. The gas is subsequently driven into the plasma-phase. Decomposition of the solid and dissociation of the gas occur in the plasma-phase, allowing the species involved to rebond in new ways, forming novel by-products.

This chapter begins by detailing the development of a model system consisting of a solid substrate and a gas-phase precursor. The motivation for the selection of this particular substrate/precursor combination is briefly reviewed and a series of experiments demonstrating the effects of a chemical reaction initiated by ultrashort pulsed laser ablation are presented. The role of adsorbed precursor molecules in the given reaction is explored, both experimentally and with a simple model.

In Chapter 4, we look more closely at the physics driving the reaction. In particular, we examine the laser-induced plasma plume in a time-resolved study of its make-up and propagation dynamics as it expands into the surrounding ambient.

This, along with an analysis of the by-products of the reaction provides a more detailed understanding of the reaction pathway and demonstrates clearly how ultra-short pulsed laser induced-plasmas can be used to drive chemistry.

3.2 Model System

In 1979, Winters and Coburn showed that silicon exposed to XeF_2 vapour undergoes spontaneous etching [53]. They also showed that in the absence of electron or ion bombardment, SiO_2 is unaffected by exposure to XeF_2. Their seminal work has led to a great many subsequent studies investigating the fluorination of silicon and silicon compounds via exposure to gaseous XeF_2 and the mechanisms by which etching can occur [54, 55, 56, 57], the role of surface adsorption in the etch process [58, 59, 60], the by-products produced during etching [61, 62, 63, 64], and the use of ion, electron, and/or UV irradiation for either inducing etching or accelerating a spontaneous etch process [65, 66, 67].

The demonstrable efficacy of XeF_2 as an etch precursor and the technological importance of silicon has led to the widespread industrial use of XeF_2 as an etchant for silicon. However, for the work discussed in this chapter and the next, it was important to select a system in which etching does not proceed spontaneously. For these reasons, the substrate/precursor combination selected as a model system with which to demonstrate the effects of UPLA done in reactive gas atmospheres is SiO_2 and XeF_2. Other substrate/precursor combinations were later investigated and are discussed briefly in Section 3.6.

Given silicon dioxide's negligible absorption at visible wavelengths, laser processing of this material with conventional continuous wave and nanosecond pulsed (ns) laser systems is difficult or impossible. However, due to the extremely high peak powers achievable with ultrashort pulses and the resulting non-linear material response to these high powers, the use of transparent materials as a test system becomes a possibility. Furthermore, the rapid deposition of energy into the sample provided by ultrashort pulses and the subsequent few picoseconds delay in the onset of ablation ensures no laser heating of the ejected material or the laser-induced plasma, allowing us to unambiguously separate direct laser-mediated effects from the interaction of the expanding plasma and the ambient. and nanosecond pulsed

(ns) laser systems is difficult or impossible. However, due to the extremely high peak powers achievable with ultrashort pulses and the resulting non-linear material response to these high powers, the use of transparent materials as a test system becomes a possibility. Furthermore, the rapid deposition of energy into the sample provided by ultrashort pulses and the subsequent few picoseconds delay in the onset of ablation ensures no laser heating of the ejected material or the laser-induced plasma, allowing us to unambiguously separate direct laser-mediated effects from the interaction of the expanding plasma and the ambient.

3.3 Instrumentation

Figure 3.1 shows schematically the experimental arrangement used in this study. To aid in the arrangement's description, the schematic is divided into four interacting systems: (i) the laser and optics train, (ii) the reaction chamber and stage, (iii) the gas delivery system, and (iv) a system for imaging the sample. The primary component of system (i) is a Ti:Sapphire chirped pulse amplification system (described in detail in Chapter 5) capable of delivering linearly polarised, 150 fs, 1 mJ pulses having a centre wavelength of 775 nm at a repetition rate of 1 kHz for a total average power of 1 W. Active power modulation of the laser beam is achieved by a rotating half waveplate combined with a fixed linear polariser, an arrangement typically referred to as analyser/polariser combination. Neutral density (ND) filters placed downstream of the analyser/polariser provide further attenuation and an iris is used to adjust the beam diameter. Ultimately, the beam is focused onto the substrate by an infinity corrected 20× microscope objective with a numerical aperture (NA) of 0.40. Average power readings of the beam are made using a thin silicon detector located between the microscope objective and the reaction chamber.

Exiting the objective, the beam enters the reaction chamber through a 5 mm thick, BK7 window[2]. The chamber is in turn mounted on a computer-controlled, three axis (x, y, z) linear translation stage. Rather than scanning the beam, features are micromachined by using the stage to scan the chamber and the sample beneath the stationary laser beam. Likewise, the beam is focused onto the sample by trans-

[2]BK7 is a low dispersion crown glass manufactured by Schott AG and widely used in optical components

lating the stage in z. A heater and thermocouple located inside the chamber, but not shown in Figure 3.1, were used to control substrate temperature.

A gaseous precursor (XeF_2 in Figure 3.1) is delivered to the reaction chamber from a gas bottle secured in a gas box. Valves VC and V3 are leak valves that are used to control the flow of gas during the experiment. Gauges P1, P2, and P3 are gas species independent capacitance manometers that are used to monitor the gas box pressure (P1) and the chamber pressure (P2 and P3). P4 is a wide range gauge that is employed to measure the base pressure of the system. Valve V4 is normally left closed during exposure of the sample to gas in order to protect gauge P4 from damage. Likewise, valve V1 is left closed during experiments and is used only as a bypass valve to speed evacuation of the chamber. The base pressure in the reaction chamber is approximately 3×10^{-5} Torr.

Finally, system (iv) provides a means for the user to image the sample during processing. A light emitting diode (LED) lamp is used to illuminate the sample. Light reflected from the sample is collimated by the 20× objective, then focused onto a CCD camera via a tube lens. A filter placed in front of the camera rejects light from the laser, preventing laser-induced damage to the CCD. Neither the tube lens nor the filter are shown in Figure 3.1.

3.4 Evidence of UPL Driven Chemistry

Figure 3.2 shows electron micrographs of four nominally square ablation pits machined in a sample of single crystal, Z-cut SiO_2. The sample was ultrasonically cleaned in acetone (10 min.), isopropyl alcohol (10 min.), and ultrapure water (5 min.), dried with nitrogen, then baked at 200°C for 2 hours or more. In order to illustrate unambiguously the effects reported, the laser parameters and scan strategy were selected to yield significant redeposition of ablated material in vacuum. The average power of the delivered beam was 1.8 mW at 1 kHz, or 1.8 μJ per pulse. Features made in the substrate by the focused, unscanned beam were measured to have a diameter of 4.25±0.25 μm for $n > 1000$ pulses. The laser fluence was estimated to be between 10 and 15 J/cm^2.

The beam was directed onto the substrate at normal incidence and the stage was scanned in the x (horizontal) direction at a constant velocity of 50 μm/sec. Between

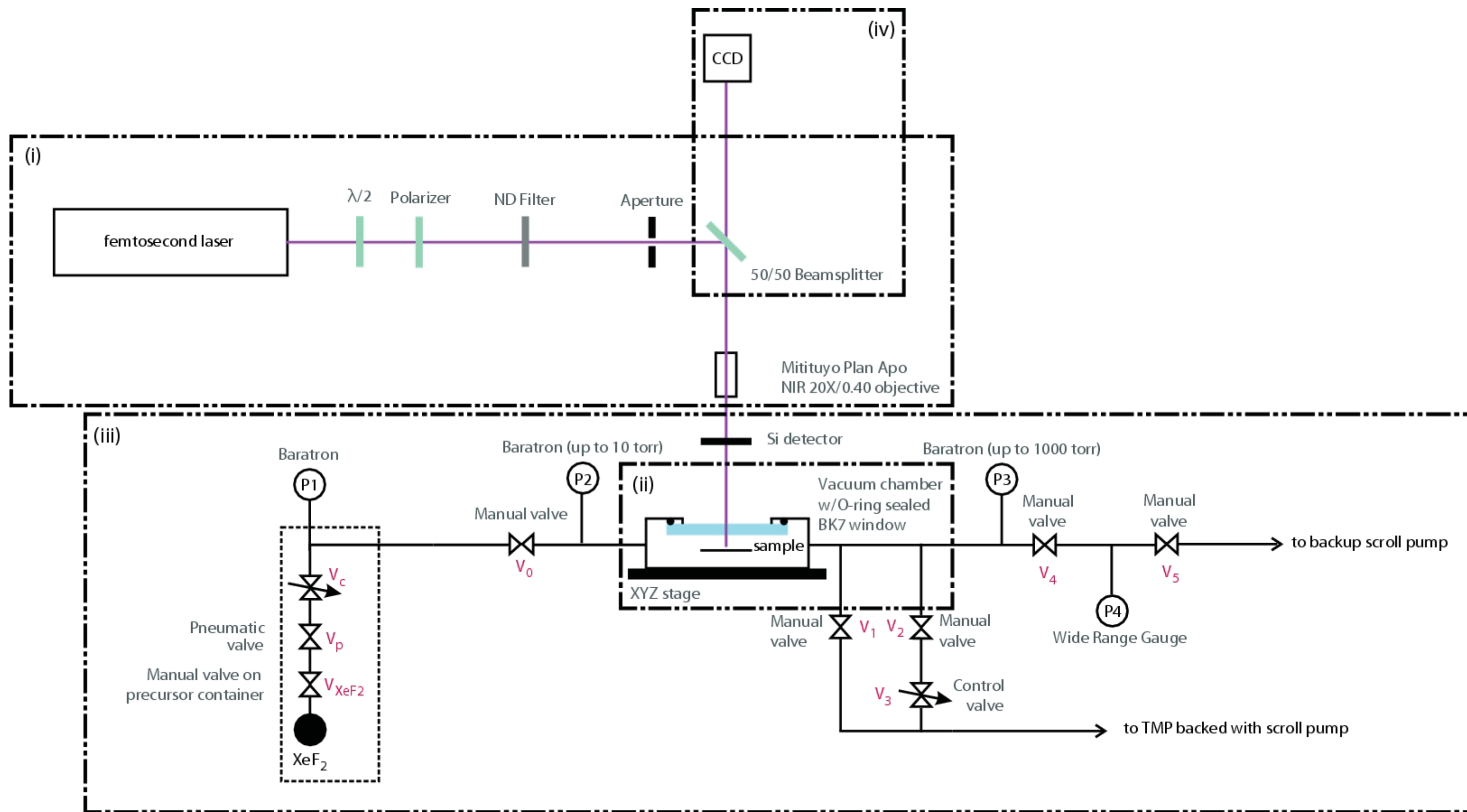

Figure 3.1. Experimental arrangement for study of laser ablation in reactive gas atmospheres.

each horizontal line, the stage was stepped 1 μm in the y (vertical) direction and the scan direction reversed. A total of 100 lines were machined for a final pit having nominal dimensions of 100 μm $\times$ 100 μm. In all images, the scan started in the upper left-hand corner, proceed horizontally, and ended in the lower left hand corner.

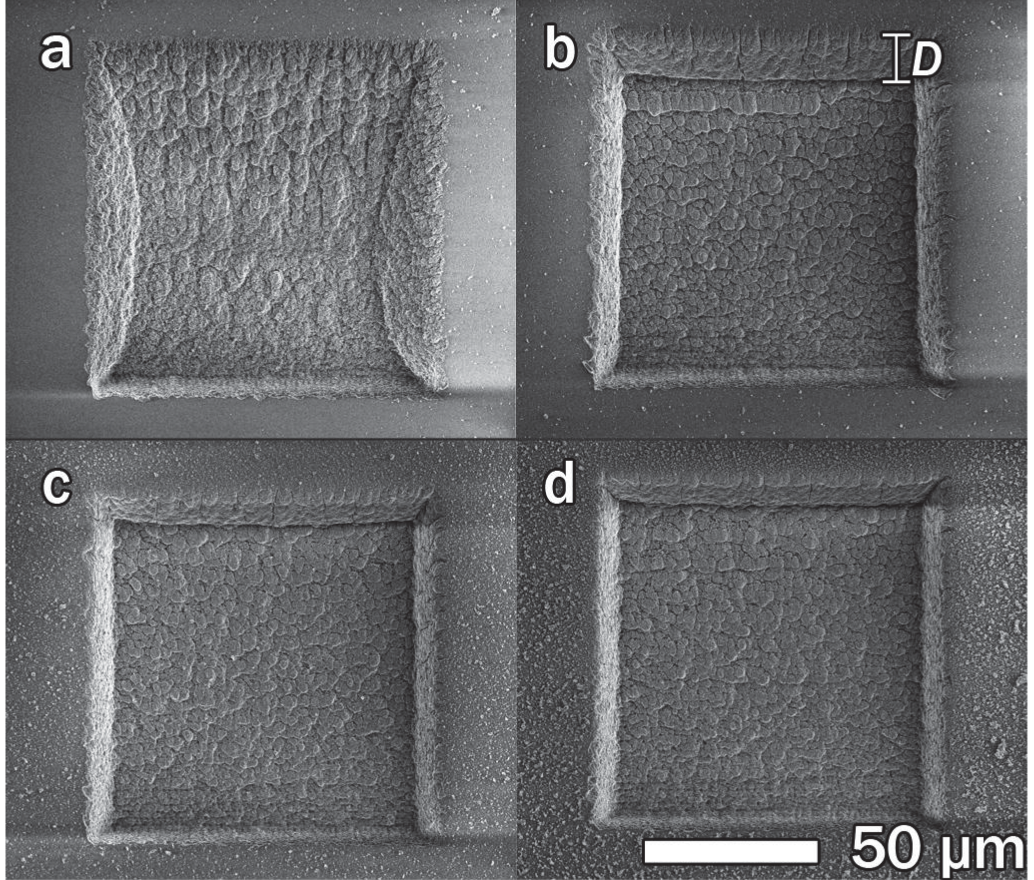

Figure 3.2. 100 μm $\times$ 100 μm pits machined in SiO_2 (a) in the absence of XeF_2 (P = 4.4×10^{-5} Torr), (b) in 500 mTorr of XeF_2, (c) in 2 Torr of XeF_2, and (d) in 4 Torr of XeF_2. D is a measure of the extent of redeposition. The values of D for (b), (c), and (d) are 10.34, 6.85, and 5.83 μm respectively.

The pit in Figure 3.2(a) was machined in high vacuum (P = 4.4×10^{-5} Torr) and exhibits significant redeposition. During ablation, material is ejected and redeposited in a radial distribution with little variation through 2π radians. Material redeposited in the direction of the scan is removed as the scan progresses, accumulating preferentially at the trailing edge of the scan pattern. Thus, the redeposition seen in Figure 3.2(a) is most pronounced at the top edge and along the sides, and

is almost completely absent from the bottom edge of the ablation pit.

The ablation pits shown in Figure 3.2(b)-(d) were machined at XeF_2 pressures of 0.5, 2, and 4 Torr, respectively. Note that the nominally square pit bottoms and rectangular sidewalls in these images are not distorted significantly by redeposited material, in contrast to the pit machined in high vacuum (Figure 3.2(a)). This illustrates that the presence of XeF_2 results in a significant reduction of redeposited material.

As a control, the pits shown in Figure 3.3 were machined in N_2 atmospheres at pressures of 1 and 10 Torr. The extent of redeposition is qualitatively the same as in high vacuum, illustrating that the reduction of redeposited material observed in the presence of XeF_2 is indeed gas specific.

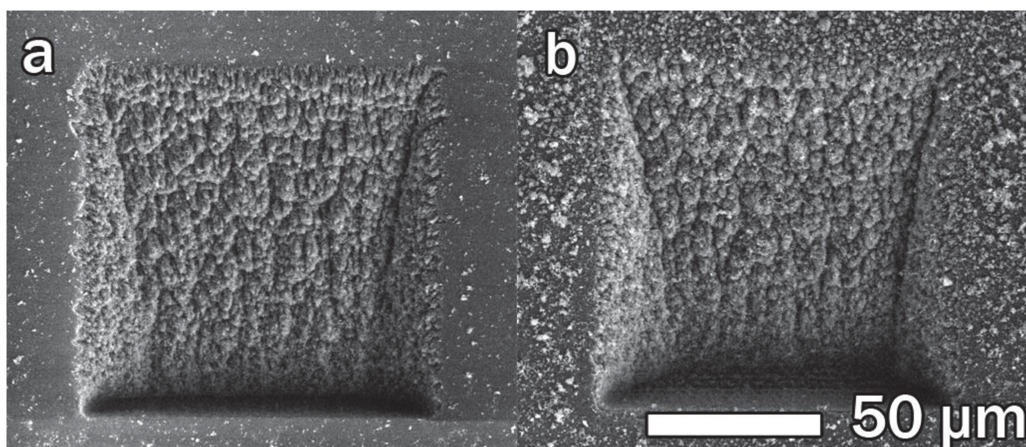

Figure 3.3. 100 μm $\times$ 100 μm control pits machined in SiO_2 using parameters identical to those used in Figure 3.2 in (a) 1 Torr N_2, and (b) 10 Torr N_2. Note the similarity of these pits to the pit shown in Figure 3.2(a) which was also machined in the absence of XeF_2.

To confirm that the effect observed requires laser illumination to drive the process, another pit was machined in high vacuum with results identical to that shown in Figure 3.2(a). Once the laser processing was complete, the sample was removed and imaged in a scanning electron microscope (SEM). The sample was then returned to the reaction chamber and exposed to XeF_2 for 10 minutes in the absence of laser illumination. A second round of SEM analysis after exposure to XeF_2 showed no change in the redeposited material, suggesting that the effect observed in Figures 3.2(b)-(d) is not due to a spontaneous reaction between the laser-modified recast material and

XeF_2.

To further verify this, a second sample was laser processed in high vacuum, then immediately thereafter, exposed to XeF_2 for 10 minutes without first being exposed to atmosphere. Subsequent SEM analysis showed qualitatively identical morphologies to that observed in the first experiment, effectively eliminating the possibility that an otherwise spontaneous reaction had been prevented due to oxidation of the recast material during the sample's transfer to the SEM.

Yet another control experiment was performed in which SiO_2 was scanned with a laser beam having a fluence just below the ablation threshold of the material during exposure to XeF_2. The scan parameters were identical to those reported above except that the box was rescanned up to five times in a single experimental run. No etching of the material was observed indicating that either no photolytic dissociation of XeF_2 occurs at sub-threshold powers of this wavelength or that ablation is a necessary condition for the reaction to proceed.

It is evident that the reduction of redeposited material results from a chemical reaction in which volatile compounds, presumably SiF_x, are formed from ablated SiO_2 and dissociated XeF_2, though this conclusion tells us little with regard to the precise reaction pathway. We can, however observe a pressure dependency of the effect. The recast material seen at the top edge of each pit is composed of loosely adhered debris and can be removed by post-ablation ultrasonication. Therefore, the apparent thickness D of this edge can be used as coarse metric of the extent of redeposition (see Figure 3.2(b)). In Figure 3.2, D is seen to decrease with increasing XeF_2 pressure. This decrease is attributed to a corresponding increase in the amount of ejected material converted to volatile species during ablation and the subsequent removal of these gas molecules by the pumping system.

3.5 The Feasibility of a Surface Reaction: A Simple Analysis

The demonstrable ability of XeF_2 to mitigate redeposition during ultrashort pulse laser ablation of $Si0_2$ by the transformation of ejected material into volatile compounds bears comparison to the well known processes of electron and ion beam-induced etching (E/IBIE). Briefly, E/IBIE is implemented in the following fashion:

a gas-phase precursor is delivered through a hollow needle positioned approximately 100 microns from the surface of a substrate located in a high vacuum system, usually an electron or ion microscope. Having adsorbed to the substrate surface, the precursor molecules are irradiated by a charged particle beam (electrons or ions). As the charged particles cross the vacuum-substrate interface, they transfer some of their energy through inelastic scattering to the adsorbates. If the energy transferred is sufficient, molecular bonds are broken and the precursor dissociates into reactive components and volatile by-products. The reactive components (fluorine in the case of XeF_2) react with the substrate to form new volatile compounds resulting in the removal of material from the substrate surface. The volatile by-products produced by the dissociation process, as well as those compounds formed during the etch process, subsequently desorb from the substrate and are removed by a pumping system.

Since E/IBIE typically relies on the presence of surface adsorbed precursor molecules and little is known about the the reaction pathway in our UPLA driven process, it is natural to ask to what extent adsorbates play a role in the volatilisation of ablated material when SiO_2 is ablated in a XeF_2 atmosphere. In general, there are two adsorbate mediated scenarios to consider, as illustrated in Figure 3.4. The first involves the dissociation of adsorbed XeF_2 molecules located on the surface directly above the ablated region, labelled region I in the figure. In this case, the energy required to dissociate the precursor molecules comes from incident photons, ejected photoelectrons, superheated substrate components ejected during ablation, or some combination thereof. A simple estimate of the amount of substrate that can be volatilised due to the dissociation of these and only these adsorbed precursor molecules can be made in the following fashion.

Knowing the dimensions of the micromachined feature and the process parameters used to produce it, the number of substrate molecules removed per laser pulse can be estimated by

$$n_a = \frac{\rho V N_a}{t_p f M} \tag{3.1}$$

where ρ is the density of the material (g/μm^3), V is the total volume removed (μm^3), N_a is Avogadro's number, t_p is the total processing time (s), f is the repetition rate of the laser (s^{-1}), and M is the molar mass of the substrate material (g/mol). If we

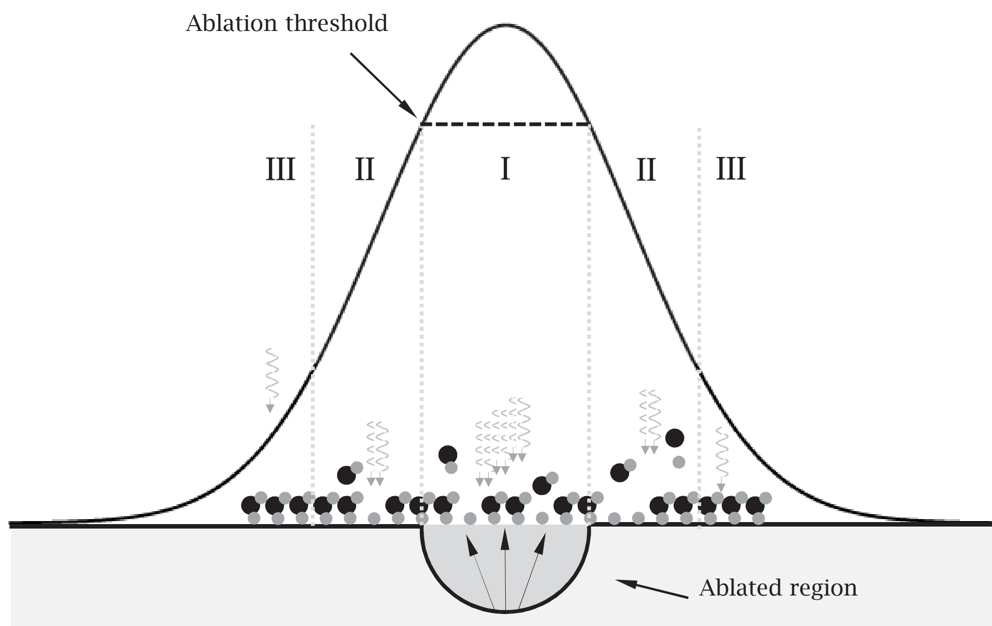

Figure 3.4. Two possible adsorbate mediated scenarios for the chemical reaction induced when SiO_2 is ablated in XeF_2 are shown. The first involves the region directly above the ablated region, I. The size of this region is determined by the spot size and intensity of the beam, and the ablation threshold of the material. Precursor dissociation in this region can proceed via a number of means including photodissociation, collisions with energetic photoelectrons, or collisions with superheated substrate components. The second scenario discussed involves pure photodissociation outside the ablation region, region II. Because the energy required to dissociate XeF_2 is higher than than that of a single 775 nm photon, photodissociation must be a two photon process. Region III represents the area in which the photon density is too low to fully dissociate the available precursor. The general approach to the analysis detailed in the text relies on the assumption of an adsorbed monolayer of precursor. The number of surface sites available in a given cross-sectional area is estimated and correlated to a maximum number of adsorbed precursors. The number of molecules of a given reaction by-product possible is then calculated and compared to the amount of material ablated. The small fraction of the total ablated material that can be reacted given the available adsorbed precursor suggests that the reaction observed is not a surface reaction.

assume that the precursor forms a monolayer on the substrate surface, the number of XeF_2 molecules available to contribute to the reaction at the ablation site is given by

$$N(r) = \pi r^2 \rho_{ss} \tag{3.2}$$

where r is the radius of the ablated feature at the surface and the density of surface sites ρ_{ss} is taken to be on the order of 10^{15} cm^{-2} [68]. If we further assume that the primary etch by-product formed is SiF_4 [61], that the precursor molecules of interest undergo complete dissociation, and that the reaction proceeds with perfect conversion efficiency (i.e. every liberated F atom contributes to the formation of SiF_4), then we find that approximately 0.28% of the total volume removed can be volatilised by adsorbates located directly above the ablation site (where $r =$ 2.25 μm).

The second scenario to consider involves the dissociation of precursor molecules adsorbed to the surface outside the ablated region, labelled region II in Figure 3.4. Unlike the previous example, in this case we assume that photodissociation is the only possible mechanism for the liberation of fluorine atoms from the adsorbed XeF_2 molecules, where the dissociating photons outside the ablated region are delivered by the tails of the beam[3] The dissociation process of interest is

$$\mathrm{XeF_2} \rightarrow 2\mathrm{F}. \tag{3.3}$$

The dissociation energy of this process is 2.78 eV [69]. Given that the central wavelength of the laser used in this experiment has a photon energy of only 1.6 eV, photodissociation of adsorbed XeF_2 would have to proceed via a multiphoton process involving the simultaneous absorption of two photons. Assuming that we have a Gaussian beam (as shown in the figure), we can express the fluence of photons at the beam waist as a function of the radial distance from the beam axis,

$$\Phi(r) = \frac{\tau}{E_\lambda} I_0 \exp\left(\frac{-2r^2}{w_0^2}\right) \tag{3.4}$$

where τ is the pulse duration, E_λ is the photon energy, I_0 is the peak intensity, and w_0 is the $1/e^2$ radius at the waist of the beam. It is assumed that all photons in the pulse arrive simultaneously allowing for perfect conversion efficiency as long as the number of photons per unit area is sufficient to drive the necessary dissociation process (i.e.

[3]Though this possibility seems to have been ruled out by the sub-ablation threshold experiments reported earlier, we continue with the analysis in the interest of rigour.

provided there are at least two photons per adsorbed precursor molecule). While this is certainly not the case, making this assumption greatly simplifies the estimate and provides an upper bound on the amount of ablated substrate whose volatilisation can be attributed to an adsorbate mediated process driven by multiphoton dissociation.

Taking 2.25 μm as the value of w_0, it is a simple matter to use Equation 3.4 to show that, at a radius of 5.23 μm, the per pulse photon fluence drops below the value required to dissociate all adsorbed XeF_2 molecules (again, assuming a monolayer coverage and a two photon process). Using this value for r in Equation 3.2, the number of molecules of SiF_4 that can be created represents the volatilisation of only approximately 1.5% of the total volume of material removed per pulse. If instead, SiF_2 is the by-product produced, this value doubles to 3.0% of the total material removed.

The small percentage of the material removed whose volatilisation can be attributed to adsorbates, as estimated by this model, suggests that gas-phase precursor molecules play a role in the volatilisation process. However, it is unknown what percentage of the material removed makes up the redeposition observed. In other words, it is difficult to determined from the data how much material is actually being volatilised by adsorbates. As a result, while suggestive, the analysis is far from conclusive.

3.5.1 The Temperature Dependence of Surface Adsorption and a Brief Foray into EBIE

To further investigate the role of adsorbates in reactions driven by UPLA in reactive gases, let's briefly turn to EBIE as a means of measuring the temperature dependence of surface adsorption. In order to proceed with this analysis, we must first note that electron beam-induced etch processes are rate-limited by the adsorbate dissociation rate which is itself limited by two factors: the flux of electrons across the vacuum-substrate interface and the adsorbate coverage of the surface. A surface exposed to a gas will have molecules both adsorbing and desorbing at any given instant. Thus, the surface coverage of a given adsorbate-adsorbent combination in equilibrium depends strongly on the residence time of the adsorbate. In turn, the residence time is a function of temperature (T) such that

$$\tau(T) = \tau_0 \exp\left(\frac{E_{des}}{k_B T}\right) \tag{3.5}$$

where E_{des} is the activation energy for desorption, τ_0 is the desorption prefactor, and k_B is the Boltzmann constant [70].

To illustrate the effect that the temperature dependence of the adsorbate population has on the etch rate, XeF_2-mediated electron beam-induced etching (EBIE) of SiO_2 was performed at sample temperatures of 24°C and 153°C. Figure 3.5 shows AFM line profiles of the etch pits generated. Each pit was etched for 15 minutes using a 4.9 nA, 30 keV electron beam scanned over a field of view consisting of 968 lines at a rate of 16.7 ms/line while XeF_2 pressure was held constant at approximately 0.4 Torr. The significant reduction in the depth of the pit etched at 153°C is a direct result of the reduction in the adsorbate coverage due to the decrease in adsorbate residence time at increased sample temperatures. This result illustrates clearly the temperature dependence expected of a process whose rate is determined largely by adsorbate coverage.

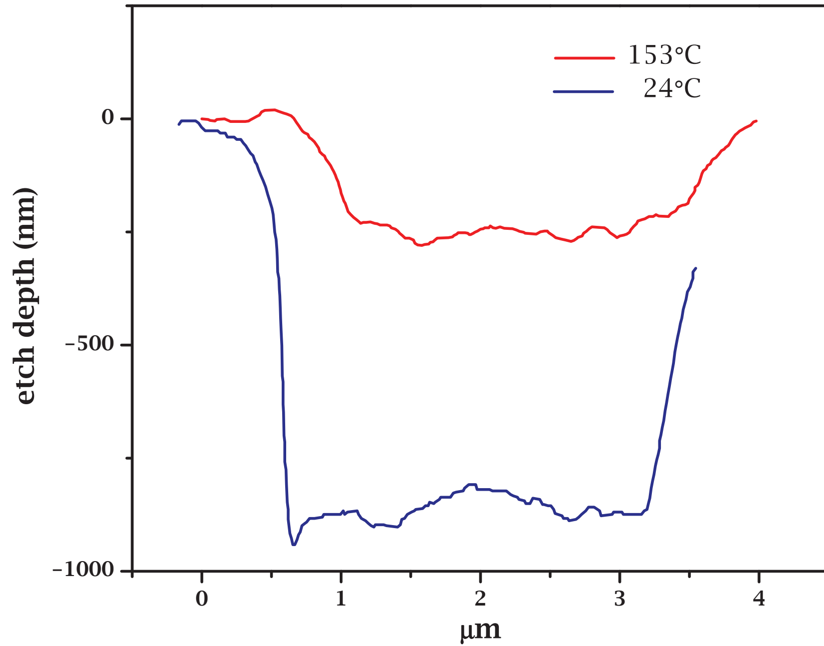

Figure 3.5. AFM line profiles of etch pits in SiO_2 generated by XeF_2-mediated EBIE performed at 24°C (blue) and 153°C (red).

The relationship between substrate temperature, adsorbate coverage, and etch

rate provides a means for further investigating the role of surface-adsorbed molecules. Toward this end, pits were again laser machined in SiO_2 using laser and scan parameters identical to those used to machine the pits shown in Figures 3.2 and 3.3. This time, however, the processing was performed on a substrate heated to 150°C. Thus, Figure 3.6(a) shows a heated SiO_2 sample machined in high vacuum. Figure 3.6(b) shows the results of a heated SiO_2 sample machined in a 0.5 Torr XeF_2 atmosphere (in these experiments, the XeF_2 pressure was limited to 0.5 Torr since above this temperature the gas condensed onto the window, effectively reducing the delivered laser power). Clearly, the elevated temperature has no significant effect on the volatilisation of the ejected material. In other words, whether or not the sample is heated, exposure to XeF_2 reduces the amount of redeposited material observed. Since, as previously demonstrated, heating reduces XeF_2 coverage, it is unlikely that adsorbed molecules play a significant role in the reaction observed during UPLA of SiO_2 in XeF_2 atmospheres.

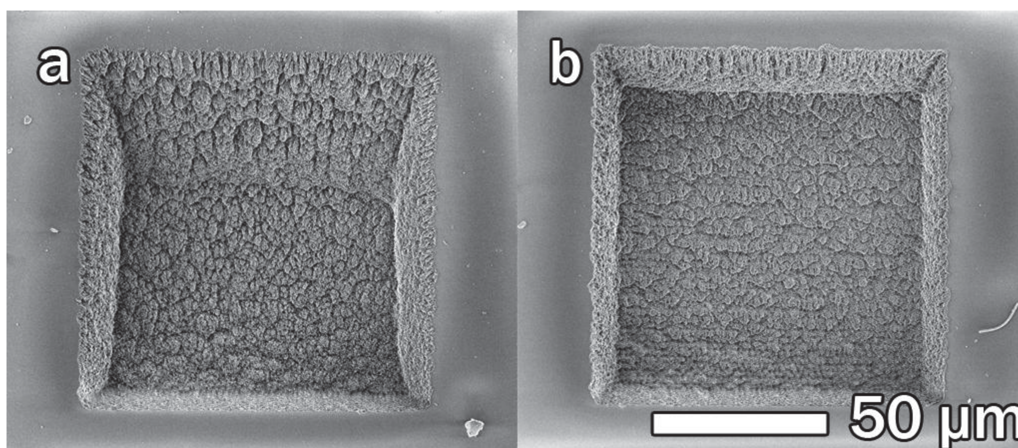

Figure 3.6. 100 μm × 100 μm pits machined in SiO_2 heated to 150°C (a) in the absence of XeF_2 (P = 4.4×10^{-5} Torr) and (b) in 0.5 Torr of XeF_2.

As an aside, careful review of the images in Figure 3.2 shows that the amount of debris in the vicinity of the etched pits increases with increasing pressure. The dynamics and make-up of laser-induced plasma plumes in gaseous environments have undergone extensive study and are relatively well understood [29, 28, 34, 32, 71]. The increase in surface debris is known to correlate with the stopping power of a gas (i.e. pressure) and has been studied as a way to mitigate potential damage to sensitive components around the substrate. The effect is observed in both N_2 and

XeF_2 environments. The propagation of the ablated material into the ambient will be examined more closely in Chapter 4. However, we note here that the presence of surface debris after ablation in XeF_2 atmospheres indicates that not all ejected material is volatilised under the conditions employed in this work.

3.6 Other Substrate/Precursor Systems Explored

Over the course of this work, a number of other substrate/precursor systems were investigated. Typically, the systems explored were identified because of their potential for industrial application. For the most part, the precursors were chosen to target chemical reactions known to create volatile compounds with some component of the substrate in the interest of reducing redeposition during laser ablation. This section very briefly describes the experiments performed and the observed results. These investigations were purely phenomenological with little or no follow up analysis performed. Nonetheless, they are reported here in the interest of completeness.

Silicon Dioxide + Chlorine: SiO_2 was machined in 1, 10, and 25 Torr of Cl_2 using scan and beam parameters identical to those used in the model system. The sample prep methodology used was also identical. Control experiments were performed in 1 and 10 Torr of N_2.

Redeposition was dramatically reduced in 1 Torr of Cl_2. No appreciable enhancement of the effect was seen at higher pressures due to the fact that the reaction was complete at 1 Torr. It is assumed that the reaction involved is similar to that observed in the model system, except that the volatile by-product formed is likely $SiCl_4$ rather than SiF_x.

Silicon + Chlorine: Si was machined in 0.35, 0.5, 1, 2, 10, and 50 Torr of Cl_2. The scan parameters used were identical to those used on the model system, but the laser power was reduced by half to 1 mW in order to account for the lower ablation threshold of Si.

While some change in the morphology of the redeposited material was observed along with a small amount of surface modification *outside* the ablated feature, there was no significant reduction of redeposition. This is a puzzling result, particularly in light of the results observer when SiO_2 was ablated in chlorine. One hypothesis posited as explanation is that the lower ablation threshold of silicon as well as

its singular stoichiometry (in comparison to SiO_2) results in much more Si in the gas phase, forcing the onset of a gas-limited regime. Another, perhaps simpler, possibility is that the experiment was performed with a contaminated gas source. Further experiments need to be done to understand this result.

Silicon Dioxide + Ammonia: SiO_2 was processed in approximately 1.75 Torr of NH_3, again with scan and beam parameters identical to those used on the model system. Reduction of redeposition was observed, but the effect was considerably smaller than that seen with SiO_2 processed in either XeF_2 or Cl_2. Since a possible candidate for the volatile by-product produced by this process is silane (SiH_4), the observed effect may be the result of the susceptibility of SiH_4 to oxidation. In this case, there would be a competing process in which SiH_4 is converted into SiO_2. However, as with all the systems described in this section, no analysis was performed to confirm this hypothesis.

Copper + Nitrous Oxide: In this case, Cu was machined in 7 Torr of N_2O using scan parameters identical to those used in the model system. The laser power, on the other hand, was reduced to 0.5 mW, again to account for the lower ablation threshold of Cu.

Since copper(II) nitrate ($Cu(NO_3)_2$ is known to sublime in vacuum, the targeted reaction in this experiment was

$$Cu + 6N_2O \rightarrow Cu(NO_3)_2 + 5N_2 \tag{3.6}$$

In fact, no effect at all was observed. In addition to repeating the experiment to verify the null result, NO_2 should also be explored as a precursor with potential for forming $Cu(NO_3)_2$. However, copper nitrate may simply be too complex a molecule, requiring many reaction steps to form, thereby making the net reaction rate extremely low.

IC Packaging + water: In this experiment, the polymer and glass bead material used to package integrated chips was UPL machined in 10 Torr of H_2O. Unlike the other experiments discussed in this chapter, this work was performed on the TripleBeam instrument. Described in detail in Chapter 4, the TripleBeam was designed and built as a major component of this project. Unlike the instrumentation described in Figure 3.1 where only the sample can be scanned, the TripleBeam has the ability to scan either the sample or the beam. For these experiments, we used

scan speeds ranging from 0.01 to 7.5 mm/s while the laser power delivered to the sample was approximately 65 mW. The laser was focused with a 10× objective (NA = 0.26) rather than the 20× objective used on the model system.

Redeposition mitigation was observed at some processing parameters, though the effect was quite small. The volatile by-product of this reaction is likely quite complex, but it is hypothesised that CO and/or CO_2 is a major component. Again, however, no analysis further analysis was undertaken.

Silicon Carbide + Xenon Difluoride: SiC was machined in XeF_2 at pressures ranging from 0.25 to 4.0 Torr. Scan parameters were identical to those used in the model system, but the average laser power was increased to between 3.0 and 3.5 mW.

In these experiments, a reduction in redeposition was occasionally observed, but the effect was very sensitive to experimental conditions and repeatability proved difficult. However, independent of the redeposition behaviour, a dramatic change in the morphology of the redeposited material was consistently observed on samples processed in XeF_2. EDS analysis performed on the morphologically altered redeposition showed a significant reduction in its silicon content when compared to redeposition formed in the absence of XeF_2. This suggests that a reaction similar to that observed in the model system takes place. According to the EDS analysis, the volatilisation of the silicon (presumably via the formation of SiF_x) resulted in the redeposition of fluorinated carbon particles (CF_x where $x < 1$). Samples on which particles were observed were rinsed in isopropyl alcohol. The effluent was reserved, placed on a clean copper sample, and allowed to evaporate. As shown in Figure 3.7, isolating the particles in this fashion revealed them to be relatively uniform in size, having diameters of approximately 200 to 250 nm.

3.7 Summary and Conclusions

The results reported in this chapter demonstrate that the process of ablating SiO_2 in XeF_2 with an ultrashort pulsed laser drives a chemical reaction that results in the volatilisation of material that would normally result in redeposition. Furthermore, the efficacy of the reaction appears to increase with increasing gas pressure, though the lowest gas pressures investigated were sufficient to volatilise most of the redeposited material observed when the ablation was instead performed in vacuum

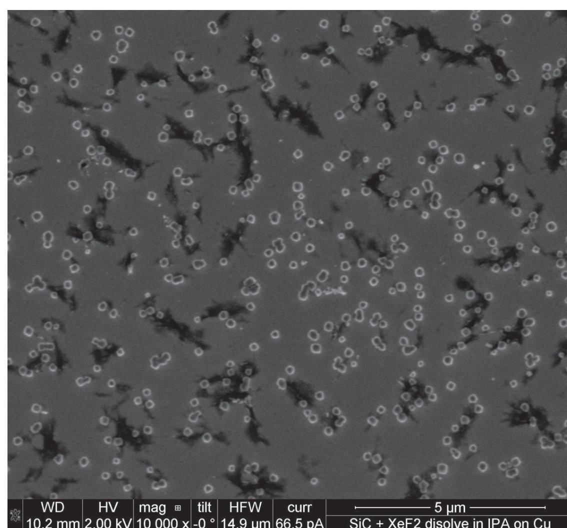

Figure 3.7. SEM image of nanoparticles (NPs) generated by laser ablation of SiC in XeF_2. Processed sample was rinsed with isopropyl alcohol. The NP suspension was applied to a copper substrate and liquid allowed to evaporate. The NPs are about 200 to 250 nm in diameter.

generated by laser ablation of SiC in XeF_2]SEM image of nanoparticles (NPs) generated by laser ablation of SiC in XeF_2. Processed sample was rinsed with isopropyl alcohol. The NP suspension was applied to a copper substrate and liquid allowed to evaporate. The NPs are about 200 to 250 nm in diameter.

or nitrogen. It has also been shown that the effect is gas dependent, occurs only during laser illumination, and that ablation is a necessary condition for the reaction to proceed. The best case estimate of the amount of ablated material that could be volatilised by an adsorbate-mediated process is 3%. However, the reaction occurs even when the adsorbate population is significantly reduced via sample heating, suggesting that the reaction is not driven by surface chemistry. Besides this though, these results tell us little about reaction pathways involved, the time scale over which the reaction occurs, or the by-products produced. These questions are explored in Chapter 4.

Chapter 4

Gas Phase Chemical Reactions Driven by UPLA-Induced Plasmas

The data and arguments presented in the previous chapter suggest that during UPLA of SiO_2 in XeF_2, the ablated substrate and precursor react to form volatile compounds. Furthermore, it would seem that this reaction occurs primarily in the gas phase rather than at the substrate surface. Unfortunately, none of the evidence presented so far provides conclusive, direct evidence to support this conclusion. Even casual observation of the ablation process, however, reveals the formation of a millimetre scale plasma. In addition, we know from the literature that the constituent components of laser-induced plasmas include energetic photoexcited prompt electrons [72, 25, 26], lower energy plasma electrons [26], ions [28], neutrals [29], clusters, and nano- [15, 73] and microparticles [12]. Given that laser ablation provides sufficient energy to decompose solid matter into its atomic and sub-atomic components, it seems feasible that as the plasma plume the expands into the ambient, energy will be transferred to the gas molecules therein. It is further plausible that the plasma excites the ambient gas molecules with sufficient energy to form reactive fragments, which can then combine with ablated material to form new by-products.

4.1 Instrumentation

In order to investigate the role of the laser-induced plasma in driving the reaction observed, the plasma plume's make-up and propagation dynamics were characterised

via fast-photography and laser induced breakdown spectroscopy. To further understand the process in question, we used a quadrupole mass spectrometer to examine the by-products produced by the reaction. Both the fast-photography and LIBS experiments were performed in the experimental set-up shown in Figure 4.1.

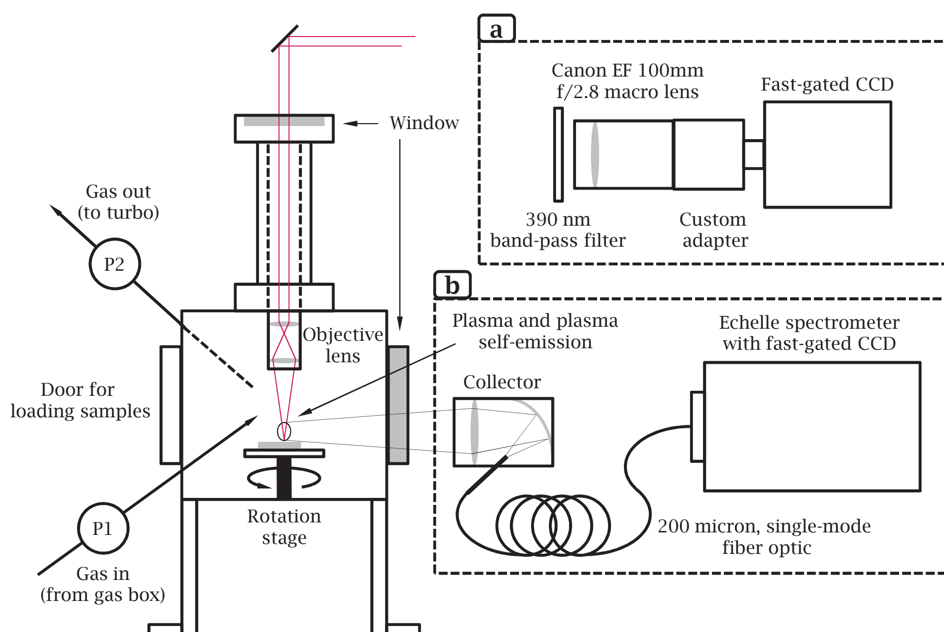

Figure 4.1. Instrumentation for studies of laser-induced plasma plume.

At the heart of this set-up is a cubic vacuum chamber having ports on all six sides. Through the bottom of the chamber, a rotary motion feedthrough controls a simple stage on which a sample can be fixed. The sample is loaded through a door on the back of the chamber, which when shut provides a seal sufficient for achieving a base pressure of $5{\times}10^{-6}$ Torr.

Through a port on its side, the chamber is pumped by a 220 litre/sec turbomolecular pump backed by a dry scroll pump. Processing gases can be introduced through a port on the opposite side of the chamber. Gauges P1 and P2 are both gas species independent capacitance manometers used to measure the pressure of the chamber during gas processing. A wide-range gauge (not shown) is used to measure the base pressure of the system. In order to prevent it being damaged, this gauge is isolated when reactive gases are introduced to the system. As with the earlier

described experiments, all processing gases are delivered from a gas box. Gas flow is regulated by two variable leak valves; one located in the gas box and the other located up stream of the turbo pump. Neither the gas box nor the leak valves are shown in the figure.

The top of the chamber is fitted with a custom adapter designed to hold a microscope objective. The objective used in these experiments has specifications identical to those of the objective used for the experiments detailed in Chapter 3 – namely, 20× magnification and an NA of 0.40. At the top of the adapter, a vacuum flange with a quartz window forms a vacuum seal. In the experiments described here, a laser beam was directed through this window and focused onto the sample via the in-chamber objective. The fixture to which the objective is mounted consists of two nested, concentric tubes threaded together (not shown in Figure 4.1). The upper tube is fixed while the lower tube, the one to which the objective is mounted, can be rotated manually by reaching into the chamber when vented. In this fashion, the vertical position of the lens, and thus the focus of the laser, can be adjusted by screwing the objective mount tube into or out of the fixed upper tube. The threads were machined with a pitch such that one rotation is equivalent to one 1 mm of adjustment.

In a fashion identical to the experiments described earlier, active power modulation and polarisation control of the laser beam are achieved through the use of a rotating half wave plate and a fixed Glan-laser polariser. Additional attenuation is provided by ND filters and/or the laser controller itself. Low group velocity dispersion broadband dielectric mirrors designed for use with ultrashort pulses were used to direct the beam to the sample. With the exception of the final steering mirror, the optics for delivering the laser and the beam path are not shown in Figure 4.1.

An optical grade, UV quartz viewport mounted in a four and a half inch, copper gasket sealed flange on the front of the vacuum chamber allows for observation of the plasma-plume. As earlier noted, we used two techniques to analyse the plasma: fast-photography and time-resolved LIBS. The instrumentation used to perform fast-photography is labelled (a) in Figure 4.1 and consists of an Andor iStar fast gated, intensified CCD (ICCD) camera having a 1024 × 1024 pixel active region, a Canon EF 100 mm f/2.8 macro camera lens, and a custom mating adapter. To study the time evolution and spatial distribution of specific atomic lines, an optical bandpass

filter can be inserted between the camera and the plume allowing only light from a specific line to be collected.

Briefly, an ICCD camera combines a CCD camera with a so-called intensifier tube (see Figure 4.2). Photons incident on an intensifier tube first strike a photocathode, emitting electrons. These photoelectrons are accelerated in an electric field toward a microchannel plate (MCP). A voltage applied across the MCP further accelerates the electrons, giving them sufficient energy to generate a cascade of secondary electrons within the MCP. The gain achievable by this amplification process can be in excess of 10,000. Upon exiting the MCP, the secondary electrons are further accelerated to a fibre optic whose input face is coated with phosphor. The photons emitted when the phosphor is excited by the incident electrons are transmitted down the fibre to the CCD where they are recorded as an image. By modulating the voltage applied to the MCP, the entire device can be gated, allowing time-resolved data to be collected. The minimum gate width quoted by the manufacturer of the Andor ICCD is less than 2 ns. To reduce dark noise, the CCD is cooled to -20°C.

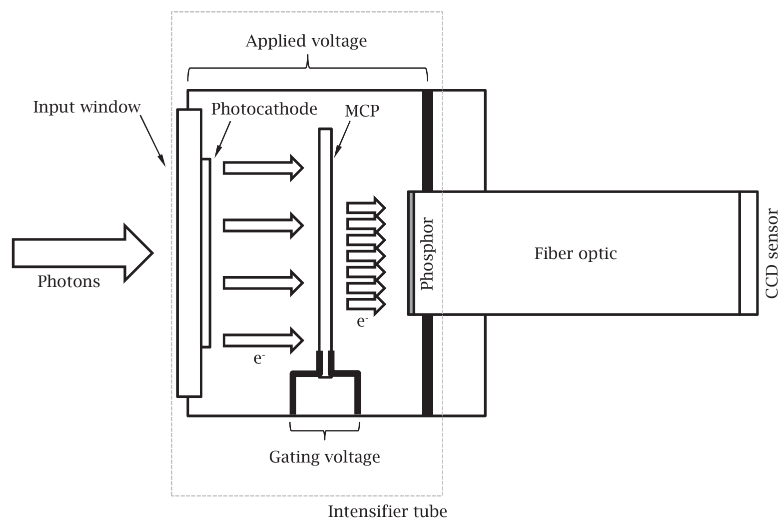

Figure 4.2. Intensified CCD schematic. The grey dotted line encompasses the sealed intensifier tube.

Replacing the fast-photography instrumentation with an Échelle spectrometer (Andor Mechelle 5000) fitted with an ICCD, as shown in the portion of Figure 4.1

labelled (b), provided for a more detailed study of the components of the plasma plume. Using this system, light emitted from the plasma is collected by an optical collector consisting of a high NA lens and a parabolic mirror. The mirror focuses the light onto the lens which, in turn, couples the light into a fibre. Selecting the appropriate fibre is critical since both spectral resolution and collection efficiency are affected by core diameter, but in competing ways. As core diameter increases, collection efficiency is improved, whereas spectral resolution is reduced. The fibre used in the experiments described here has a silica core with a diameter of 200 μm and a fluorine silica cladding with a diameter of 220 μm, giving the fibre better than 99% transmission at wavelengths between 900 and 250 nm.

Échelle spectrometers use Échelle gratings to produce high resolution spectral dispersion over large spectral intervals. Échelle gratings have fewer grooves per millimetre than conventional gratings, but when used at high angles, they produce high diffraction orders. The diffraction orders tend to overlap withÉchelle gratings, so the typical Échelle spectrometer incorporates a dispersing element that optically separates the orders in the axis perpendicular to the axis in which the orders are produced. In the Michelle 5000, this is achieved by a proprietary prism configuration giving the device a maximum resolution of $\lambda/\Delta\lambda = 6000$ when an acceptance slit having a width of 10 μm is used. For the experiments described here, the spectrometer was operated without a slit. Thus, the 200 μm fibre used constitutes the acceptance aperture width, giving the device in this configuration a nominal spectral resolution of $\lambda/\Delta\lambda \approx 1100$ which translates to a FWHM of 0.18 nm at 200 nm and 0.45 nm at 500 nm. The Échelle spectrometer used in these experiments was wavelength calibrated with a mercury-argon calibration source. Detalle et al [74] provide a good review of Échelle spectrometers, comparing them to conventional Czerny-Turner spectrometers for LIBS applications.

To investigate the by-products produced during the observed laser-induced reaction, a quadrupole mass spectrometer was attached to the experimental apparatus described in Figure 3.1 between valve V_0 and the vacuum cell. Valves V_1, V_2, and V_4 were closed and the vacuum system was altered in order to pump the vacuum cell through the mass spectrometer. In order to control the vacuum level in the device, the spectrometer was fitted with a leak valve located between it and the vacuum cell. The vacuum level in the spectrometer was measured with a wide-range gauge

and not allowed to go above 10^{-5} Torr during the experiment.

All experiments discussed in this section were performed on SiO_2 samples that were ultrasonically cleaned for ten minutes in acetone. They were then rinsed in an isopropyl alcohol bath for ten minutes, followed by an additional five minute rinse in ultrapure water. Both rinses were done in an ultrasonic cleaner as well. The samples were then dried with nitrogen and baked for two hours or more at 200°C.

4.2 Procedure and Results

In order to study the interaction of the laser-induced plasma plume with the ambient, and the role this interaction plays in driving the chemical reaction observed in the experiments detailed in Chapter 3, we began with a series of LIBS experiments in which we compared the time-resolved optical emission spectra of SiO_2 ablated in 2 Torr of xenon to that of SiO_2 ablated in 2 Torr of XeF_2. Figure 4.3 concisely shows the results of these experiments. Each spectrum is the integrated signal from ten consecutive measurements, each one of a single ablation event using a pulse energy of approximately 200 μJ. The sample was moved between each laser shot to provide a clean, unablated region from which to collect the data. The exposure time for each measurement was 200 ns with gate delays[1] $\Delta\tau$ form 0 to 5 μs in 1 μs increments. The experiments leading to the data in Figures 4.3(a) and 4.3(b) were performed in xenon and with $\Delta\tau = 0$ μs and $\Delta\tau = 1$ μs, respectively. Figures 4.3(c) and 4.3(d) show the results of experiments performed in XeF_2, with respective gate delays identical to those used in 4.3(a) and 4.3(b).

A number of atomic silicon lines are observed in the spectrum collected when SiO_2 is ablated. Table 4.1 catalogues these lines, complete with their energy levels, probabilities, and transition configurations. The very presence of the lines allows us to conclude, first, that SiO_2 is decomposed into elemental silicon and oxygen during UPLA[2]. Closer examination of the spectra collected in xenon reveals that silicon neutrals (SiI) are the primary atomic species produced in UPL-induced plasma plumes produced with the given process conditions. Some weak, singly ionised silicon (SiII)

[1] The gate delay is the amount of time between the arrival of the pulse at the sample and the start of the measurement.

[2] It is not clear why no oxygen lines were observed, but the presence of the strong silicon signal is clear evidence of ablation driven decomposition of the sample.

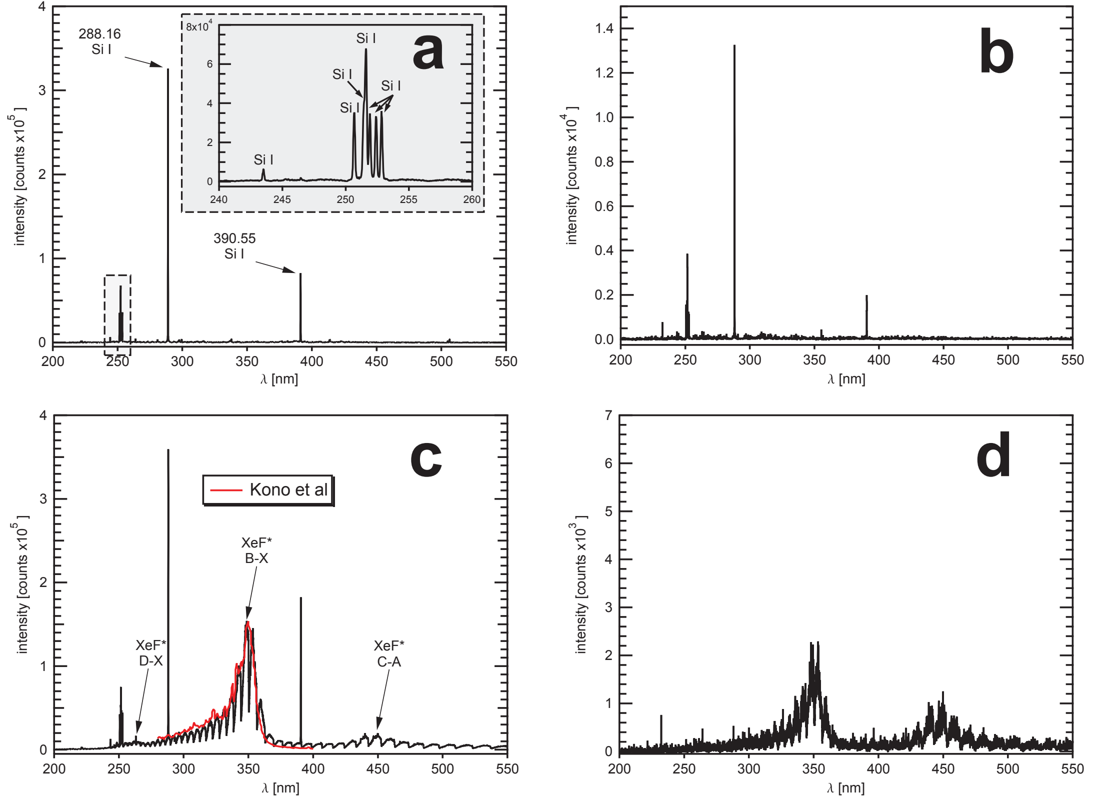

Figure 4.3. Optical emission spectra of SiO_2 ablated in Xe (a and b) and XeF_2 (c and d). Each spectrum is the integrated signal from ten separate ablation events. The exposure time used to collect each data set was 200 ns with gate delays of 0 ns (a and c) and 1000 ns (b and d). The normalised spectrum plotted in red in figure (c) is taken from $XeF^*(B{\rightarrow}X)$ transition data published by Kono et al [75].

and xenon (XeII) lines are also observed in the first 200 ns of the plume evolution (see Figure 4.9). However, these lines are not observed at longer delay times. The strong SiI lines, on the other hand, persist for at least 1.2 μs when the ablation is performed in inert environments (see Figure 4.3(b)). As expected, the intensity of the neutral lines decreases with time as the plasma expands into the ambient. Similar results are seen when the experiment is performed in a nitrogen atmosphere.

When SiO_2 is ablated in a XeF_2 atmosphere, SiI lines with similar intensities are again observed. In addition to these neutral lines, though, a continuum spectrum is also observed (Figure 4.3. A review of the literature reveals that this signal is characteristic of excited states of the XeF^* excimer [77, 78, 75, 79]. When XeF_2 is excited, it undergoes fragmentation. The possible diatomic dissociation products

Atom/ion	λ [nm]	Energy levels		g_kA_{ki} (10^8s^{-1})	Transition	
		E_k [eV]	E_i [eV]		Upper	Lower
SiI	243.52	5.8708	0.7810	2.21	$3s^23p3d\ ^1D^\circ_2$	$3s^23p^2\ ^1D_2$
SiI	250.69	4.9538	0.0096	2.74	$3s^23p4s\ ^3P^\circ_2$	$3s^23p^2\ ^3P_1$
SiI	251.43	4.9296	0.0000	2.22	$3s^23p4s\ ^3P^\circ_1$	$3s^23p^2\ ^3P_0$
SiI	251.61	4.9538	0.0277	8.40	$3s^23p4s\ ^3P^\circ_2$	$3s^23p^2\ ^3P_2$
SiI	252.92	4.9296	0.0096	1.65	$3s^23p4s\ ^3P^\circ_1$	$3s^23p^2\ ^3P_1$
SiI	252.41	4.9201	0.0096	2.22	$3s^23p4s\ ^3P^\circ_0$	$3s^23p^2\ ^3P_1$
SiI	252.85	4.9296	0.0277	2.71	$3s^23p4s\ ^3P^\circ_1$	$3s^23p^2\ ^3P_2$
SiI	263.12	6.6192	1.9087	3.18	$3s^23p3d\ ^1P^\circ_1$	$3s^23p^2\ ^1S_0$
SiI	390.55	5.0823	1.9087	0.39	$3s^23p4s\ ^1P^\circ_1$	$3s^23p^2\ ^1S_0$
SiII	412.81	12.8393	9.8367	8.94	$3s^24f\ ^2F^\circ_{5/2}$	$3s^23d\ ^2D_{3/2}$
SiII	413.09	12.8393	9.8388	13.90	$3s^24f\ ^2F^\circ_{7/2}$	$3s^23d\ ^2D_{5/2}$
SiII	504.10	12.5253	10.0664	2.80	$3s^24d\ ^2D_{3/2}$	$3s^24p\ ^2P^\circ_{1/2}$
SiII	505.60	12.5254	10.0739	8.70	$3s^24d\ ^2D_{5/2}$	$3s^24p\ ^2P^\circ_{3/2}$

Table 4.1. Wavelength, energy levels, probability, and transition configurations of Si lines observed during LIBS [76].

include XeF + F, Xe + F_2, and/or XeF^+ + F^-. Xe + F_2 formation is unlikely due to the large separation of the F atoms in the ground state and XeF^+ + F^- formation requires energies in excess of between 9.5 eV [75] and 11 eV [77]. Thus, XeF + F formation tends to dominate.

The resulting XeF^* excimers have five excited states, labelled X, A, B, C, and D. State-to-state transitions result in characteristic photoemission. Table 4.2 enumerates these states, along with their electronic configurations, radiative transitions, and lifetimes [75, 80]. One transition of note is the C→A transition whose long lifetime has led to the use of XeF as a laser gain medium. Thus, the technical relevance of XeF has led to its in-depth study allowing the identification of spectra in the literature identical to that observed in Figures 4.3c and d. To illustrate, the spectra resulting from the B→X transition during photoexcitation of XeF_2 at 154 nm, as published in Kono et al [75], has been normalised to and plotted against the continuum spectrum in Figure 4.3c. D→X and C→A transitions were also identified and are labelled accordingly.

Excimer State	Electronic Config.	Radiative Trans.	λ [nm]	Lifetime [ns]
X	$^2\Sigma^+_{1/2}$	ground state	–	–
A	$^2\Pi_{1/2,3/2}$	none	–	$\leq 10^{-4}$
B	$^2\Sigma^+_{1/2}$	B→X	≈ 350	14
C	$^2\Pi_{3/2}$	C→A	≈ 460	93±5
D	$^2\Pi_{1/2}$	D→X	≈ 260	19.1±0.5

Table 4.2. Table of XeF^* excimer states, their electronic configurations, radiative transitions, and lifetimes. See Figure 4.12 for energy levels.

Though reduced in intensity, the same XeF^* transitions are observed in Figure 4.3(d), a full 1 μs later. Notably, though, all the SiI lines observed at $\Delta\tau = 1$ μs in the xenon atmosphere and at $\Delta\tau = 0$ μs in the XeF_2 atmosphere are missing. This suggests that the atomic silicon produced during laser ablation is consumed in the reaction responsible for the effects observed in the experiments detailed in Chapter 3. Additionally, it would appear that the reaction does indeed proceed in the gas-phase as earlier results suggested and that it is energetically driven by the laser-induced plasma.

To corroborate these data and to further study the dynamics of the plasma plume, we directly imaged it as it expanded the into ambient. The time-resolved images shown in Figure 4.4 are of the plume expanding into 2 Torr of nitrogen (top row) and 2 Torr of XeF_2 (bottom row). Each individual image represents the integration of two sets of ten images. One set of images was taken through a 390 nm bandpass filter (±7 nm at FWHM), effectively resolving the spatio-temporal evolution of the atomic silicon. The other other set was unfiltered (panchromatic) and shows the extent of the plasma plume. The two sets were combined to form a composite image. The exposure time for each image is 50 ns and the gain setting used for the unfiltered images was identical for experiments performed in N_2 and XeF_2. The gain was increased for the filtered images, but again, was the same across gas atmospheres. In addition to providing improved temporal resolution due to increased collection efficiency, this technique allows us to spatially resolve individual plume components.

Comparison of these two image sets reveals some important differences. First, the plasma expands more rapidly in nitrogen and reaches a greater extent than it

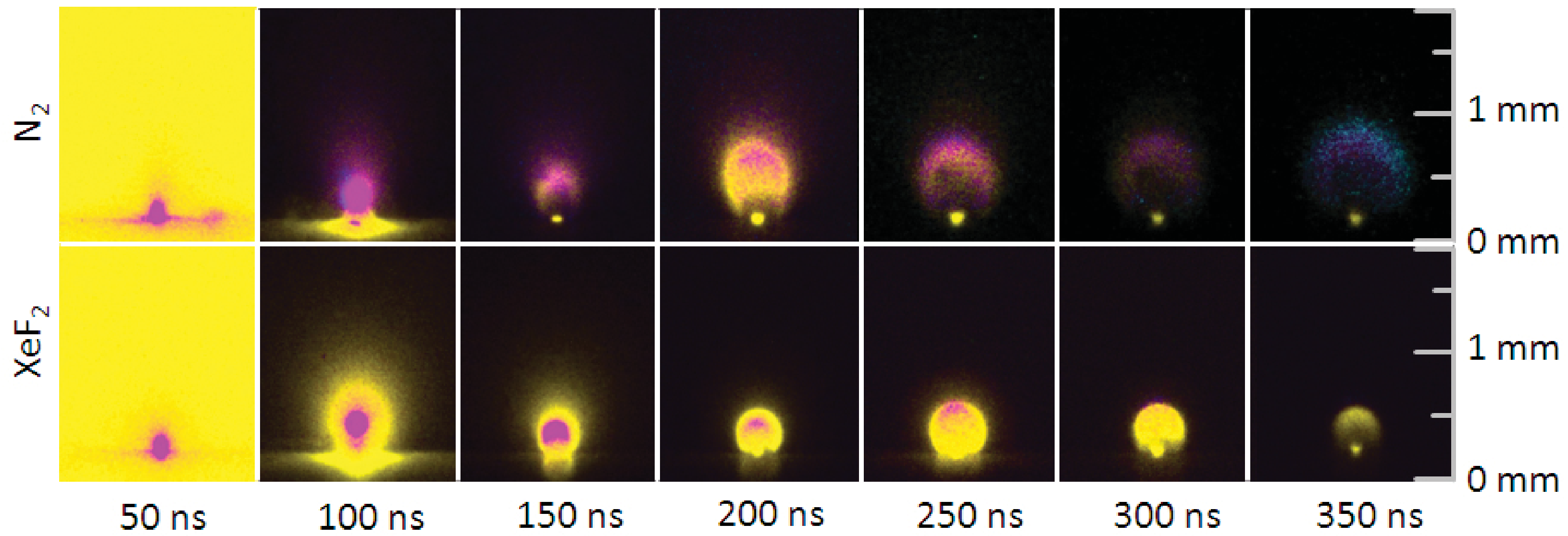

Figure 4.4. Composite, time-resolved CCD images of the expansion of the plasma plume into N_2 (top row) an XeF_2 (bottom row) atmospheres. Each image consists of 20 separate images integrated together. All images were false coloured to distinguish the unfiltered, panchromatic signal (yellow) and the signal from the 390 nm silicon neutral line (magenta and blue – magenta pixels indicate a region of the image in which 390 nm emission and panchromatic emission overlay one another while blue pixels indicate 390 nm emission alone).

does in XeF_2. It also appears that the plume in XeF_2 is more intense over a longer period of time. Of greater interest is the behaviour of the filtered Si 390.55 nm line, which can be taken to be representative of the elemental silicon present in the plasma plume. In nitrogen, the atomic silicon is distributed throughout the plume and as previously noted, persists for the life of the plume. This is to be expected, since as observed in the spectrum in Figure 4.3(a) and (b), silicon is the primary emitting species when ablation is performed in Xe and N_2 atmospheres with the given laser parameters. In fact, over the spectral range measured, the LIBS spectrum shows almost no other source of emission in Xe and N_2 atmospheres.

In XeF_2, however, the filtered Si 390.55 nm line is confined to the centre of the plume suggesting that the excitation of the reactive gas extends beyond the envelope of the expanding ablated material. There are two likely mechanisms for this observed phenomenon: excitation of the ambient due to emitted electrons and collisional energy transfer. The particular mechanism responsible depends on the interval of time over which the effect is observed. As will be explained below, excitation due to fast photoelectrons is observed early in the time series (0 to 100 ns), while later in the time series, the transfer of energy to the ambient via collisions drives the gas into an excited state.

As noted at the beginning of this chapter, the generation of fast photoelectrons has been observed by numerous researchers. In two very relevant papers, Issac et al. [25, 26] showed evidence of two distinct populations during the nanosecond pulsed laser irradiation of silver targets in nitrogen, argon, and carbon dioxide atmospheres. The distribution of the first population was sharply peaked, having a temporal width closely tracking the temporal profile of the laser pulse. The authors referred to these electrons as prompt electrons and measured them to have a maximum temperature of about 60$\pm$5 eV. The second distribution was smaller in amplitude and longer in duration (several μs) and appeared after the laser pulse was no longer incident on the sample. These electrons had a temperature of about 2$\pm$0.5 eV. The authors attributed the first population to photoexcited hot electrons escaping the laser-sample interaction volume before the laser energy is transferred to the lattice through collisions. The second population was attributed to plasma electrons. Hot photoelectron emission is also observed during femtosecond pulsed laser irradiation of dielectrics and is considered an important component of the physics of ablation

during and immediately after the absorption of the pulse [81].

With energies on the order of tens of eV, prompt photoelectrons can drive the ambient gas into an excited state. Both experiment [82, 83, 84] and theory [85] show that the lifetime of excited states of neutral nitrogen are less than 45 ns, with many low level states having lifetimes less than 10 ns. In contrast, when dissociative excitation by electron impact of XeF_2 was used to populate the the XeF(C) state, the XeF(C$\rightarrow$A) transition was measured to have a lifetime of 93$\pm$5 ns [86]. Furthermore, collisionally driven "afterglow fluorescence" was shown to persist for hundreds of nanoseconds, depending on the pressure of the XeF_2 ambient [87].

Effects due to fast photoelectrons and the long lifetime of the excited states of the XeF^* excimer can be observed by comparing the images spanning the time interval 0 to 100 ns in Figure 4.4. In both N_2 and XeF_2, the burst of fast photoelectrons that coincides with photon absorption and leads to ablation excites the ambient producing emission of sufficient intensity that the CCD saturates (yellow background in the 50 ns images). The filtered 390 nm light emitted by the excited silicon, however, clearly shows the actual shape and extent of the plasma plume at this early stage. Note that in the first 50 ns, the shape and extent of the plume is largely independent of the atmosphere in which it is formed (see the first data point in Figure 4.5).

From 50 to 100 ns, the relationship between the filtered emission and the panchromatic emission is clearly different in the two atmospheres. The panchromatic and filtered emission overlay one another in N_2, while the volume generated by the panchromatic signal (yellow) extends well beyond that of the filtered signal (magenta) in XeF_2. This is ascribed to the difference in lifetimes between the excited states of N_2 and XeF^*. The short lifetimes of nitrogen excited states (from <10 to 45 ns [82, 83, 84, 85]) ensure a rapid decay of the emission signal excited by photoelectrons, and a corresponding rapid contraction of the panchromatic excitation volume after the excitation source is removed. Conversely, the long lifetime of the XeF^*(C$\rightarrow$A) transition (93$\pm$5 ns [86]) results in a slower decay of the emission excited by photoelectrons, and a correspondingly slower contraction rate of the panchromatic excitation volume. The contracting photoelectron excitation volume is captured in the 100 ns image acquired in XeF_2.

Examination of the XeF_2 images over the interval from 150 to 350 ns interval (5

images) reveals that the plume appears to be initially composed of a silicon core with a panchromatic shell. Furthermore, the plume appears to evolve very slowly, with both components (core and shell) maintaining their respective spatial orientations relative to one another. The silicon component grows dimmer and more diffuse over time, disappearing nearly completely by 300 ns, after which the intensity of the panchromatic emission drops off significantly. Figure 4.5 compares the integrated intensity of the 390 nm emission in both N_2 and XeF_2. In XeF_2,emission from excited silicon atoms goes to zero 350 ns after the delivery of the pulse. In N_2, we see emission from the SiI line out to 1.2 μs, corroborating the data presented in Figure 4.3.

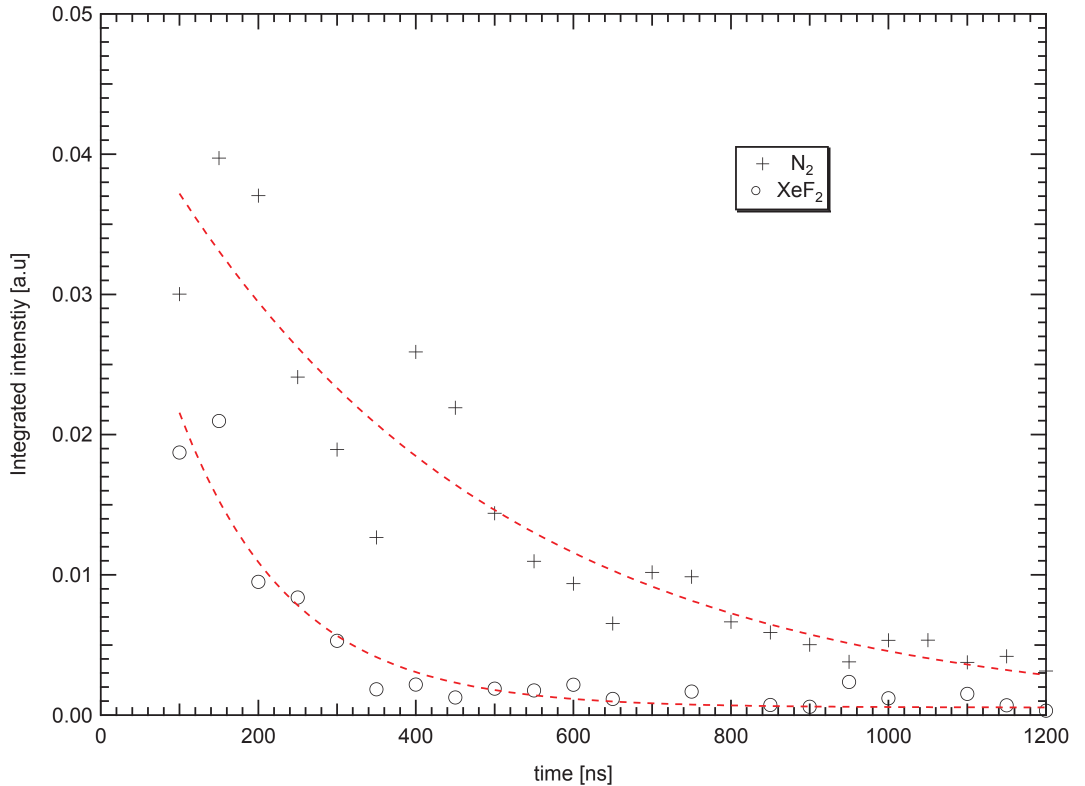

Figure 4.5. Time-resolved integrated intensity of the 390.55 nm emission from Figure 4.4. The red dashed lines are provided to help guide the reader's eye. Note that the emission is effectively quenched at 350 ns in XeF_2, whereas in N_2 it persists to at least 1.2 μs.

Since it is unlikely that silicon atoms emitting at different wavelengths would be spatially discrete, we attribute the panchromatic shell to the excitation of the

ambient via collisions with the expanding silicon. The ablated silicon expands with sufficient energy to drive the ambient XeF_2 into an excited state, where it undergoes fragmentation forming $XeF^* + F$ as discussed earlier. Knock-on collisions between gas molecules drives still more gas molecules into excited states, generating a layer of reactive species at the wave front of the propagating atomic silicon.[3]

Not only is this reactive layer observable in the XeF_2 images in Figure 4.4, its effect can be seen when modelling the propagation of the plume into the ambient. To describe the dynamics of plumes propagating into inert ambient gasses, Amoruso et al. [29] developed a simple Newtonian model balancing the force due to the pressure of the ambient with the time rate of change of momentum of the plume, such that

$$\frac{d}{dt}\left[\left(M_a + \frac{2}{3}\pi\rho_g R\left(t\right)^3\right) v_a\left(t\right)\right] = -2\pi R\left(t\right)^2 p_g, \quad \frac{dR}{dt} = v_a\left(t\right) \tag{4.1}$$

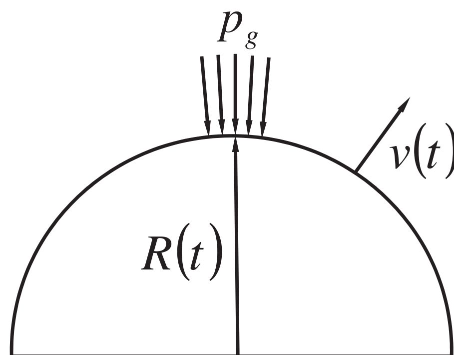

Figure 4.6. Model of plume expansion into a background gas.

where M_a is the mass of the atomic plume, ρ_g is the density of the ambient gas, p_g is the pressure of the ambient gas, R is the radius of the expanding plume front, and v_a is its velocity as illustrated in Figure 4.6. The initial conditions are $R\left(0\right) = 0$ and $v_a\left(0\right) = v_{a,0}$. The mass of the gas swept away by the expanding plume at a distance R and a time t is given by the term $2/3\pi\rho_g R\left(t\right)^3$. The mass of the ablated material, M_a, and the initial velocity, $v_{a,0}$, are free parameters that can be adjusted to fit the model to the data.

[3] It is unlikely that so-called plasma electrons as measured by Issac et al. [25, 26] play a role in this process given that their reported energies are lower than the energy required to induce fragmentation forming excitation in XeF_2 (approximately 7 eV [77]).

Figure 4.7 plots results of the numerically solved model against the measured 390.55 nm data. Using an initial velocity of 7500 m/s and an ablated mass of 6.0×10^{-12} kg for values of the fitting parameters $v_{a,0}$ and M_a respectively, the model accurately predicts the expansion of the plume in N_2. In experiments performed on iron samples under different conditions ($\lambda = 527$ nm,$\tau_p = 300$ fs, $\phi = 0.6$ J/cm^2, and 45°C angle of incidence), Amoruso et al. measured the initial velocity of the plume to be 1.6×10^4 m/s, about twice the value at which our best fit occurs. The best fit for their data gave a mass for the atomic plume of 1.1×10^{-11} kg, again about double our value. It must be emphasised, however, that their experimental conditions were considerably different than ours and that material properties play an important role in the efficacy of ultrashort pulsed laser ablation.

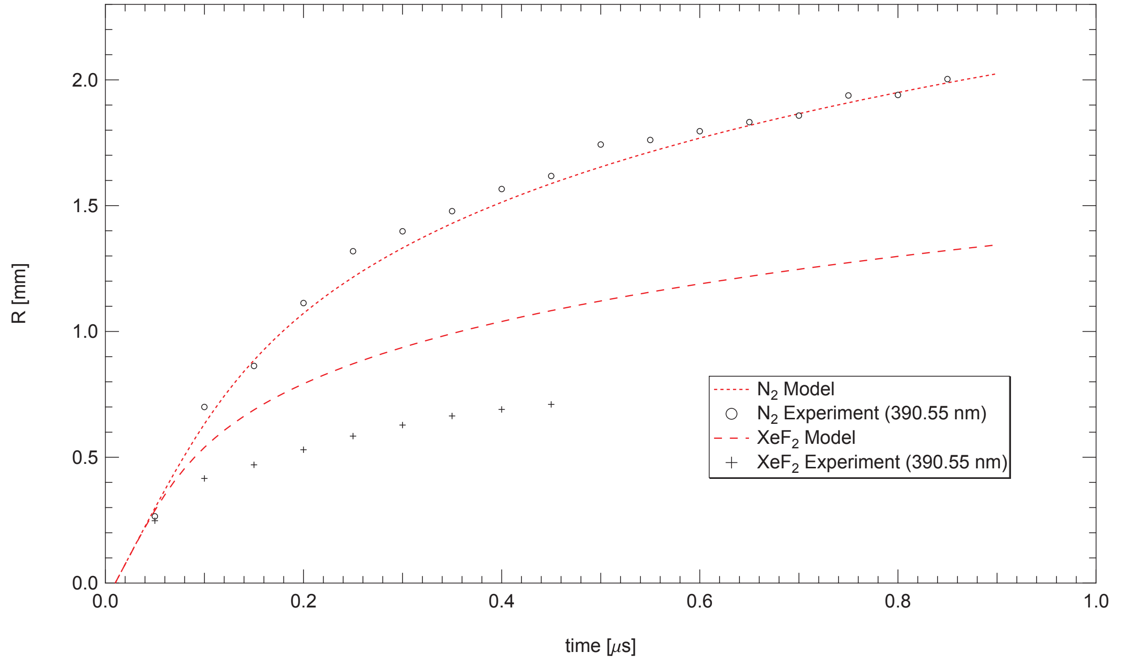

Figure 4.7. Modelled versus measured values of plume expansion into N_2 and XeF_2 atmospheres using the fitting parameters $v_{a,0}$=7500 m/s and M_a=6.0×10^{-12} kg. While the model clearly predicts the plume's expansion into nitrogen, it greatly over estimates the plume's extent in XeF_2. This is due to the fact that the model ignores both the reaction kinetics and the role the reaction plays in quenching the emission from atomic silicon.

For the XeF_2 data, there is a marked divergence between the measured and predicted results when these same fitting parameters are used. Upon closer consid-

eration, this is to be expected. The reaction responsible for the effects observed in Chapter 3 is one in which silicon is converted to SiF_X. As the plume expands into the ambient, the expansion front of atomic Si collides with XeF_2 molecules, forming a shell of excited XeF*, as previously discussed. As the expansion front undergoes fluorination, the characteristic emission by which the atomic silicon is observed is quenched, resulting in the observable reduction in its extent. The reaction can also be observed occurring at the centre and back of the silicon plume where turbulence may play a role, but it is the reaction at the expansion front that is responsible for the discrepancy between the modelled and observed results.

The effective sudden increase in mass that the ablated species undergoes as it is converted to SiF_x results in a proportional decrease in velocity as momentum is conserved. However, given that no emission characteristic of fluorinated silicon species is observed in the spectral range over which the experiment was performed, we were unable to directly measure this decrease. Inelastic processes such as collision-induced vibrational modes will also contribute to the stopping power of a reactive gas, but again, these were not measured in this experiment.

Once the silicon is consumed, direct collisional excitation of the ambient by the ablated material can no longer occur. As a result, one would expect the intensity of the emission from the ambient to decay rapidly as knock-on collisions become the main contributing factor. This is indeed what is observed in Figure 4.4 at 350 ns in XeF_2. It is at this time delay that Figure 4.5 shows the integrated intensity of the 390 nm line going to near zero. The low intensity emission measured hundreds of nanoseconds later as shown in Figure 4.3(d) is due to inter-ambient collisionally-driven “afterglow fluorescence” identical to that observed by Eden et al [87].

4.2.1 Characterisation of the Plasma

In addition to the identification of specific atomic species and excimers, careful analysis of the plasma self-emission can provide a more complete characterisation of laser-induced plasmas. Tempered by careful consideration of the thermodynamic state of the plasma at a given time, well established techniques in which line intensities are compared relative to one another yield estimates of the plasma’s electron temperature and density.

Consider a plasma as a dynamical system of electrons, atoms, ions, and photons.

When in true thermodynamic equilibrium (TE), the ionisation and radiation processes that drive this system are balanced by their inverse processes (recombination and absorption, respectively). This concept is known as the principle of detailed balancing. Furthermore, statistical mechanics describes each component of a system in TE by distributions whose functional form depends on the plasma temperature. For instance, the energy distribution of electrons in a plasma in TE is a Maxwellian function of the temperature T_p of the plasma. In turn, the distribution of atoms and ions in excited states follows a Boltzmann distribution law such that [88, 89],

$$\frac{n_k}{n} = \frac{g_k}{P_Z} \exp\left(-\frac{E_k}{k_B T_p}\right) \tag{4.2}$$

where n_k is the population of atoms or ions in the upper (k^{th}) energy level, n is the number density of atoms, E_k and g_k are the energy and degeneracy of the upper energy level, P_Z is the partition function of ionisation stage Z, and k_B is the Boltzmann constant[4]. Similarly, for a given temperature, the distribution of photon energies is described by Planck's function,

$$E(\nu) = \frac{8\pi h \nu^3}{c^3} \frac{1}{e^{h\nu/k_B T} - 1} \tag{4.3}$$

where ν is the photon frequency, h is Planck's constant, and c the speed of light.

Unfortunately, plasmas in thermodynamic equilibrium provide little opportunity for analysis via optical emission spectroscopy since, according to the principle of detailed balancing, all emitted light is reabsorbed by the plasma. These plasmas are typically referred to as optically thick. In optically thin plasmas, however, detailed balancing does not hold and photons can escape the plasma. Their energy distribution consequently deviates from Equation 4.3 and the resulting radiative cooling effectively alters the distribution of electrons, atoms, and ions as well.

If the losses due to radiative processes are significantly smaller than collisionally-induced transitions, and the plasma is sufficiently stable temporally (i.e. stationary) and spatially homogeneous, it is said to be in local thermodynamic equilibrium (LTE). The standard typically applied is the so-called McWhirter criterion and is expressed as

$$n_i X_{ik} = n_k X_{ki} > 10 n_k A_{ki} \tag{4.4}$$

[4] $Z = 0$ corresponds to excited neutral atoms, $Z = 1$ to singly ionised atoms, etc.

where n_i is the population of atoms in energy level i, X_{ik} is the collisionally induced transition rate from the i to the k energy level (note: i to k is an excitation process, whereas k to i is a de-excitation process), and A_{ki} is the radiative decay rate.

In essence, for plasmas in LTE, radiative processes are decoupled from collisional ones. Thus, while the Planck distribution no longer holds for photons, Equation 4.2 is still valid for ions and neutral atoms. Thus,

$$T_p = T_e = T_{i/a} \neq T_\nu \tag{4.5}$$

where T_p is again the plasma temperature, T_e is the electron temperature, $T_{i/a}$ is the temperature of ions and excited neutral atoms, and T_ν is the temperature that characterises the distribution of photon energies, but is no longer described by Equation 4.3.

In the results presented here, we assume that the plasma is optically thin and in LTE during the first 200 ns of its lifetime. The validity of this assumption is bolstered by the fact that in the XeF_2 atmosphere, collisional processes, which must dominate for LTE to hold, are observed driving the ambient into an excited state over the first 350 ns. Furthermore, the emission from the excited ambient dims only after the energetic Si atoms responsible for the collisions are converted to SiF_x – a process that, again, ultimately results in a decreased particle velocity as momentum is conserved. The observable dependency of emission intensity on collisional events, as well as the relatively constant intensity of this emission over the course of this process, suggests that radiative cooling in not significant during the prescribed time interval.

From Griem [88], we know that in an optically thin plasma the integrated intensity I_{ki} of a spectral line is given by

$$I_{ki} = \frac{hc}{4\pi\lambda_{ki}} A_{ki} n_k L \tag{4.6}$$

where λ_{ki} is the transition wavelength, A_{ki} is the transition probability, and L is the characteristic length of the plasma. Combining Equations 4.2 and 4.6 and taking the natural log of both sides yields

$$\ln\left(\frac{I_{ki}\lambda_{ki}}{g_k A_{ki}}\right) = -\frac{1}{k_B T} E_k + \ln\left(\frac{hcLn}{4\pi P_Z}\right). \tag{4.7}$$

.

Plotting the term on the left against the upper level energy E_k for several line intensities of the same ionisation state Z, yields a line, the negative slope of which is inversely proportional to T (the second term on the right side is constant)[5]. Plots of this sort are typically referred to as Boltzmann plots. Figure 4.8 is an example of one such Boltzmann plot taken from data collected during the first 200 ns of the Xe experiments. The lines that were used are the SiI lines from 243.52 to 263.12 nm listed, along with their transition parameters, in Table 4.1. Averaging the results from three separate experiments, the electron temperature was measured to be 8900±1800 K (0.77±0.16 eV) in Xe and 12800±2000 K (1.1±0.17 eV) in XeF_2 using this method. These values are in reasonably good agreement with other UPL-induced plasma temperatures cited in the literature. T_e was measured at longer time delays, but the assumption of LTE looses validity as the plasma cools. For this reason, these values are not reported here.

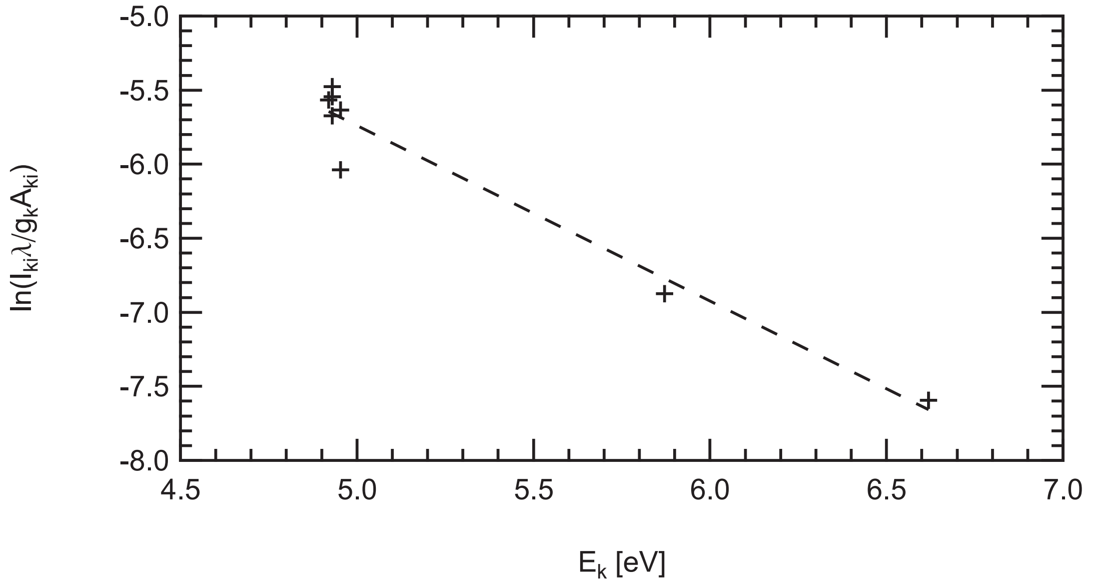

Figure 4.8. An example of the Boltzmann plot method used for measuring electron temperature T_e of a plasma. This plot was taken from data collected during the first 200 ns of a plume generated in a xenon atmosphere. The slope of the best fit line is m=-1.1845 yielding $T_e = -1/mk_B$ =9797 K.

The Saha-Boltzmann equation is typically employed to measure the electron density n_e. Unlike the method used to calculate the electron temperature which must

[5] As noted in Equation 4.5, T is equivalent to the electron temperature.

use data from atoms or ions in the same ionisation state Z, the Saha-Boltzmann equation compares data from both atoms and ions such that

$$n_e = \frac{I^*_{ki,Z}}{I^*_{ki,Z+1}} 6.04 \times 10^{21} T^{3/2} \times \exp[(-E_{k,Z+1} + E_{k,Z} - \chi_Z)/k_B T] cm^{-3} \quad (4.8)$$

where

$$I^*_{ki,Z} = \frac{I_{ki,Z}\lambda_{ki,Z}}{g_{k,Z}A_{ki,Z}} \quad (4.9)$$

and χ_Z is the ionisation of the species in ionisation stage Z [90]. Figure 4.9 shows the silicon ion lines used to measure n_e and Table 4.1 lists the upper state energies E_k, transition probabilities A_{ki}, and degeneracy g_k required by Equation 4.8. Over the first 200 ns, n_e of the plasma plume in the nitrogen atmosphere was measured to be $2.25\times10^{15}\pm6.07\times10^{14}$ cm^{-3} (for T_e = 8900 k). As with the T_e measurements reported earlier, this value of n_e is in reasonably good agreement with values cited in the literature. Because the Si II lines were not visible over the continuum emitted by the XeF* B→X and C→A transitions, no n_e measurement could be made in XeF_2.

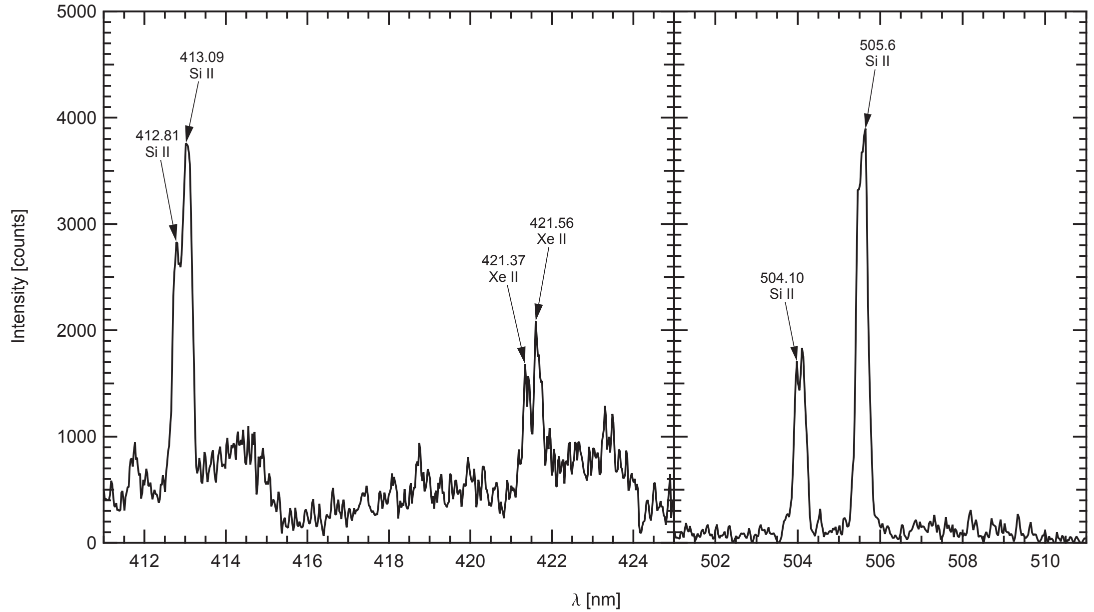

Figure 4.9. Si ion lines used to measure n_e. Note the break in the x-axis.

4.2.2 Reaction By-Products

Having demonstrated that the reaction identified in Chapter 3 is indeed a gas-phase reaction, that it proceeds to completion in the first 350 ns of the plume's expansion, that it is driven primarily by collisions, and having determined the characteristics that define the plasma (T_e and n_e), we now turn to our attempts to characterise the by-products of the reaction via quadrupole mass spectrometry.

Quadrupole mass spectrometers separate gas ions based on their mass-to-charge ratio (m/z). A gas introduced to the spectrometer is first ionised via electron impact ionisation. The newly produced ions are then accelerated along the axis of symmetry of four cylindrical rods, also known as the quadrupole. Opposing pairs of rods are electrically connected and an oscillating voltage is applied between one set of rods and the other. For a given oscillation frequency, only ions of certain charge-to-mass ratios will reach the detector, located at the end of rods. Ions with a charge-to-mass ratio unmatched to the oscillating field will collide with the quadrupole rods, never reaching the detector. With *a priori* knowledge of the trajectory of an ion of a given mass for a given oscillating frequency, the device can be used to detect ions of different mass by scanning through a range of oscillation frequencies.

To perform the experiments described in this section, we connected a Pfeiffer PrismaPlus QMG 220 compact quadrupole mass spectrometer (also called a Residual Gas Analyser or RGA) to the experimental set-up shown in Figure 3.1. The connection was made at valve V_0 via a stainless steel vacuum tube having an inner diameter of 1 inch. As shown in Figure 4.10, a leak valve (V_{RGA}) was placed between the RGA and the vacuum chamber in which the experiment was performed in order to control the vacuum level in the RGA as measured by gauge P5. Valves V_1, V_2, and V_4 in Figure 3.1 were closed during the experiments so that the vacuum cell was pumped through the RGA. The base pressure of this system was 6.0×10^{-6} mbar.

The Pfeiffer PrismaPlus is capable of measuring atoms and molecules with masses of up to 300 amu. The ionising electrons are generated by a tungsten filament and the ion detector is a continuous dynode secondary electron multiplier. The maximum operating pressure of this system is 1×10^{-4} mbar, hence the need for leak valve V_{RGA}.

In order to analyse the specific by-products of the reaction, a single crystal, Z-cut SiO_2 sample prepared in a fashion identical to that described in Section 3.4

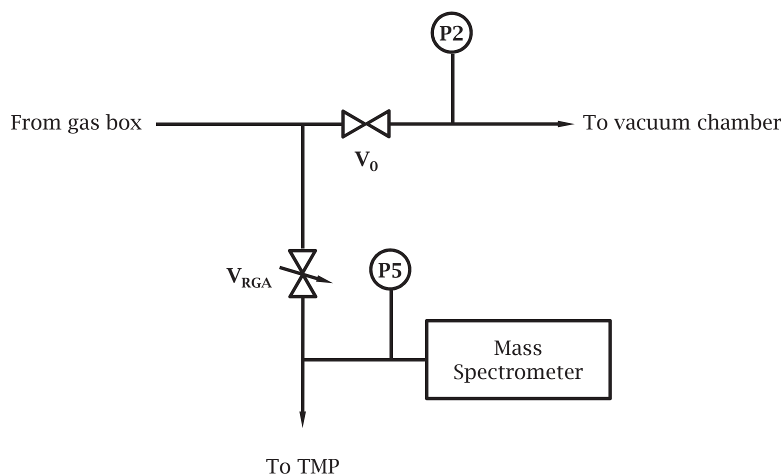

Figure 4.10. Arrangement of the mass spectrometer used to characterise reaction by-products. This arrangement was added to the set up in Figure 3.1 where valve V_0 and gauge P2 were first identified. Valve V_{RGA} is a leak valve used to control the flow into the mass spectrometer. Valves V_1, V_2, and V_4 in Figure 3.1 were closed during the experiments so that the vacuum cell was pumped through the mass spectrometer.

was placed in the vacuum cell. The cell was then pumped down and an RGA scan was initiated. The scan was set to detect SiF, SiF_2, SiF_3, SiF_4, Si_2F_6, Xe, XeF, and XeF_2. Once the RGA signal reached a reasonable baseline, laser processing of the sample commenced. The processing was performed with an average laser power of 100 mW and scan parameters identical to those used in Chapter 3 – namely, a scan velocity of 0.050 mm/s and a y-step of 1 μm. After approximately 15 minutes of SiO_2 ablation, XeF_2 was introduced to the vacuum. No attempt was made to restrict the flow of gas into the processing chamber. Thus, the pressure inside the cell increased to near the vapour pressure of XeF_2 or about 5.3 mbar. The flow to the RGA was restricted via valve V_{RGA}, ensuring that the pressure stayed below the RGA's maximum operating pressure.

Figure 4.11 shows that the main reaction by-product measured is SiF_2, with small amounts of SiF and SiF_3 recorded. While very little, or in some cases, no SiF4 was detected, cracking patterns for Si-F system published by Winters and Houle [62] attribute SiF_3^+ mass spectra to the dissociation of SiF_4 by the mass spectrometer. Thus, the small amount of SiF_3 observed is likely due to the presence of SiF_4. Si_2F_6,

XeF, and XeF_2 signals remained at background levels throughout the experiments[6]. Si_2F_6, XeF, and XeF_2 data are not shown in Figure 4.11 for clarity.

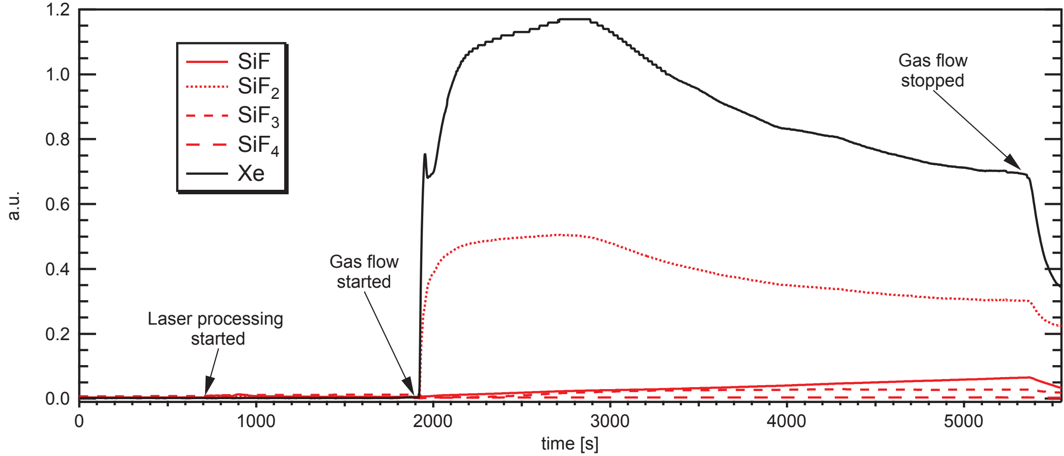

Figure 4.11. RGA analysis of by-products produced when the plasma generated by ultrashort pulsed laser ablation of SiO_2 interacts with XeF_2 in the gas-phase. SiF_2 is the main by-product recorded by the mass spectrometer, with small amounts of SiF and SiF_3 detected. Little or no SiF_4 and no Si_2F_6 (not shown) was detected. The SiF_3 signal is likely due to device dissociated SiF_4.

This experiment was repeated numerous times over a range of processing conditions (i.e. different laser powers, scan parameters, and gas pressures). SiF_2 was consistently observed to be the primary by-product recorded by the RGA, with small levels of SiF and SiF_3 always detected. Considering the widely cited work of Winters et al. [91, 62] in which SiF_4 was found to be the primary by-product produced during both spontaneous and ion-mediated reactions between silicon and XeF_2, our results at first seemed somewhat surprising. In a separate work, however, Dagata et al. [92] showed that silicon samples heated to up to 1000 K in the presence of either F_2 or NF_3 produce significant quantities of SiF_2 as a by-product. Winters and Plumb [93] later revised their conclusions showing SiF_4 production decreases and SiF_2 becomes the dominant by-product when silicon at elevated temperatures is exposed to XeF_2. While the gas-phase, plasma-mediated process described in this work is quite different from the surface reactions explored by Winters et al., it is

[6]The fact that fluorinated xenon compounds were not detected suggests that XeF and XeF_2 are dissociated by the RGA into their constituent parts, adding to the Xe produced by plasma-induced dissociation of the XeF_2.

quite clearly a related phenomenon. Thus, considering the very high temperature of the plasma, the prevalence of SiF_2 in the reaction by-products is perhaps not so surprising after all.

4.3 Conclusions

The results presented in this chapter and the last have clearly demonstrated the ability of ultrashort pulsed lasers to drive chemical reactions in the gas-phase. We have further uncovered the details of how the specific reaction that occurs when SiO_2 is ablated in a XeF_2 atmosphere proceeds. In the first phase of the process, photons excite electrons in the substrate through a non-linear or multi-photon absorption process[7]. Having gained sufficient energy to overcome the work function of the substrate, high energy photoelectrons are ejected into the ambient, driving it into an excited state. Via either coulombic explosion or the transfer of energy from excited electrons trapped in the bulk to the lattice (or both), the substrate is violently decomposed into its constituent silicon and oxygen atoms. The resulting solid density plasma expands away from the surface and into the ambient at supersonic velocities.

The expansion of the plasma begins picoseconds after the arrival of the pulse. By this time, the excitation volume of the ambient is shrinking as it cools. However, as the super-heated, electron-dense plasma expands, it collides with the ambient, re-exciting it while at the same time retarding the plume's expansion. In its excited state, XeF_2 forms an excited dimer, freeing a single, very reactive, fluorine atom. The slowing silicon atoms in the plasma plume react with the liberated fluorine, forming new products, primarily silicon difluoride. Fluorinated silicon compounds are all volatile and as such, are pumped away by the vacuum system, significantly reducing the amount of redeposition observed in the absence of XeF_2. Figure 4.12 illustrates in detail the reaction pathway just described.

[7]Non-linear absorption is the reason why ablation can occur at a wavelength to which SiO_2 is normally transparent.

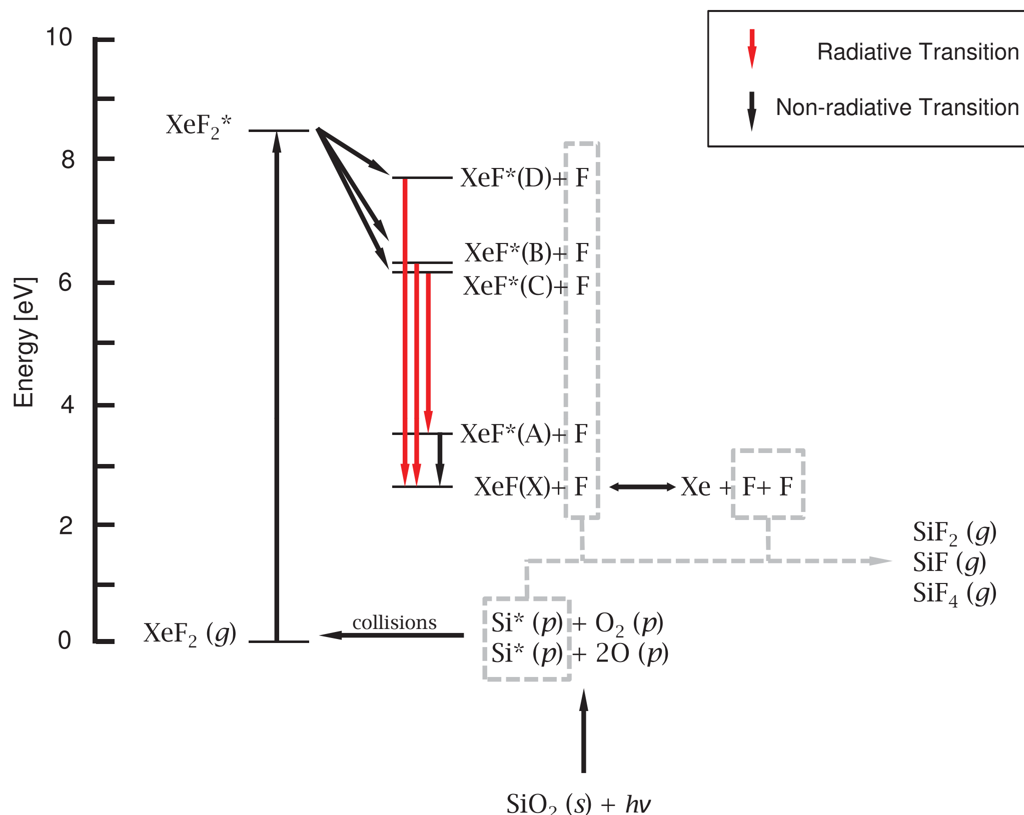

Figure 4.12. The reaction pathway for the formation of fluorinated silicon compounds during UPL ablation of SiO_2 in a XeF_2 atmosphere. Laser ablation of solid (s) SiO_2 creates a plasma (p) of excited silicon atoms Si^* that collisionally drives XeF_2 gas (g) into an excited state. Excited xenon difluoride XeF_2^* undergoes non-radiative fragmentation forming an excited dimer, or excimer, in one of three states; B, C, or D. Transitions between these states and certain lower energy states are radiative, with characteristic emission spectra (see Table 4.2). The formation of a dimer liberates a fluorine atom. In the ground state (X), the excimer can further fragment producing yet another fluorine atom. Atomic fluorine produced during this process reacts spontaneously with the atomic Si to form fluorinated silicon compounds. The primary compound formed is SiF_2 gas (g), but SiF and SiF_4 are also produced in smaller amounts. SiF_3 was also observed through mass spectrometry, but this is attributed primarily to the cracking of SiF_4 during analysis. The energy axis in this figure applies to the excimer states only.

Chapter 5

TripleBeam Design and Development

5.1 Introduction

During the course of this research, considerable effort went into the design, development, and construction of a complex scientific instrument that combines a scanning electron microscope, a focused ion beam (FIB), and an ultrashort pulsed laser. The success of this effort and the efficacy of the instrument for use in both basic research and as an industrial tool is illustrated by FEI Company's support of its development over the four years ranging from 2009 to 2012. The design challenges faced, the technical problems addressed, and the safety and usability issues considered represent many hours of work. This chapter attempts to distill this effort into a cogent discussion focusing first on the details of each major technology component, followed by the specifics of their integration. The chapter will close by briefly presenting the sample work done to characterise and validate the instrument.

5.2 Overview

The combination of SEM and FIB, often referred to as a DualBeam, is a well established technology pairing that is widely used for a range of industrial and research applications including failure analysis, defect analysis, circuit edit, metrology, lamella preparation, MEMs prototyping, device fabrication, lithography and mask repair,

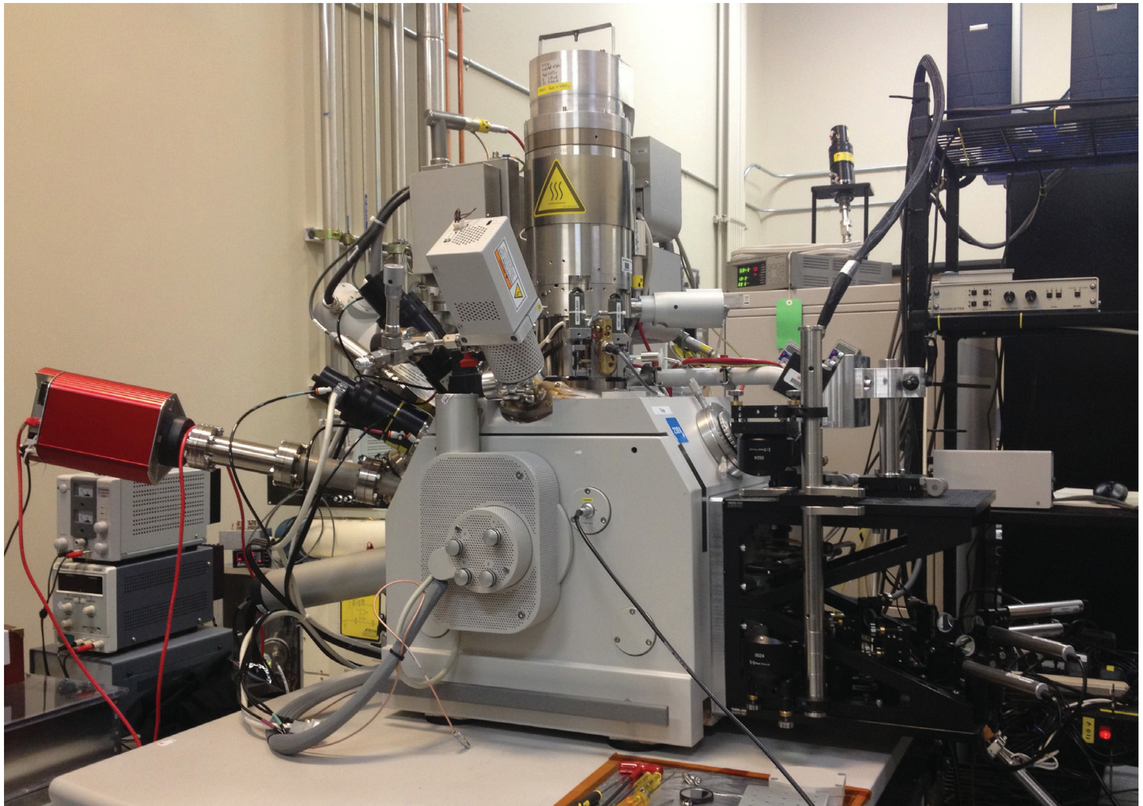

Figure 5.1. The TripleBeam System.

and tomography. The demonstrable breadth of the application space to which such a tool is relevant is largely attributable to a process synergy that results when SEM and FIB are implemented on a single platform. Users can modify samples and devices, both reductively and additively, on length scales of tens-of-nanometres to tens-of-microns via the FIB, then image and analyse the results of said processing in situ via SEM imaging and electron induced analytical techniques such as energy dispersive spectroscopy and electron backscatter diffraction (EBSD). In addition, the length scales for both material removal and material deposition can be extended downward to the nanometre scale through the use of electron beam-induced processing (electron beam-induced deposition and etching) techniques [70].

While both ion and electron beam-induced processing can produce microscopic structures with very high resolution, these techniques are often prohibitively slow. Furthermore, very hard (e.g. tungsten carbide) and non-conductive materials are widely known to be difficult to process with charged particle beam techniques. Ultrashort pulsed lasers, on the other hand, can machine nearly any material. Using

UPLs, material removal rates four to six orders of magnitude faster than typical FIB techniques have been demonstrated. The extremely short pulse durations that are characteristic of UPLs ensure that any material irradiated with sufficient energy is super heated (via photon-electron coupling) and undergoes explosive evaporation on a time scale too short to enable significant coupling of the incident energy to the lattice (i.e. photon- and/or electron-lattice coupling). In this way, UPLs remove material with little or no concomitant thermal damage to the bulk substrate or to adjacent structures. In short, ultrashort pulsed laser ablation typically results in a small heat affected zone.

While the development of an integrated SEM-FIB-UPL (henceforth referred to as the TripleBeam) was initially motivated by the need to speed processes normally performed by FIB or to enable ones not possible by current methods, a host of other applications are potentially made available by its invention. For instance, in situ laser-based characterisation techniques such as Raman spectroscopy and laser-induced breakdown spectroscopy become available as a means of producing correlative analytical data. The ability to deposit nanometre-scale metallic features in a controlled fashion via electron and/or ion beam-induced deposition (E/IBID) makes surface enhanced Raman spectroscopy (SERS) targetable to specific sites and may improve the spatial resolution of the technique. Additionally, characteristic X-rays that are generated during UPL ablation [94, 95, 96, 97] are driving the on-going investigation of the feasibility of laser-induced X-ray spectroscopy as a new characterisation technique. In the same way that SERS is made more efficacious given the E/IBID capabilities of the instrument, the fabrication, excitation, and in situ characterisation of plasmonic structures is also made possible by the TripleBeam. Thus, in addition to being an instrument for materials processing and/or rapid nano- or micro- prototyping, the TripleBeam is also a tool for the general investigation of phenomena involving the interaction of light and matter.

5.3 Laser

The laser system used in the development of the TripleBeam is a Ti:Sapphire chirped pulse amplification system produced by Clark-MXR (Dexter, MI, USA). Nominally, this laser outputs a train of 150 fs, 1 mJ pulses having a wavelength of 775 nm

(E_p = 1.6 eV) at a repetition rate of 1 kHz for a total maximum output power of 1 W. As shown in Figure 5.2, there are five major sub-components of the laser. At its most basic level, the theory of operation of the laser is as follows: the erbium doped fibre oscillator is pumped by a telecommunications grade laser diode. The output of the oscillator is a train of low energy, high repetition rate pulses. Before being injected into the amplifier, these pulses are positively chirped by the pulse stretcher. Positive chirping temporally stretches a pulse such that its low frequency components propagate ahead of its high frequency components. Moving from the lower lever to the upper, the stretched pulse is then injected into the regenerative amplifier cavity. The regenerative amplifier cavity is a multi-pass optical resonator with a Ti:Sapphire crystal as the gain medium. The Ti:Sapphire crystal is pumped by a frequency doubled, Nd:YAG laser. With each pass through the gain medium, the pulse is amplified. As the gain curve saturates, the pulse is selected in its most amplified state by a Pockels cell and sent to the compressor. There, the pulse is compressed to its final state via negative chirping and finally, output.

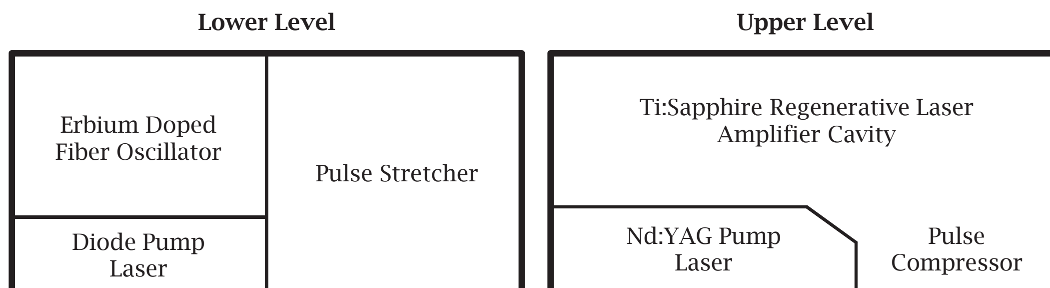

Figure 5.2. Main sub-components of the TripleBeam's laser.

5.3.1 Erbium Doped Fibre Oscillator

The oscillator used in the TripleBeam's laser is a stretched pulse additive pulse mode-locked (APM) erbium-doped fibre ring laser whose design is based on the work of Tamura, Ippen, Nelson, and Haus [98, 99, 100]. The specific design used (shown in Figure 5.6) generates a 38 MHz train of low energy pulses which are frequency doubled, then stretched, and finally amplified in the regenerative amplifier (Section 5.3.2). A complete theoretical explanation of APM is beyond the scope of

this thesis, but a general description of the oscillator's operation is given here. The following discussions of mode-locking and group velocity dispersion (GVD) serve as background for this discussion.

5.3.1.1 Mode-locking

All lasers produce light over a range of frequencies. The bandwidth of this range of frequencies is a function of both the geometry of the laser cavity and the gain medium used. Laser cavities typically consist of a gain medium located between two mirrors. Light reflected from the mirrors passes through the gain medium and is amplified. As the light bounces between the mirrors, it either constructively or destructively interferes according to the principle of superposition. Constructive interference leads to standing waves. These standing waves are typically referred to as longitudinal modes. Given a mirror separation L, constructive interference is only possible for those wavelengths of light where

$$\frac{m\lambda_m}{2} = L \tag{5.1}$$

where m is a positive integer known as the mode order and λ_m is the wavelength of the mathematically allowed mode. The separation between modes is typically expressed in terms of frequency:

$$\Delta\nu = \frac{c}{2L} \tag{5.2}$$

where c is the speed of light.

Equation 5.1 defines which modes are mathematically possible given the geometrical constraints of the amplifying cavity, but it is the gain medium that determines which modes are actually supported by any given laser system. All gain mediums amplify a range of frequencies in a process known as gain broadening. The physical mechanisms responsible for broadening are varied and determine whether the broadening is homogeneous (affecting all radiating quantum systems equally) or inhomogeneous (different absorbing and/or radiating quantum systems affected by different frequency components). The extent of this broadening across frequencies is referred to as the gain bandwidth. Any possible longitudinal mode with an unsaturated gain greater than the cavity losses will be supported. Figure 5.3 illustrates

how the mathematically allowed modes and the gain bandwidth of a given gain medium intersect to produce real modes supported and output by a laser system.

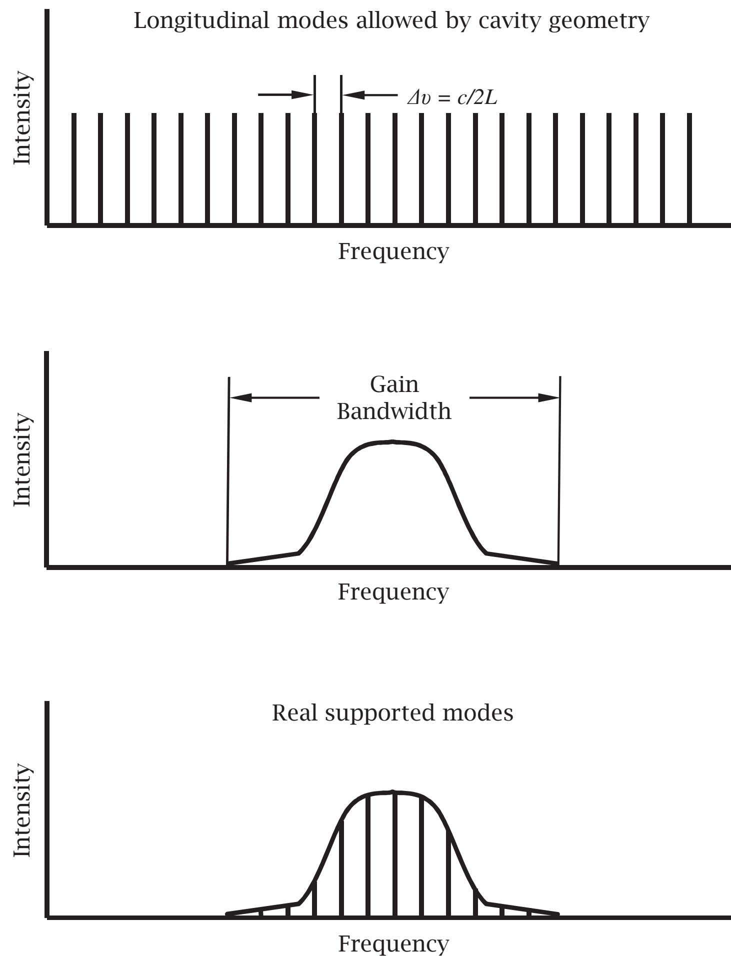

Figure 5.3. Longitudinal modes supported by a laser system are a function of the intersection of the modes that can exist given a cavity geometry and the gain bandwidth of the amplifying medium. Any mathematically allowed mode with an unsaturated gain greater than the cavity losses will be supported.

In a continuous wave laser, supported longitudinal modes oscillate with no fixed phase relative to one another. However, when the phases of oscillating longitudinal modes are fixed relative to one another, they will periodically constructively interfere. For a given instant in time, constructive interference occurs at a specific location within the cavity, while at all other locations the modes interfere destruc-

tively. The location at which constructive interference occurs is a smooth, continuous function of time. The result is a wave packet that travels back and forth between the mirrors of the cavity. Each time the wave packet reflects off the output mirror, some of its energy is transmitted as a laser pulse. When operating in this regime, the laser is said to be mode-locked.

Thus, the period (T) of the output pulse from a mode-locked laser is a direct result of the transit time of the pulse inside the cavity, which is, in turn, a function of the cavity length or $T = 2L/c$. The temporal width τ_p of the laser pulse is determined by the number of modes N, the frequency spacing of these modes as given by Equation 5.2, and the temporal distribution of the pulse intensity. For a Gaussian temporal distribution, τp is given by

$$\tau_p = \frac{TBP}{N\Delta\nu}. \tag{5.3}$$

Here we see that the greater the number of longitudinal modes supported by the laser system, the shorter the pulse. The term TBP in Equation 5.3 is the so-called time-bandwidth product and is determined by the temporal shape of the pulse. For instance, given a Gaussian distribution, the time-bandwidth product is 0.144. For a hyperbolic secant squared distribution, it is 0.315. For any given distribution, Equation 5.3 represents the shortest possible pulse and any pulse meeting this criteria is said to be bandwidth limited. In real laser systems, the actual pulse duration depends on factors such as the actual distribution of the pulse and the dispersion in the cavity or along the beam path.

There are two general methods of mode-locking: active mode-locking and passive mode-locking. Actively mode-locked systems typically employ acousto- or electro-optic modulators (A or EOM) inserted into the laser cavity to modulate the amplitude or frequency of the longitudinal modes. In an AOM, a piezoelectric transducer sets up a standing acoustic wave in a transparent medium. The acoustic wave stretches and compresses the medium inducing periodic changes in the medium's index of refraction. This periodic change in the index of refraction induces so-called sidebands that are up-shifted and down-shifted in frequency according to the Debye-Sears effect [101]. Thus, for a longitudinal mode of frequency ω passing through an AOM driven by an electrical signal having a sinusoidal frequency Ω, sidebands will be generated having frequencies $\omega \pm \Omega$. These sidebands can compete with the

longitudinal modes for amplification in the gain medium, effectively reducing the amplitude of the mode. However, if Ω is equivalent to the cavity mode spacing (Equation 5.2), each longitudinal mode supported by the cavity will generate phase-locked modes at the same frequency as its neighbouring modes. The net effect is that all supported modes become phase-locked, generating a pulsed output.

Passive mode-locking involves the use of a optical components whose transmission characteristics depend on the intensity of the incident light. Perhaps the most common method of passive mode-locking involves the use of saturable absorbers. A saturable absorber is an optical device in which low intensity light is absorbed, while light with a sufficiently high intensity is transmitted. When such a device is inserted in a laser cavity, high intensity pulses pass through the device and are amplified by the gain medium, while low intensity, continuous-wave radiation is absorbed. Repeated amplification of the pulse and the continuous rejection of low intensity modes results in spontaneous mode-locking.

Additive pulse mode-locking [102] is a specific passive mode-locking technique that uses the concept of an artificial saturable absorber wherein cavity losses are decreased with increased intensity without the use of an actual saturable absorber. APM is conceptually illustrated in Figure 5.4 where two resonator cavities, one containing the gain medium and the other a nonlinear fibre, are coupled via a semi-transparent mirror. Some fraction of the light generated in the main laser cavity (the one containing the gain medium) is transmitted through the mirror and is injected into a fibre resonator. The phase shift of the light as it propagates through the fibre is a strong function of its intensity. As a consequence of this so-called self-phase modulation (SPM), the low intensity portions of the pulse undergo a phase shift different from that induced in the high intensity portion of the pulse. The two cavities are designed to have identical round-trip times so that the amplified pulse and the phase-modulated pulse interfere at the semi-transparent mirror. The fibre and path length are selected such that the peak of the phase-modulated pulse interferes constructively with the amplified pulse, while the tails of the modulated pulse interfere destructively having acquired a π phase shift relative to the peak. The net result is a mode in which the peak of the pulse is enhanced while the tails are attenuated and the pulse duration is effectively decreased.

The fibre oscillator used in the TripleBeam's laser employs a specialised version of

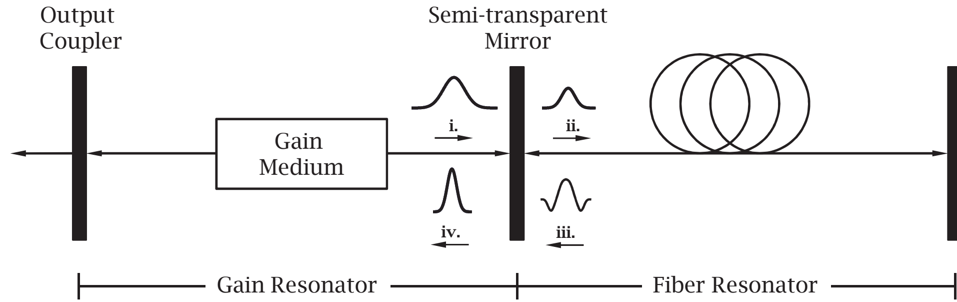

Figure 5.4. Additive pulse modelocking schematic. APM is achieved when i.) some fraction of the light generated in the gain resonator ii.) is coupled into the the fibre. SPM induces a π phase shift iii.) on the tails of the pulse relative to its peak. The phase shifted pulse interferes with the returning amplified pulse at the semi-transparent mirror resulting in a pulse iv.) with an enhanced peak and attenuated tails.

APM called polarising APM. Polarising APM uses the so-called Kerr effect wherein the index of refraction of a medium is altered in response to an electric field. The change in the index of refraction Δn is given by

$$\Delta n = \lambda K E^2 \tag{5.4}$$

where K is the Kerr constant and E is the electric field. If the electric field in Equation 5.4 is the electric field of a pulse propagating through it (rather than an externally applied field), the pulse will undergo intensity dependent self-phase modulation. Recall that elliptically polarised light is the superposition of two separate, linearly polarised electric fields of unequal phase and/or amplitude. Thus, elliptically polarised light propagating through an isotropic Kerr medium undergoes an intensity dependent rotation of its axes as each component experiences a phase-shift where the extent of the shift depends on the component's amplitude.

The schematic in Figure 5.5 illustrates how polarising APM exploits this phenomenon to achieve mode-locking. A properly aligned quarter-wave plate converts a linearly polarised pulse into an elliptically polarised one. Given sufficient intensity, the component electric field vectors of the elliptically polarised pulse undergo a phase shift relative to one another as they propagate through the Kerr medium. This results in a rotation of the pulse's polarisation axes such that the major axis

of the polarisation ellipse aligns with the polarisation axis of an analyser. Thus, polarisation control and self-phase modulation is leveraged to modulate pulse amplitude and as a result, high intensity modes are supported while low intensity ones get excluded. There are a great many optical configurations available to implement subtly different APM schemes. The interested reader is directed to [103] for a more complete review of APM techniques.

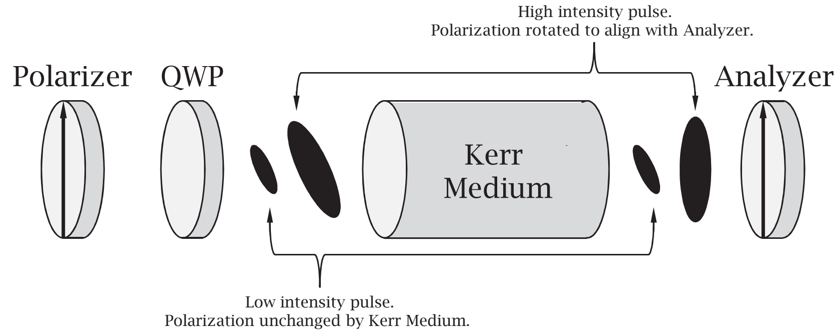

Figure 5.5. Generalised APM schematic. Depending on its intensity, the pulse's component field vectors are phase shifted relative to one another as it propagates through a Kerr medium. This phase shift induces a rotation of the polarisation ellipse. The analyser is adjusted to pass the high amplitude components. The small tilted ellipse on either side of the Kerr medium represents a single pulse of low intensity at two different time periods. The large ellipse is a pulse of high intensity.

In order to form the stable train of low energy seed pulses amplified by the regenerative amplifier as described in Section 5.3.2, the TripleBeam laser combines optical fibres having different group velocity dispersion characteristics. Further description of this aspect of the laser's operation requires a discussion of group velocity dispersion.

5.3.1.2 Group Velocity Dispersion

Optical pulses are made up of a band continuously varying optical frequencies (see discussion in Section 5.3.2). Each frequency component that makes up a pulse propagating through space has a phase velocity v_p defined as

$$v_p \equiv \frac{\omega}{k}. \tag{5.5}$$

The pulse itself has a group velocity v_g defined as

$$v_g \equiv \frac{\partial \omega}{\partial k}. \tag{5.6}$$

In each equation, ω is the instantaneous angular frequency and k the angular wave number ($k = \frac{2\pi}{\lambda}$). The function $\omega(k)$ is known as the dispersion relation and provides a means for describing the relationship between propagation velocities (v_p and v_g) and the index of refraction of the medium in which the pulse is propagating. For instance, for low power pulses propagating in free space, ω is proportional to k and the phase velocity and the group velocity are equal. For a pulse propagating through a dispersive medium, however, different wavelengths travel at different velocities resulting in a perturbation of the pulse's temporal profile. This is known as group velocity dispersion (GVD) and is typically quantified by the dispersion parameter D_{GVD} such that

$$D_{GVD} = \frac{d}{d\lambda}\frac{1}{v_g} \approx -\frac{\lambda}{c}\frac{\partial n^2(\lambda)}{\partial \lambda^2} \tag{5.7}$$

where n is the index of refraction of the medium. If D_{GVD} is less than zero, the medium is said to have positive or normal GVD and the low frequency components of a pulse propagating through it will travel faster than the high frequency components. The pulse is then said to be positively chirped. On the other hand, if D_{GVD} is greater than zero, the medium is said to have negative or anomalous dispersion. The result is a negatively chirped pulse or one in which the high frequency components travel faster than the low frequency ones.

The design of the fibre oscillator employed in the TripleBeam laser is illustrated in Figure 5.6. The erbium-doped fibre is the gain medium and has a positive GVD, while the GVD of the passive fibre is negative. By combining fibres having opposite GVD characteristics in a single ring laser configuration, the circulating pulse is alternately stretched and compressed. As a pulse is stretched in time, its peak power is decreased. This reduction in peak power is greatest as the pulse enters the gain medium allowing for greater overall amplification without the associated non-linear or intensity dependent phase shifts that result in the distortion of the temporal and spatial profile of the pulse. Due to the positive GVD of the erbium-doped fibre, by the time the pulse exits the gain medium and enters the passive fibre, it has been fully compressed in time, effectively minimising its duration. The net result is a

more uniform (both spatially and temporally), higher energy ultrashort pulse than is typically achievable by other designs. In the specific case of the TripleBeam's oscillator, the output is a 38 MHz train of 1550 nm pulses. This pulse train is then frequency doubled, resulting in a train of 775 nm, 100 nJ pulses, each having a duration of less than 150 fs. The following section discusses how these these pulses are stretched and then amplified in the Regenerative Amplifier.

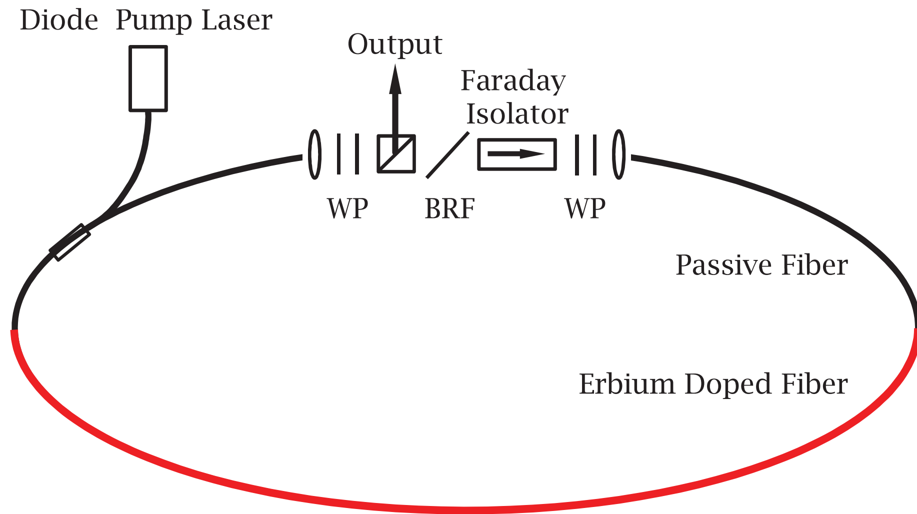

Figure 5.6. Erbium doped fibre oscillator design. The waveplates (WP) and birefringent filter (BRF) provide polarisation control. The Faraday isolator is the Kerr medium. It also provides for uni-directional operation.

5.3.2 Chirped Pulse Amplification and the Regenerative Amplifier

The process of positively chirping a pulse prior to its amplification and then compressing it before outputting it is known as chirped pulse amplification (CPA). As a technique for amplifying ultrashort pulses, it was developed in the 1980's at the University of Rochester by Donna Strickland and Gérard Mourou [9]. Pulses having ultrashort durations have very high peak powers, even at relatively small pulse energies (recall that power is defined as the derivative of energy with respect to time or $P = \frac{dE}{dt}$). For this reason, prior to the invention of CPA, the output intensity that could be achieved by normal amplification of ultrashort pulses was limited by

the damage threshold of the gain medium.

CPA works by taking advantage of a fundamental fact that the spectral width of a laser pulse and its duration are Fourier transform pairs of one another. Mathematically, if $E(t)$ and $E(\omega)$ represent the evolution of a pulse with respect to time and frequency respectively, we can generalise the time and frequency Fourier transforms of a pulse as

$$E(t) = \frac{1}{2\pi}\int_{-\infty}^{\infty} E(\omega)e^{-i\omega t}\,\mathrm{d}\omega \tag{5.8}$$

and

$$E(\omega) = \int_{-\infty}^{\infty} E(t)e^{i\omega t}\,\mathrm{d}t. \tag{5.9}$$

Applying basic Fourier theory, we can calculate the pulse duration Δt[1] and bandwidth $\Delta\omega$ using the standard power-rms definition as appropriate for functions with negative or complex values:

$$\sigma_t^2 = \frac{\int_{-\infty}^{\infty}\left(t-\bar{t}\right)^2 |E(t)|^2\,\mathrm{d}t}{\int_{-\infty}^{\infty}|E(t)|^2\,\mathrm{d}t}, \quad \text{where } \bar{t} = \frac{\int_{-\infty}^{\infty} t\,|E(t)|^2\,\mathrm{d}t}{\int_{-\infty}^{\infty}|E(t)|^2\,\mathrm{d}t} \tag{5.10}$$

and

$$\sigma_\omega^2 = \frac{\int_{-\infty}^{\infty}\left(\omega-\overline{\omega}\right)^2 |E(\omega)|^2\,\mathrm{d}t}{\int_{-\infty}^{\infty}|E(\omega)|^2\,\mathrm{d}\omega}, \quad \text{where } \overline{\omega} = \frac{\int_{-\infty}^{\infty} \omega\,|E(\omega)|^2\,\mathrm{d}\omega}{\int_{-\infty}^{\infty}|E(\omega)|^2\,\mathrm{d}\omega} \tag{5.11}$$

where $\bar{t}$ (or $\overline{\omega}$) and σ_t (or σ_ω) are analogous to the mean and standard deviation of a probability density function [104, 105]. Defining $\sigma_t \equiv \Delta t$ and $\sigma_\omega \equiv \Delta\omega$ and applying the Cauchy-Schwarz inequality, it can be shown that for Gaussian pulses the minimum permissible time-bandwidth product is

$$\Delta t \Delta\omega \geq \frac{1}{2}. \tag{5.12}$$

The consequence of this physical relationship is that pulses of short duration must necessarily have large bandwidths and it is precisely because of its wide gain bandwidth that titanium doped monocrystalline sapphire, commonly referred to as Ti:Sapphire, is widely used as the gain medium for solid-state ultrashort pulsed lasers.

[1] for this analysis we represent pulse duration with Δt rather than τ_p in order to make the mathematical analogy with the Heisenberg uncertainty principle explicit.

CPA employs the use of diffractive optical elements such as gratings or prisms to temporally separate the spectral components of the pulse prior to amplification. When the spectral components or instantaneous frequencies of an optical pulse are time dependent, that pulse is said to be chirped. As briefly discussed at the end of Section 5.3.1, a pulse in which the low frequency (long wavelength) components lead the high frequency (short wavelength) ones is positively chirped. Conversely, negatively chirped pulses are ones in which the high frequency components lead. Typically, CPA laser systems positively chirp pulses prior to amplification using an optical system appropriately referred to as a stretcher. Figure 5.7 shows a common configuration for a grating-based stretcher [106]. In this example, the ultrashort pulse enters the stretcher through a dichroic mirror. The gratings disperse the spectral components of the pulse through a pair of collimating lenses that help confine the pulse spatially. A single round-trip takes each pulse through both gratings and both lenses twice, but the path length of red components is shorter than that of the blue components. The result is that the pulse exits the stretcher with its red components leading its blue ones. Effectively, the pulse is stretched in time, resulting in a reduction in its peak power.

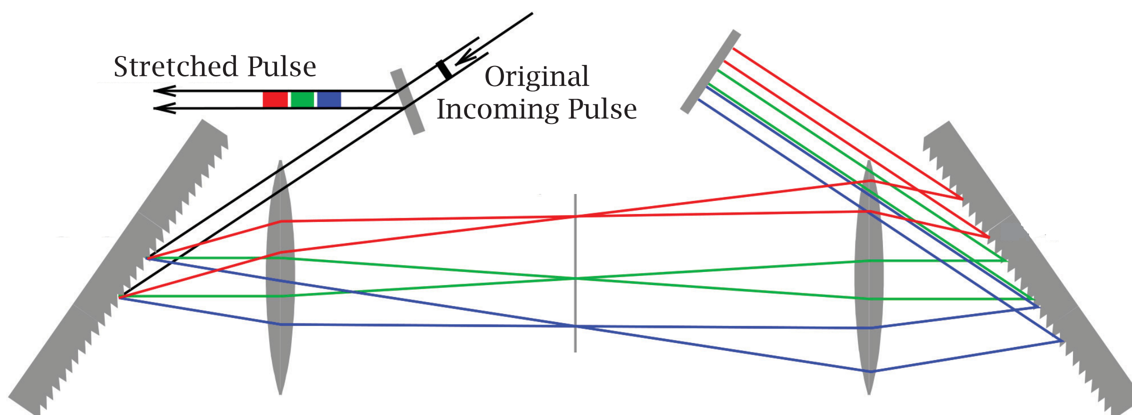

Figure 5.7. Typical grating-based stretcher configuration used in laser amplifiers that employ chirped pulse amplification. The path length of the red components is shorter than that of the blue components resulting in a positively chirped pulse.

The reduction in the peak power of the pulse allows for its amplification without the risk of damage to the gain medium. The TripleBeam laser employs a method of amplification known as regenerative amplification. In a regenerative amplification

scheme, the pulse is trapped in the laser resonator and makes multiple passes through a gain medium in which a population inversion has been induced, typically via an optical pump. The energy level diagram shown in Figure 5.8 for Ti:Sapphire is typical of a four level laser system and schematically describes the energy states of bound electrons in the gain medium. The absorption (pump) band for Ti:Sapphire is broad, but peaks at $\lambda = 500$ nm, while the most efficient output transition occurs at a wavelength of 800 nm. The population inversion required for lasing is achieved by the immediate decay of excited electrons to a metastable state having a relatively long lifetime. In the case Ti:Sapphire, the lifetime of this metastable state is 3.2 μs at room temperature. The transition to the uppermost state due to absorption of the pump energy and the non-radiative relaxation from this state to the metastable state occurs on a much shorter time scale. In essence, the long lifetime of the metastable state delays the re-population of the state labelled E_1 in Figure 5.8. The net result is that the number density of electrons in a higher energy state is greater than the number density of electrons in the lower state (i.e. a population inversion). Thus, by virtue of statistics, a resonant incident photon is more likely to initiate an emission transition than a transition to a higher energy state resulting from the photon's absorption. For each photon "in" that initiates an emission transition (and does not get reabsorbed), we get two photons "out." The net effect is the coherent amplification of the incident light.

A detailed schematic of the TripleBeam laser's regenerative amplifier cavity (regen cavity) is shown in Figure 5.9. The 38 MHz train of low energy, stretched pulses coming from the fibre oscillator enter the upper level through a periscope (the point labelled "injection" in Figure 5.9) and are directed into polarising beamsplitter BS1. The pulses are S polarised relative to BS1, allowing them to be reflected into the Faraday rotator. Combined with a half-waveplate, the Faraday rotator transmits pulses in one direction without changing their polarisation states, while inducing a change in polarisation when pulses are transmitted from the opposite direction. In this case, the polarisation state is unchanged when passing through the Faraday rotator/waveplate combination from BS1 to BS2. The S polarised pulses can thereby enter the regen cavity upon reflection from BS2 into the Pockels cell. The regen cavity is the region defined by the beam path M2 $\rightarrow$ M3 $\rightarrow$ DM2 $\rightarrow$ DM1 $\rightarrow$ DM2 $\rightarrow$ M3 $\rightarrow$ M2. The Pockels cell is then activated in order to select a single pulse,

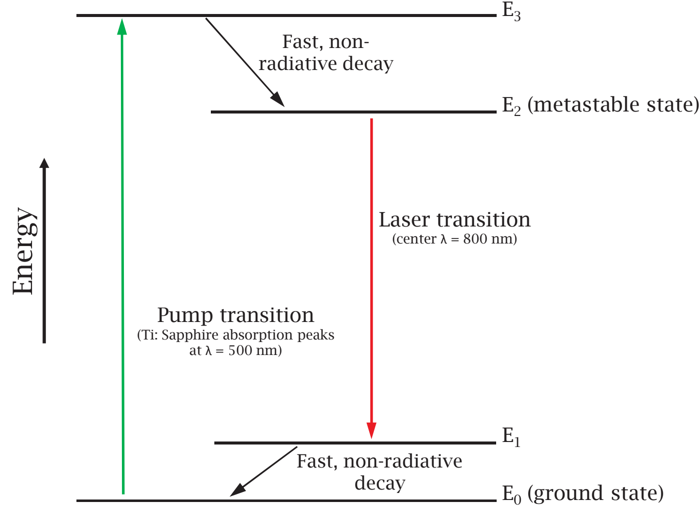

Figure 5.8. A schematic of the energy states of bound electrons in a Ti:Sapphire crystal used as the gain medium in a regenerative laser amplifier. The metastable state has a relatively long lifetime (3.2 μs at room temperature) making possible the population inversion required to achieve lasing.

whose polarisation state is changed from S to P. The single, now P polarised pulse can pass through BS2 and is thereby trapped in the regen cavity and makes multiple passes through the Ti:Sapphire gain medium. As briefly mentioned earlier, the gain medium itself is pumped by a Q switched, frequency doubled Nd:YAG laser that enters the regen cavity through dichroic mirror DM1 and exits to a beam dump via DM2. With each pass the pulse makes through the gain medium, it extracts energy stored by the pump process and is amplified.

Pulse amplification is typically described by the Frantz-Nodvik equation [107, 108]:

$$\phi_{out} = \phi_{in} \ln\left[1 + g_0 \left(\exp\left(\phi_{in}/\phi_{sat}\right) - 1\right)\right] \tag{5.13}$$

where ϕ_{out} is the output fluence of a pulse after a single pass through the gain medium with a saturation fluence ϕ_{sat}. g_0 is known as the small signal gain. Assuming that the excited state lifetime of the gain medium is much longer than any other process involved in amplification, the small signal gain can be expressed as

$$g_0 = \frac{\phi_{sto}}{\phi_{sat}} \tag{5.14}$$

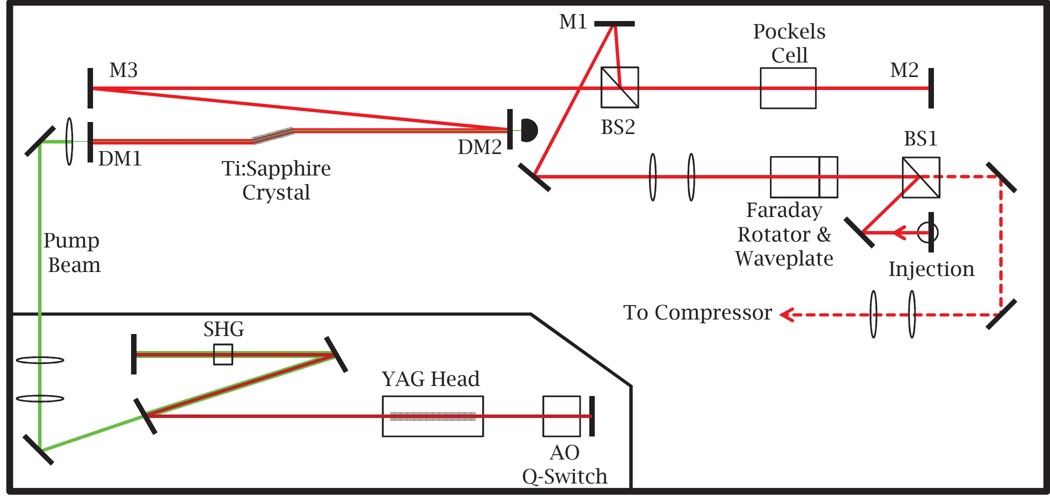

Figure 5.9. Detailed schematic of the TripleBeam laser's upper level including the Nd:YAG pump laser and the regen cavity.

where ϕ_{sto} is the pump fluence or energy density stored in the medium (J/cm^2). The saturation fluence, ϕ_{sat} (J/cm^2), is the fluence of an input pulse that leads to a $\frac{1}{e}$ reduction in the gain. ϕ_{sat} is an intrinsic property of the material related to the gain cross section σ_e by

$$\phi_{sat} = \frac{h\nu}{\sigma_e} \tag{5.15}$$

where h is the Plank constant and ν is the frequency of the emission transition. The saturation fluence for Ti:Sapphire is 1 J/cm^2 at 800 nm.

The Frantz-Nodvik equation (5.13) can be generalised for an arbitrary number of passes through a gain medium as long as the overall amplification time remains short relative to the excited state lifetime of the gain medium [109]. To do so, consider the nth pass in a regenerative amplifier. Equation 5.13 then becomes

$$\phi_{out,n} = \phi_{sat} \ln\left[1 + G_n\left(\exp\left(\phi_{in,n}/\phi_{sat}\right) - 1\right)\right] \tag{5.16}$$

where G_n is the gain for a specific pass n and can be calculated using the relationship

$$G_n = \exp\left(\frac{\phi_{sto,n}}{\phi_{sat}}\right). \tag{5.17}$$

The initial energy density stored in the gain medium can be calculated from observable quantities:

$$\phi_{sto} = \frac{E_p \alpha}{2w} \cdot \frac{\lambda_p}{\lambda_L} \tag{5.18}$$

where E_p is the energy incident on the gain medium from the pump beam, α is the fraction of the pump radiation absorbed, w is the $1/e^2$ radius of the pump beam where it enters the medium, and λ_p and λ_L are the pump and laser wavelengths, respectively. Each nth pass through the gain medium lowers ϕ_{sto}, making the $n^{th}+1$ value of ϕ_{sto}

$$\phi_{sto,n+1} = \phi_{sto,n} - (\phi_{out,n} - \phi_{in,n}) \tag{5.19}$$

where $\phi_{in,n}$ is calculated from the previous pass such that

$$\phi_{in,n} \rightarrow \phi_{in,n+1} = \Gamma\phi_{out,n} \quad (\Gamma < 1) \tag{5.20}$$

where Γ is a loss factor to account for cavity losses.

A generalised plot of pulse energy as a function of the number of passes through the amplifier is shown in Figure 5.10. Qualitatively, each pass reduces the amount of energy stored in the gain medium. After some finite number of passes, any additional gain is offset by cavity losses. At this point, the gain medium is said to have reached saturation.

Typically, in a regenerative amplification system, the pulse is released from the cavity at the peak of the gain curve. This is referred to as cavity dumping. Figure 5.11 shows oscilloscope traces of real laser pulses a) transiting a saturated gain medium and b) a cavity dumping event achieved by careful timing of the Pockels cell enable signal (see Figure 5.9). Enabling the Pockels cell changes the polarisation state of the pulse from P back to S so that it can be reflected out of the regen cavity at BS2. Passing through the Faraday rotator, the pulse is once again P polarised so that it can pass through BS1 and on to the compressor.

Upon exiting the regen cavity, the pulse is sent to an optical component called a compressor. Figure 5.12 shows the configuration of a typical grating-based compressor [106]. The stretcher and compressor in a CPA system are conjugate pairs. Thus, whereas the stretcher described in Figure 5.7 positively chirps the pulse, the

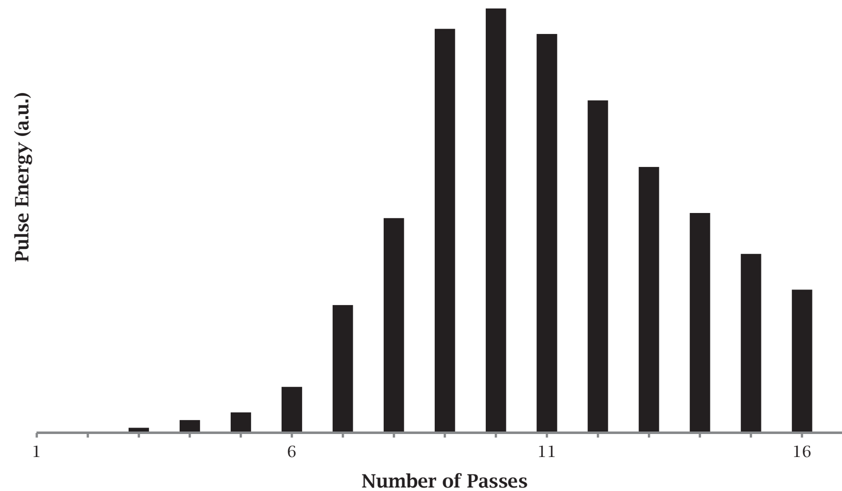

Figure 5.10. Gain curve resulting from the amplification of a hypothetical pulse illustrating gain saturation. If this were an actual gain curve, the pulse would be released from the regen cavity after the tenth pulse.

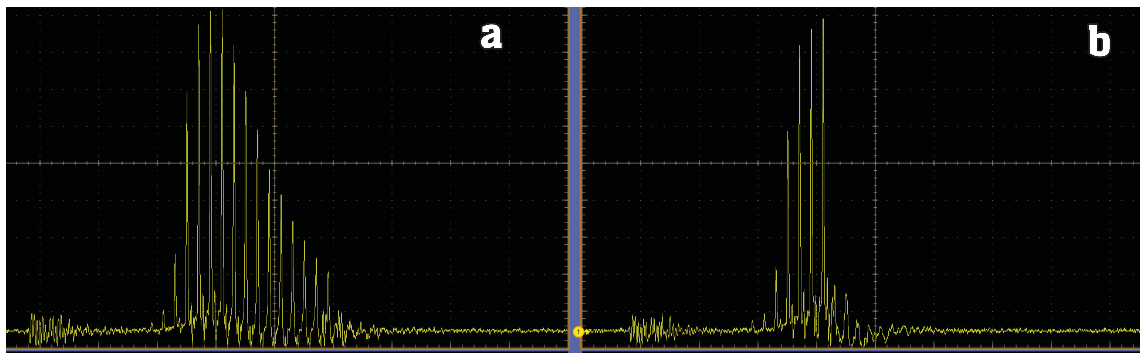

Figure 5.11. Oscilloscope traces of actual laser pulses transiting a Ti:Sapphire gain medium. In Figure a) the gain medium is saturated, whereas in Figure b) the cavity is "dumped" at the top of the gain curve. Releasing the pulse at the top of the gain curve ensures its maximum amplification.

compressor must necessarily negatively chirp it. In Figure 5.12, the stretched pulse, with its red components leading its blue ones, enters the compressor from the left. The optical path takes the pulse through both gratings, reflects it off a mirror, and directs it back through the gratings before outputting it through a beamsplitter. The length of this path is shorter for the blue components than it is for the red ones. As a result, the blue wavelengths "catch up" to the red ones, effectively rebuilding the

pulse in time.

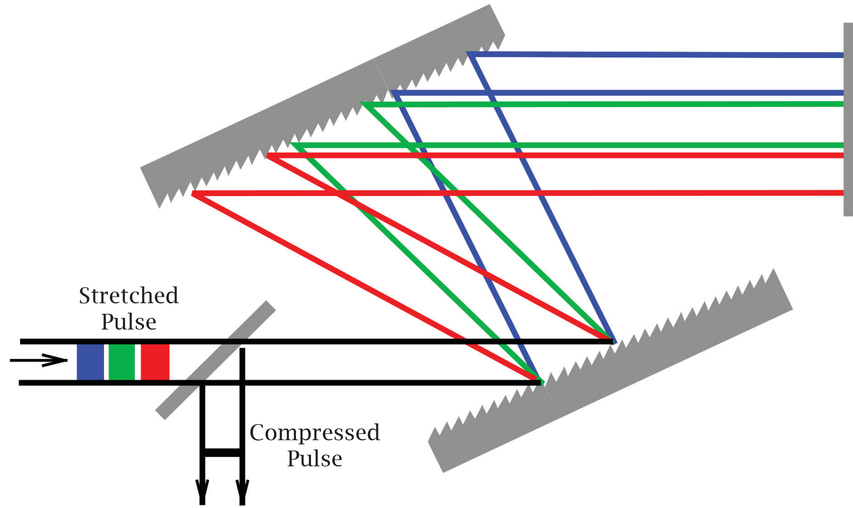

Figure 5.12. Typical grating-based stretcher configuration. The stretcher and compressor in a CPA system are conjugate pairs, so if the stretcher positively chirps the pulse, the compressor must negatively chirp it. In this case, the path length of the blue components is shorter than that of the red components and the pulse is "rebuilt."

In summary, Figure 5.13 details the evolution of a pulse as it progresses through a chirped pulse amplification laser system such as the one described in this section. The low intensity, ultrashort seed pulse delivered by the oscillator is temporally stretched in the stretcher, effectively lowering its peak power. The lowered peak power allows for its amplification in the regenerative amplifier cavity without the risk of damage to the gain medium. The stretched pulse is then rebuilt in the compressor, resulting in a final ultrashort pulse with very high peak powers.

5.4 DualBeam™

DualBeam is the trademarked name given a suite of instruments developed by FEI Company, Hillsboro, OR, USA that combine a scanning electron microscope and a focused ion beam. They are widely used in industry for materials analysis and characterisation, failure analysis, process control, sample preparation, and rapid prototyping of nanoscale structures. The microanalysis capabilities of DualBeams are regularly enhanced through the addition of instrumentation enabling complimentary

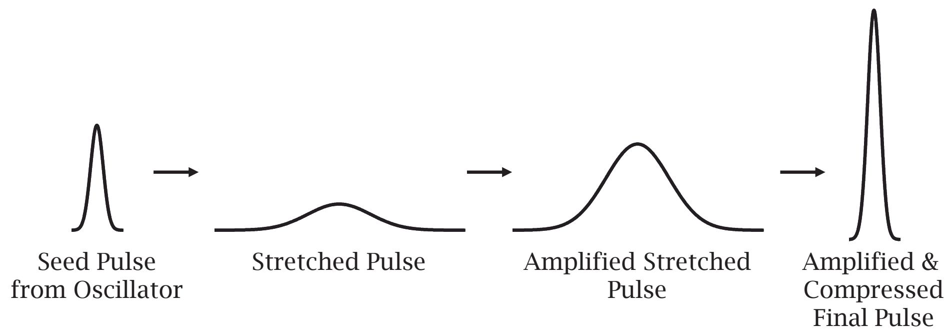

Figure 5.13. Evolution of a pulse as it progresses through a chirped pulse amplification laser system.

techniques such as energy dispersive X-ray spectroscopy and electron backscatter diffraction.

The DualBeam system used in the work described here is a customised Quanta™ 3D FEG equipped with EDS and EBSD systems, both from Oxford Instruments, Oxfordshire, UK and described in Section 5.5. The Quanta 3D FEG combines a high current (65 nA) FIB and a field-emission SEM capable of operating in three vacuum modes: high vacuum (less than $6{\times}10^{-4}$ Pa), low vacuum (10 to 130 Pa), and as an environmental SEM (ESEM – 10 to 4000 Pa). The ion and electron columns are arranged at 52° with respect to one another allowing their respective beams to be focused coincidently at a point 10 mm below the electron column's objective lens. Samples are manipulated by a five axis (x, y, z, tilt, and rotation) goniometer stage with a minimum step of 300 nm, a nominal repeatability of 2 μm at 0° tilt, and a tilt range of -15° to 75°. The instrument is equipped with a variety of detectors including an Everhart-Thornley secondary electron detector (SED), a solid-state backscattered electron detector (BSD), a channel detection electron multiplier (CDEM) for secondary ion and ion-induced secondary electron imaging, and a gaseous SED (GSED) for use in ESEM mode. An infrared CCD camera provides for in-chamber viewing. The vacuum chamber itself is equipped with 21 ports which can accommodate plasma cleaners, gas injector systems (GIS) for applications requiring gas chemistry, and electrical feedthroughs. As will be discussed, it is through the use of one of these ports that the ultrashort pulsed laser was incorporated.

Two following subsections give an brief overview of FIB and the SEM. Because these technologies are well known and widely used, the history and technical details

of FIB and SEM will be covered in a fashion just sufficient to provide a cursory background from which to discuss the specifics of the implementation of the technology on the Quanta.

5.4.1 FIB

Throughout their 40+ year history, focused ion beams have been used for direct maskless implantation and doping [110, 111, 112], ion beam lithography [113], mask repair [114, 115], and secondary ion mass spectroscopy (SIMS) [116, 117]. Today though, they are primarily used for defect and failure analysis of integrated circuits, for TEM lamella preparation, and to a lesser extent, for editing integrated circuits and for machining micro and nanostructures. The fact that these particular FIB applications have become those most commonly practised is largely a function of the most notable effect energetic ions have on samples with which they interact. Because ions are massive, when accelerated to high energies they can transfer sufficient momentum to atoms at or near the surface of a target to remove them, a process typically referred to as sputtering. With a focused beam of ions, material removal can be controlled on a sub-micron scale. Thus, FIBs are regularly used as micro-scalpels for revealing subsurface features or for cutting thin samples from devices and bulk materials for analysis in TEMs.

As a complement to FIB's capacity for small scale material removal, FIB can be used to selectively deposit a range of materials from metals to insulators. By introducing a gas-phase precursor through a hollow needle positioned close to the target surface, precursor molecules adsorb to the surface, typically in a monolayer or less. As the ions from the focused beam cross the substrate-vacuum interface, they transfer some of their energy to electrons in the bulk. Electrons scattered in this fashion that subsequently escape the sample are referred to as secondary electrons (SE). The molecular bonds of adsorbed molecules can be broken by SE, causing the precursor to dissociate into reactive components and volatile by-products. The reactive components bond to the surface to form deposits, while the volatile by-products desorb from the surface and are removed by the pumping system responsible for creating the vacuum.[2] This process enables the direct writing of sub-micron features

[2]If the particular precursor employed, when dissociated, reacts with the substrate to form a new volatile compound, the result leads to material removal rates greater than those possible with

and is typically referred to as ion beam-induced deposition. Combing the FIB's reductive capabilities (sputtering) with its additive ones (IBID), complex micro- and nanostructures can be fabricated *in vacuo*.

In addition to enabling IBID, secondary electrons generated when energetic ions impact a surface can be used to form images in much the same way images are formed via SEM (see next section). In general, the depth to which ions penetrate (i.e. the ion range) is considerably smaller than it is for electrons – typically less than 50 nm for ions accelerated to 30 keV versus tens of microns for 30 keV electrons. However, ions incident on crystalline samples undergo an effect known as channelling. Channelling occurs when incident ions enter the target in a direction parallel to a low-indexed crystallographic axis [118]. If incident ions enter a target in such a way that electronic losses rather than nuclear ones dominate, the range of the ions is greatly increased making it less likely that ion-induced secondary electrons will be emitted from the sample. The net result is that grains having different crystallographic orientations exhibit different levels of contrast. In particular, grains in which channelling is significant appear darker as illustrated in Figure 5.14.

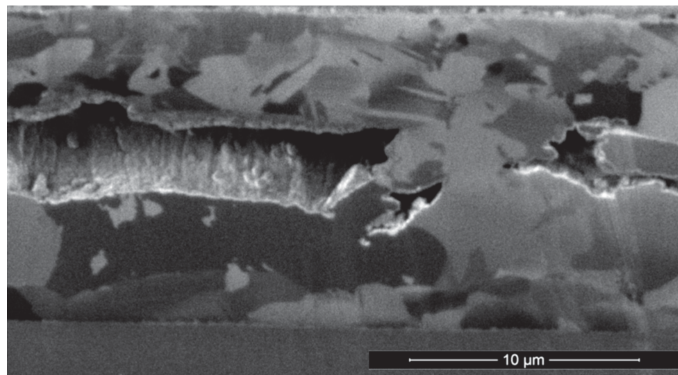

Figure 5.14. An example of ion channelling. Channelling is significant in grains that appear dark.

Focused beams of ions can be formed from many different ion species utilising a variety of source technologies. By far the most widely used ion source technology for FIB, and the one used in the the Quanta's FIB, is the gallium liquid metal ion source (Ga^+ LMIS). The high brightness, relatively long life, reliability, and stable emission of positive gallium ions that Ga^+ LMIS provides is largely responsible for

FIB alone. This process is typically referred to as etch enhancement, or EBIE.

its ubiquity.

A typical Ga^+ LMIS is shown in Figure 5.15. It consists of a hairpin support structure, each end of which is spot-welded to an electrode. Welded to the apex of the hairpin is a tungsten emitter attached to a coiled wire reservoir of Ga metal. A current is passed through the hairpin support, melting the Ga. The liquid Ga wets the emitter and a high voltage ($\approx$ 10 kV) is applied to a nearby electrode called an extractor. As the surface tension of the liquid metal balances the force applied by the induced electric field, the liquid Ga at the tip of the emitter is drawn into a characteristic conical shape called a Taylor cone, first described by Sir Geoffrey Taylor in 1964 [119]. The small ($\approx$ 5 nm) radius formed at the tip of the Taylor cone serves to further enhance the electric field until ions begin to evaporate from the surface in a process generally referred to as field evaporation.

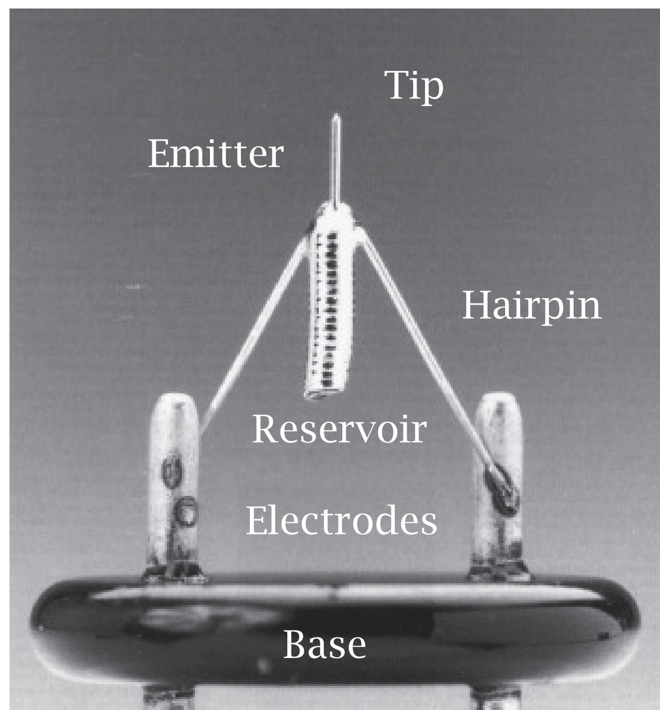

Figure 5.15. A typical gallium liquid metal ion source. A current passed through the hairpin melts gallium in the reservoir, which flows over the emitter. A voltage applied to an extractor (not shown) induces a high electric field at the emitter, forming a Taylor cone. The small radius of the Taylor cone further enhances the field, producing ions through field evaporation. Figure courtesy of FEI Company.

In the Quanta's FIB, also called Sidewinder™, the LMIS is typically operated

such that it provides around 2 μA of total ion current I_{tot}. All but 65 nA of this is apertured at the extractor, making this the maximum probe current I_{probe} that can be delivered to the sample. The Sidewinder is a two lens column, both of which are three element, electrostatic lenses. The first is located in the so-called gun region. In addition to the first lens, this region contains the LMIS source, the extractor, and a probe forming aperture strip containing fifteen apertures of varying diameters capable of providing a range of probe currents from 65 nA to 1 pA. In order to prevent source contamination, the gun region is differentially pumped, maintaining approximately two orders of magnitude higher vacuum (10^{-7} to 10^{-8} Torr) than the rest of the column. To preserve this vacuum level when the system is vented, a pneumatic isolation valve can be actuated to seal the differential pumping aperture from atmosphere.

The function of the first lens is to collimate the beam. Because ions are massive, they move relatively slowly (compared to electrons), even when accelerated to 30 keV. As a result, Coulombic interaction effects such as radial broadening due to space charge and energy broadening due to the Boersch effect can lead to the degradation of FIB performance. In general, both radial and energy broadening increase the probe size, the former due to an increase in spherical aberration and the latter due to increased chromatic aberrations. Space charge can be reduced by either decreasing the amount of charge in a given volume or by increasing the volume over which the charge acts. Accordingly, propagating a relatively broad, collimated beam (i.e. without cross-overs) through the column ensures that space charge is held to a minimum by maximising the cross-sectional area of the beam over the length of its path.

The second and final Sidewinder lens is the objective lens responsible for focusing the beam to its final diameter, nominally 5 nm at 30 keV. The lens is mechanically designed in such a way that the envelope of the column is tapered, forming a truncated cone. As illustrated in Figure 5.21, this allows the FIB and the SEM, the end of which is also tapered, to be arranged in such a way that their beams focus to the same location as described at the beginning of this section. Between the first and second lens three parallel plate dipoles, a Faraday cup, and two octupoles provide additional functionality. The top two dipoles provide beam steering, one in x and the other in y, for alignment and beam shift. The third dipole is a beam blanker

which, when enabled, directs the beam off the sample and into the Faraday cup, providing the user a means of "shutting off" the beam without disabling the source. One of the octupoles is used to stigmate and rotate the beam, while the pair of them work in concert to scan the beam through the centre of the second lens. The Sidewinder column is designed to be operated at a range of accelerating voltages from 2 to 30 kV.

5.4.2 SEM

First developed commercially in 1952 by Charles Oatley, scanning electron microscopy is a standard technique for imagining structures too small to be imaged with light. It's well known that due to diffraction, the resolution of any imaging system is limited by the wavelength of the elementary particle from which the image is formed. Thus, diffraction limited images formed with blue photons have higher resolution than those formed using red photons. Basic quantum mechanics tells us that matter also has a wavelength (the de Broglie wavelength) and that the wavelength of a matter particle is inversely proportional to its momentum such that

$$\lambda = \frac{h}{p} = \frac{hc}{\sqrt{KE^2 + 2KEm_0c^2}} \tag{5.21}$$

where h is Planck's constant and p is momentum, KE is kinetic energy, m_0 is the rest mass of the particle, and c is the speed of light. Using this simple equation, it's easy to show that energetic electrons have very small wavelengths. As an illustration, consider a photon and an electron, both having an energy of 4 eV. The wavelength of the photon is approximately 310 nm while the electron's wavelength is only around 6 Å. At an energy of 30 keV, typical in SEM, an electron has a wavelength on the order of 7 pm. Thus, it is the wave-particle duality of matter that makes high resolution imaging with SEM possible.

The basic theory of operation of the scanning electron microscope is relatively simple, but requires some preliminary discussion of electron scattering as background. Consider a beam of energetic free electrons incident on a sample. As the electrons cross the vacuum-substrate interface, they are scattered within the sample both elastically and inelastically. Elastic scattering occurs when electrons interact with substrate nuclei. In the classical mechanics model of elastic scattering, the

electron's trajectory is perturbed by the Coulombic attraction between the positively charged nucleus and the negatively charged electron. As a result, the electron is scattered through an angle θ that depends on the electron's proximity to the nucleus, typically referred to as the impact parameter, and the electron's velocity. Specifically, for a given electron velocity, the shorter the distance between the electron and the nucleus, the larger the scattering angle. Likewise, for a given impact parameter, a slow moving electron is scattered over a larger θ than a fast moving one. Due to the great difference in the masses of the two particles, this model assumes the nucleus remains at rest and the total momentum and energy of the scattering system is conserved. Furthermore, the model assumes that atomic electrons play no role in elastic scattering other than to screen the nuclear charge.

When energetic free electrons incident on a sample, also called primary electrons (PE), interact with bound electrons in the bulk, the PE lose energy in a process generally referred to as inelastic scattering. There are a number of important loss mechanisms by which this can occur. In the case of plasmon-induced losses, incident electrons suffer energy losses up to about 50 eV by exciting oscillating, longitudinal charge-density waves of valence and conduction electrons in the substrate (bulk plasmons). The scattering angles associated with plasmon-induced losses are typically below 10 mrad. PE can also knock out inner shell electrons resulting in the ionisation of the atom. Inner shell ionisation is the mechanism responsible for the characteristic X-ray generation exploited by EDS and is described in more detail in Section 5.5.1. The energy losses associated with inner shell ionisation depend on the ionisation energy of the shell being ionised. Reimer [120] notes that ionisation energies, hence energy loss values, range from 110 eV for ionisation of the beryllium K shell to 80 keV for the gold K shell. Obviously, the energy of the PE must be greater than or equal to the ionisation energy of the shell in question in order for this process to occur. When the ionisation energy of a bound electron is very small relative to the energy transferred in a collision, the bound electron is considered quasi-free and the scattering event is a form of Compton scattering. The energy losses associated with these electron-electron collisions are no greater than $E/2$ with scattering angles between 0°and 90°.

In a SEM, free electrons emitted from an electron source (PE) are accelerated to high energies and focused via a series of magnetic and/or electrostatic lenses to

a small spot on a sample. As discussed above, PE are scattered as they enter the sample, either by nuclear interactions (elastic scattering) or electronic ones (inelastic scattering). As shown in Figure 5.16, these scattering events can generate electrons that subsequently exit the sample. Elastically scattered electrons whose trajectory allows them to exit the sample are referred to as backscattered electrons (BSE). PE and BSE that scatter inelastically as well as formerly bound electrons that have been set free in a scattering process can also reach the sample-vacuum interface, but may or may not have sufficient energy to escape into the vacuum. Those that do escape are referred to as secondary electrons (SE). By convention, SE are those free electrons that have energies of 50 eV or less while BSE have energies greater than 50 eV. Because they leave the sample from very near the surface, SE primarily provide topographical information. On the other hand, BSE yield is largely a function of the atomic number Z of the atoms in the neighbourhood of the electron-sample interaction. As a result, BSE can provide information on the material phases present in a sample.

In order to form an image, the electron beam is scanned across the sample in a raster pattern. The number of SE and BSE emitted for a given beam current and energy is a function of the topography and composition of the sample in the region illuminated by the beam, a region generally referred to as a pixel. Thus, as the beam is scanned across the sample, each pixel generates a different number of electrons depending on the conditions of the sample at that location. The electrons emitted at each pixel are collected by an appropriate detector. The number of electrons collected at each pixel is digitally converted to a grey scale value between pure black (zero electrons) and pure white. Each pixel position and intensity value is then mapped to a corresponding pixel position and intensity on a computer screen, thereby forming an image.

The SEM on the Quanta is designed to operate at beam energies between 200 and 30,000 eV with probe currents continuously adjustable up to 200 nA. Operating at 30 keV in SE mode, the nominal resolution of the Quanta SEM is 1.2 nm. Additionally, a differential pumping aperture can be quickly installed in the final lens bore of the objective lens allowing the Quanta to be used as an environmental SEM. Employing a special gaseous secondary electron detector, rather than the conventional Everhart-Thornley detector (ETD), ESEM can be used to image “wet” or charging

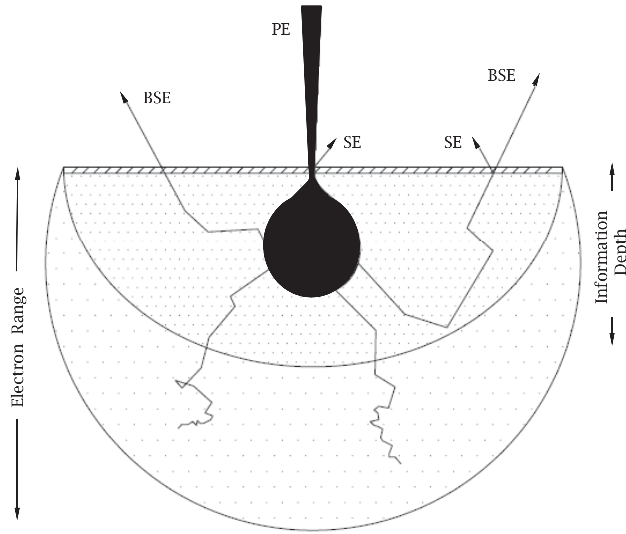

Figure 5.16. SE can be generated by both the primary electron beam (PE) and BSE, but due to their low kinetic energy, can come only from very near the sample surface. As a result, SE provide topographical information. Having higher energies, BSE can escape from deeper in the sample. BSE yield is largely a function of the atomic number, Z, of the atoms in the sample and can provide material phase information. Electrons below the information depth will have insufficient energy to escape the sample independent of their trajectory [120]

.

samples, without the need to metal coat them, by allowing for the introduction of a gaseous atmosphere into the specimen chamber.

5.5 Analysis Techniques

The DualBeam system used to develop the TripleBeam is equipped with both energy dispersive X-ray spectroscopy and electron backscatter diffraction systems. EDS and EBSD were used as analysis techniques throughout the work presented in this dissertation. The following two sections provide a brief overview of these techniques.

5.5.1 Energy Dispersive X-ray Spectroscopy

As a starting point for the discussion of EDS, recall that electrons are arranged around the nucleus of an atom in orbitals, each defined by the energy of the electrons occupying it (see Figure 5.17). The energy of the electrons in a given orbital is restricted to discrete values and the lowest energy orbitals, those most tightly bound, are filled first. The energy state of a given orbital is defined by the principle quantum number n. The orbital with the least energy, where $n = 1$ is referred to as the K shell. The next highest energy orbital ($n = 2$) is the L shell and it is divided into three subshells – L1, L2, and L3. The M shell has a principle quantum number $n = 3$ and is divided into subshells M1 through M5[3]. Each of the L and M subshells have different quantum configurations and energies.

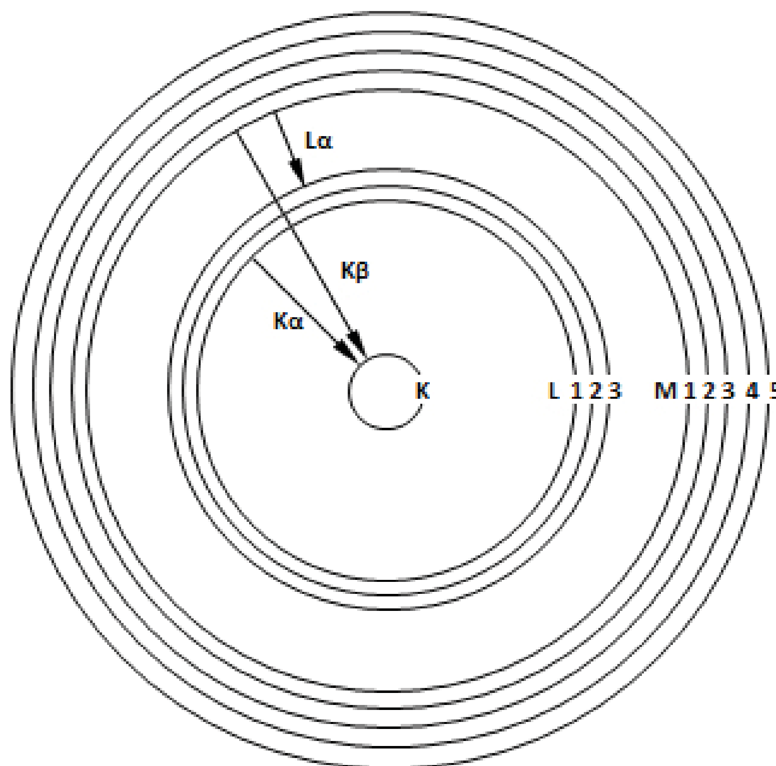

Figure 5.17. A schematic of the K, L, and M orbitals and Kα, Kβ, and Lα transitions.

EDS is a microanalytical technique that provides both qualitative and quantita-

[3]There is an N shell as well ($n = 4$), with seven subshells, but for the energies at which we typically operate (up to 30 keV), no transitions from the N shell occur.

tive information on the chemical composition of a sample under study. As previously discussed, the inner shell electrons of atoms in a sample can be unbound by collisions with energetic electrons delivered via either SEM or TEM. When the atom is ionised in this fashion, the electrons in higher energy shells decay to the lower energy shell, emitting a photon (X-ray) in the process. The energy and wavelength of the emitted photon is given by the difference in the two energy levels. The transition responsible for a given photon is labelled according to the shell in which the vacancy occurs and the shell from which the vacancy is filled. Thus, as illustrated in Figure 5.17, a photon emitted due to a vacancy in the K shell filled by a decay event originating in the L shell is referred to as a Kα X-ray. Likewise, if that K shell vacancy is filled by a decay event originating in the M shell, the emitted photon is referred to as a Kβ X-ray.

Since each atom has a unique shell configuration, X-ray emission is characteristic of the material. Spectra are collected via solid state, silicon based detectors where incident X-rays generate electron-hole pairs that are converted to a voltage. Knowing *a priori* the energy required to generate an electron hole pair in the detector, the energy of the ionising X-ray can be determined by a pulse processor. Finally, a multi-channel analyser interprets and displays the full X-ray spectrum for analysis by the user.

The EDS system used for all the EDS analysis presented in this dissertation is an Oxford Instruments X-Act with a 10 mm^2 silicon drift detector.

5.5.2 Electron Backscatter Diffraction

Another microanalytical technique available on the TripleBeam and used in this dissertation is electron backscatter diffraction. EBSD is a technique whereby a beam of electrons interacts with a sample in such a way as to provide information about the crystallographic structure of the sample. The specifics of this process are illustrated in Figure 5.18 where a tilted sample (typically titled 20° relative to the beam) is shown being bombarded by a high energy, focused electron beam. As they interact with the nuclei of atoms in the crystal lattice, the beam's electrons elastically scatter in all directions, with every possible trajectory. A rigorous treatment of the interaction between the incident electrons and the lattice atoms requires the use of Bloch's theorem. Bloch's theorem states that the energy eigenfunction of an electron

in a periodically repeating lattice can be written as the product of a plane wave and a periodic Bloch function $u_{n\mathbf{k}}$ such that the resulting wavefunction or Bloch wave is expressed as

$$\Psi_{n\mathbf{k}}(\mathbf{r}) = e^{i\mathbf{k}\cdot\mathbf{r}} u_{n\mathbf{k}}(\mathbf{r}) \tag{5.22}$$

where n is the index of refraction and $\mathbf{k}$ is the wave vector. Representing the elastically scattered electrons as Bloch waves, we can see that some number of these backscattered electrons will constructively interfere as they satisfy the Bragg condition

$$n\lambda = 2d_{hkl} \sin\theta \tag{5.23}$$

where n is the diffraction order, λ is the wavelength of the electrons given by their energy, d_{hkl} is the lattice spacing, and θ is the diffraction angle.

The trajectories of BSE satisfying the Bragg condition form two diffraction cones at each lattice plane, one above and one below. All such diffraction cones produced by lattice planes can be detected on a phosphor screen placed in the path of the electrons as they exit the sample, where they are observed as so-called Kikuchi lines. Thus, these Kikuchi lines, an example of which is shown in Figure 5.19, are conic section projections of the Bragg scattered diffraction cones and can be indexed to characterise the crystalline nature of a sample. Furthermore, by scanning the beam and applying the appropriate computer algorithm, an EBSD map of a sample can be produced highlighting material phases and grain boundaries.

In general, EBSD is a highly surface sensitive technique. As such, it is an ideal tool for analysing the extent of the damage induced during ultrashort pulsed laser ablation as illustrated in Section 5.7.2. The EBSD system installed on the Triple-Beam system and used for all the EBSD analysis presented in this dissertation is an Oxford Instruments HKL Channel 5 “Premium System” with a Nordlys IIs ultra-sensitve camera.

5.6 Integration

The ultimate goal behind the integration of the DualBeam and an ultrashort pulsed laser is not simply to combine two previously disparate bits of technology, but to

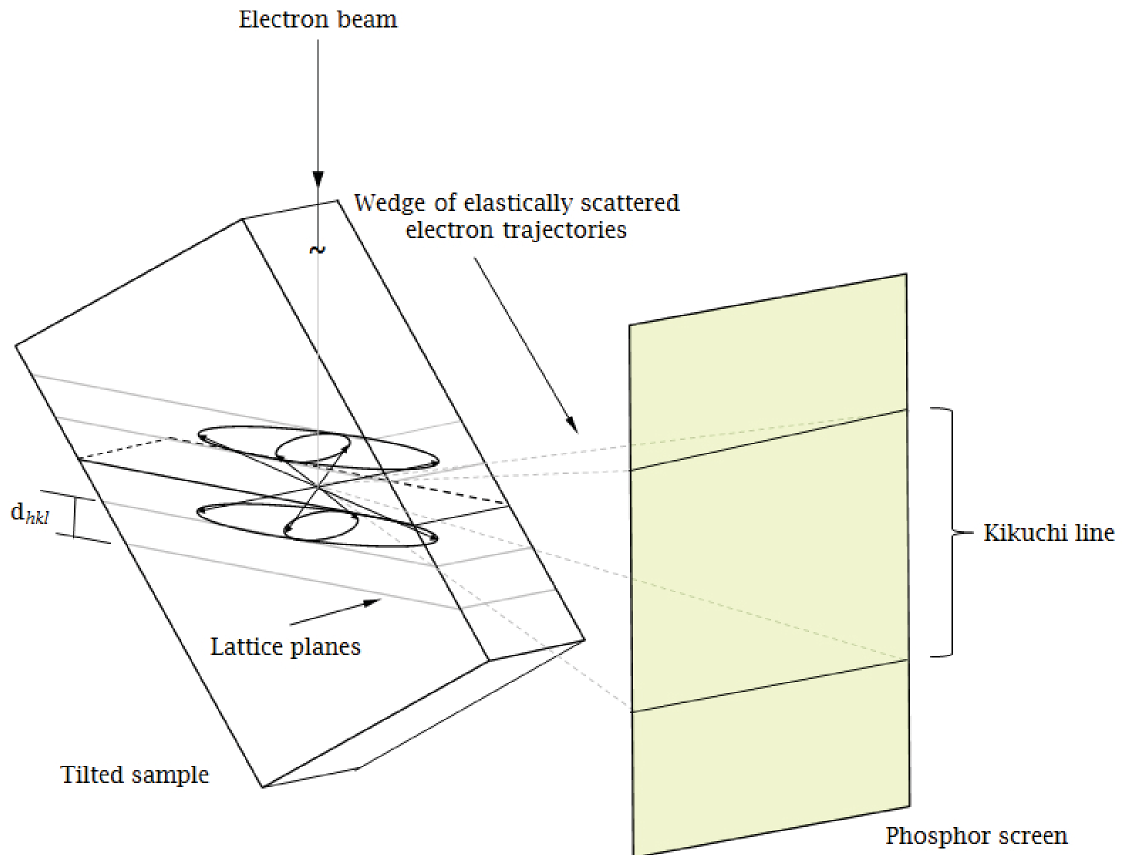

Figure 5.18. In electron backscatter diffraction, elastically scattered electrons satisfying the Bragg conditions interfere to form diffraction cones. The resulting Kikuchi lines that can be observed on an appropriately oriented phosphor screen are conic section projections of these diffraction cones. When indexed, they provide information about the crystallinity of the sample.

develop a system whose whole is greater than the sum of its parts. In spite of this goal, the TripleBeam is a tool developed in a research environment, where expediency sometimes trumps full functionality. As a result, over the course of the instrument's four year development, the design process has been something of an organic one, where component systems underwent redesign as weaknesses were identified and time and resources permitted. The design detailed here is the end result of this effort and little or no discussion of the process leading to it is provided other than to note that, while each iteration is hardly discrete, the current design is roughly the third version of the tool.

Sometime between the second and third iterations (in early 2010), our group

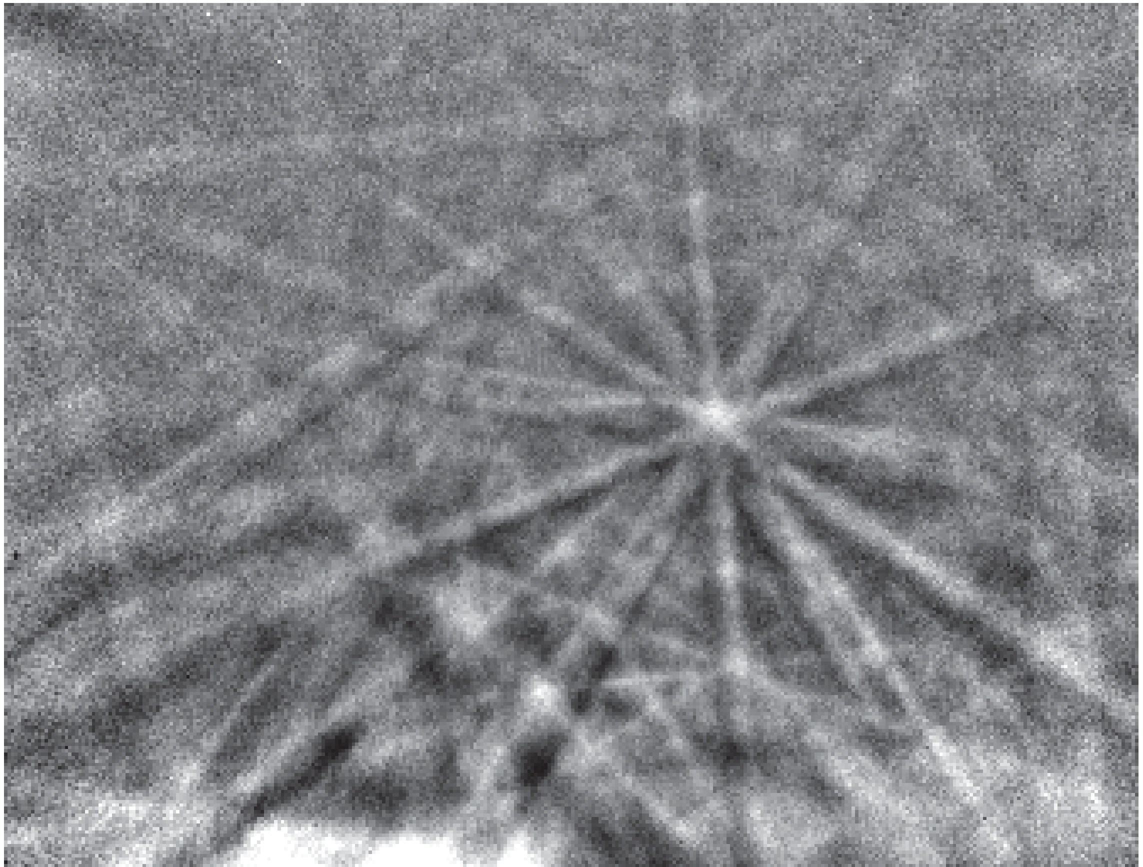

Figure 5.19. An example of the Kikuchi lines formed during EBSD analysis of a copper sample.

entered into a collaboration with Dr. Tresa Pollock's group in the Material Science Department at the University of California, Santa Barbara (UCSB). Dr. Pollock was interested in building a TripleBeam system for the three-dimensional characterisation and reconstruction of materials, particularly metal super-alloys for the aerospace industry. Having demonstrated this capability on the first TripleBeam system, a collaboration to help the Pollock group design a third iteration was entered into with the expressed intent of providing access to expert users in academia and industry alike. As a result of this ongoing collaboration, some details of the joint FEI-UCSB design are necessarily incorporated into the version presented here – particularly with respect to beam delivery and sample control. Dr. Pollock's system is currently in use and plans are in place to build a third system. More discussion of the work of the Pollock group is included in Section 5.7.

The following discussion of our efforts to integrate an ultrashort pulsed laser

and the DualBeam will focus on five general topics: beam delivery, beam control, beam stability and auto-alignment, sample control, and contamination mitigation. Each topic is associated with at least one design element and will be addressed individually. Figure 5.20 gives a schematic overview of the instrument as currently configured while Figure 5.21 shows the inside of the specimen chamber. Throughout the following discussion, these figures will be referenced frequently.

5.6.1 Beam Delivery

As seen in the schematic overview of the TripleBeam system, the laser beam is propagated through free space. A common inquiry regarding this design concerns the possibility of delivering the beam via fibre optics. While it may at first seem a convenient delivery method, there are a number of problems with this approach. Foremost is the fact that, due to dispersion, normal ultrashort pulses are stretched when propagated through optical fibres. Not only does this lengthen the duration of the pulse, effectively eliminating the benefits of ultrashort behaviour, but it also separates the spectral components of the pulse, delivering the redder components before the bluer ones. It is possible to deliver ultrashort pulses via fibre, but the pulses must first be negatively chirped[4]. Dispersive media such as fibres induce positive chirp, so that as a negatively chirped pulse passes through the fibre, it is "reconstructed." The degree to which the pulse is negatively chirped must be matched to the total dispersion of the fibre. This requires tuning the length of the fibre such that the pulse is completely reconstructed at the very moment it exits the fibre. Even when perfectly tuned though, a system such as this is capable of delivering only pulses of very low energy. The reason for this is that as the pulse is reconstructed, its duration is made smaller, effectively increasing the peak power of the pulse. The optical power of ultrashort pulses having energies greater than just a few nanojoules is sufficient to damage the fibre.

Free space propagation of the beam is attractive from an applications perspective as well. While the work described in Chapters 3 and 4 was primarily done by scanning the sample beneath a fixed beam, it is more often desirable to scan the beam, keeping the sample fixed. For a beam propagated through free space, this is

[4]Recall from Section 5.3.2 that negatively chirped pulses are ones in which the high frequency components (blue) lead the low frequency ones (red).

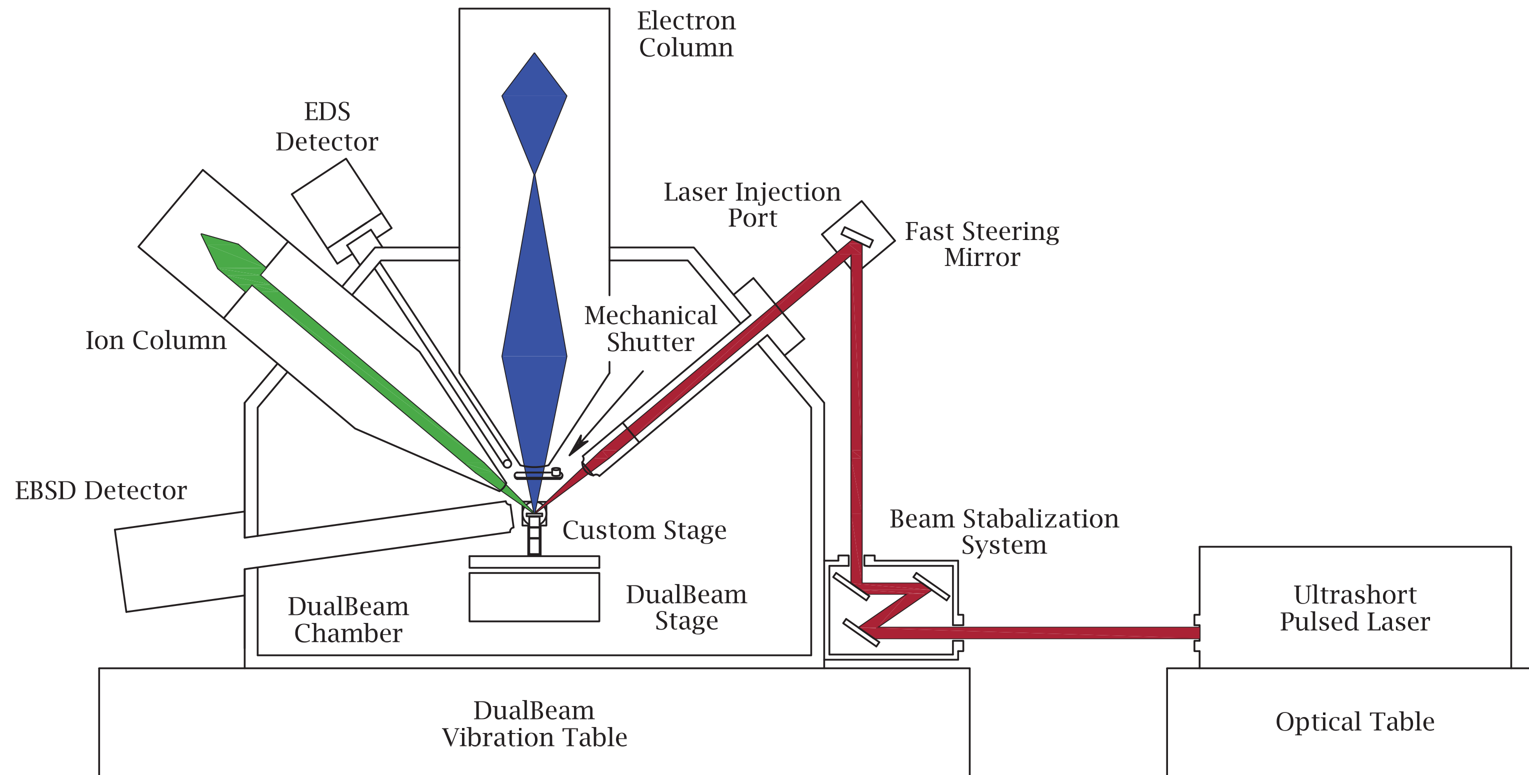

Figure 5.20. Schematic of the TripleBeam layout and the general beam path of the laser.

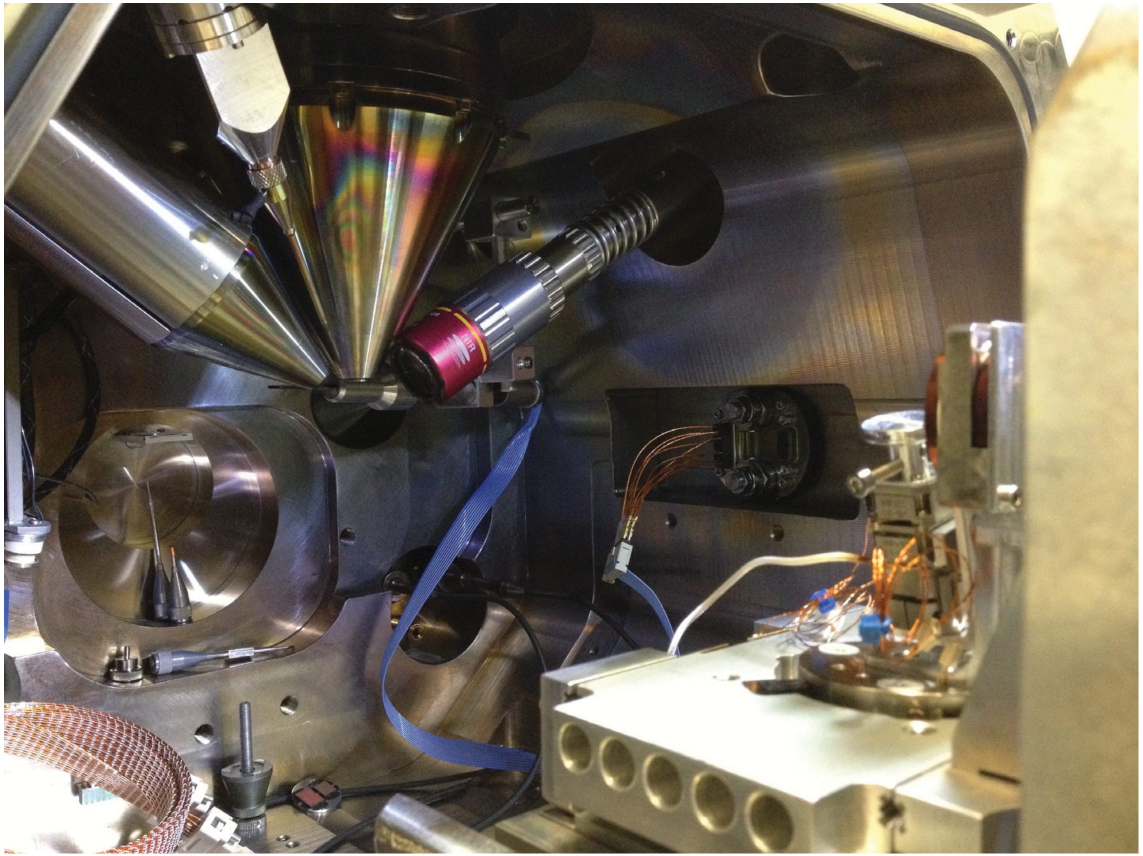

Figure 5.21. Specimen chamber of the TripleBeam system. The laser enters the chamber from the right side of the image and is focused by the (red) Mitutoyo microscope objective, as described in the text. The Attocube stage is also shown attached to the open chamber door.

very easily achieved through the use of mirrors (see the discussion of beam control below). Scanning a beam delivered to the sample via a fibre would require mechanically scanning the fibre itself, a proposition that would require a considerable engineering effort as well as severely restricting the range of scan speeds available.

In the design presented here, the beam is delivered to the sample through a so-called laser injection port (LIP). At its most basic, the LIP is simply an O-ring sealed vacuum viewport attached to a beam tube, which is in turn, attached to a microscope objective. In spite of its simplicity, though, the LIP has gone through a number of design iterations. The latest version is shown in Figure 5.22. With this design, the laser beam can be made confocal with both the SEM and the FIB. Manually adjusting the three micrometer dials allows the focused spot to be

positioned in the xy plane normal to the direction of propagation of the beam. The focus (z) can be adjusted by rotating the focus ring. The laser beam enters the system through the input window, which is made of optical grade borosilicate glass, and is focused by a microscope objective attached to the LIP at the objective adaptor as seen in Figure 5.21. A number of different objectives can be used in TripleBeam. The three most commonly used in this work are 5× (NA = 0.14) and 10× (NA = 0.26) Mitutoyo Plan Apo, infinity corrected, near infrared objectives and a 3× flat field, telecentric lens.

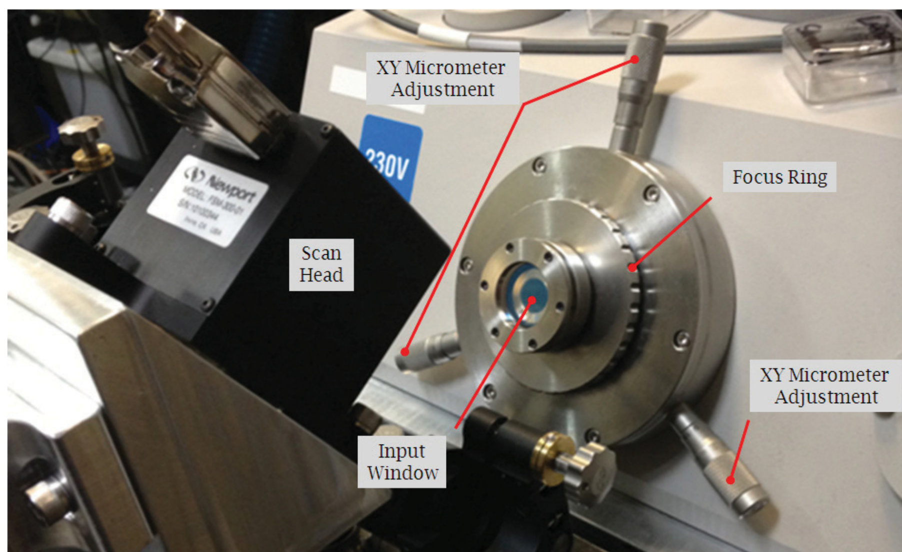

Figure 5.22. The laser injection port of the TripleBeam system as mounted on the instrument. The beam tube and objective adaptor, along with an attached objective, can be seen in the view of the chamber interior shown in Figure 5.21. The x and y position (relative to the beam normal) of the focused spot is controlled via the three micrometer dials. This adjustment is not orthonormal. The position of the focused spot along the beam normal (z) is controlled by the focus ring.

5.6.2 Beam Control

The hardware that the TripleBeam uses to control the laser beam is a fast steering mirror (FSM) from Newport Corporation. The FSM uses four voice coils arranged in push-pull pairs to provide fast, high bandwidth, two axis motion of a 1 inch mirror mounted to a single flexure suspension. Built in sensors and an optical feedback

loop deliver position information to a controller/driver that delivers current to the voice coils to tilt the mirror, providing for accurate point-to-point moves and high repeatability.

The FSM is mounted outside the chamber, directly in front of the input window of the LIP, as can be seen in Figure 5.22. The location of the FSM relative to the sample and the objective lens directly impacts the scan sensitivity, or the distance the beam travels at the sample for a given voltage applied to the voice coils. In order to scan an area of a given size, the scan sensitivity must first be calibrated in both x and y. The calibration routine involves focusing the beam at the sample, machining a feature with a single pulse, applying a known voltage to the scan coils, machining another feature, and measuring the distance between the two features with the SEM. This is typically done when the tool is initially set up or any time the mirror is moved.

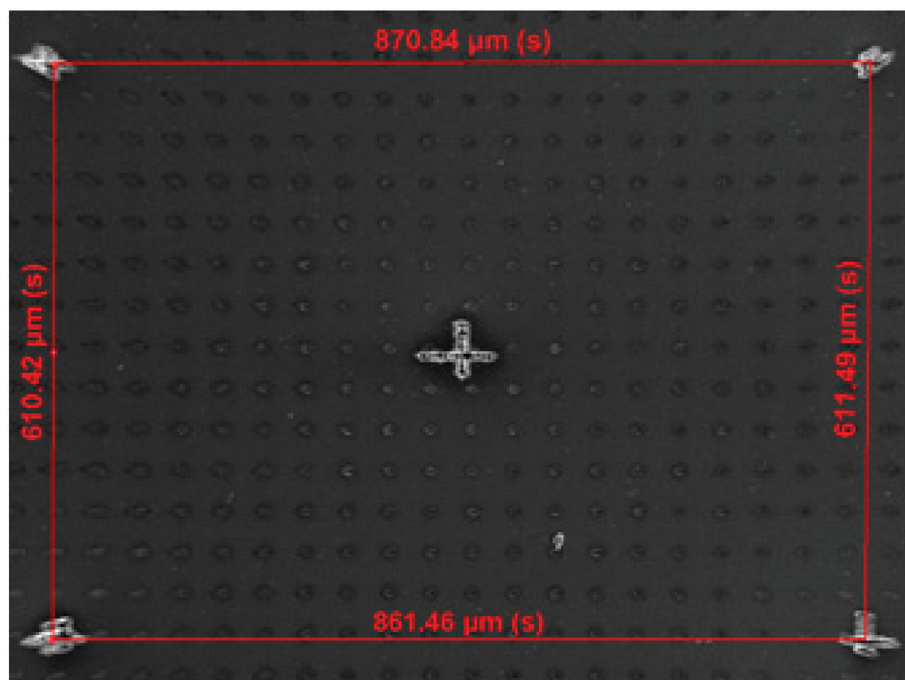

Figure 5.23. Output of the scan field distortion routine used to determine the extent of the scan field as well as the area over which the lens produces a usable spot.

Scan field distortions are induced as the beam is moved away from the centre of lens. The extent and severity of these distortions depends on the lens being used. In order to determine the absolute extent of the scan field (i.e. the point at which

the beam is clipped) as well as the area over which the lens produces a usable spot, a regular grid of features is machined into the sample while the beam is scanned through the entire lens field. An example of one such test is shown in Figure 5.23. Using this method, it has been found that the 10× infinity corrected objective gives a usable scan field of about 700 μm.

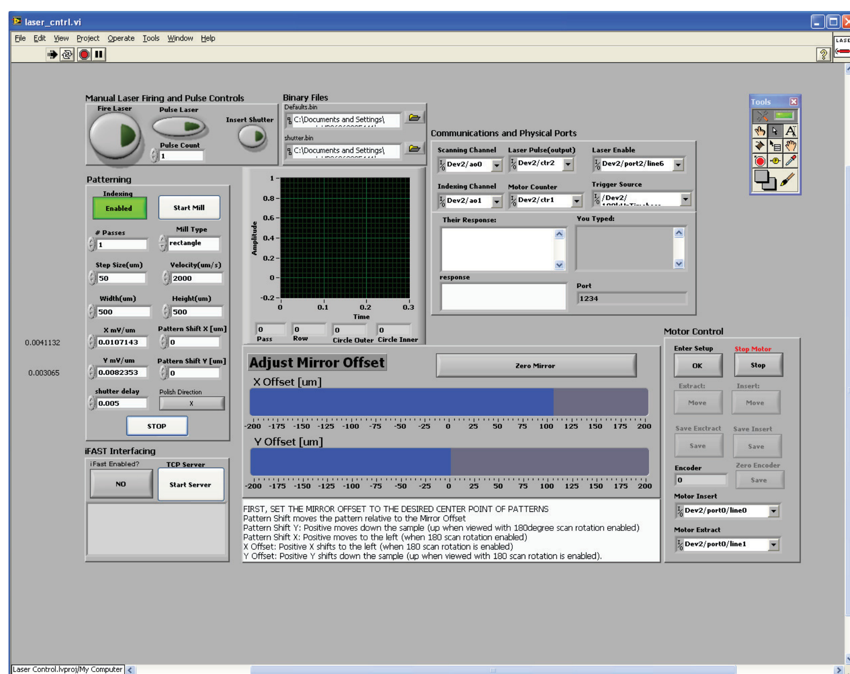

Figure 5.24. A screen-shot of the LabView UI developed to communicate with the laser and the FSM.

To communicate with the FSM and the laser, we built a custom LabView user interface (UI). From this UI, the operator can control the size and shape of the scan field, specify the scan speed and the scan logic (scan order, number of passes, etc.), and calibrate the scan sensitivity. The UI also communicates with the electronic shutter of the laser, allowing the operator to deliver any number of pulses at will or to synchronise the beam delivery with the scan. A screen-shot of the UI is shown in Figure 5.24.

Microscope functions and automated routines can be programmed through the use of iFast™, FEI's application builder. To synchronise iFast with our LabView interface, a small program was written that allows iFast to call LabView as a stand-alone executable. User defined parameters can be passed to LabView and values

returned to iFast. In this way, iFast can use LabView to control the laser and the FSM. As an example, consider a typical slice-and-view routine for 3D reconstruction of sample volumes, a simplified version of which is outlined in Figure 5.25. In this example, LabView would normally be called synchronously, meaning that iFast would wait for a return value from LabView before continuing with the routine. If desired though, LabView can be called asynchronously, allowing the laser and scan to run in parallel with the iFast routine.

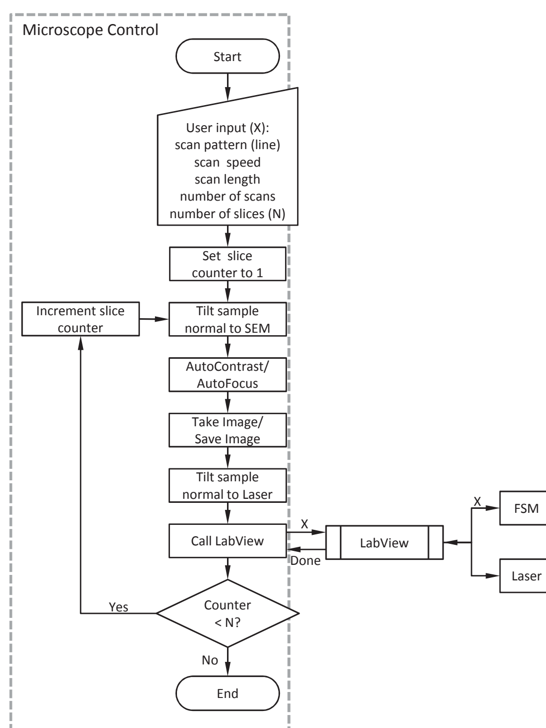

Figure 5.25. A simplified slice-and-view routine illustrating how computer control of the laser and FSM are integrated with computer control of the DualBeam.

5.6.3 Beam Stability/Auto Alignment

In order to ensure that the laser could be employed for uses other than as a third beam on the TripleBeam system (e.g. the work discussed in Chapters 3 and 4), the laser and the DualBeam were left physically decoupled. As seen in Figure 5.20, the laser is located on a separate optical table. Through the use of fixed steering

mirrors, the laser beam is directed to the TripleBeam where still more mirrors steer it through the input window of the LIP. Due to the length of the beam path combined with the inherent pointing instability from which all lasers suffer to some extent, frequent realignment of the laser beam was required prior to the development of a beam stabilisation system.

A separate but related issue concerns alignment in general. The TripleBeam has a vibration isolation system which floats the chamber and FIB and SEM columns on pneumatic cylinders during operation. To align the laser, the laser beam is directed through the LIP window, through the in-chamber objective, and focused to a location in space roughly 10 mm below the polepiece of the SEM. At the intensities used for alignment, focusing the laser in atmosphere causes the break-down of air and the formation of a visible and audible plasma of a size on the order of 1 mm in diameter. For this reason, the alignment procedure is typically performed with the chamber vented and the chamber door open, allowing the operator to use the plasma as visible alignment indicator in two ways. First, the very formation of the plasma confirms that the beam is going through the lens. Secondly, once the plasma is struck, it can be used to adjust the location of the laser's focus in order to ensure that it is close to the eucentric point of the SEM.

During this process, the tool is vented, the vibration isolation system is deactivated, and the instrument is said to be "parked." Once the laser is roughly aligned, the door is closed, the chamber is pumped down, and the system is again floated. Because the laser is decoupled from the rest of the system, transitioning from a parked state to a floating state changes the position of the steering mirrors, scan head, and LIP window relative to the beam. Thus, aligning while the system is parked and later floating the system induces misalignments that can be difficult to correct. The realignment process is time consuming, difficult, and prone to error and as such, brought into question the repeatability of experimental conditions early in the tool's development. Initially, this issue was surmounted by overriding the deactivation of the vibration isolation system, thereby preventing the chamber from parking during alignment. The chamber would then be 'blocked" against the system table to prevent the now floating instrument from rotating as its centre of mass shifted when the door was opened. While adequate as an initial work-around, it was hardly an elegant solution and was still subject to small but noticeable variations

in the alignment condition.

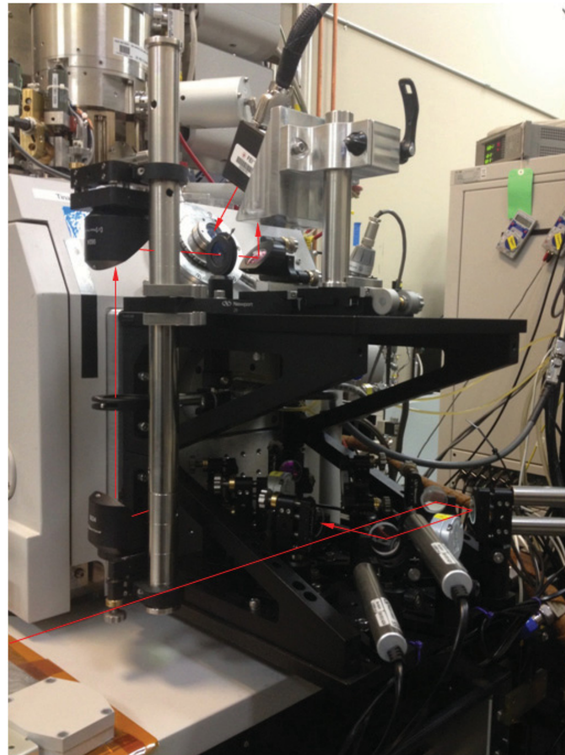

Figure 5.26. The two-levels of the beam stabilisation system. The beam enters the lower level, where it is steered by series of fixed and motorised mirror. Given some arbitrary input angle (within a specified range), the beam always exits the lower level at the same angle and position, thereby ensuring a consistent alignment condition.

The TripleBeam's beam stabilisation system (BSS) both corrects for misalignments due to beam drift (pointing stability) and provides for a stable alignment condition independent of the operational state of the TripleBeam. At its most fundamental, the BSS ensures that the angle at which the beam exits the system is fixed given any arbitrary input angle over a prescribed range of angles. Thus, once aligned to the in-chamber microscope objective, this alignment is unchanged by either normal beam drift or the position of the chamber. Furthermore, achieving identical alignment conditions from experiment to experiment is trivial as long as the new input angle does not fall outside the acceptable range.

Shown in Figure 5.26, the BSS has two levels, stacked one on top of the other, and is mounted to the side of the TripleBeam via a custom designed plate. As shown, the beam enters the system from the laser on the lower level where it is steered via

a series of fixed and motorised mirrors to a periscope, which relays it to the upper level. On the upper level, it is directed onto the FSM and ultimately, through the LIP. It is on the lower level where the beam stabilisation and auto alignment occur and Figure 5.27 details the beam path through this portion of the system.

Upon entering the lower level, the beam is steered onto two computer controlled, motorised mirrors, MM1 and MM2. After leaving MM2, the beam is steered through two beam samplers, BS1 and BS2. A portion of the beam is directed by each beam sampler onto one of two corresponding position sensitive detectors, PSD1 and PSD2. The position sensitive detectors (PSD) use lateral-effect photodiodes to determine the position of the beam on the detector. A negative feedback loop controls the step size and direction of the mirror motors based on the difference between the location of the beam on the PSDs and a set-point position. Specifically, the signal from PSD1 is used to control MM1. Likewise for PSD2 and MM2. In this fashion, the position and incident angle of the beam on the lower periscope mirror remains constant independent of the angle at which the beam enters the system.

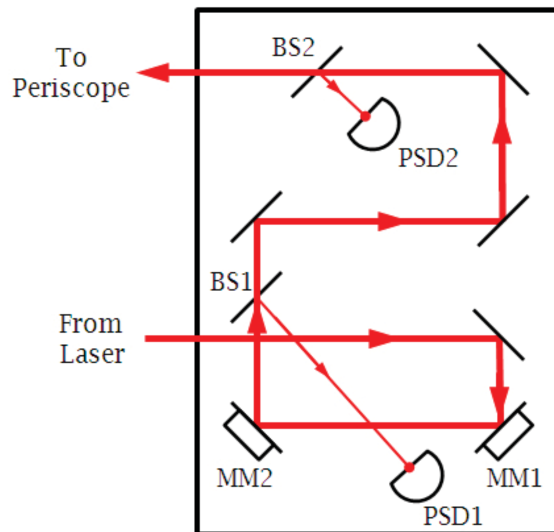

Figure 5.27. The actual path the beam takes through the lower level of the beam stabilisation system. MM1 and MM2 are computer controlled mirrors whose position is determined by the location of the beam on PSD1 and PSD2, respectively.

5.6.4 Sample Control

The Quanta 3D FEG DualBeam comes standard with a 5-axis (x, y, z, tilt, and rotation) motorised stage with 50 mm of travel in x and y and 25 mm of travel in z. The tilt range is -15° to 75° and it can rotate infinitely through 360°. The minimum step size the stage can move in x, y, and z is 300 nm with a repeatability of 2 μm at 0° tilt and 4 μm at 52° tilt. While these specifications make the Quanta's stage a very flexible sample control system, to truly test the limits of the TripleBeam system required a stage with higher resolution, a smaller minimum step size, and better repeatability.

Through the collaboration with UCSB, a custom sample control system using stacked piezoelectric nanopositioners mounted to a rotary stepper positioner was designed and tested, with one lab verifying the other's results. Both the nanopositioners and the rotary stepper were manufactured by Attocube, while the mount was custom designed in collaboration with Dr. Pollock's group. Figure 5.28 shows the details of this design and the actual system as installed on the TripleBeam can be seen in Figure 5.21.

Using this system, one degree of freedom (rotation) is lost and the range of travel is considerably diminished in x, y, and z (3 mm in x and y and only 2.5 mm in z) when compared to the standard DualBeam stage, but significant gains are made in resolution and repeatability. Because the custom stage is mounted on the standard DualBeam stage, however, course positioning moves can be performed through the regular DualBeam UI making the range of travel restrictions imposed by the custom stage a non-issue.

Both the nanopositioners and the rotary stepper are closed loop systems with position encoders. The x, z, and rotation axes all use resistive encoders, giving x and z a minimum step size of 25 nm with a closed loop sensor resolution of approximately 200 nm, a repeatability of 1 to 2 μm, and a sub-nanometre fine positioning resolution. The rotation axis has a minimum step size of 1 m° with a sensor resolution of around 6 m°, a repeatability of approximately 50 m°, and a fine positioning resolution on the order of μ°. The y axis nanopositioner has an integrated optoelectronic encoder that provides higher resolution than that achievable using resistive encoders. The closed loop sensor resolution of the y axis is 10 nm with 50 nm repeatability and sub-nanometre fine positioning resolution. The decision to provide the y axis with

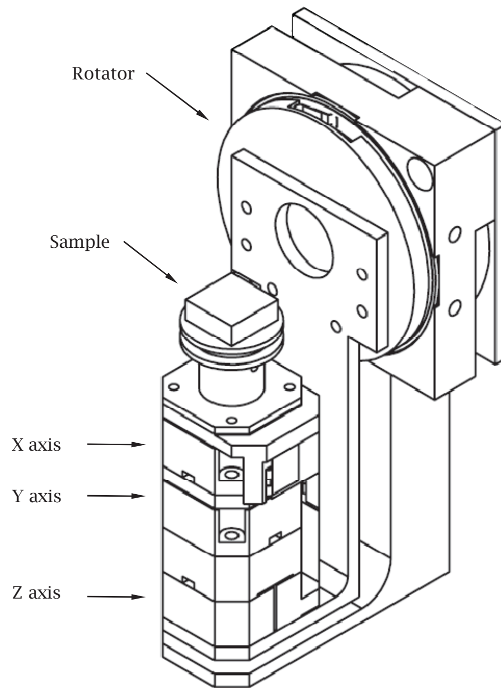

Figure 5.28. The TripleBeam system's custom stage. Stacked piezoelectric nanopositioners mounted to a rotary stepper positioner provide high resolution, high repeatability computer controlled, 4-axis sample positioning. (Image courtesy of Dr. McLean Echlin, University of California, Santa Barbara)

higher resolution stems from the need for high positional accuracy during serial sectioning applications as discussed in Section 5.7.

Communication with the 4-axis piezoelectric motion controller is achieved by a stand alone executable written in C. Identical to the way LabView can be called to control the laser and the FSM, this executable can be be called from iFast providing control of the stage through the microscope during automated routines. During normal operation, however, "manual" control of the stage (via the piezoelectric controller) is required since this functionality has not yet been incorporated into the DualBeam's UI.

5.6.5 Contamination Mitigation

Given the appropriate processing parameters, laser ablation can remove huge volumes of material at rates far in excess of those achievable via FIB sputtering. In work preliminary to that discussed in this dissertation, material removal rates as high as 7 million $\mu m^3/s$ were demonstrated. Even when less aggressive processing parameters are used, material removed via laser ablation leaves the sampled surface at supersonic velocities. In vacuum, where there are few ambient gas molecules with which it can collide, the mean free path of this ejected material is long, allowing for redeposition on surfaces tens of centimetres distant. As a result, the effect of contamination of sensitive components including detectors, stage encoders, light optics, and the SEM and FIB columns has to be considered when laser ablation is performed inside a DualBeam system.

That said, it has been shown that for ablation plumes produced by nanosecond pulses the fastest component of the ejected material is along the normal to the sample [34]. Furthermore, plumes are more peaked and this effect enhanced for plumes produced by femtosecond pulses [27]. Thus, given that the sample is tilted away from the SEM and toward the focusing objective for the vast majority of the ablation performed on the TripleBeam, the component most in danger of being damaged by laser-induced deposition is the microscope objective. In order to prevent this damage from occurring, a glass cover is placed between the sample and the lens. Since glass is non-conductive, charge can and does build up on the cover. The result is a marked decrease in SEM performance. To eliminate this effect, the glass cover is now coated with a thin film of indium tin oxide (ITO), making it conductive yet still transparent. Over time, debris builds up on this glass cover, occluding the lens, and effectively reducing the laser power that can be delivered, at which point the cover is removed and replaced.

In spite of the fact that most of the ejected debris is directed away from the SEM, under certain conditions and over time contamination-induced degradation of SEM performance has been observed. Typically, this manifests itself as uncorrectable astigmatism of the electron beam and is a result of charging of material somewhere along the beam path. Most of the time, the offending material is found in the pole piece of the column and can be removed relatively easily. On occasion, we have found deposited material as high up in the column as the probe forming aperture,

in which case the aperture strip was replaced. Failure due to high-voltage breakdown has never occurred over the course of this project. Nonetheless, contamination of the column is certainly something to be avoided. Toward this end, a mechanical shutter, mounted on a linear motor, was installed to effectively block the line-of-site path from the sample to the lens bore. The shutter can be inserted between the sample and the lens bore of the SEM during laser ablation and retracted during imaging.

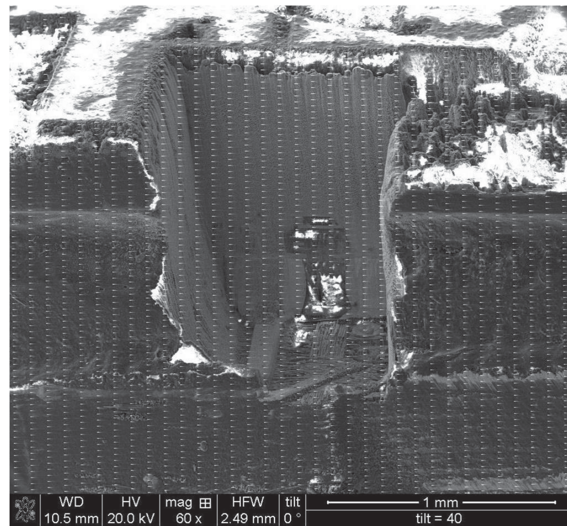

Figure 5.29. The effect of detector saturation due to "gentle" ablation being performed during SEM imaging. The pitch of the dot pattern is correlated to the repetition rate of the laser and the scan rate of the electron beam. Depending on processing conditions, detector saturation can be much more extreme than this, causing the entire image to bleach (or go white). This effect can persist for seconds after the processing is finished. Flickering is sometimes observed for up to a minute or two after the detector "recovers."

The location of the FIB column and stage encoders relative to the ablation site make contamination of these components improbable. In fact, no deleterious effect on their performance has been observed due to laser-induced deposition over the four year course of the project.

If laser ablation and SEM imaging are performed simultaneously, the Everhart-Thornley secondary electron detector saturates due to the burst of photoelectrons that are ejected from the sample as the pulse interacts with the sample. Depending on the fluence of the beam, the sample being processed, and the bias on the detector

grid, saturation can be complete, bleaching the entire image and taking seconds for the detector to recover, or it can result in a regular pattern of bright dots overlaying the image as shown in Figure 5.29.

If imaging is stopped and a negative bias is applied to the detector grid during laser ablation, detector recovery times are considerably shorter, even under very aggressive ablation conditions. Nonetheless, the impact this phenomenon has on the lifetime of the detector in unclear. Over the course of the project, the ETD has been replaced once and its failure could not be conclusively attributed to laser-induced contamination.

5.6.6 Ongoing Development Effort

The ability to deliver photons to a sample inevitably leads one to consider the detection of photons produced at the sample. A number of light-based characterisation techniques are available – including Raman Spectroscopy, Surface Enhanced Raman Spectroscopy (SERS), Coherent Anti-Stokes Raman Spectroscopy (CARS), Laser Induced Breakdown Spectroscopy, and cathodoluminescence (CL) spectroscopy – that can provide chemical, structural, and crystallographic information. Currently, there is an effort to add light collection and detection capabilities to the the TripleBeam system with the intent of exploring the in situ implementation of one or more of these techniques.

5.7 Instrument Characterisation and Validation

A great deal of effort has gone into exploring the capabilities of the TripleBeam system. In addition to the ultrashort pulsed laser-driven surface chemistry discussed in the next chapter, the system's efficacy has been explored for a range of applications including defect and failure analysis of More-than-Moore [121] interconnect technologies such as through silicon vias (TSVs) and copper bumps, depackaging of electronic devices, "a-thermal" annealing of FIB-induced depositions [122, 123], laser-induced X-ray spectroscopy, in situ surface plasmon polariton studies, in situ multiphoton excitation of fluorescent markers for correlative microscopy of life science samples, and serial sectioning for 3-dimensional characterisation of materials and devices. A discussion of every one these efforts is beyond the scope of this dissertation. How-

ever, work developing serial sectioning techniques for 3D materials reconstruction across a range of length scales demonstrates the "whole-greater-than-the-sum-of-its-parts" capability of the system to enable previously unattainable results. Therefore, as a means of highlighting the synergistic potential of the instrument, this section will detail the results of our 3D characterisation efforts.

5.7.1 The Need for 3D and the Gap in Length Scales

With the ultimate goal of developing computational tools for materials modelling, materials scientists have a growing need for technologies that can characterise materials in three dimensions across length scales ranging from tens of nanometres to hundreds of micrometers, or even millimetres. Viewed as critical to remaining globally competitive, recent efforts to speed the design and development of new materials by recent national and international programs such as the Materials Genome Initiative [124] have heightened the urgency. While the main thrust of these efforts is computational, it is widely acknowledged that generating accurate and extensive sets of data on materials properties from which material behaviour can be modelled is difficult, time consuming, and often material dependent using state of the art techniques. As a result, new technologies with the potential to produce multi-modal data on a wide range of materials, spanning the relevant length scales, and with a short time to data are currently highly sought after.

There are two general methods for collecting three-dimensional materials data. The first is X-ray computed tomography, also called μCT, and the second is serial sectioning. X-ray tomography uses the transmission of X-rays through a sample at a variety of projections to reconstruct a three dimensional image. The absorption (and by extension, the transmission) of X-rays by the sample is a function of the density or atomic number of the material under analysis. Thus, samples made up of aggregated materials having very different densities provide the best contrast and on this sort of sample, typical commercially available μCT instruments can produce images having resolutions of one to five microns over volumes with diameters as large as 200 mm. Samples made up of high density materials, however, may not have sufficient transmission to form images at all[5]. Furthermore, in composite materials

[5]High density materials can be imaged with resolutions on the order of 50 nm, but only with synchrotron sources, putting this capability well beyond the realm of commercially available in-

where the components are of similar densities, distinguishing grain boundaries can be difficult. Finally, artefacts such as beam hardening, wherein the centre of a sample absorbs more X-rays than the edges, can complicate the acquisition and interpretation of data. In spite of these shortcomings, μCT has the advantage of being non-destructive (i.e. the sample remains intact through the course of the experiment).

By contrast, serial sectioning is a destructive technique where samples are physically sliced or polished, then this polished face imaged. This "slice and view" process is repeated iteratively, forming a stack of two dimensional images from which the three dimensional volume is digitally reconstructed. Typically, the technique is performed by one of two methods. In the first method, the sample is "sliced" by mechanically polishing and then "viewed" by optical microscopy, (and sometimes SEM). The resolution achievable by serial sectioning in general is determined both by the thinness of the slices that can be achieved by the particular slicing method employed and the resolution of the system used to image each slice. For mechanical serial sectioning, the resolution is typically on the order of microns in the slice (z) direction and 100's of nanometres in the $x-y$ plane. Care must be taken during the polishing process to prevent artefacts introduced by sample heating. For instance, with any serial sectioning method, ensuring that a known and uniform thickness is maintained from slice to slice is critical to preventing distortions in the size and relative location of the grains in the reconstruction. Thermal expansion of the sample resulting from heat generated during polishing can affect the accuracy of the sectioning process, producing undesirable artefacts in the final reconstruction even when efforts are undertaken to ensure slice uniformity [125]. Finally, while large volumes can be accessed by mechanical serial sectioning, the process is laborious and time consuming, making time-to-data a potential issue with this technique.

Another method of serial sectioning involves the used of a FIB to slice the sample, followed by the use of a SEM to image it, in the manner illustrated in Figure 5.30. FIB serial sectioning provides much better resolution than either μCT or serial section by mechanical means – typically around 10 nm in z and 2 to 5 nm in the transverse direction. Furthermore, the sample damage induced during FIB milling typically is on the order of only about 1 nm per 1 keV of ion energy. Relative

struments.

to mechanical polishing, FIB sputtering induces little damage in the sample. The typical instrument used to perform FIB serial sectioning is the DualBeam, where software controlled scripts ensure consistent slice thickness and enable the entire process to be automated. Thus, while FIB methods can provide repeatable results at unprecedented resolution without operator supervision, the maximum volumes accessible by FIB are quite small – typically on the order of a thousand cubic microns.

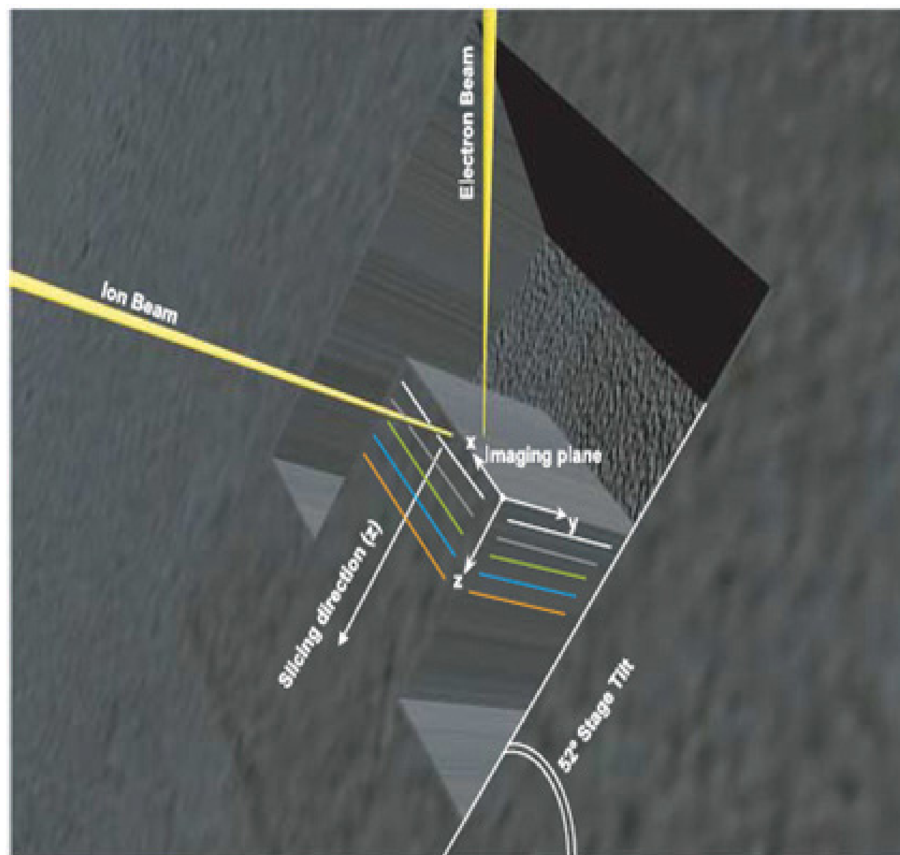

Figure 5.30. Geometry used for FIB serial sectioning. The laser serial sectioning technique described here uses and identical geometry, only with the ion beam replaced with an ultrashort pulsed laser beam. Figure is courtesy of FEI.

If one image is to be captured per slice, note that there is a practical limit to the real dimensions of the area that can be imaged and that this limit is dictated by the slice thickness. By way of illustration, consider the notion of a voxel. If the slice direction is labelled z, a voxel can be no smaller in z than the actual thickness of the slice itself. Thus, for a given number of pixels in a two dimensional image

to be used as a slice in a three dimensional reconstruction, the maximum actual dimensions of the area of the image can be no larger than the product of the slice thickness and the number of pixels in the longest dimension in order to ensure at least one pixel per voxel. Thus, for a relatively high resolution image made up of 2058 pixels in the horizontal dimension, the maximum horizontal field width of the image should be no larger than about 20 μm for a slice thickness of 10 nm, and no more than 2 mm for a slice thickness of 1 μm.

The observant reader will note a gap in the length scales accessible by the current state-of-the-art techniques. At the minimum slice thickness of each technique, there are two orders of magnitude separating the accessible length scales. While it may be obvious that accurately and reproducibly creating thinner slices via mechanical means is challenging, it may not be so apparent that extending FIB to thicker slices is equally difficult. The challenge here lies not so much in making a thick slice, but in making that thick slice over a large area in a reasonable length of time while maintaining planarity. Redeposition, curtaining, and the characteristically low sputter rate of FIB milling all conspire to make uniform, large area FIB milling impractical with currently available technologies.

5.7.2 A Tool for Bridging the Gap

When used as a serial sectioning tool, the TripleBeam bridges this length scale gap. Figure 5.31 illustrates some of its capabilities in this capacity with an approximately 3.6 million μm^3 three dimensional reconstruction of a geological sample, serially sectioned in 200 nm slices over an area approximately 240 $\times$ 240 μm using the TripleBeam's ultrashort pulsed laser[6]. While numerous methods for producing thin slices with the laser were explored, we found that laser serial sectioning done in a manner identical to FIB serial sectioning produces the fastest, most accurate, and cleanest results. The images used to generate the reconstruction were collected with the instrument's backscattered electron detector (BSE), providing contrast based on the atomic number Z of the component materials. Thus, figure (a) shows a high Z material embedded in a mineral matrix. In figure (b), the matrix has been removed to better visualise the material of interest. In this example, the entire

[6]To produce these results, the laser was focused with the 10$\times$ Mitutoyo objective discussed earlier.

process was fully automated, taking 8 hours of unattended instrument time. Due to the fact that this work was carried out prior to the integration of either the Attocube sub-stage or the scan head, slicing was performed by moving the sample under a fixed beam. Thus, while each actual slice took approximately 2 seconds, stage moves, stage and detector settling time, auto focus and auto-contrast, and especially imaging constituted the vast majority of the processing time required.

Follow on work demonstrated the ability to produce slices as small as 100 nm in short runs (up to 10). However, because this work was done before the current sample and beam control capabilities had been developed, limitations of the repeatability of the standard DualBeam stage prevented the collection of a full data set. Nonetheless, this suggests that laser produced slices of dimensions smaller than those already demonstrated are possible. It should be noted though, that as the slice thickness decreases, any damage layer induced by the laser will have a larger impact on the final results.

In an attempt to quantify the damage layer, the TripleBeam was used to laser machine a tungsten carbide sample containing 11% cobalt (WC-Co) with tungsten grains that are approximately 10 μm. To do so, a region of interest was exposed with the laser by machining away a 350 $\times$ 350 $\times$ 200 μm volume, a process that took approximately 10 minutes (Figure 5.32. WC-Co is a very hard material. Removing a similar volume via FIB milling would have required multiple days of work, illustrating the ability of the TripleBeam to process a wide range of materials. Once exposed, the laser was used to polish the surface to be analysed in a fashion identical to that used for FIB serial sectioning.

The images in Figure 5.33 show the results of these efforts. Clearly, the overall surface finish of the cut-face is very good (figure (b)), and compares favourably to mechanical polishing (compare figure (a), which has been mechanically polished with figure (c), which has been polished). At higher magnifications, sub-wavelength periodic ripples are observed (figure (c)). In order to further analyse these features, a protective platinum cap was deposited over the cut face and the features were cross sectioned. The view in cross section shown in figure (d) reveals the features to have a pitch of approximately 250 nm or $\lambda/3$ and a depth of 75 to 100 nm. Due to the distinctive shape of the features it produces, this effect has been given the descriptive moniker "shark-finning". While the origin of shark-finning is currently unknown, it

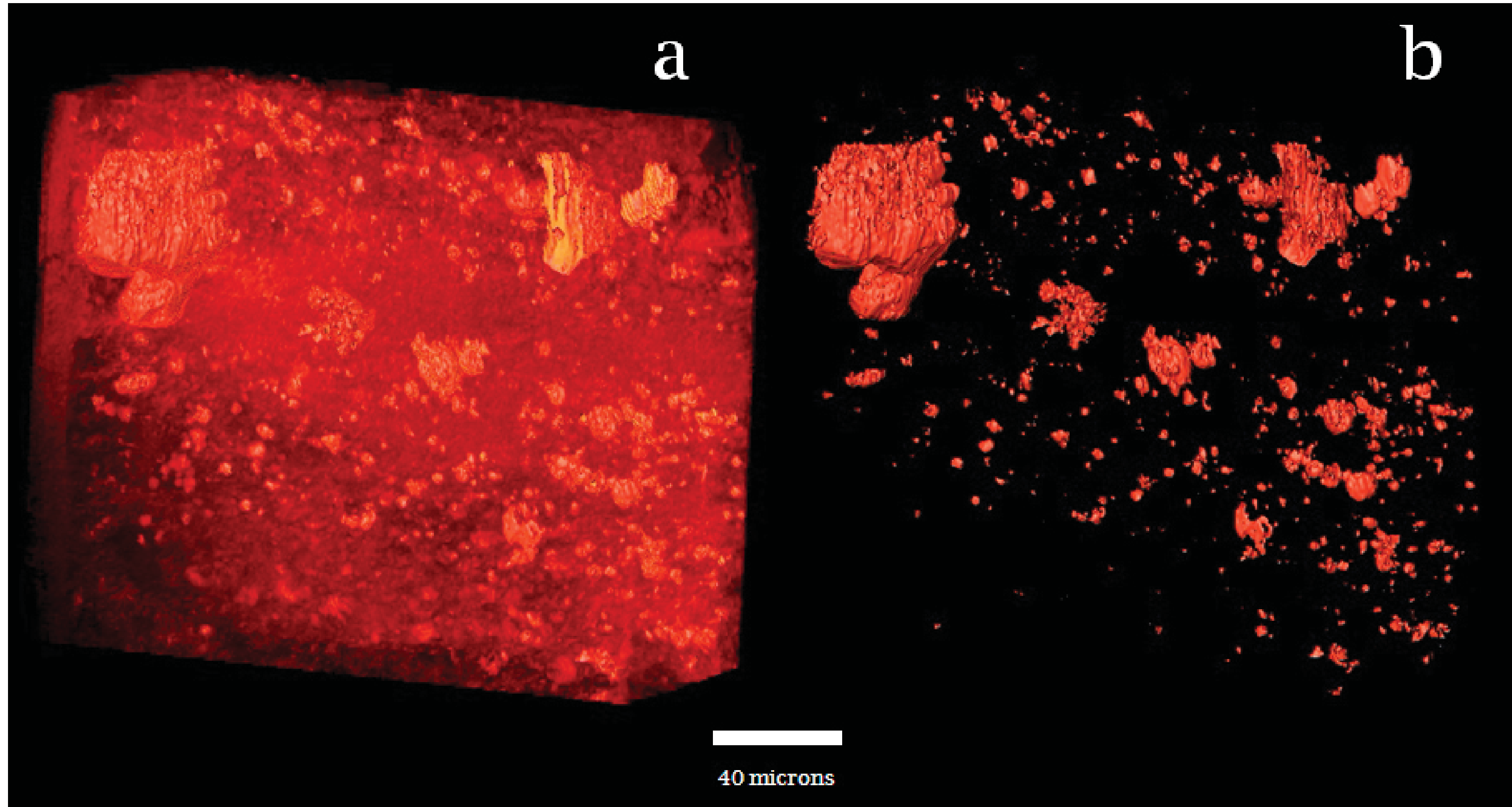

Figure 5.31. A three dimensional reconstruction of a 3.6 million μm^3 geological sample serially sectioned with the laser in 200 nm slices. BSE data were collected during an automated 8 hour run. The left hand image shows a high Z material embedded in a mineral matrix. The matrix has been removed in the right hand image to highlight the material of interest.

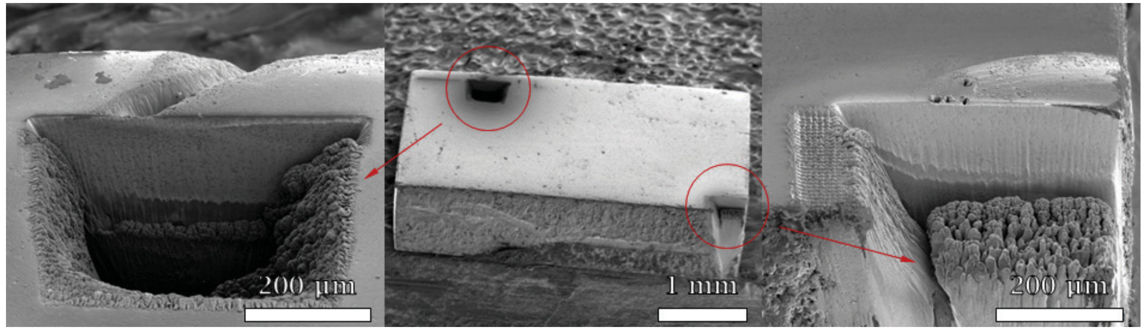

Figure 5.32. SEM micrographs of bulk material removal on a WC-Co sample via UPL as performed on the TripleBeam system. The centre image shows the entire sample with two pits machined in it, one in the field and one at the sample's edge. The left and right images are details of the these two pits prior to UPL polishing.

is similar in appearance to a widely researched phenomenon known as laser-induced periodic surface structures (LIPPS) [126, 127, 128, 129, 130, 131, 132, 133, 134, 135]. A more detailed discussion of LIPPS can be found in Section 6.4.

As a means of probing the extent of the damage layer induced by the laser, TEM diffraction was used to analyse the crystalline structure of the laser machined WC-Co in the region near the cut face[7]. A thin slice was cut from the sample and irradiated with the electron beam. The resulting diffraction patterns are shown in the lower images in Figure 5.34. The location of the electron probe on the sample is shown as a red cross on the upper images. As a control, a measurement was taken approximately 200 nm away from the cut face, into the bulk of the sample as shown in the left-most pair of images. On just the other side of the cut face boundary, another measurement was made. The resulting diffraction pattern is characteristic of an amorphous material, as expected given the presence of the platinum deposited in this location in order to protect the cut face during cross-sectioning. The centre image shows the results of a measurement made at the interface, where evidence of a damage layer or heat affected zone would be expected to be greatest. Comparing the diffraction pattern collected in the bulk of the sample to the one collected at the interface, it is clear that the material at the interface is still highly crystalline, suggesting that the heat deposited by the laser at the depth of the measurement

[7]This work was done by FEI colleagues in Holland as part of the TripleBeam development effort.

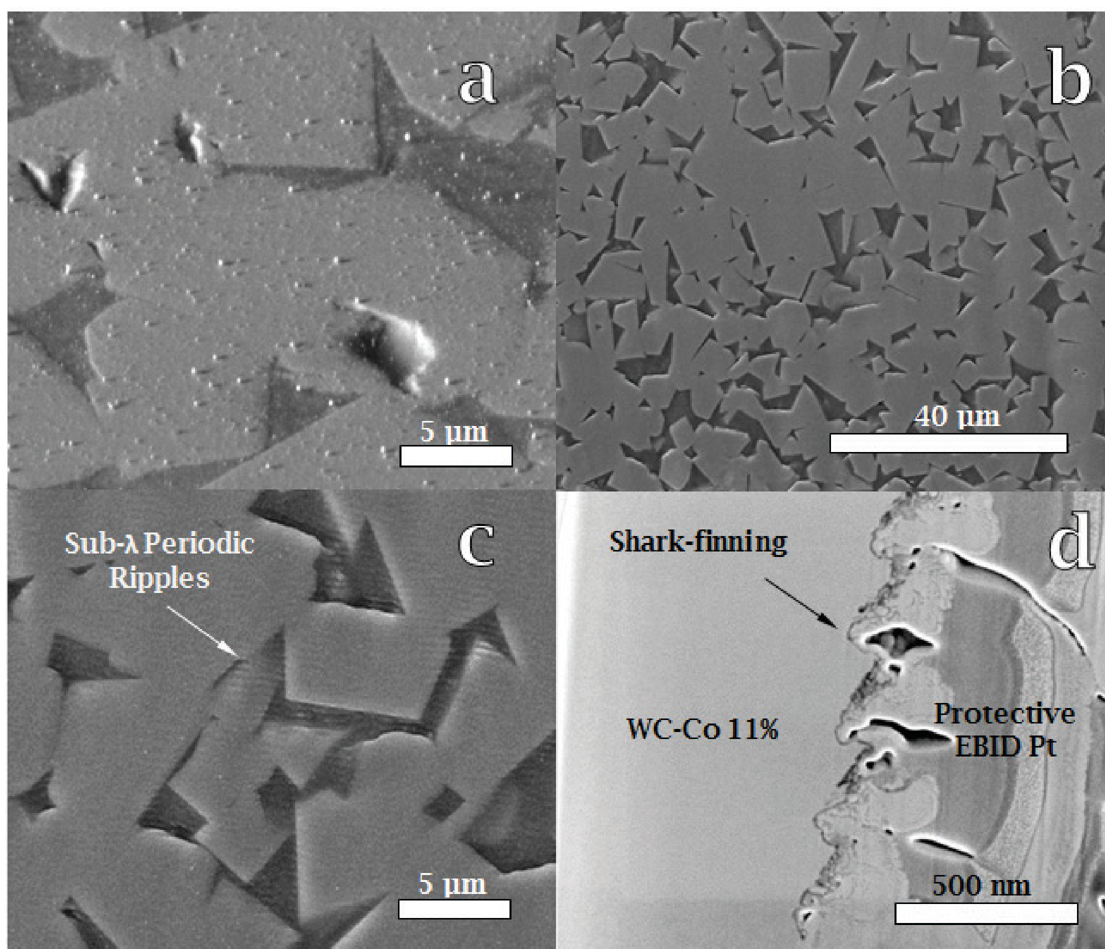

Figure 5.33. SEM analysis of a laser polished WC-Co sample. Figure (b) is an overview of the results. The quality of the finish compares favourably to surface finishes achievable via mechanical polishing, as seen by comparing figure (a) (mechanically polished) with figure (c) (laser polished). At higher magnification, sub-wavelength periodic ripples, or "shark fins" are observed (figure (c)). Figure (d) is a higher magnification SEM image of the shark fins illustrating that the pitch (or wavelength) of the features is approximately 250 nm and that they have a depth of 75 to 100 nm.

was insufficient to melt the sample.

While this is broadly consistent with what is known about the "a-thermal" nature of ultrashort pulsed laser ablation, it is still somewhat surprising. Earlier work done by our group investigating the extent of the heat affected zone in silicon showed that, while small, a damage layer does exist. By way of illustration, Figure 5.35

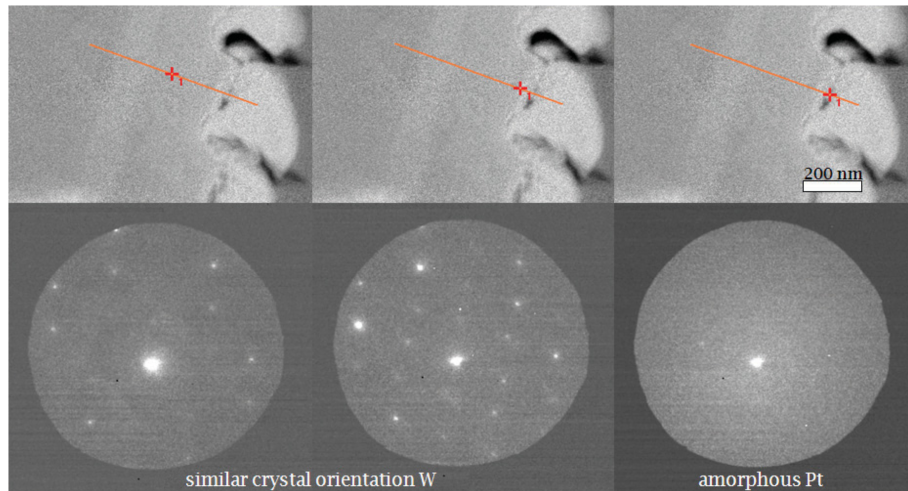

Figure 5.34. TEM diffraction analysis of laser polished WC-Co. The location of the electron probe is given by the red cross on the upper images. No difference is apparent between the crystalline structure of the bulk (lower left hand diffraction pattern) and that of the material at the UPL polished interface (lower middle diffraction pattern), suggesting very little laser-induced thermal damage. Diffraction images were collected with an FEI TF20 operating at an acceleration voltage of 200 keV.

is a TEM image of a via machined into a silicon sample at a fluence two orders of magnitude above the ablation threshold of silicon. At the bottom of the image, the regular lattice of crystalline silicon is seen. At the top of the image is a platinum layer deposited first by electron beam (to ensure no sputtering of the interface), and then, to increase the rate of deposition, FIB. In between is a layer of amorphous Si on the order of 20 nm thick. It is this layer that constitutes the HAZ. When extremely aggressive processing conditions are used, our investigations show that the amorphous layer produced in silicon during ultrashort pulsed laser processing can be larger still – on the order of microns. In short, ultrashort pulsed lasers can and do induce some sample damage, albeit considerably less than that induced by nanosecond and CW lasers.

The apparent absence of damage observed in our WC-Co sample is therefore something of a curiosity. Due to the material response to laser heating, it may be that the induced damage layer in this case is very small and the resolution of the method chosen to measure it in this experiment is insufficient to detect it. As a starting point for analysing this conjecture, recall from Chapter 1 that the thermal

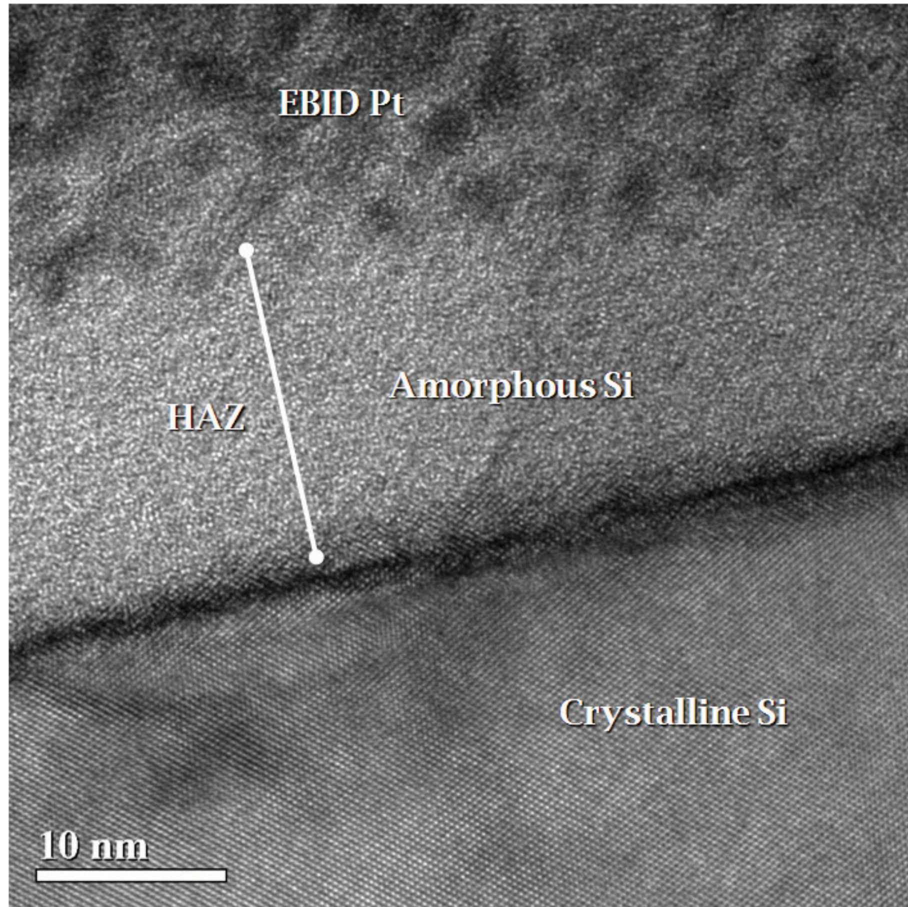

Figure 5.35. TEM analysis of the heat affected zone in UPL machined silicon showing ≈20 nm of amorphous silicon constituting the HAZ.

diffusion length L_{th} of a material over the duration of its irradiation by a laser pulse having a temporal width τ is given by

$$L_{th} = 2\sqrt{D\tau} \tag{5.24}$$

where D is the diffusivity of the material. The diffusivity can be calculated from known parameters by

$$D = \frac{k}{\rho c_p} \tag{5.25}$$

where k is the thermal conductivity (W/(m·K)) of the material, ρ is its density (kg/m^3), and c_p is its specific heat capacity (J/(kg·K). The thermal properties of WC-Co depend somewhat on its cobalt content and published values of k an c_p vary con-

siderably. From Equation 5.25, the diffusivity of the WC-11%Co sample used in these experiments is estimated to be 23 mm^2/s where 80 W/(m·K), 14.4 g/cm^3, and 0.24 J/(g·K) were the values used for k, ρ, and c_p respectively . The diffusivity of silicon on the other hand is 88 mm^2/s. By Equation 5.24 then, the thermal diffusion lengths over the course of a 150 fs pulse for WC-Co and Si are approximately 3.7 nm and 7.3 nm respectively – with WC-Co being about a factor of two smaller. Comparing the fluence used to machine the WC-Co (and therefore the amount of energy deposited in the sample) to that used in the Si experiment is difficult since only a small (and unknown) fraction of the laser pulse is used to create the cut face in WC-Co, but as in the case of the silicon processing, it is clear that the fluence used is well above the ablation threshold of the material. Thus, given the small HAZ observed in silicon and the difference in the thermal diffusion lengths of the two materials, it is not unreasonable to estimate the laser-induced damage layer in WC-Co to be on the order of 10 nm. Under the experimental conditions used to investigate the damage layer, it is unlikely that a 10 nm HAZ could be detected.

The damage layer induced during laser processing is well known to be a convolution of the processing conditions used and the material response to the laser heating, but here it has been shown that in two different material types, the Triple-Beam system's ultrashort pulsed laser can be used to accurately machine features with very little concomitant damage. This is relevant to three dimensional materials characterisation not only because damage induced during serial sectioning produces artefacts, but also because a small or non-existent damage layer makes the collection of multiple data types, such as electron backscatter diffraction (EBSD) and energy dispersive X-ray spectroscopy (EDS), more representative of the unperturbed sample. In fact, a large damage layer will prevent the ability to collect EBSD data.

Multi-modal data is important in 3D materials characterisation for at least two reasons. First, different data types provide different information about the material. The collection of secondary electrons provides topological information, backscattered electrons give information based on atomic number, EDS gives elemental information, and EBSD gives crystallographic information. Perhaps more importantly though, multi-modal data aids in what can be one of the most difficult and rate-limiting processes necessary to produce useful information from serial sectioning data: segmentation. Segmentation is the process of correlating each feature of inter-

est in the volume under study with every voxel associated with that object in the 3D representation of the volume. As part of this process, care must be taken to ensure that each 2D data file that makes up the 3D stack is oriented such that the data is consistent relative to the data in the neighbouring 2D data files. In other words, the data in one 2D data file must correspond spatially to the data in the 2D data files that both precede and follow it. In the absence of proper spatial registration of the data, artefacts and discontinuities arise and propagate, reducing the validity of the model. Furthermore, only once the data has been properly segmented can the microstructural characteristics that make up a volume be quantified using computational methods. Given the massive volume of data generated during 3D materials characterisation, segmentation is performed by computerised algorithms in all but the simplest of models. With more data types available as input during segmentation, more accurate and precise segmentation results in better reconstructions that provide more information.

In addition to its applicability across relevant length scales, the ready availability of multiple analysis techniques provided by the TripleBeam further illustrate its efficacy as a 3D materials characterisation platform. As already demonstrated in Figure 5.31, backscattered electron data can provide contrast based on the atomic number of a sample's constituent components. The EDS and EBSD capabilities of the system provide chemical and crystallographic data respectively. An example of the multi-modal capabilities of the instrument is given by Echlin et al. [136] who used the second ever TripleBeam system, developed in collaboration with our group[8], to reconstruct a 1.4×10^6 μm^3 polycrystalline nickel sample from both SEM and EBSD data. Using a different slicing method wherein the ablating laser is scanned normal to the surface to be analysed, they generated their data in 300 nm slices over a 250 $\times$ 75 μm area. Each slice required multiple passes with the laser, resulting in a per slice time of approximately 20 seconds. Early on, this same method was explored by the author and rejected due to the poor surface finish that results due to the Gaussian shape of the beam, especially on samples whose composite materials have different ablation thresholds. The homogeneity of the crystalline sample analysed by Echlin et al. likely provided an ideal case for the application of this method,

[8]While not listed as an author on the Echlin et al. paper, the author of this dissertation is acknowledged as a contributor.

and they make mention of possible refinements to their process for the purpose of improving surface roughness.

To better understand the impact laser processing has on the ability to collect EBSD data, a controlled experiment was performed in which a series of features were UPL machined into a single crystal (100) copper sample at a range of pulse energies and with both single and multiple shots per feature. EBSD was then used to study the crystal quality and orientation (30 keV, approximately 1 nA, 200 nm pitch). Figure 5.36 details the results where, in the top series of eight images, SEM micrographs of the features produced are shown, each labelled with the pulse energy and number of shots employed to produced it. The middle series of eight images are the corresponding electron backscatter pattern (EBSP) band contrast images. High band contrast is indicative of crystal quality and in these images, white pixels correspond to areas of high band contrast (good crystal quality), grey pixels correspond to an average crystal quality, and black pixels represent either poor quality crystalline structure or regions in which no Kikuchi patterns could be generated. Thus, this series serves as a qualitative guide to the eye, where lighter features indicate less damage and darker features indicate more damage. The final eight images again correspond to the eight SEM micrographs at the top of the figure, this time measuring the crystal orientation. Here, dark blue pixels are indicative of (100) crystal orientation, light blue pixels show off-axis (100) orientation, and white pixels are either other crystal orientations or regions in which no EBSP could be collected, suggesting amorphisation of the sample. Again, these images serve as a qualitative guide to the eye where the whiter the feature, the more likely the material is to be amorphous and therefore, to have been damaged by laser processing.

From this analysis, it is apparent that the greatest contributing factor in the ability to collect EBSD data in laser processed materials is the number of pulses used to create a feature. In fact, EBSP collected on features machined at high pulse energies compare well to ones machined at low energies as the long as the number of pulses used to do so is minimised. It is unclear at this point whether there is more actual damage induced in the sample by multi-pulse irradiation or if the poor EBSD results are a function of the increased surface roughness observed in these features. Nonetheless, it is clear that the operating parameters best suited to machining features in preparation for EBSD analysis involve the use of pulse

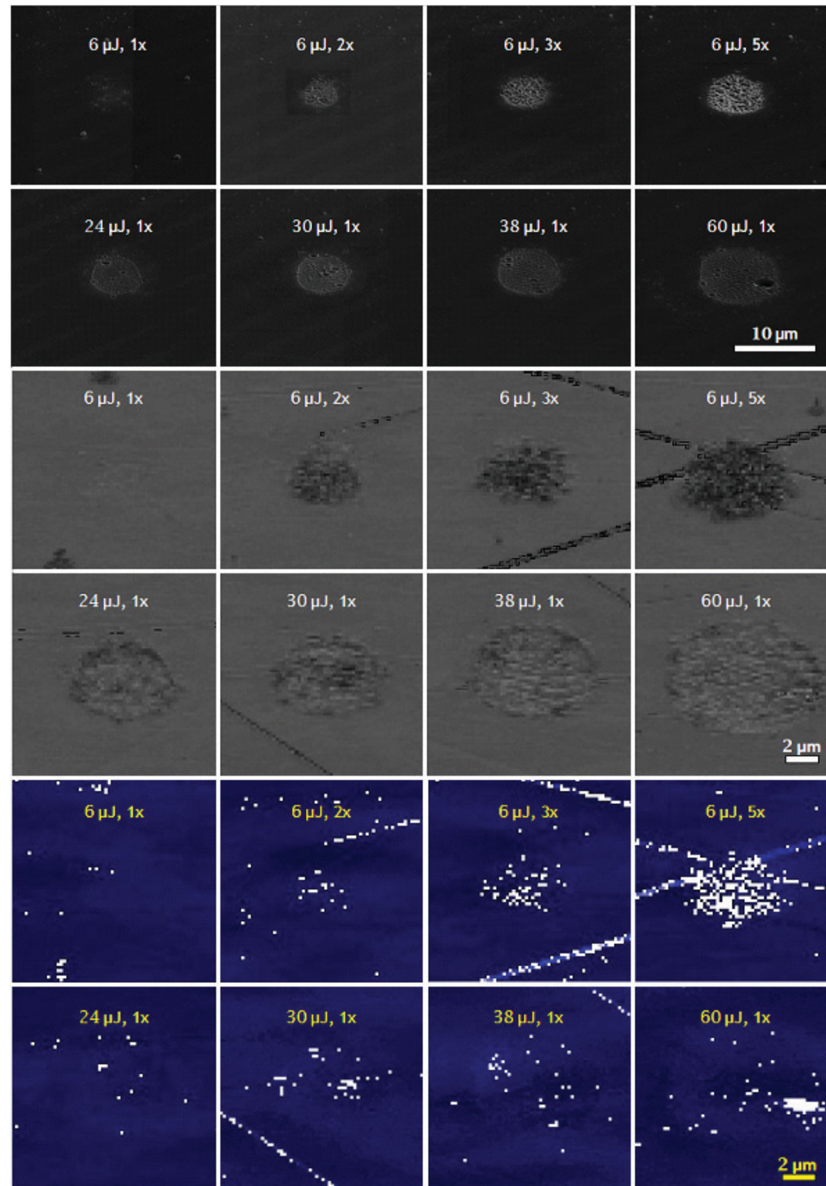

Figure 5.36. EBSD analysis of features laser machined at a range of fluences and with both single and multiple shots per feature. The top series of images are SEM micrographs of eight laser machined features. The top four were machined at the same low pulse energy, but with up to 5 pulses per feature. The next four were machined with only one shot each, but at a range of pulse energies. The middle series of eight images corresponds to the top eight SEM micrographs and measure the relative band contrast of the EBSP. Here, lighter features have qualitatively higher crystallinity than darker features. Thus dark features suggest regions that have been damaged by laser processing. The final eight images again correspond to the SEM micrographs, but this time measure crystal orientation. White regions are indicative of areas that have undergone amorphisation.

energies sufficient to produce the desired feature or surface in the fewest number of laser pulses. This corroborates behaviour observed during the processing of WC-Co where shark-finning was minimised when the cut face was prepared with as few laser passes as possible. Subsequent attempts to re-polish the cut face in order to eliminate the shark-fins altogether only exacerbated the effect.

5.8 Conclusion

In this chapter, the design and development of a new tool for materials processing and analysis was presented in detail. The fundamental components of the tool – a Ti:Sapphire, chirped pulse amplification, ultrashort pulsed laser and a DualBeam system – were reviewed and the theories of their operation detailed. While in the interest of time, the evolution of the design was only briefly mentioned, the final iteration of the component systems developed to integrate the two systems into a final TripleBeam instrument were discussed in detail. Most importantly though, results characterising materials in three dimensions were presented in order to illustrate the whole-greater-than-its-parts capability of the instrument to produce previously unachievable results. Indeed, the TripleBeam's ability to perform materials analysis on length scales ranging from tens of nanometres (via FIB) to hundreds of millimetres, combined with its multi-modal data collection capabilities, make it ideally suited to this task.

However, as suggested in the introduction to this chapter, the capabilities of the instrument extend beyond materials processing and rapid nano- or micro- prototyping. As a platform for exploring the interaction of light and matter, the TripleBeam's capabilities have only begun to be explored. In the next chapter, we bend the instrument to just this task, using it to explore a topic for which little literature currently exists; namely, ultrashort pulsed laser-induced surface chemistry. As part of this investigation, a previously unknown technique is reported which uses electron beam-induced deposition to template UPL-induced deposits, again demonstrating the synergistic potential of the TripleBeam as an experimental platform.

Chapter 6

Laser-Induced Surface Chemistry

6.1 Introduction and Background

CW and nanosecond pulsed laser-induced surface chemistry resulting in the deposition of metals (and less often, dielectrics) has been well researched and thoroughly characterised. Rytz-Froidevaux et al.[38], Houle[39], and Herman[40] have all produced good reviews of the technology. In general, the dissociation mechanisms by which laser-induced deposition proceeds are broken down into two categories, photolysis and pyrolysis. Typically, the characteristics of the system under study (i.e the substrate, precursor, laser wavelength, pulse characteristics, and experimental configuration) determine which of these processes dominates. Photochemical and catalytic dissociation are occasionally referred to in the literature, but are typically special cases of photolysis or pyrolysis.

One exception to this is the exotic photochemical process discussed by Houle wherein a molecule adsorbed to the surface of a doped semiconductor results in band bending and a shift in the Fermi level at the surface of the substrate. Upon illumination with photons of energy greater than the band gap, electron-hole pairs are created. Depending on the dopant type (n- or p-) and whether or not a bias is applied to the surface, one or both charge carriers can diffuse toward the molecule and drive dissociation – a process which is clearly neither photolytic nor pyrolytic. However, this dissociation mechanism is nearly exclusively attributed to etch processes, and it is mentioned here in the interest of being thorough and will not be discussed in more detail in this chapter.

While not discussed extensively in the literature, another interesting mechanism is plasmonic dissociation. Typically, plasmonic dissociation is thought to accompany photolytic dissociation when an amplification of the electric field of the laser due to plasmonic resonances in nanometre scale metal structures drives locally enhanced dissociation. For instance, Chen and Osgood [137] observed enhanced deposition of cadmium on nanoparticles of cadmium irradiated with a $\lambda = 257$ nm CW laser in a dimethyl cadmium (Me_2Cd) and argon atmosphere (1 and 1000 Torr respectively). On similarly sized nanoparticles of gold, normal deposition with no enhancement was observed. The structures deposited on the Cd nanoparticles had a characteristic elliptical shape, the long axis of which was aligned with the electric field, whereas this feature was absent on the Cd deposited on gold. That, and the fact that the lack of enhanced growth on gold can be explained by the absence of a plasma resonance at 257 nm, suggests that plasmonic dissociation is the mechanism responsible for the shape of the observed enhancement.

Both photolytic- and pyrolytic-mediated laser-induced deposition processes suffer from poor spatial resolution. The use of CW lasers to drive laser-induced deposition processes that rely on pyrolysis results in the diffusion of heat outside the focal region, effectively limiting the minimum achievable feature size. Photolytic processes typically use lasers that emit UV light where the photodissociation cross section of most molecules of interest is largest. Unfortunately, the efficacy with which UV radiation dissociates adsorbed molecules makes gas-phase dissociation more likely as well. The resulting over-spray that occurs as solids precipitate to the surface produces a smearing of the deposited feature, negatively impacting the ultimate achievable resolution. Because UPLs can achieve such high focal intensities, these lasers have demonstrated the ability to induced nonlinear effects in a variety of physical systems, particularly with regard to ablation. Their application to laser-induced deposition holds promise for improving the spatial resolution of these processes, particularly with regard to those processes driven by photolysis where wavelengths at which the precursor is transparent may be used to drive nonlinear dissociation only in the focal region of the laser. In spite of this, the application of ultrashort pulsed lasers to LID has received very little attention in the literature (see Chapter 2).

In this chapter, we report on novel, in situ TripleBeam experiments exploring the

use of ultrashort pulsed lasers for direct write laser-induced deposition. In addition, we demonstrate the synergistic potential of the TripleBeam system by highlighting a new technique for achieving high rate deposition of sub-diffraction limited features using the electron beam as a templating tool. A number of the effects observed are unreported elsewhere and will be fertile areas for future investigations. The discussion begins with a brief review of the physics of photolysis and pyrolysis.

6.1.1 Photolysis

Photolytically driven deposition involves the dissociation of surface adsorbed or gas-phase precursor molecules by the direct absorption of one or more photons. Energy transferred to the molecule by the photon or photons drives transitions between vibrational, electronic, and/or rotational states. Figure 6.1 shows the standard representation of the potential energy E of a molecular system versus its bond length r or internuclear distance where each horizontal line represents a vibrational state. When the energy of the molecule exceeds the dissociation energy E_d, the internuclear distance grows sufficiently large that the molecule becomes unstable and dissociates.

In the case of electronic excitation, photolytic dissociation can occur through a number of different pathways as illustrated in Figures 6.2(a) through (d) [38] where the upper potential energy curves are representative of the molecule with an excited electronic structure. In the pathway depicted in (a), dissociation occurs when an excited electronic structure makes the molecule inherently unstable, with no minimum value of the potential energy curve for finite values of r. In contrast, for the pathway shown in (b) the molecule is stable in its excited electronic state, but the energy imparted by $h\nu$ is higher than the excited state's point of stability (i.e. the continuum energy of the excited state) and the internuclear distance again grows sufficiently large for dissociation to occur. In (c) and (d), the excited states are stable and the energy imparted by $h\nu$ is lower than the continuum energy of these excited states, but either through collisions with other molecules or interactions with a surface, the energy curves are coincident with potential energy curves that have a dissociation pathway (shown in red) at the energy level to which the molecule has been promoted. In the case of the pathway illustrated in (c), the overlapping pathway is unstable. In (d), the continuum energy of the coincident pathway is

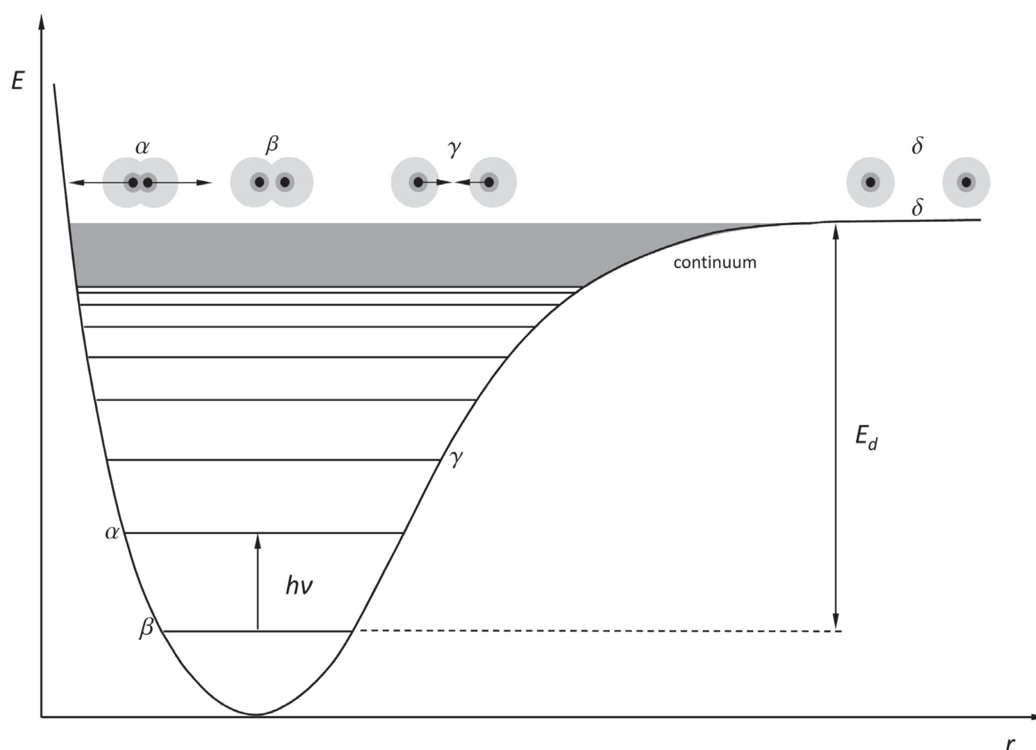

Figure 6.1. Potential energy versus internuclear distance of the vibrational states (horizontal lines) of a molecular system. In photolysis, a molecular system gains energy through the absorption of one or more photons of energy $h\nu$. When the vibrational energy of the system reaches the continuum and exceeds the dissociation energy E_d, the molecule is no longer stable and dissociation occurs, as illustrated schematically by the diatomic systems shown across the top of the figure (the arrows indicate the direction of the interatomic forces).

smaller than $h\nu$.

Because photolysis involves the direct absorption of a photon or photons by the molecule itself and not by the substrate, photolytic laser-induced deposition is typically "substrate independent." This is not to imply that the substrate is irrelevant to the process. As shown in Figures 6.2(c) and (d), surfaces can provide pathways for dissociation not available to molecules in the gas phase. Furthermore, chemisorbed and/or physisorbed molecules can have a higher absorption cross section than gas-phase molecules. In this context, "substrate independent" simply means that photons absorbed by the substrate do not play a role in the dissociation process. As a result, for a system driven by photolysis, deposition can occur on

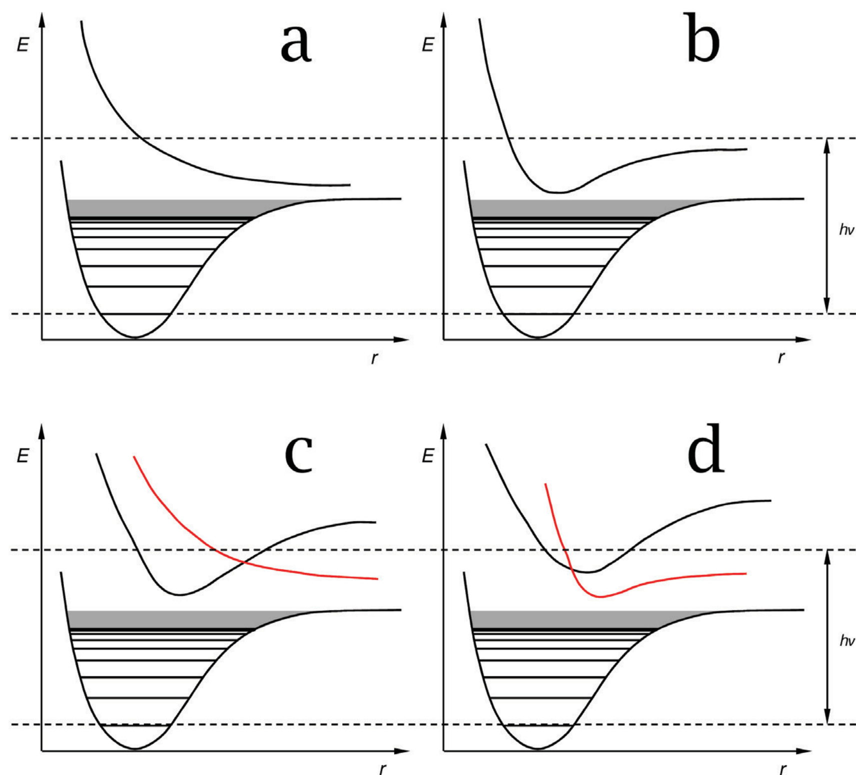

Figure 6.2. Pathways for dissociation of molecules with photo-excited electronic structures. In (a), the molecule is unstable in its excited state. For (b), the excited state is stable, but the energy imparted by the photon ($h\nu$) is higher than the continuum energy of the excited state. The excited states in Figures (c) and (d) overlap states that provide a pathway to dissociation (shown in red) at the energy level achieved through absorption of $h\nu$. These scenarios typically involve interactions with surfaces or collisions with other molecules.

substrates which are transparent to the dissociating photon.

6.1.2 Pyrolysis

pyrolysis, on the other hand, is highly substrate dependent. During pyrolytically driven laser-induced deposition, photons are absorbed by the substrate, leading to a local increase in temperature. Precursors adsorbed to the surface in the neighbourhood of the laser heating consequently undergo dissociation. Alternatively, molecules in the gas-phase, but near the surface, can be dissociated by convective

heat transfer. Thus, the absorption characteristics and thermal properties of the substrate, as much as the dissociation energy of the precursor, determine whether a pyrolytic process can occur.

Sample heating due to laser irradiation is a complex process. Given a surface heated by a focused laser beam having a Gaussian intensity profile such that

$$I(r) = I_0 \exp\left(\frac{-2r^2}{w_0^2}\right) \tag{6.1}$$

where I_0 is the peak intensity, and w_0 is the $\frac{1}{e^2}$ spot radius at the waist of the beam, the rise in temperature ΔT is given by

$$\Delta T(r, z, W) = \frac{P(1-R)}{2\pi^{1/2} w\kappa} N(r, z, W) \tag{6.2}$$

where $W = \alpha w$, α is the absorption coefficient, w is the laser spot size, P is the beam power, and R is the reflectivity of the substrate at the laser wavelength, and κ is the thermal conductivity of the substrate. $N(r, z, W)$ is an integral expression describing "the reduction of temperature rise caused by finite penetration" [138]. For the limiting case of when the absorption depth is much smaller than the laser spot size (i.e. $1/\alpha \ll w$), $N(0, 0, W) = 1$ as $W \to \infty$ giving a maximum temperature rise at the surface of

$$\Delta T_{surface} = \frac{P(1-R)}{2\pi^{1/2}\kappa w} \tag{6.3}$$

assuming that the reflectivity and thermal conductivity of the substrate do not change with temperature.

While this very simple approximation holds for some cases of CW laser heating, it yields wildly inaccurate results when applied to substrate heating due to ultrashort pulses. The physical processes involved in ultrashort pulse absorption and the coupling of energy to the lattice is complex, depending on numerous factors including material type (i.e. conductor, semiconductor, dielectric, biological, etc.), substrate geometry, pulse duration, and pulse wavelength. The topic of heating in materials illuminated by UPLs has received significant attention in the literature and many models have been developed for a range of specific cases [139, 140, 141, 142, 143, 144, 145, 146, 147, 148]. One particularly straight forward treatment is provided by Dadap et al. [149], where they calculated the temperature rise due to

single and multiple ultrashort pulse irradiation of a semi-infinite slab of silicon by solving the thermal diffusion equation:

$$\frac{\partial T}{\partial t} = \kappa \nabla^2 T + T_0 \sum_{n=0}^{N-1} \delta \left(t - \frac{n}{f} \right) R(r, t = 0) Z(z, t = 0), \quad \text{for } z \geq 0,\ r \geq 0 \quad (6.4)$$

where T is the temperature, κ is the thermal diffusivity, N the number of laser pules, f the repetition rate of the laser, $\delta\left(t - n/f\right)$ is a delta function representing the arrival of the pulse, and T_0 is the rise in surface temperature due to a single pulse given by

$$T_0 = \frac{\phi\alpha(1 - R)}{\rho C} \quad (6.5)$$

where ϕ is the fluence of the laser, and R, α, ρ, and C are the reflectivity, absorption coefficient, density, and heat capacity of the substrate, respectively. In Equation 6.4

$$R(r, t = 0) = \exp\left[- \left(\frac{r}{r_0} \right)^2 \right] \quad (6.6)$$

is the radial temperature distribution (where r_0 is the beam radius) and

$$Z(r, t = 0) = \exp\left(-\alpha z\right) \quad (6.7)$$

is the surface normal temperature distribution. As in Equation 6.5, α is the absorption coefficient of the substrate material at the laser wavelength. To find a solution, Equation 6.4 is subject to the boundary conditions

$$\frac{\partial T}{\partial t} = 0, \quad \text{for } z = 0 \text{ and } t > 0. \quad (6.8)$$

In order for Equation 6.4 to be valid, a number of conditions have to be met. Namely, the mean free path of phonons within the material must be much smaller than the absorption depth of the laser ($\approx 10\ \mu$m for $1/e$ attenuation), κ should be independent of temperature, and the time scale of κ must be much shorter than the time it takes for the lattice to heat.

The single pulse ($N = 1$) solution to Equation 6.4 is

$$
\begin{aligned}
T(r,z,t) =& \frac{T_0}{2}\left\{\exp\left(-\alpha z + \frac{t}{\tau_z}\right) \times \mathrm{erfc}\left(\sqrt{\frac{t}{\tau_z}} - \frac{\alpha z}{2}\sqrt{\frac{\tau_z}{t}}\right)\right\} \\
& \times \left\{\frac{s}{s+\frac{t}{\tau_z}} \exp\left(-\frac{s}{s+\frac{t}{\tau_z}}\frac{r^2}{r_0^2}\right)\right\}
\end{aligned}
\tag{6.9}
$$

where $\tau_z = (\alpha\kappa)^{-1}$ is the thermal diffusion time scale and $s = (\alpha r_o/2)^2$ is a dimensionless parameter describing the initial thermal profile. Extending this model to the steady state case where $N \to \infty$ underestimates the rise in temperature of the sample due to the semi-infinite model of the substrate used. To describe laser heating of a finite sample, Dadap et al. restricted their analysis to multi-pulse heating on a time scale much larger than that required for heat to diffuse across the thickness L of the sample. They further restricted their model to samples having lateral dimensions much larger than their thicknesses. Making these assumptions, they could focus their analysis along the radial dimension, effectively eliminating the z variable. To still further simplify the model, they approximate a CW source by requiring that $f \gg \tau_z^- 1$ and replacing the peak intensity I_0 of the laser with the average intensity I_{CW} such that

$$
I_{CW} = I_0 f \tau_p \tag{6.10}
$$

where the product of the laser repetition rate f and the pulse duration τ_p is essentially the duty cycle of the laser. If the laser is turned on at time $t = 0$, the sample heating over a circular area with a radius of $a \gg r_0$ is given by

$$
\begin{aligned}
T_{CW}(r,t) =& T'_{CW}\frac{1-\exp(\alpha L)}{\alpha L}\frac{r_0^2}{a^2}\left\{\frac{1-\exp(-\kappa K_{loss}^2 t)}{\kappa K_{loss}^2}\right. \\
& \left. + \sum_{n=2}^{\infty}\frac{J_0\left(\frac{\beta_{0n} r}{a}\right)\exp\left(\frac{-\beta_{0n}^2 r_0^2}{4a^2}\right)}{[J_0(\beta_{0n})]^2}\left(\frac{1-\exp\left[-\kappa\left(K_{loss}^2+\frac{\beta_{0n}^2}{a^2}\right)t\right]}{\kappa\left(K_{loss}^2+\frac{\beta_{0n}^2}{a^2}\right)}\right)\right\}
\end{aligned}
\tag{6.11}
$$

where T'_{CW} is the heating rate from the laser given by

$$
T'_{CW} = \frac{I_{CW}\alpha(1-R)}{\rho C} \tag{6.12}
$$

and $J_0(\beta_{0n} r/a)$ is the zeroth-order Bessel function, β_{0n} is the nth root of its derivative with respect to r, and K_{loss} is an added heat loss parameter.

Dadap et al. used this model to illustrate an interesting dependency of sample temperature on laser repetition rate. They calculated the single shot and steady state heating of a silicon sample from an ultrashort pulsed laser having a wavelength of 800 nm at different fluences and repetition rates. A subset of their results is shown in Table 6.1. Notice that for high repetition rate, low fluence pulses, the steady state sample heating can be significantly higher than for cases in which much higher fluences, but lower repetition rates are used.

Wavelength [nm]	Fluence [mJ/cm^2]	Repetition Rate [Hz]	Single Pulse Heating [K]	Steady State Heating [K]
800	0.3	10^8	0.1	65
800	10	10^5	4	3

Table 6.1. Single pulse and steady state sample heating results modelled using different laser fluences and repetition rates. Low single pulse fluences can result in higher sample temperatures than pulses much larger fluences, given that the low fluence pulses are delivered at sufficiently high repetition rates.

Thus, we can see that pyrolysis depends on the complex interdependence of the sample properties, the laser parameters, and the precursor. However, if we assume that the reflectivity and thermal conductivity of the substrate do not change with temperature, that the deposit is small, and we further neglect any diffusion and/or desorption of the precursor and limit our analysis to the centre of the temperature distribution, we can approximate the deposition rate by an Arrhenius law dependency on surface temperature such that

$$R(T) = R_0 \exp\left(\frac{E_a}{k_B T}\right) \tag{6.13}$$

where R_0 is proportionality constant, E_a is the activation energy, and k_B is Boltzmann's constant.

However, while the rate of a pyrolytic process is mainly driven by the surface temperature, the flux of precursor molecules into and out of the reaction zone due to diffusion and desorption play a significant role in the actual rate of deposition. Sophisticated models have been developed that take into account these factors and others, including the temperature dependence of substrate properties, the radial

and depth distributions of the temperature, non-uniformly and transiently heated substrates, and material discontinuities. The interested reader is directed to the reviews mentioned at the beginning of this chapter for references.

Finally, it should be noted that the dominant mechanism responsible for a deposition can change during the course of the process. For instance, a deposition may start as a photolytic process, but change to a pyrolytic one as the deposit itself absorbs laser energy and heats up. In general, the rates of pyrolytic deposition are faster and the depositions are more pure than for photolytic deposition.

6.2 Instrumentation: A Note on Gas Delivery

Unlike the work described in Chapters 3 and 4, the majority the work described here was performed in the TripleBeam system[1]. In its current configuration, the laser enters the TripleBeam opposite the gas injector system. During laser processing, the sample is typically tilted so that the sample surface is normal to the incident beam. In this position, the sample faces away from the GIS making it impossible to deliver gas to the surface in the normal fashion (i.e. through the GIS needle directly). To overcome this shortcoming in the system's geometry, a custom sample stub was fabricated having an integral gas delivery system as shown in the inset in Figure 6.3. This gas delivery system consists of a hollow needle mounted to a standard 0.5 inch sample stub with vacuum compatible conductive epoxy. The 0.5 inch stub is typically circular, but was cut along a chord of the circle to form a flat edge, providing clearance for the outlet of the needle to be brought close to the sample surface. By mounting the needle to the stub at an angle and grinding flat the bottom edge of the outlet side, the portion of the needle through which the gas is delivered was made to lie directly on the sample. The top edge of the needle's outlet was also ground back to prevent it from shadowing the electron beam.

The post normally used to fix the sample stub to the stage was cut short and a hole was drilled into a 1 inch stub to accommodate it. In this way, a sample and the 0.5 inch stub, with the needle now attached, can be affixed to the 1 inch stub with carbon tape such that the outlet of the needle rests on the sample. A copper

[1]Early attempts to induce deposition described briefly in the next section were performed in the set up described in Figure 3.1

tape strap is placed near the end of the needle to ensure its position remains fixed during stage moves. Once the entire assembly is attached to the system stage, one end of a Viton tube is connected to the inlet of the needle and the other attached to the outlet of the GIS, allowing for the delivery of gas from the GIS to the sample. The GIS is run manually from the user interface of the TripleBeam.

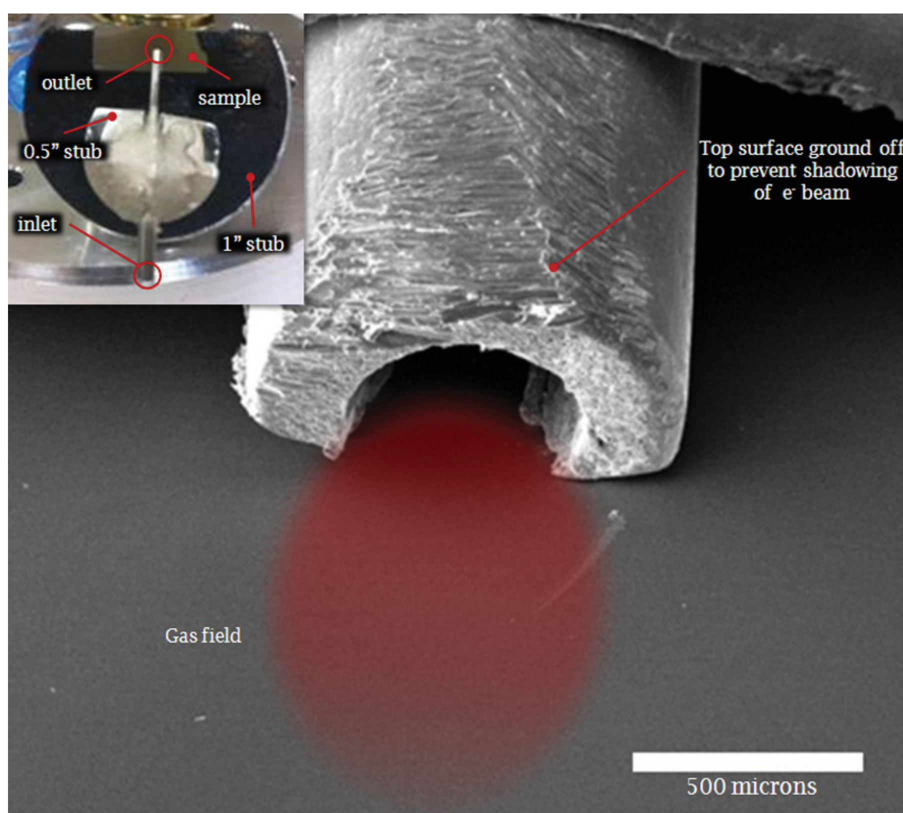

Figure 6.3. On-stub gas delivery assembly. The inset shows the entire assembly as described in the text. The approximate gas field is represented by the red oval at the outlet of the delivery needle.

When a GIS is used to deliver gas in the standard fashion, the GIS needle is brought close to the sample, but remains physically separate. The GIS needle's location in space is fixed, while the sample is moved beneath it. Using the custom configuration as described above, the usable sample area is limited by the fixed nature of the gas delivery. Figure 6.3 shows an electron micrograph of the outlet end of the needle as configured on the custom system. The red oval shows approximately the extent of the gas delivery and, by extension, the area usable for performing deposition experiments.

Care was taken to calibrate the gas field prior to performing laser-induced deposition experiments. This was done by performing a series of electron beam-induced platinum depositions using (trimethyl) methylcyclopentadienylplatinum ($Pt(MeCp)Me_3$) as a precursor across the gas field. Three separate depositions were made for each of seven different e-beam doses. The location of each deposit was randomised with respect to its location in the gas field. The height of each deposit was then measured by a Digital Instruments 3100 AFM in tapping mode. Figure 6.4 shows the results. The nearly linear trend exhibited at deposition times greater than 20 seconds shows that in the area investigated, the gas field is uniform to within the standard deviation of our ability to measure deposition rate.

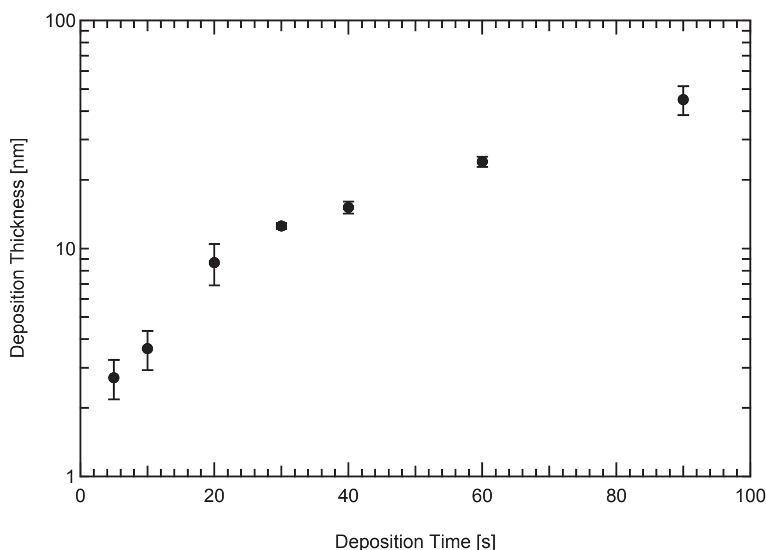

Figure 6.4. To calibrate the gas field produced by the custom, on-stub gas delivery assembly, the deposition rate was measured at twenty-one randomised locations within the field. The trend reveals a gas field with good uniformity.

6.3 Experimental Background

Early attempts to induce deposition using an ultrashort pulsed laser were performed primarily on silicon using high pressures (5 to 10 Torr) of tetrakis (trifluorophosphine) platinum ($Pt(PF_3)_4$) as a precursor. The experiments were performed in the ex situ cell detailed in Figure 3.1. The results of these experiments were largely disappointing yielding uncontrolled, delocalised depositions typically occurring in

regions where ablation had occurred first. In addition, the morphology of the deposits was often odd and results were difficult to reproduce. On the occasion when an experiment did yield deposits that merited analysis, EDS analysis showed relatively low concentrations of fluorine and phosphorous relative to typical EBID. Interestingly, the F and P content was seen to increase with distance from the focal area of the beam, possibly suggesting a pyrolytic process wherein fluorine and phosphorous compounds were volatilised more thoroughly at locations in which the change in surface temperature was greatest. However, little follow up analysis was performed simply due to the experimental difficulties encountered.

One interesting side note, however, is the result of an experiment performed in 10 Torr of $Pt(PF_3)_4$ at laser powers between 300 and 500 μW in 25 μW increments. The laser was focused 200 μm above the surface of a silicon sample with a 20× (NA = 0.40) Mitutoyo Plan Apo, infinity corrected, near infrared microscope objective for 10 minutes at each power, each time over a different region of the sample. Three data points were collected at each power. The result was a series of highly dendritic pillars or clusters of pillars approximately 10 to 50 μm tall, representatives of which are shown in Figure 6.5. Given that the fluence was calculated to be quite low at the sample surface (15.3 mJ/cm^2 at 300 μW and 25.5 mJ/cm^2 at 500 μW), it's not unreasonable to attribute this result to the dissociation of the precursor in the gas phase. The precipitation of solids out of the gas phase may further explain the stacking morphology of the deposits. EDS analysis showed that the deposits had lower fluorine and phosphorous content than is typical of EBID. The repeatability of the technique was good with 21 out of 24 attempts forming deposits, though the morphology was markedly varied from deposit to deposit.

With the development of the TripleBeam system, the ability to perform controlled laser-induced surface chemistry experiments is greatly improved. In particular, the ability to capture real-time, high resolution images of the sample enables far better control of the beam alignment and focus. In addition, being able to immediately image and analyse the results of each experiment without breaking vacuum or transferring the sample to another instrument significantly increases the time to data. Finally, and perhaps most importantly, the unique integration of technologies provided by the TripleBeam enabled the discovery of a new process that would likely have gone unrealised had the experiments been performed on separate instruments.

Figure 6.5. Dendritic Pt structures formed via LID of $Pt(PF_3)_4$. The laser power used to for the left structure was 350 μW, while for the right structure it was 400 μW. It is likely that dissociation occurred in the gas-phase, suggesting a photolytic dissociation mechanism.

The initial laser-induced deposition (LID) work performed on the TripleBeam involved the use of dicobalt octocarbonyl ($Co_2(CO)_8$) as a precursor for cobalt deposition and it was found that very pure laser-induced cobalt deposition is relatively easy to achieve. However, the results presented in the rest of this chapter were achieved using (trimethyl) methylcyclopentadienylplatinum ($Pt(MeCp)Me_3$) as a precursor for platinum deposition. The motivation for using this particular precursor as a test platform is that it provides for more contrast (with respect to deposit purity) relative to EBID than $Co_2(CO)_8$ does, since both EBID and LID produce very pure cobalt deposits. EBID of platinum using $Pt(MeCp)Me_3$, on the other hand, produces relatively low purity deposits ($\approx$15 to 20% Pt), making any improvement gained via LID easier to detect.

6.4 LID: Procedure and Results

Using the TripleBeam system, laser-induced platinum deposition was attempted on a number of different substrates including gold, platinum, carbon (graphite), clear glass, and black glass. The gold samples were custom made four-point probe test beds and consisted of 250 nm gold films evaporatively deposited onto 300 to 500 nm of SiO_2 thermally grown onto a silicon substrate. The platinum samples were pure, uncoated platinum foil and the graphite was harvested from a standard EM-grade

carbon specimen mounts[2]. The clear glass was cut from an optical grade quartz (SiO_2) microscope slide and the black glass from an ND filter with an optical density of 2.0. With the exception of the graphite, the samples were all ultrasonically cleaned in acetone (10 min.), isopropyl alcohol (10 min.), and ultrapure water (5 min.), dried with nitrogen, then baked at 200°C for 2 hours or more. For each substrate, the scan parameters used were identical – namely, the laser was scanned over a predefined area in a serpentine pattern of overlapping lines at a rate of 1000 μm/s. Between lines, the beam was stepped 2 μm. The direction of the scan alternated from horizontal to vertical with every other pass over the scan area. The number of passes was typically varied, but each material received up to 500 passes. To focus the laser, a 3× ThorLabs anti-reflection coated (800 - 1100 nm) telecentric scan lens was filled with a 5 mm diameter beam. This lens has a flat image plane, ensuring a consistent spot size over a 2 × 2 mm scan field[3]. The nominal spot diameter achievable using these focusing conditions is approximately 35 μm. The laser power used to induce deposition varied from substrate to substrate. On substrates with lower ablation thresholds (i.e. Au and Pt), the power was lowered to prevent ablation. In fact, great care was taken to use fluences well below the ablation threshold of the material. Typically, the power was considered sufficiently low if no ablation occurred during three minutes of unscanned irradiation of the sample. Table 6.2 lists the power delivered to each sample. Finally, no electron beam irradiation of the deposit area was performed while the gas was flowing. Furthermore, no electron imaging was performed for at least 30 minutes after the gas flow had been stopped in order to unambiguously attribute any observed results to laser induced deposition rather than EBID.

With the exception of clear glass, deposition was observed on all substrates tested. Though they varied, rates were typically very low and were not directly measured in these experiments. Qualitatively though, deposition on black glass and carbon was observed after far fewer laser passes than deposition on Au and Pt. To

[2]Carbon specimen mounts are made from spectrographically pure graphite rods in which the total impurity level does not exceed 2 ppm.

[3]The vendor specified scan field for this lens is 14 mm × 14 mm, but due to the long distance between the scan mirror and the entrance pupil of the lens and the subsequent reduction in the input angle, only the reported field dimensions could be achieved. This is, however, more than sufficient given the requirements of these experiments.

Substrate	Laser Power [μW]	Result	Qualitative Rate
Au	115.9	Deposition	Higher than Pt
Pt	121.4	Deposition	Lower than Au
C	207.4	Deposition	Higher than Au
Black Glass	195.2	Deposition	Higher than Au
Clear Glass	108.8 to 817.4	No Deposition	–

Table 6.2. Substrates, laser powers, and results of attempted LID.

reiterate, no deposition was observed on clear glass.

EDS analysis was performed on the deposits formed on Au and black glass and the results are reported in Figures 6.6 and 6.7. Figure 6.6 compares EDS analysis of laser-induced deposition of platinum on gold to a reference spectrum taken on gold alone (no LID Pt) and a spectrum of platinum deposited via EBID with a 5 keV electron beam on a silicon substrate. All EDS spectra were captured with a 20 keV beam. Because there were no peaks in common to all three signals, the data were normalised to the background at 3.5 keV. With reference to the "LID Pt" data shown in the figure, a clear platinum signal can be seen, particularly at energies corresponding to the Lα^1, Lβ^1, and Lβ^2 lines for Pt. The Pt Mα line is very close to the Au Mα line, and as a result, the presence of platinum is seen as a shift of the "LID Pt" curve toward the Pt Mα line relative to the "EBID Pt" data. While it has been established that it is indeed platinum that was deposited, the most noteworthy feature of this data is the near absence of a carbon signal in the platinum on gold data. By comparison, the EBID platinum has a significant carbon Kα peak. While not a quantitative assessment of the purity of the deposit, the data do lead to the conclusion that LID deposited on gold is more pure (i.e. contains less carbon) than EBID platinum deposited on silicon[4]

The EDS analysis of the LID deposition on black glass yields considerably different results. As seen in Figure 6.7, a Pt Mα peak is again observed, this time without the obfuscation of the gold line. Silicon and oxygen Kα lines are also observed, as expected from a deposit on glass. Note, however, the strong carbon Kα

[4]The strong Si Kα line observed in both the "Au Only" and the "LID Pt" data is due to the silicon/silicon dioxide substrate on which the gold was deposited.

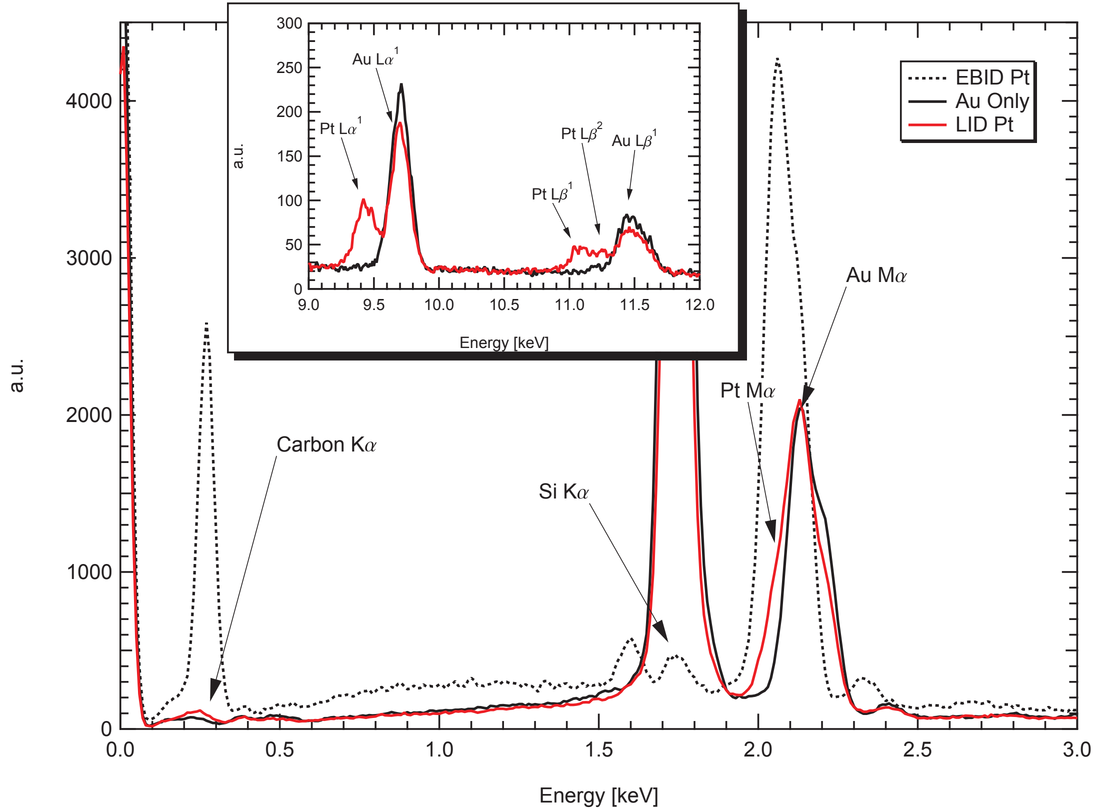

Figure 6.6. A comparison of EDS analysis of laser-induced platinum deposition on gold to a reference spectrum taken of gold without laser-induced platinum deposition and a spectrum of platinum deposited via EBID. The absence of a significant carbon signal in the LID Pt spectrum suggests purity greater than EBID Pt. The arbitrary units (a.u.) designation on the y-axis is a product of the normalisation process.

peak in the "LID Pt" signal[5]. Again, while these data don't reveal the relative quantity of carbon in the LID deposited Pt, they do suggest qualitatively a much high carbon content than that observed in the LID Pt deposited on gold and likely a higher content than that typically observed for electron beam-induced deposition of platinum.

Beyond the relative purity of the deposits, perhaps the most notable difference observed across these experiments were differences in deposit morphology. Depositions induced on both Au and Pt demonstrated marked periodicity and coherence, while depositions induced on carbon and black glass did not. Figure 6.8 are micro-

[5]The observant reader will note a broadening of the carbon peak in the LID Pt data. This is likely due to the presence of boron, whose Kα line is at 0.183 keV.

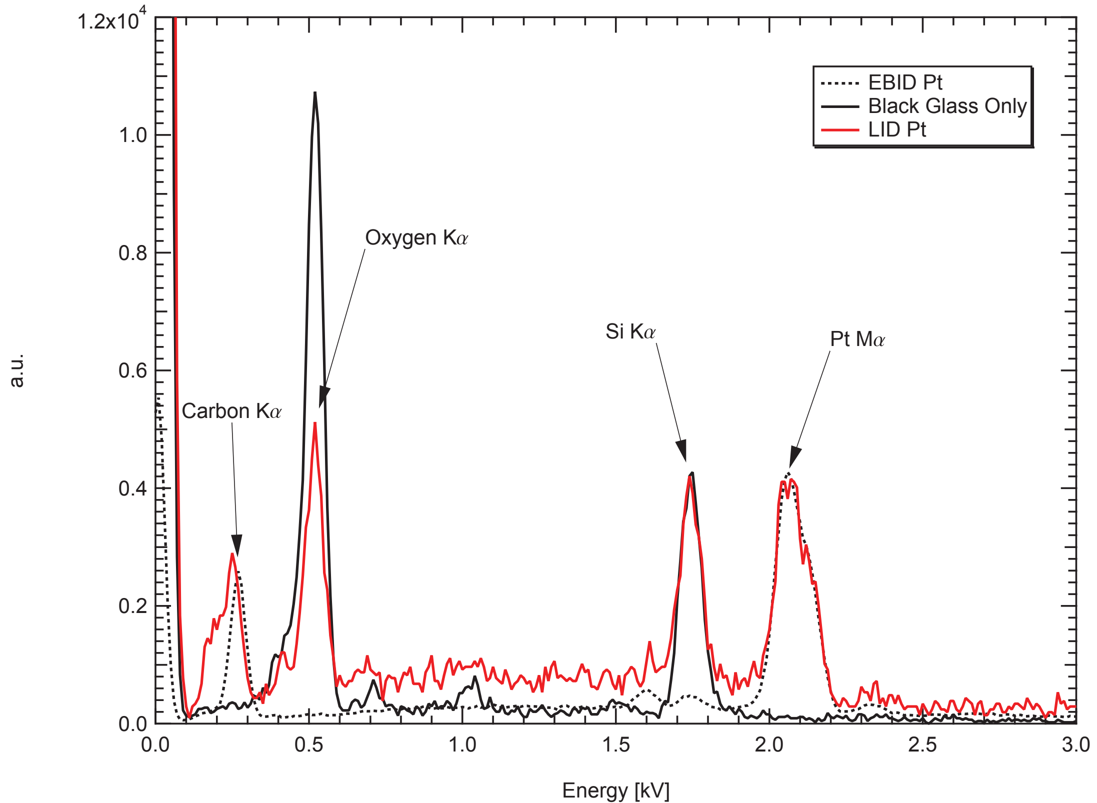

Figure 6.7. A comparison of EDS analysis of laser-induced platinum deposition on black glass to a reference spectrum taken of black glass with no laser-induced platinum deposition and a spectrum of platinum deposited on silicon via EBID. The strong carbon signal observed in the LID Pt spectrum suggests a much high carbon content than that observed in the LID Pt deposited on gold and likely a higher content than that typically observed for electron beam-induced deposition of platinum.

graphs illustrating these differences on gold (a) and black glass (b). The orientation of the polarised electric field of the laser beam is indicated by the white arrow.

While these experiments failed to produce results as dramatic as those reported by Haight et al. [41] in which 100 nm chromium lines were deposited using $\lambda =$ 400 nm, 120 fs pulses to photolytically dissociate $Cr(CO)_6$, there are still some interesting observations to be made from these results. First, it should be recognised that the fact that deposition occurred on the black glass and carbon, but did not occur on the clear glass is evidence of a pyrolytic dissociation process. Both carbon and the black glass are good absorbers of 775 nm light[6]. SiO_2, on the other

[6]The black glass is an ND filter and is designed to have a flat absorption curve over a broad

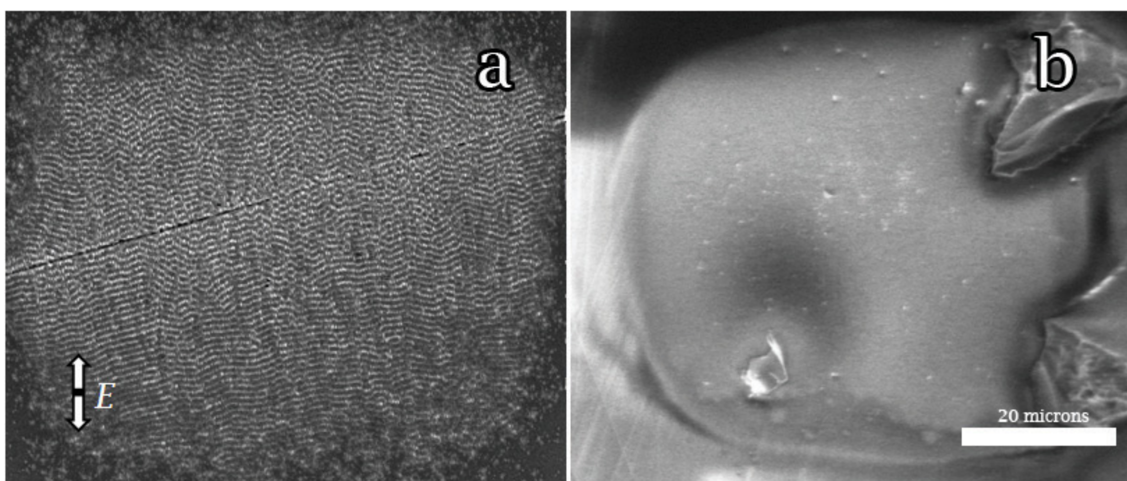

Figure 6.8. Ultrashort pulsed laser-induced platinum deposits of using Pt(MeCp)Me_3 as the precursor. Figure (a) is on a gold substrate, while the deposit in figure (b) is on black glass. Note the difference in morphology. The arrow in the lower left hand corner shows the direction of the polarised electric field of the incident laser.

hand, absorbs very little light at 775 nm[7]. The fact that deposition occurred on the absorbing mediums, but not on the transparent one would seem to rule out a photolytic effect in favour of one driven by substrate heating. The qualitatively observed high(er) deposition rate seems to further support this conclusion.

However, since gold is even more reflective at 775 nm[8] than quartz is transparent, gold should undergo very little heating at this wavelength. Thus, the observation of LID on gold would seem to argue the case for a different dissociation mechanism driving LID on gold. The marked difference in the carbon content observed via EDS analysis provides still further evidence for separate dissociation mechanisms for LID on gold versus on black glass. Typically, though, one would expect depositions produced through pyrolytic processes to have higher purity than those resulting from other dissociation mechanisms [40]. However, at low temperatures, pyrolysis is a far less efficient process than it is at high temperatures. Given the low fluence (20 mJ/cm^2) and the low repetition rate (1 kHz) of the laser used to form these deposits, combined with the strong dependency of the steady state surface temper-

range of wavelengths.

[7]SiO_2 is approximately 92% transmissive at 775 nm.

[8]Gold is approximately 95% reflective at 775 nm.

ature on repetition rate[9], it is likely that any pyrolytic process driving dissociation under these conditions is a low temperature one.

Nonetheless, while pyrolysis is unlikely responsible for the the result observed on gold, the clear inability to induce photolysis on quartz at a range of laser fluences (see Table 6.2), makes a photolytic process equally unlikely. Furthermore, the periodicity of the deposit seems to suggest that the deposition is in some way mediated by the laser's electric field. To help resolve this conundrum, we turn to the literature.

A significant body of literature exists exploring the formation of laser-induced periodic surface structures (LIPPS) [126, 127, 128, 129, 130, 131, 132, 133, 134, 135]. The majority of this work focuses on the formation of wavelength and sub-wavelength scale ripples formed via the removal or reordering of material at the substrate surface during short and ultrashort pulsed laser irradiation. However, Brueck and Ehrlich observed similar structures during "UV laser *photolysis* of organometallic molecular gases near a substrate surface"[150] (emphasis mine). Most authors now attribute the formation of LIPSS to surface plasmons generated by and interacting with the incident laser radiation.

Plasmons are quanta of oscillations induced when free charge carriers in a plasma are driven by an oscillating electric field. In a conducting medium, plasma oscillations result in density waves of carriers typically referred to as "Langmuir waves." Thus, plasmons are the quasi particles resulting from the quantisation of such plasma waves. In metals, the movement of loosely bound electrons relative to their their associated ions can be driven by the electromagnetic field of incident light. In fact, the optical properties of metals are dictated by the response of surface plasmons to the field. Given a density of free electrons N having charge e and mass m, the plasma frequency ω_p of a metal is given by

$$\omega_p^2 = \frac{Ne^2}{\epsilon_0 m} \tag{6.14}$$

where ϵ_0 is the relative permittivity of the free space. If the frequency of light incident on the surface of a metal is below the metal's plasma frequency, electrons in the metal screen the incident field and the light is reflected. If the frequency of the light is higher than ω_p, the electrons cannot respond quickly enough to screen the field and the light is transmitted. The plasma oscillations responsible for these

[9]As demonstrated by Dadap et al. [149] and discussed in detail in Section 6.1.2.

effects are referred to as surface plasmons. Longitudinal oscillations known as bulk plasmons are also possible, but because the the electric field of incident photons is transverse, bulk plasmons cannot be excited by light.

According to Huang et al.[135], surface plasmons generated when an ultrashort pulse impinges on a metal surface interfere with the incoming laser irradiation. As with all interference phenomena, the principle of superposition applies leading to regions of field enhancement due to constructive interference and regions where destructive interference cancels the field altogether. Given a laser pulse of sufficient fluence, the interference pattern induces permanent ripples on the sample surface, the net result being the formation of LIPPS whose orientation is always perpendicular to the polarisation of the electric field. The superposition of the laser's electric field and the field of the laser-induced surface plasmon produce a resultant vector $\mathbf{G}$ given by

$$\mathbf{G} = \mathbf{k_i} - \mathbf{k_s} \tag{6.15}$$

where $\mathbf{k_i}$ and $\mathbf{k_s}$ are the wave vectors of the incident laser radiation and the surface plasmon respectively and $|\mathbf{k_x}| = 2\pi/\lambda_\mathbf{x}$ where x=i,s. For any arbitrary incident angle θ defined as the angle $\mathbf{k_i}$ makes with the surface normal, the wavelength Λ of $\mathbf{G}$ is given by

$$\Lambda = \frac{\lambda_i}{\frac{\lambda_i}{\lambda_s} \pm \sin\theta} \tag{6.16}$$

which is also the period of the LIPSS. Thus, for an incident laser with $\mathbf{k_i}$ normal to the surface, θ is zero and $\Lambda = \lambda_s$. Furthermore, λ_s can be calculated from the frequency dependent, complex dielectric constant such that

$$\lambda_s = \lambda_i \left(\frac{\epsilon_1 + \epsilon_d}{\epsilon_1 \epsilon_d} \right)^{1/2} \tag{6.17}$$

where ϵ_d is the dielectric constant for the dielectric at the surface interface (i.e. for free space, $\epsilon_d = 1$) and ϵ_1 is the real part of the frequency dependent, complex dielectric constant

$$\epsilon(\omega) = \epsilon_1(\omega) + i\epsilon_2(\omega). \tag{6.18}$$

For metals, ϵ_1 is negative, so $\lambda_s = \Lambda$ is always some fraction of the laser wavelength, λ_i.

Analysis of the laser-induced platinum deposition on gold shown in Figure 6.8 suggests that surface plasmons play a role in the formation of the coherent pattern observed. Direct measurement of the period of the pattern Λ yields a value close to the wavelength of the laser. Given that λ_s is calculated from Equation 6.17 to be $0.98\lambda_i$,[10] this is consistent with a model of surface plasmon interference with a laser at normal incidence where $\Lambda = \lambda_s$. With the exception of the perturbation of the pattern near the scratch running through the centre of the deposit, its normal orientation relative to the polarisation of the electric field is also consistent with a surface plasmon effect.

Beyond just playing a role in the formation of the observed pattern, however, it is proposed that the observations reported here show that the mechanism responsible for the dissociation of the precursor is neither pyrolytic nor photolytic, but is instead driven by surface plasmons. To our knowledge, surface plasmon-mediated laser-induced deposition has been reported only in the context of enhancement of photolytic processes[150, 137]. Given the demonstrated inability to photolytically dissociate $Pt(MeCp)Me_3$ with 1.6 eV (775 nm) photons, the lack of substrate heating expected given the reflectivity of gold, and the morphology of the deposit, a surface plasmon-mediated dissociation process is likely the mechanism responsible for the deposition observed. It also accounts for the higher deposition rate qualitatively observed on gold versus platinum (see Table 6.2), since the frequency of the laser used to perform deposition is closer to the plasmon resonance for gold than for platinum.

The proposed mechanism involves the local enhancement of the electric field at the surface where constructive interference between laser-induced surface plasmons and the laser field itself occurs. While not sufficient to modify the surface under the conditions used in these experiments, the superposition of fields provides sufficient energy to dissociate the precursor. Once dissociation is initiated, the resulting metallic deposit likely provides further enhancement of the field and this positive feedback mechanism drives deposition at a higher rate, while maintaining the coherent nature of the initial deposition. On substrates with empty conduction bands and

[10] A value of -23.4 was used for ϵ_1 as reported by Ordal et al [151].

large band gaps (dielectrics), the absence of free electrons precludes the existence of surface plasmons. Thus, on these substrates, with Pt(MeCp)Me_3 as the precursor, and a photon energy of 1.6 eV, deposition occurs either via pyrolytic dissociation or not at all. The observed lack of a coherent structure in the morphology of these deposits further supports the proposition that the mechanism driving deposition on metallic substrates involves a plasmonic dissociation mechanism.

6.5 EBID Templated LID: Ongoing Efforts

While the results reported above are novel and scientifically interesting, poor spatial resolution and low deposition rates make them somewhat limited with respect to their practical application. Through the course of this research, however, it was found that both the rate and the resolution of ultrashort pulsed laser-induced deposition can be enhanced via electron beam-induced templating. In this process, electron beam -induced deposition is used to deposit a thin, arbitrarily shaped deposit. The deposit is then illuminated with ultrashort laser pulses while being exposed to the precursor of choice. Deposition proceeds preferentially on the template deposit, but at rates faster than EBID. In this fashion, features smaller than the diffraction limit of the laser wavelength can be deposited. As an example, Figure 6.9 shows a serpentine pattern of platinum produced using this technique. The lines are on the order of 60 to 70 nm wide with a 250 nm pitch.

To explore the deposition rate of this technique, we produced a series of 3 μm $\times$ 7 μm rectangular platinum EBID deposits of varying thicknesses on gold with a 0.48 nA, 20 keV beam. For each measurement, we produced two deposits. We then illuminated one of each pair of deposits with an ultrashort pulsed laser in the presence of Pt(MeCp)Me_3, producing an EBID templated LID deposit and a standard EBID deposit at each data point. The gas flow conditions were identical for both processes.

LID was performed with an average delivered laser power of 195 μW (195 nJ pulse energy). As with earlier experiments, the laser was scanned over the area of interest in a serpentine pattern of overlapping lines at a rate of 1000 μm/s. Between lines, the the beam was stepped 1 μm. Ten passes were made over each deposit using these parameters and the direction of the scan alternated from horizontal to vertical with every other pass. By numerically convolving the area of the beam with the area

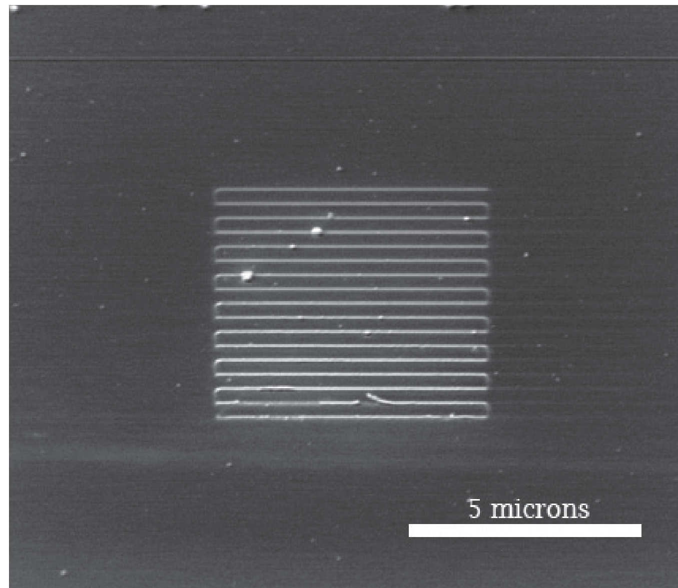

Figure 6.9. A serpentine pattern of 60 to 70 nm wide Pt lines deposited via EBID templated LID demonstrating the ability to produce sub-diffraction limited features using this technique.

of the deposit and multiplying this convolved area by the photon fluence of the pulse, we calculated that each deposit received a dose of approximately 6.6×10^{13} photons.

A Digital Instruments 3100 AFM was used in tapping mode to find the volume of each deposit and the results are presented in Figure 6.10. Deposit height data rather than volume data was collected for the four "EBID only" data points between 80 and 160 seconds. Therefore, for these data, volumes were calculated from their dimensions rather than directly via AFM. As a result, they are likely over estimated.

The data show a number of interesting features. First, note that for low EBID doses (60 seconds and below) the volumes of those deposits that were illuminated with the laser have volumes roughly equivalent to the volumes of the corresponding EBID only deposits. Sometime after the EBID volume exceeds 0.5 μm^3 – corresponding to a thickness of about 24 nm – the LID deposits exhibit a sharp increase in volume. In later experiments, we observed significant LID on EBID templates as thin as 10 nm. In any case, there appears to be an EBID threshold below which LID does not start. Note also the rate of LID with respect to the rate of standard EBID. Not only is it very fast by comparison, but it also appears to depend to some extent on the thickness of the EBID template. At some point, of course, this dependency

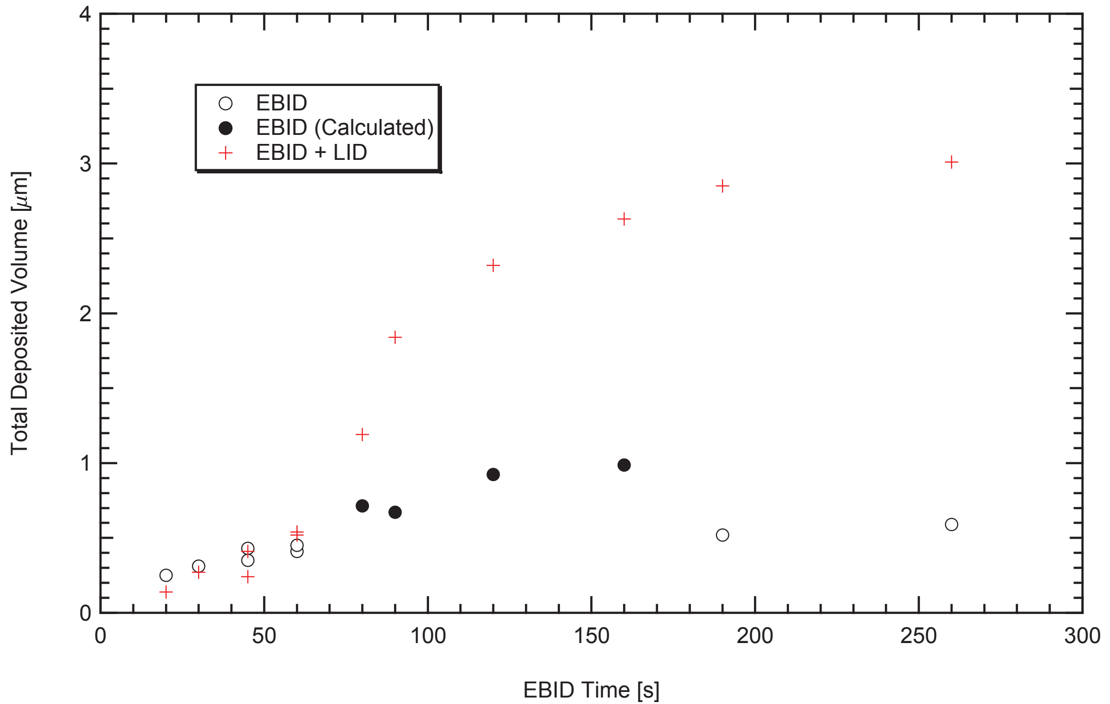

Figure 6.10. Deposited volume of EBID templated LID as a function of EBID dose. Data for solid circles are calculated from AFM measurements of height and are likely over estimated.

disappears and the LID rate appears to saturate.

The mechanism behind the phenomenon of EBID templated LID is, as yet, still unclear and is the focus of ongoing research. However, an examination of the morphology of deposits produced in this way and the discovery of a dependency of said morphology on the substrate, may provide some clues. Figure 6.11 shows tapping mode AFM scans of two 3 $\times$ 7 μm, EBID templated LID Pt deposits produced using precursor conditions, electron beam, laser, and scan parameters identical to those used in the rate studies. The average thickness of the EBID template used to produce both features was around 10 nm. Gold was used as the substrate for the feature in Figure 6.11(a). The substrate in figure (b) is silicon with a 300 to 500 nm thermal oxide layer (SiO_2) grown on top. Both features received identical electron doses, but the LID on the gold substrate received 25 passes with the laser, while that on the SiO_2/Si substrate received only 10.

A number of differences are immediately apparent. First, the deposit formed on Au is highly localised with very straight sidewalls. On the SiO_2/Si substrate,

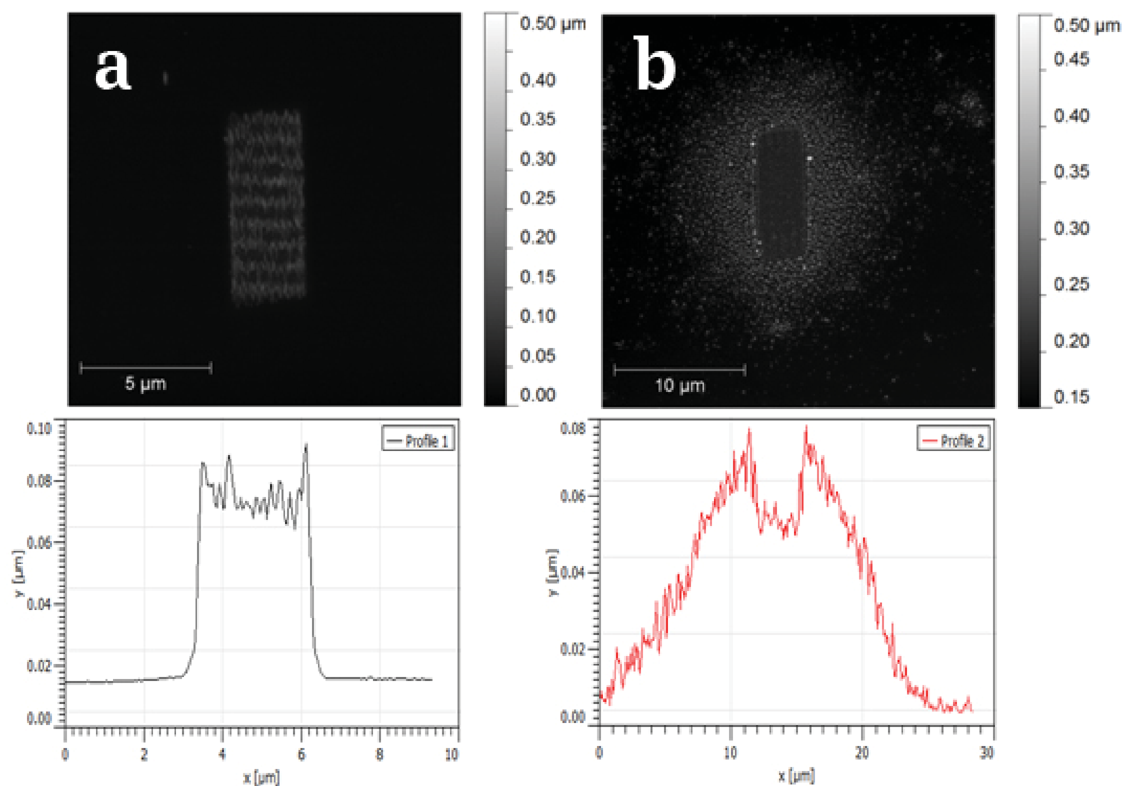

Figure 6.11. AFM images of EBID templated LID of Pt on (a) gold and (b) SiO_2 on Si.

however, while localisation does occur, a halo of LID deposition also occurs outside the bounds of the EBID template. Subsequent experiments show that untemplated LID does indeed occur on this substrate and that the rate of deposition is quite high. The occurrence of this "spontaneous" LID deposition (i.e. LID deposition without a mediating EBID template) on SiO_2 is curious, especially given our earlier reported failed efforts to form deposits on clear glass suggesting that photolysis plays little or no role in the dissociation of Pt(MeCp)Me_3 when 775 nm light is employed. Clearly, this result begs the question – is the silicon underlying the SiO_2 playing a role in the dissociation process?

Pyrolytic dissociation of the precursor at the SiO_2 surface due to laser-induced heating of the silicon 500 nm below has been considered as a possible mechanism for the observed LID phenomenon. At a wavelength of 775 nm, the absorption coefficient of Si is approximately 1000 cm^{-1} meaning that $1/e$ or 36% of any light not reflected (or about 67% of the incident light) is absorbed in the top 10 μm

of silicon. However, according to the thermal analysis done by Dadap et al. [149] (see Table 6.1), silicon heated with a laser fluence of 10 mJ/cm^2 at a repetition rate of 100 kHz undergoes a steady state temperature increase of only 3 K. In our experiment, the laser fluence is approximately 20 mJ/cm^2, but the repetition rate is two order of magnitude smaller at 1 kHz. Due to the strong dependency of sample temperature on laser repetition rate that Dadap et al. [149] demonstrated, the increase in temperature at the silicon surface is likely to be even lower in our experiment. Couple that with the low thermal conductivity of quartz and it seems unlikely that the thermal energy supplied by the heated silicon to the surface of the SiO_2 is sufficient to initiate pyrolytically driven LID given our experimental parameters.

Another possible dissociation mechanism considered involves the generation of high energy photons through the nonlinear processes of second and third harmonic generation (SHG, THG). In 1961, Franken et al. [152] used the newly invented ruby laser, focused into a quartz sample, to generate photons having twice the energy of the incident photons. A year later, Armstrong et al. [153] and Bloembergen et al. [154] established the theory of SHG. Second harmonic generation from silicon interfaces has been used as a chemical and crystallographic characterisation method for decades[155]. Most relevantly, Dadap et al. [149] showed that SiO_2/Si interfaces illuminated with ultrashort pulses ($\lambda = 800$ nm) efficiently generate SHG photons and Kolthammer et al. [156] characterised the reflection and transmission of SHG generated by UPL illumination of silicon samples having 200 to 800 nm thermal oxide layers (SiO_2).

While it has been shown that photolysis of Pt(MeCp)Me_3 does not occur when illuminated with 1.6 eV photons, the ability to generate photons having twice that energy via SHG processes seems to provide for the possibility of a photolytic dissociation mechanism on samples with an SiO_2-Si interface. However, efficient SHG is highly dependent on the incident angle of the primary beam. Whereas SHG typically requires an acute incident beam angle, the deposition experiments described here were performed at normal incidence, reducing the likelihood of SHG. Thus, the mechanism responsible for the observed effect is currently not understood and is the focus of ongoing research.

Another noteworthy effect observed in Figure 6.11 is the difference in deposit

morphology depending on the substrate on which the deposit is produced. On gold, the deposit exhibits periodic and coherent banding similar to that seen on non-templated gold (Figure 6.8, only more highly ordered. The period of the banding is on the order of the wavelength of the laser light and is oriented normal to the polarisation of the electric field. These bands are absent from the deposits formed on the SiO_2/Si substrate.

Figures 6.12(a) and (b) shows detailed tapping mode AFM images of the morphologies of the deposits on gold and on the SiO_2/Si substrate, respectively. At this magnification it is evident that the banding is made up of 350 to 400 nm long, roughly prolate spheroid grains with widths of less than 200 nm. The grains are horizontally separated by typically less than 50 nm, with their minor axes aligned in horizontal bands. The bands themselves have a vertical separation of approximately 500 nm and the space between grains is filled with a close-packed aggregate of roughly spherical particles with diameters typically less than 50 nm. By contrast, the deposits on the SiO_2/Si substrate exhibit none of the periodicity seen in those features deposited on gold, being comprised instead of clusters approximately 400 nm in diameter. These clusters are made up of aggregated particles similar to those observed between the grains in figure (a).

The dependence of the morphology of the deposit on the substrate on which it is formed extends to the rate at which deposition occurs. On the gold substrate, the deposition rate is much lower than on the SiO_2/Si substrate. To illustrate, we formed a 3×7 μm EBID Pt template straddling the boundary between the gold film and the SiO_2/Si substrate of the four-point probe test bed samples described earlier such that half the deposit was on the gold while the other half was on the SiO_2/Si. The gas conditions, electron beam, laser, and scan parameters were identical to those used to produce the EBID templated LID features described earlier.

The left hand image in Figure 6.13 was captured after five full laser scans had been completed over the entire pattern, delivering equivalent photon doses to both halves of the template. Note that the gold is in the upper half of these images, while the SiO_2/Si fills the lower half. The higher rate of deposition on the EBID template over the SiO_2/Si substrate relative to the one on gold is readily apparent. In addition, the spontaneous (i.e. non-templated LID) halo seen in Figure 6.11(b) is observed at an earlier stage. Close examination of the small amount of deposition

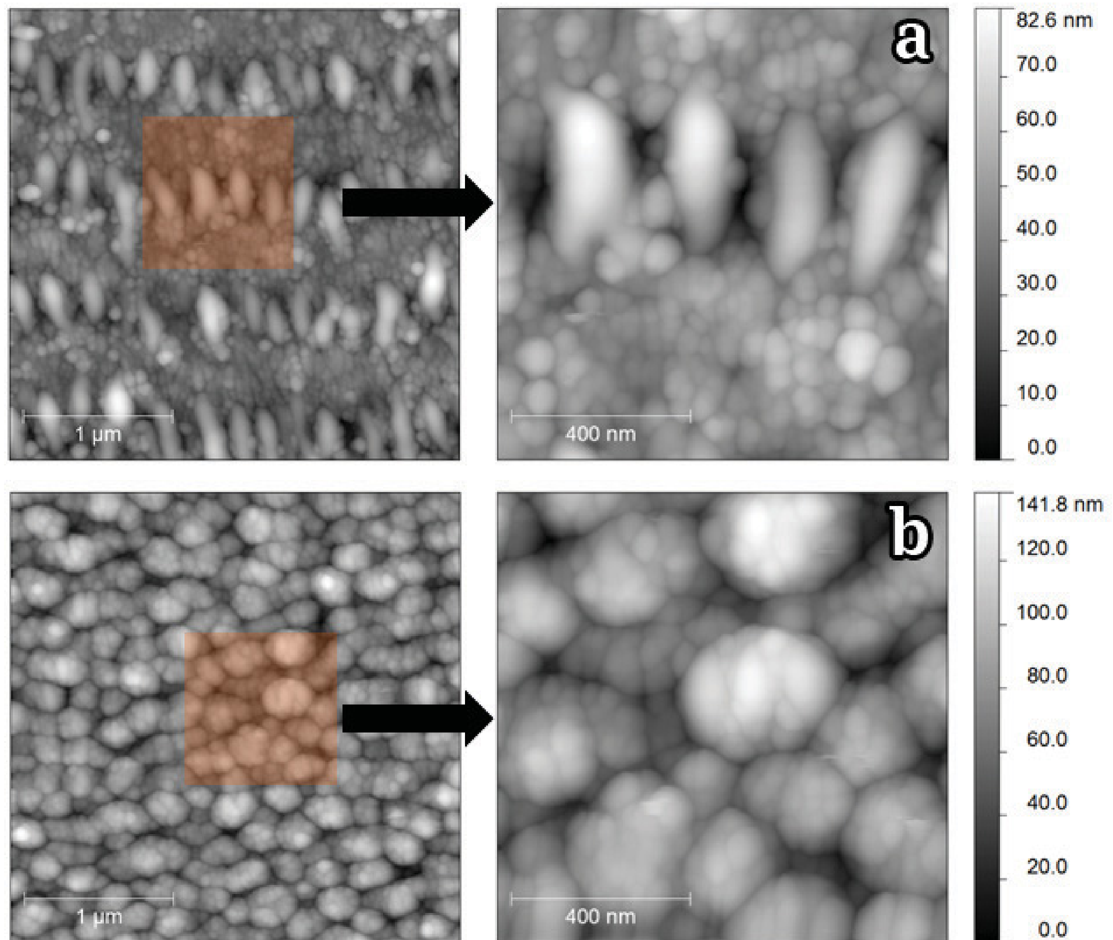

Figure 6.12. AFM images of the morphologies of the deposits on (a) gold and on the (b) SiO_2/Si substrate. The banding is made up of 350 to 400 nm long, roughly prolate spheroid grains with widths of less than 200 nm. The grains are horizontally separated by typically less than 50 nm, with their minor axes aligned in horizontal bands. The bands themselves have a vertical separation of approximately 500 nm and the space between grains is filled with a close-packed aggregate of roughly spherical particles with diameters typically less than 50 nm. By contrast, the deposits on the SiO_2/Si substrate exhibit none of the periodicity seen in those features deposited on gold, being comprised instead of clusters approximately 400 nm in diameter. These clusters are made up of aggregated particles similar to those observed between the grains in figure (a).

forming on the template over gold reveals the very early stages of the periodicity observed in Figure 6.11(a), especially near the edge of the interface. The right hand

image was captured after 25 laser passes over an area in which multiple templates were deposited. Highly resolved deposition with the characteristic banding is observed on the template over the gold substrate, while the spontaneous halo of LID has progressed to point of obscuring the templated LID on the SiO_2/Si substrate.

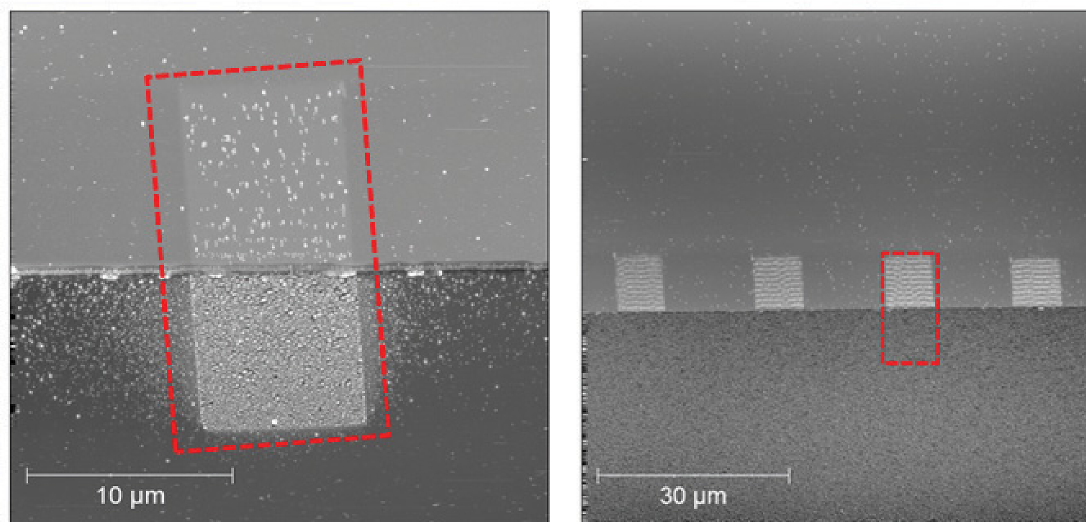

Figure 6.13. AFM images of an EBID templated LID of Pt straddling a gold-SiO_2 interface illustrating the differences in both morphology and deposition rate. The left hand image was captured after five full laser scans had been completed over the entire pattern, delivering equivalent photon doses to both halves of the template. The right hand image was captured after 25 laser passes over an area in which multiple templates were deposited. Note that the gold is in the upper half of these images, while the SiO_2/Si fills the lower half.

6.6 Summary and Future Work

6.6.1 Non-Templated LID

The ability to induced platinum deposition on a gold substrate in the absence of sample heating and with photons having demonstrably insufficient energy to dissociate the organometallic precursor used, suggests a mechanism for dissociation other than pyrolysis or photolysis. The coherent periodicity observed in the deposits and the orientation of this periodicity relative to the polarised electric field of the in-

cident laser radiation further suggests that the mechanism is a field-mediated one. A review of the literature on the modification of surfaces via laser-induced periodic surface structures suggests that constructive interference between the transverse electric field of the incident laser and laser-induced surface plasmons sufficiently enhance the field to induce dissociation and ultimately, deposition.

As quanta of oscillations induced when free charge carriers in a plasma are driven by an oscillating electric field, the existence of plasmons and plasmonic behaviour in solids requires the presence of free charge carriers. The fact that periodicity is observed only in deposits formed on metal, whereas no periodicity is observed in deposits formed on dielectrics, suggests (a) that the mechanisms responsible in these two cases are different and (b) that surface plasmons play a role in deposition on metals. In addition, the fact that the wavelength of the periodic pattern Λ is on the order of the wavelength of incident laser radiation λ as predicted for a beam normal to the surface and that the deposition rate is higher on gold than on platinum, where the plasmon resonance of gold is closer to the frequency of the incident laser light, further supports this conjecture.

To further explore this phenomenon, studies investigating the dependency of the deposition morphology and rate on laser wavelength and incident angle are planned. Two effects are expected as the wavelength decreases, or alternatively, the photon energy increases. First, if the observed periodicity is indeed the result of constructive interference, the wavelength of this periodicity should decrease with decreasing wavelength, closely tracking the laser wavelength for an irradiating beam having normal incidence. Secondly, parallel deposition experiments on non-absorbing substrates should at some sufficiently high photon energy induce deposition via photolytic decomposition. At this wavelength, deposition on gold will have competing decomposition mechanisms which should manifest as a reduction in the periodic order observed in the deposit morphology. Whether this disordering influence manifests itself suddenly with the onset of photolysis, or gradually with increasing photon energy after the photolytic threshold is reached will depend on the complicated interdependency of the photolytic threshold and the plasmon resonance of the material. If photolysis occurs at or very near the plasmon resonance of the material, it is feasible that the surface plasmon-mediated dissociation mechanism will dominate and the periodicity persist until a wavelength sufficiently far from

resonance is employed.

Studies investigating the effect of the incident angle of the laser on Λ provide yet another method of understanding the extent to which surface plasmons play a role. Huang et al. [135] observed that as the angle of the incident beam with the surface normal increases, the wavelength of laser-induced periodic surface structures decreases. If surface plasmons are indeed the driving mechanism for the observed platinum deposition on gold, the wavelength of the periodic structures observed in the deposits should likewise decrease with increasing incident angle.

6.6.2 EBID Templated LID

In this chapter, a previously unreported technique is described in which EBID is used to form a template for UPL-induced deposits, again demonstrating the synergistic potential of the TripleBeam as an experimental platform. While the exact mechanisms driving EBID templated laser-induced deposition are still unclear, the demonstrable ability to produce highly resolved and/or sub-diffraction limited features at rates higher than typical EBID, makes EBID templated LID an attractive technique.

A number of odd and poorly understood effects were observed in the course of this work. Foremost among these, is the apparent dependency of the deposit morphology on the underlying substrate. On gold, EBID templated LID deposits exhibit a characteristic coherent band pattern similar to, but much more well defined and pronounced than those observed on non-templated LID of platinum on gold. As with the non-templated deposits on gold, these bands have a wavelength on the order of the incident laser wavelength and are oriented perpendicular to the polarisation of the electric field of the laser. EBID templated LID performed on a 300 to 500 nm of SiO_2 thermally grown over a silicon substrate did not exhibit banding. The rate of deposition on EBID templated gold was significantly enhanced over the rate on non-templated gold.

It has been proposed that platinum nanocrystallites present in the thin EBID templates may play a role. Observed by a number of authors [157, 158, 159] in deposits formed from both organometallics and $Pt(PF_3)_4$, these nanocrystallites typically have diameters on the order of 5 nm and are embedded in a carbon matrix. The enhancement of electromagnetic fields by arrays of nanoparticles is a well docu-

mented effect [160, 161, 162]. In fact, surface enhanced Raman spectroscopy (SERS) relies on this effect. Furthermore, Le et al. [163] and Nordlander et al. [164] showed that plasmonic resonances of nanoparticles can interact with surface plasmons in thin films to yet further enhance fields in nanoparticle-film systems.

Thus, it is proposed that the mechanism for EBID templated LID is the enhancement of the laser field due to the presence of nanocrystallites in the EBID template. Furthermore, the enhanced field likely interacts with surface plasmons when the process is performed on metal substrates, providing still further enhancement and inducing the observed substrate dependency of the deposit morphology. Because a finite deposit thickness is required for the formation of nanocrystallites, this may also provide an explanation the threshold behaviour observed in Figure 6.10. Efforts are currently under way to better understand this phenomenon via modelling informed by detailed TEM analysis of the deposits before and after LID.

In the process of exploring EBID templated LID, a halo of LID deposition was observed outside the bounds of the EBID template on SiO_2/Si substrates. Subsequent experiments show that untemplated LID does indeed occur on this substrate and that the rate of deposition is quite high. SiO_2 is transparent to the laser wavelength used and photons at this wavelength have previously been shown to have insufficient energy to photolytically dissociate Pt(MeCp)Me_3. With the intent of determining the extent to which second harmonic generation is responsible for this effect, spectroscopic studies of the light reflected during UPL illumination of these substrates is the focus of ongoing efforts.

Chapter 7

Summary and Concluding Remarks

The ready availability of titanium doped sapphire (Ti:Sapphire) ultrashort pulsed lasers made possible by the efforts of Strickland and Mourou [9], Moulton [165], and Sibbett [166], among others, has led to the broad application of the technology to the study of the fundamental physics of the interaction of light and matter. Hundreds of researchers exploring a wide range of topics and technologies including ultrashort pulse generation, ultrashort pulse propagation, the optics of ultrashort pulses, and the application of ultrashort pulses to the study of ultrafast processes including ultrafast spectroscopy, femtochemistry, and ultrashort pulsed laser ablation have produced a vast body of literature.

The particular study of the complex, multi-step processes involved in ultrashort pulsed laser ablation has been thoroughly investigated over a wide range of laser parameters, on a wide variety of materials, in different environments, and by numerous methods. A great deal of the resulting literature concerns itself with the nature of the material removed during laser ablation, the formation of a plasma plume, and the interaction of the ablated material with the atmosphere in which the ablation is performed. However, very little work has been done studying laser ablation in reactive environments.

By studying millimetre-scale plasma-driven chemical reactions that occur in the gas-phase when ultrashort pulsed laser ablation (UPLA) is performed in reactive gas atmospheres, this dissertation extends the current body of knowledge regarding the

effects of background gases on the laser-induced plume of materials ejected during UPLA. The results reported have demonstrated that the process of ablating SiO_2 with an ultrashort pulsed laser in a XeF_2 atmosphere drives a chemical reaction that results in the volatilisation of material that would normally result in redeposition. Through the use of a combination of electron beam-induced etching (EBIE), laser-induced breakdown spectroscopy (LIBS), spatially resolved fast photography, plasma diagnostics, and mass spectrometry, the reaction has been shown to proceed in the gas-phase rather than via an adsorbate-mediated process.

In the first phase of a complex process, photons excite electrons in the substrate through a non-linear or multi-photon absorption process. Having gained sufficient energy to overcome the work function of the substrate, high energy photoelectrons are ejected into the ambient, driving it into an excited state. Via either coulombic explosion or the transfer of energy from excited electrons trapped in the bulk to the lattice (or both), the substrate is violently decomposed into its constituent silicon and oxygen atoms. The resulting solid density plasma expands away from the surface and into the ambient at supersonic velocities.

The expansion of the plasma begins picoseconds after the arrival of the pulse. By this time, the volume of the ambient excited by fast photoelectrons is shrinking as it cools. However, as the super-heated, electron-dense plasma expands, it collides with the ambient, re-exciting it while at the same time retarding the plume's expansion. In its excited state, XeF_2 forms an excited dimer, freeing a single, very reactive, fluorine atom. The slowing silicon atoms in the plasma plume react with the liberated fluorine, forming new products, primarily silicon difluoride. Fluorinated silicon compounds are all volatile and as such, are pumped away by the vacuum system, significantly reducing the amount of redeposition observed in the absence of XeF_2.

Reactive plasmas, or plasmas "composed of multiple reactive species that continuously transform into each other and that also generate new species as a result of numerous chemical reactions in the ionised gas phase," have recently been identified as an important nanofabrication tool [51, 52]. The methods typically employed to produce reactive plasmas involve the formation of the plasma in the gas-phase using gaseous precursors. The technique developed in this work is quite different in that the plasma is formed first in a solid substrate via the rapid, localised deposition of energy from an ultrashort laser pulse. The plasma then expands into the reactive

gas. The gas is subsequently driven into the plasma-phase. Decomposition of the solid and dissociation of the gas occur in the plasma-phase, allowing the species involved to rebond in new ways, forming novel by-products.

The methods and model system described here provide a well developed methodology for studying and applying ultrashort pulsed laser-induced plasma-driven gas-phase chemical reactions.

During the course of this research, considerable effort went into the design, development, and construction of a complex scientific instrument that combines a scanning electron microscope, a focused ion beam, and an ultrashort pulsed laser. The success of this effort and the efficacy of the instrument for use in both basic research and as an industrial tool is illustrated by FEI Company's support of its development over the four years ranging from 2009 to 2012.

Referred to as the TripleBeam, the development of the instrument was initially motivated by the need to speed processes normally performed by FIB or to enable ones not possible by current methods. However, a host of other applications are potentially made available by its invention. For instance, in situ laser-based characterisation techniques such as Raman spectroscopy and laser-induced breakdown spectroscopy become available as a means of producing correlative analytical data. The ability to deposit nanometre-scale metallic features in a controlled fashion via E/IBID makes surface enhanced Raman spectroscopy targetable to specific sites and may improve the spatial resolution of the technique. Additionally, characteristic X-rays that are generated during UPL ablation [94, 95, 96, 97] are driving the on-going investigation of the feasibility of laser-induced X-ray spectroscopy as a new characterisation technique. In the same way that surface enhanced Raman spectroscopy is made more efficacious given the E/IBID capabilities of the instrument, the fabrication, excitation, and in situ characterisation of plasmonic structures is also made possible by the TripleBeam. Thus, in addition to being an instrument for materials processing and/or rapid nano- or micro- prototyping, the TripleBeam is also a tool for the general investigation of phenomena involving the interaction of light and matter. The ultimate goal behind the development of the TripleBeam was not simply to combine two previously disparate bits of technology, but to develop a flexible, integrated system whose whole is greater than the sum of its parts.

The design challenges faced, the technical problems addressed, and the safety

and usability issues considered represent many hours of work. Thus, in this dissertation, the design and development of the TripleBeam was presented in detail. The fundamental components of the tool – a Ti:Sapphire, chirped pulse amplification, ultrashort pulsed laser and a DualBeam system – were reviewed and their theories of operation outlined. While in the interest of time, the evolution of the design was only briefly mentioned, the final iteration of the component systems developed to integrate the two systems into a final TripleBeam instrument were discussed in detail. Results on the characterisation of large volumes of materials in three dimensions were presented in order to illustrate the whole-greater-than-its-parts capability of the instrument to produce previously unachievable results. Indeed, the TripleBeam's ability to perform materials analysis on length scales ranging from tens of nanometres (via FIB) to hundreds of millimetres, combined with its multi-modal data collection capabilities, make it ideally suited to this task.

However, as earlier suggested, the capabilities of the instrument extend beyond materials processing and rapid nano- or micro- prototyping. As a platform for exploring the interaction of light and matter, the TripleBeam's capabilities were applied to the task of exploring ultrashort pulsed laser-induced surface chemistry – a topic for which little literature currently exists.

Early efforts exploring UPL-induced deposition produced uncontrolled deposition of platinum via the gas-phase photodissociation of tetrakis (trifluorophosphine) platinum ($Pt(PF_3)_4$). With the development of the TripleBeam system, the ability to perform controlled laser-induced surface chemistry experiments was greatly improved. In particular, the ability to capture real-time, high resolution images of the sample enabled far better control of the beam alignment and focus. In addition, being able to immediately image and perform EDS analysis of the results of each experiment without breaking vacuum or transferring the sample to another instrument significantly increased the time to data.

Switching precursors to (trimethyl) methylcyclopentadienylplatinum ($Pt(MeCp)Me_3$), UPL-induced platinum deposition was attempted on a variety of different substrates including gold, platinum, carbon, and clear and opaque glass. Deposition of Pt was demonstrated on all substrates except clear glass. EDS analysis was performed on the deposits formed on Au and black glass and compared to EBID of Pt on silicon. The absence of a significant carbon signal in the EDS spectrum of Pt deposited

on gold suggests a purity greater than EBID Pt. A strong carbon signal was observed in the EDS spectrum of Pt deposited on black glass suggesting a much high carbon content than that observed in the LID Pt deposited on gold and likely a higher content than that typically observed for electron beam-induced deposition of platinum. The marked difference in the EDS signals of Pt on Au versus Pt on black glass suggest different dissociation mechanisms. Deposition on black glass is a pyrolytic process and the high carbon content of the deposit suggests that it is a low temperature one.

The ability to induce platinum deposition on a gold substrate in the absence of sample heating and with photons having demonstrably insufficient energy to dissociate the organometallic precursor suggests a mechanism for dissociation other than pyrolysis or photolysis. Coherent periodicity observed in the deposits and the orientation of this periodicity relative to the polarised electric field of the incident laser radiation suggests that the mechanism is a field-mediated one. A review of the literature on the modification of surfaces via laser-induced period surface structures suggests that constructive interference between the transverse electric field of the incident laser and laser-induced surface plasmons sufficiently enhance the field to induce dissociation and ultimately, deposition. The fact that periodicity is observed only in deposits formed on metal, whereas no periodicity is observed in deposits formed on dielectrics, suggests (a) that the mechanisms responsible in these two cases are different and (b) that surface plasmons play a role in deposition on metals. In addition, the fact that the wavelength of the periodic pattern Λ is on the order of the wavelength of incident laser radiation λ as predicted for a beam normal to the surface and that the deposition rate is higher on gold than on platinum, where the plasmon resonance of gold is closer to the frequency of the incident laser light, further supports this conjecture. Beyond just playing a role in the formation of the observed pattern, it is proposed that the observations reported here show that the mechanism responsible for the dissociation of the precursor is neither pyrolytic nor photolytic, but is instead driven solely by surface plasmons. To our knowledge, surface plasmon-mediated laser-induced deposition has been reported only in the context of the enhancement of photolytic processes[150, 137].

To further explore this phenomenon, studies investigating the dependency of laser wavelength and incident angle are planned. Two effects are expected as the

wavelength decreases, or alternatively, the photon energy increases. First, if the observed periodicity is indeed the result of constructive interference, the wavelength of this periodicity should decrease with decreasing wavelength, closely tracking the laser wavelength for an irradiating beam having normal incidence. Secondly, parallel deposition experiments on non-absorbing substrates should at some sufficiently high photon energy induce deposition via photolytic decomposition. At this wavelength, deposition on gold will have competing decomposition mechanisms which should manifest as a reduction in the periodic order observed in the deposit morphology. Whether this disordering influence manifests itself suddenly with the onset of photolysis, or gradually with increasing photon energy after the photolytic threshold is reached will depend on the complicated interdependency of the photolytic threshold and the material's plasmon resonance. If photolysis occurs at or very near the plasmon resonance of the material, it is feasible that the surface plasmon-mediated dissociation mechanism will dominate and the periodicity persist until a wavelength sufficiently far from resonance is employed.

Studies investigating the effect of the incident angle of the laser on Λ provide yet another method of understanding the extent to which surface plasmons play a role. Huang et al. [135] observed that as the angle of the incident beam with the surface normal increases, the wavelength of laser-induced periodic surface structures decreases. If surface plasmons are indeed the driving mechanism for the observed platinum deposition on gold, the wavelength of the periodic structures observed in the deposits should likewise decrease with increasing incident angle.

Plasmonics may also play a role in the mechanism behind a previously unreported technique described in this thesis in which electron beam induced deposition is used to template UPL-induced deposits. The proposed mechanism for the observed dependency of the deposit morphology on the underlying substrate, along with the increase in deposition rate, is the enhancement of the laser field due to platinum nanocrystallites with diameters on the order of 5 nm embedded in the EBID produced template. It is further likely that the enhanced field interacts with surface plasmons when the process is performed on metal substrates, providing still greater enhancement and inducing the observed substrate dependency of the deposit morphology. Because a finite deposit thickness is required for the formation of nanocrystallites, this may also provide an explanation for the threshold behaviour

observed in a deposition rate study. Efforts are currently under way to better understand this phenomenon via modelling informed by detailed TEM analysis of the deposits before and after LID.

With a rich potential application space driven by fundamental physics, ultrashort pulsed laser-induced chemistry can be seen as both an end in itself and as a means for exploring the complex interaction of light and matter. The work detailed in this dissertation produced methodologies, instrumentation, and analysis relevant to both the fundamental physics and the application of ultrashort pulsed-laser induced chemistry.

Bibliography

[1] E. Matthias, M. Reichling, J. Siegel, O. W. Kding, S. Petzoldt, H. Skurk, P. Bizenberger, and E. Neske. The influence of thermal diffusion on laser ablation of metal films. *Applied Physics A*, 58(2):129–136, 1994.

[2] M. D. Shirk and P. A. Molian. A review of ultrashort pulsed laser ablation of materials. *Journal of Laser Applications*, 10(1):18–28, 1998.

[3] S. Nolte, C. Momma, H. Jacobs, A. Tunnermann, B. N. Chichkov, B. Wellegehausen, and H. Welling. Ablation of metals by ultrashort laser pulses. *Journal of the Optical Society Of America B*, 14(10):2716–2722, 1997.

[4] B. N. Chichkov, C. Momma, S. Nolte, F. Von Alvensleben, and A. Túnnermann. Femtosecond, picosecond and nanosecond laser ablation of solids. *Applied Physics A: Materials Science and Processing*, 63(2):109–115, 1997.

[5] R. W. Schoenlein, W. Z. Lin, J. G. Fujimoto, and G. L. Eesley. Femtosecond studies of nonequilibrium electronic processes in metals. *Physical Review Letters*, 58(16):1680–1683, 1987.

[6] S. K. Sundaram and E. Mazur. Inducing and probing non-thermal transitions in semiconductors using femtosecond laser pulses. *Nature Materials*, 1(4):217–224, 2002.

[7] M. Lenzner, J. Krüger, S. Sartania, Z. Cheng, C. Spielmann, G. Mourou, W. Kautek, and F. Krausz. Femtosecond optical breakdown in dielectrics. *Physical Review Letters*, 80(18):4076–4079, 1998.

[8] A. P. Joglekar, H. H. Liu, E. Meyhfer, G. Mourou, and A. J. Hunt. Optics at critical intensity: Applications to nanomorphing. *Proceedings of the National Academy of Sciences of the United States of America*, 101(16):5856–5861, 2004.

[9] D. Strickland and G. Mourou. Compression of amplified chirped optical pulses. *Optics Communications*, 56(3):219–221, 1985.

[10] C. V. Shank, R. Yen, and C. Hirlimann. Time-resolved reflectivity measurements of femtosecond-optical-pulse-induced phase transitions in silicon. *Physical Review Letters*, 50(6):454, 1983.

[11] C. V. Shank, R. Yen, and C. Hirlimann. Femtosecond-time-resolved surface structural dynamics of optically excited silicon. *Physical Review Letters*, 51(10):900, 1983.

[12] M. C. Downer, R. L. Fork, and C. V. Shank. Femtosecond imaging of melting and evaporation at a photoexcited silicon surface. *Journal of the Optical Society Of America B*, 2(4):595–599, 1985.

[13] A. Cavalleri, K. Sokolowski-Tinten, J. Bialkowski, M. Schreiner, and D. von der Linde. Femtosecond melting and ablation of semiconductors studied with time of flight mass spectroscopy. *Journal Of Applied Physics*, 85(6):3301–3309, 1999.

[14] T. Y. Choi and C. P. Grigoropoulos. Plasma and ablation dynamics in ultrafast laser processing of crystalline silicon. *Journal Of Applied Physics*, 92(9):4918–4925, 2002.

[15] S. Amoruso, R. Bruzzese, N. Spinelli, R. Velotta, M. Vitiello, X. Wang, G. Ausanio, V. Iannotti, and L. Lanotte. Generation of silicon nanoparticles via femtosecond laser ablation in vacuum. *Applied Physics Letters*, 84(22):4502–4504, 2004.

[16] S. Amoruso, C. Altucci, R. Bruzzese, C. De Lisio, N. Spinelli, R. Velotta, M. Vitiello, and X. Wang. Study of the plasma plume generated during near IR femtosecond laser irradiation of silicon targets. *Applied Physics A: Materials Science & Processing*, 79(4-6):1377–1380, 2004.

[17] T. H. Her, R. J. Finlay, C. Wu, S. Deliwala, and E. Mazur. Microstructuring of silicon with femtosecond laser pulses. *Applied Physics Letters*, 73(12):1673–1675, 1998.

[18] T. H. Her, R. J. Finlay, C. Wu, and E. Mazur. Femtosecond laser-induced formation of spikes on silicon. *Applied Physics A: Materials Science & Processing*, 70(4):383, 2000.

[19] D. Riedel, J. L. Hernandez-Pozos, R. E. Palmer, and K. W. Kolasinski. Fabrication of ordered arrays of silicon cones by optical diffraction in ultrafast laser etching with SF_6. *Applied Physics A: Materials Science & Processing*, 78(3):381–385, 2004.

[20] H. R. Dehghanpour, P. Parvin, B. Sajad, and S. S. Nour-Azar. Dose and pressure dependence of silicon microstructure in SF_6 gas due to excimer laser irradiation. *Applied Surface Science*, 255(8):4664–4669, 2009.

[21] B. K. Nayak and M. C. Gupta. Ultrafast laser-induced self-organized conical micro/nano surface structures and their origin. *Optics and Lasers in Engineering*, 48(10):966–973, 2010.

[22] C. Wen, H. Yang, X. Li, Y. Cui, X. He, X. Duan, and Z. Li. Transmission electron microscopy investigation of crystalline silicon surface irradiated by femtosecond laser pulses in different background atmospheres. *Applied Physics A: Materials Science & Processing*, pages 1–7, 2012.

[23] B. K. Nayak, M. C. Gupta, and K. W. Kolasinski. Ultrafast-laser-assisted chemical restructuring of silicon and germanium surfaces. *Applied Surface Science*, 253(15):6580–6583, 2007.

[24] B. K. Nayak, M. C. Gupta, and K. W. Kolasinski. Spontaneous formation of nanospiked microstructures in germanium by femtosecond laser irradiation. *Nanotechnology*, 18(19):195302, 2007.

[25] R. C. Issac, P. Gopinath, G. K. Varier, V. P. N. Nampoori, and C. P. G. Vallabhan. Twin peak distribution of electron emission profile and impact ionization of ambient molecules during laser ablation of silver target. *Applied Physics Letters*, 73(2):163–165, 1998.

[26] R. C. Issac, G. K. Varier, P. Gopinath, S. S. Harilal, V. P. N. Nampoori, and C. P. G. Vallabhan. Prompt electron emission and collisional ionization of ambient gas during pulsed laser ablation of silver. *Applied Physics A: Materials Science & Processing*, 67(5):557–561, 1998.

[27] O. Albert, S. Roger, Y. Glinec, J. C. Loulergue, J. Etchepare, C. Boulmer-Leborgne, J. Perrière, and E. Millon. Time-resolved spectroscopy measurements of a titanium plasma induced by nanosecond and femtosecond lasers. *Applied Physics A: Materials Science & Processing*, 76(3):319, 2003.

[28] S. S. Harilal, C. V. Bindhu, M. S. Tillack, F. Najmabadi, and A. C. Gaeris. Internal structure and expansion dynamics of laser ablation plumes into ambient gases. *Journal of Applied Physics*, 93(5):2380, 2003.

[29] S. Amoruso, R. Bruzzese, X. Wang, and J. Xia. Propagation of a femtosecond pulsed laser ablation plume into a background atmosphere. *Applied Physics Letters*, 92(4):041503, 2008.

[30] S. Amoruso, G. Ausanio, A. C. Barone, R. Bruzzese, L. Gragnaniello, M. Vitiello, and X. Wang. Ultrashort laser ablation of solid matter in vacuum: a comparison between the picosecond and femtosecond regimes. *Journal of Physics B: Atomic Molecular and Optical Physics*, 38(20):L329–L338, 2005.

[31] S. Noël, J. Hermann, and T. Itina. Investigation of nanoparticle generation during femtosecond laser ablation of metals. *Applied Surface Science*, 253(15):6310–6315, 2007.

[32] S. S. Harilal, Beau O'Shay, Yezheng Tao, and Mark S. Tillack. Ambient gas effects on the dynamics of laser-produced tin plume expansion. *Journal of Applied Physics*, 99(8):083303, 2006.

[33] T. Lehecka, A. Mostovych, and J. Thomas. Long duration light emission from femtosecond laser-target interactions. *Applied Physics A: Materials Science & Processing*, 92(3):727–741, 2008.

[34] D. Bleiner and T. Lippert. Stopping power of a buffer gas for laser plasma debris mitigation. *Journal of Applied Physics*, 106(12):123301–5, 2009.

[35] J. Sun and J. P. Longtin. Inert gas beam delivery for ultrafast laser micromachining at ambient pressure. *Journal of Applied Physics*, 89(12):8219, 2001.

[36] W. Perrie, M. Gill, G. Robinson, P. Fox, and W. O'Neill. Femtosecond laser micro-structuring of aluminium under helium. *Applied Surface Science*, 230(1-4):50–59, 2004.

[37] B. Sajad, P. Parvin, and M. A. Bassam. SF_6 decomposition and layer formation due to excimer laser photoablation of SiO_2 surface at gas-solid system. *Journal of Physics D: Applied Physics*, 37(24):3402–3408, 2004.

[38] Y. Rytz-Froidevaux, R. P. Salath, and H. H. Gilgen. Laser generated microstructures. *Applied Physics A: Solids and Surfaces*, 37(3):121–138, 1985.

[39] F. A. Houle. Basic mechanisms in laser etching and deposition. *Applied Physics A: Materials Science & Processing*, 41(4):315–330, 1986.

[40] I. P. Herman. Laser-assisted deposition of thin films from gas-phase and surface-adsorbed molecules. *Chemical Reviews*, 89(6):1323–1357, 1989.

[41] R. Haight, P. Longo, and A. Wagner. Metal deposition with femtosecond light pulses at atmospheric pressure. *Journal of Vacuum Science and Technology A: Vacuum, Surfaces and Films*, 21(3):649–652, 2003.

[42] H. Zhang, M. Tang, J. McCoy, and T. H. Her. Deposition of tungsten nanogratings induced by a single femtosecond laser beam. *Optics Express*, 15(10):5937–5947, 2007.

[43] S. Amoruso, R. Bruzzese, N. Spinelli, and R. Velotta. Characterization of laser-ablation plasmas. *Journal of Physics B: Atomic, Molecular and Optical Physics*, 32:R131R172, 1999.

[44] W. Soer, D. Klunder, M. van Herpan, L. Bakker, and V. Banine. Debris mitigation for EUV sources using directional gas flows. *Proceedings of SPIE*, 6151, 2006.

[45] S. S. Harilal, B. O'Shay, Y. Tao, and M. S. Tillack. Ion debris mitigation from tin plasma using ambient gas, magnetic field and combined effects. *Applied Physics B: Lasers & Optics*, 86(3):547–553, 2007.

[46] R. M. Osgood and T. F. Deutsch. Laser-induced chemistry for microelectronics. *Science*, 227(4688):709–714, 1985.

[47] J. Boulmer, B. Bourguignon, J. P. Budin, and D. Débarre. Time of flight study of low pressure laser etching of silicon by chlorine. *Applied Surface Science*, 43(1-4):424–431, 1989.

[48] A. Aliouchouche, J. Boulmer, B. Bourguignon, J. P. Budin, D. Débarre, and A. Desmur. Laser etching of silicon by chlorine: effect of post-desorption collisions and chlorine in-diffusion on the laser desorption yield. *Applied Surface Science*, 69(1-4):52–58, 1993.

[49] J. J. Ritsko, F. Ho, and J. Hurst. Laser-assisted chemical etching of copper. *Applied Physics Letters*, 53(1):78, 1988.

[50] D. Débarre, A. Aliouchouche, J. Boulmer, B. Bourguignon, and J.P. Budin. The role of gas-phase in the laser etching of Cu by CCl_4. *Applied Surface Science*, 96-98:453–456, 1995.

[51] K. Ostrikov. Colloquium: Reactive plasmas as a versatile nanofabrication tool. *Reviews Of Modern Physics*, 77(2):489, 2005.

[52] K. Ostrikov, E. Neyts, and M. Meyyappan. Plasma nanoscience: from nanosolids in plasmas to nano-plasmas in solids. *Adv. Phys.*, 62(2):113–224, 2013.

[53] H. F. Winters and J. W. Coburn. Etching of silicon with XeF_2 vapor. *Applied Physics Letters*, 34(1):70–73, 1979.

[54] D. E. Ibbotson, D. L. Flamm, J. A. Mucha, and V. M. Donnelly. Comparison of XeF_2 and F-atom reactions with Si and SiO_2. *Applied Physics Letters*, 44(12):1129–1131, 1984.

[55] S. Joyce, J. G. Langan, and J. I. Steinfeld. Reactions of XeF_2 with thermally grown SiO_2. *Surface Science*, 195(1-2):270–282, 1988.

[56] B. Roop, S. Joyce, J. C. Schultz, and J. I. Steinfeld. Comparison of Si(100) and Si(111) surfaces after moderate to high exposures of XeF_2. *Surface Science*, 173(2-3):455–464, 1986.

[57] M. Watanabe, Y. Mori, H. Sakai, T. Iida, S. Koide, E. Maeta, K. Sawabe, and K. Shobatake. Surface characterization of 3C-SiC exposed to XeF_2. *Japanese Journal of Applied Physics Part 2: Letters & Express Letters*, 43(3A):L346–L348, 2004.

[58] V. M. Bermudez. Study of fluorine (XeF_2) adsorption and of oxygen fluorine coadsorption on silicon using infrared reflection absorption-spectroscopy. *Journal of Vacuum Science & Technology A: Vacuum Surfaces and Films*, 10(6):3478–3485, 1992.

[59] C. W. Lo, D. K. Shuh, V. Chakarian, T. D. Durbin, P. R. Varekamp, and J. A. Yarmoff. XeF_2 etching of Si(111) - the geometric structure of the reaction layer. *Physical Review B*, 47(23), 1993.

[60] H. Nienhaus and W. Monch. Fluorine adsorption on GaAs(110) surfaces and the onset of etching after XeF_2 exposures. *Applied Surface Science*, 104:95–100, 1996.

[61] H. F. Winters. Etch products from the reaction of XeF_2 with SiO_2, Si_3N_4, SiC, and Si in the presence of ion-bombardment. *Journal of Vacuum Science & Technology B*, 1(4):927–931, 1983.

[62] H. F. Winters and F. A. Houle. Gaseous products from the reaction of XeF_2 with silicon. *Journal of Applied Physics*, 54(3):1218–1223, 1983.

[63] M. J. Mitchell, M. Suto, L. C. Lee, and T. J. Chuang. Chemiluminescence from F and XeF_2 etching reactions with silicon. *Journal of Vacuum Science & Technology B*, 5(5):1444–1449, 1987.

[64] F. A. Houle. Dynamics of SiF_4 desorption during etching of silicon by XeF_2. *Journal of Chemical Physics*, 87(3):1866–1872, 1987.

[65] D. J. Oostra and A. E. de Vries. Chemical sputtering by ions, electrons and photons. *Nuclear Instruments and Methods in Physics Research Section B: Beam Interactions with Materials and Atoms*, 18(1-6):618–624, 1986.

[66] P. G. M. Sebel, L. J. F. Hermans, and H. C. W. Beijerinck. Reaction layer dynamics in ion-assisted Si/XeF_2 etching: Ion flux dependence. *Journal of Vacuum Science & Technology A*, 17(6):3368–3378, 1999.

[67] S. J. Randolph, J. D. Fowlkes, and P. D. Rack. Focused electron-beam-induced etching of silicon dioxide. *Journal of Applied Physics*, 98(3):1–6, 2005.

[68] H. F. Winters, D. B. Graves, D. Humbird, and S. Tougaard. Penetration of fluorine into the silicon lattice during exposure to F atoms, F_2, and XeF_2: Implications for spontaneous etching reactions. *Journal of Vacuum Science & Technology A*, 25(1):96–103, 2007.

[69] P. S. Bagus, B. Liu, D. H. Liskow, and H. F. Schaefer III. Electron correlation and the reality of xenon difluoride. *Journal of the American Chemical Society*, 97(25):7216–7219, 1975.

[70] I. Utke, P. Hoffmann, and J. Melngailis. Gas-assisted focused electron beam and ion beam processing and fabrication. *Journal of Vacuum Science and Technology B: Microelectronics and Nanometer Structures*, 26(4):1197–1276, 2008.

[71] J. N. Leboeuf, K. R. Chen, J. M. Donato, D. B. Geohegan, C. L. Liu, and A. A. Puretzky. Modeling of plume dynamics in laser ablation processes for thin film deposition of materials. *Physics of Plasmas*, 3(5):2203–2209, 1996.

[72] H. Cronberg, M. Reichling, E. Broberg, H. B. Nielsen, E. Matthias, and N. Tolk. Effects of inverse bremsstrahlung in laser-induced plasmas from a graphite surface. *Applied Physics B*, 52:155–157, 1991.

[73] S. Senadheera, B. Tan, and K Venkatakrishnan. Critical time to nucleation: graphite and silicon nanoparticle generation by laser ablation. *Journal of Nanotechnology*, 2009, 2008.

[74] V. Detalle, R. Héon, M. Sabsabi, and L. St-Onge. An evaluation of a commercial Échelle spectrometer with intensified charge-coupled device detector for materials analysis by laser-induced plasma spectroscopy. *Spectrochimica Acta Part B: Atomic Spectroscopy*, 56(6):1011–1025, 2001.

[75] M. Kono and K. Shobatake. Photodissociative excitation processes of XeF_2 in the vacuum ultraviolet region 105180 nm. *Journal of Chemical Physics*, 102(15), 1995.

[76] National Institute of Standards and Technology Atomic Spectra Database. `http://physics.nist.gov/PhysRefData/ASD/lines_form.html`, 2013.

[77] W. K. Bischel, D. J. Eckstrom, Jr H. C. Walker, and R. A. Tilton. Photolytically pumped XeF (C→A) laser studies. *Journal Of Applied Physics*, 52(7):4429–4434, 1981.

[78] G. Black, R. L. Sharpless, D. C. Lorents, D. L. Huestis, R. A. Gutcheck, T. D. Bonifield, D. A. Helms, and G. K. Walters. XeF_2 photo-dissociation studies. 1. quantum yields and kinetics of XeF(B) and XeF(C). *The Journal Of Chemical Physics*, 75(10):4840–4846, 1981.

[79] V. Tcheremiskine, O. Uteza, A. Aristov, M. Sentis, and L. Mikheev. Photolytical XeF (C→A) laser amplifier of femtosecond optical pulses: gain measurements and pump efficiency. *Applied Physics B*, 91(3-4):447–454, 2008.

[80] H. Helm, L. E. Jusinski, D. C. Lorents, and D. L. Huestis. KrF laser excitation of the $D_{1/2} \leftarrow X_{1/2}$ transition of XeF. *The Journal of Chemical Physics*, 80(5):1796–1800, 1984.

[81] N. Bulgakova, R. Stoian, A. Rosenfeld, I. Hertel, and E. Campbel. Fast electronic transport and coulomb explosion in materials irradiated with ultrashort laser pulses. In C. Phipps, editor, *Laser Ablation and its Applications*, pages 17–36. Springer US, 2007.

[82] R. A. Copeland, J. B. Jeffries, A. P. Hickman, and D. R. Crosley. Radiative lifetime and quenching of the $3p^4d^0$ state of atomic nitrogen. *The Journal of Chemical Physics*, 86(9):4876–4884, 1987.

[83] Q. Zhu, J. M. Bridges, T. Hahn, and W. L. Wiese. Atomic transition-probability measurements for prominent spectral lines of neutral nitrogen. *Physical Review A*, 40(7):3721–3726, 1989.

[84] G. J. Bengtsson, J. Larsson, S. Svanberg, and D. D. Wang. Natural lifetimes of excited states of neutral nitrogen determined by time-resolved laser spectroscopy. *Physical Review A*, 45(5):2712–2715, 1992.

[85] N. W. Zheng and T. Wang. Theoretical resonance transition probabilities and lifetimes for atomic nitrogen. *Chemical Physics*, 282(1):31–36, 2002.

[86] R. Waynant and J. Eden. Spontaneous emission lifetime of the C→A band of the XeF molecule. *IEEE Journal of Quantum Electronics*, 15(2):61–63, 1979.

[87] J. G. Eden and S. K. Searles. XeF^* ($C_{1/2}$) radiative lifetime measurement. *Applied Physics Letters*, 30(6):287–290, 1977.

[88] H. R. Griem. *Principles of Plasma Spectroscopy*. Cambridge University Press, 2005.

[89] G. Cristoforetti, A. De Giacomo, M. Dell'Aglio, S. Legnaioli, E. Tognoni, V. Palleschi, and N. Omenetto. Local thermodynamic equilibrium in laser-induced breakdown spectroscopy: Beyond the McWhirter criterion. *Spectrochimica Acta Part B: Atomic Spectroscopy*, 65(1):86–95, 2009.

[90] V. K. Unnikrishnan, K. Alti, V. B. Kartha, C. Santhosh, G. P. Gupta, and B. M. Suri. Measurements of plasma temperature and electron density in laser-induced copper plasma by time-resolved spectroscopy of neutral atom and ion emissions. *Pramana - Journal of Physics*, 74(6):983–993, 2010.

[91] Y. Y. Tu, T. J. Chuang, and H. F. Winters. Chemical sputtering of fluorinated silicon. *Physical Review B*, 23(2):823–835, 1981.

[92] J. A. Dagata, D. W. Squire, C. S. Dulcey, D. S. Y. Hsu, and M. C. Lin. MPI/MS detection of SiF and SiF_2 radicals produced from the reaction of F_2 and NF_3 with silicon. *Chemical Physics Letters*, 134(2):151–155, 1987.

[93] H. F. Winters and I. C. Plumb. Etching reactions for silicon with F atoms: Product distributions and ion enhancement mechanisms. *Journal of Vacuum Science & Technology B: Microelectronics and Nanometer Structures*, 9(2):197–207, 1991.

[94] D. Salzmann, Ch Reich, I. Uschmann, E. Förster, and P. Gibbon. Theory of K_α generation by femtosecond laser-produced hot electrons in thin foils. *Physical Review E*, 65(3):036402, 2002.

[95] C. Reich, I. Uschmann, F. Ewald, S. Düsterer, A. Lübcke, H. Schwoerer, R. Sauerbrey, E. Förster, and P. Gibbon. Spatial characteristics of K_α X-ray emission from relativistic femtosecond laser plasmas. *Physical Review E: Statistical, Nonlinear, and Soft Matter Physics*, 68(5 2):564081–564088, 2003.

[96] C. G. Serbanescu, J. A. Chakera, and R. Fedosejevs. Efficient K_α X-ray source from submillijoule femtosecond laser pulses operated at kilohertz repetition rate. *Review Of Scientific Instruments*, 78(10):103502, 2007.

[97] W. Hong, Y. He, T. Wen, H. Du, J. Teng, X. Qing, Z. Huang, W. Huang, H. Liu, X. Wang, X. Huang, Q. Zhu, Y. Ding, and H. Peng. Spatial and temporal characteristics of X-ray emission from hot plasma driven by a relativistic femtosecond laser pulse. *Laser and Particle Beams*, 27(1):19–26, 2009.

[98] K. Tamura, E. P. Ippen, H. A. Haus, and L. E. Nelson. 77-fs pulse generation from a stretched-pulse mode-locked all-fiber ring laser. *Opt. Lett.*, 18(13):1080–1082, 1993.

[99] K. Tamura, E. P. Ippen, and H. A. Haus. Pulse dynamics in stretched-pulse fiber lasers. *Applied Physics Letters*, 67(2):158–160, 1995.

[100] H. A. Haus, K. Tamura, L. E. Nelson, and E. P. Ippen. Stretched-pulse additive pulse mode-locking in fiber ring lasers: theory and experiment. *IEEE Journal of Quantum Electronics*, 31(3):591–598, 1995.

[101] P. Debye and F. W. Sears. On the scattering of light by supersonic waves. *Proceedings of the National Academy of Sciences of the United States of America*, 18(6):409–414, 1932.

[102] E.P. Ippen, H.A. Haus, and L.Y. Liu. Additive pulse mode locking. *Journal of the Optical Society Of America B*, 6(9):1736–1745, 1989.

[103] K. R. Tamura. *Additive Pulse Mode-Locked Erbium-Doped Fiber Lasers*. PhD thesis, Massachusetts Institute of Technology, 1994.

[104] C. Hirlimann. Pulsed optics. In C. Rulliére, editor, *Femtosecond Laser Pulses: Principles and Experiments*, pages 25–56. Springer, New York, NY, 2nd edition, 2005.

[105] B. E. A. Saleh and M. C. Teich. Appendix a: Fourier transform. In *Fundamentals of Photonics*, pages 918–927. John Wiley & Sons, Inc., 2001.

[106] Wikipedia. Chirped pulse amplification — Wikipedia, the free encyclopedia, 2012. Online; accessed 2 August, 2012.

[107] Lee M. Frantz and John S. Nodvik. Theory of pulse propagation in a laser amplifier. *Journal Of Applied Physics*, 34(8):2346–2349, 1963.

[108] F. Salin. How to manipulate and change the characteristics of laser pulses. In C. Rulliére, editor, *Femtosecond Laser Pulses: Principles and Experiments*, pages 175–194. Springer, New York, NY, 2nd edition, 2005.

[109] H. J. Teunissen. *Multipass Amplifier for Terawatt Ti:Sapphire Laser System*. PhD thesis, University of Twente, 2007.

[110] R. H. Reuss, D. Morgan, A. Goldenetz, W. M. Clark, D. B. Rensch, and M. Utlaut. Fabrication of bipolar transistors by maskless ion implantation. *Journal of Vacuum Science and Technology B: Microelectronics and Nanometer Structures*, 4(1):290–294, 1986.

[111] M. M. Boenke, M. C. Wu, S. Wang, W. M. Clark Jr, E. H. Stevens, and M. W. Utlaut. DBR laser with nondynamic plasma grating formed by focused ion beam implanted dopants. *IEEE Journal of Quantum Electronics*, 25(6):1294–1302, 1989.

[112] A. J. De Marco and J. Melngailis. Maskless fabrication of JFETs via focused ion beams. *Solid-State Electronics*, 48(10-11 SPEC. ISS.):1833–1836, 2004.

[113] J. Melngailis. Focused ion beam lithography. *Nuclear Instruments and Methods in Physics Research B*, 80-81(PART 2):1271–1280, 1993.

[114] J. R. A. Cleaver, H. Ahmed, P. J. Heard, P. D. Prewett, G. J. Dunn, and H. Kaufmann. Focused ion beam repair techniques for clear and opaque defects in masks. *Microelectronic Engineering*, 3(1-4):253–260, 1985.

[115] T. Liang, A. Stivers, R. Livengood, P. Y. Yan, G. Zhang, and F. C. Lo. Progress in extreme ultraviolet mask repair using a focused ion beam. *Journal of Vacuum Science and Technology B: Microelectronics and Nanometer Structures*, 18(6):3216–3220, 2000.

[116] F. A. Stevie. Focused ion beam secondary ion mass spectrometry (FIB-SIMS). In Lucille A. Giannuzzi and Fred A. Stevie, editors, *Introduction to Focused Ion Beams*, pages 269–280. Springer US, 2005.

[117] L. A. Giannuzzi and M. Utlaut. A review of Ga^+ FIB/SIMS. *Surface And Interface Analysis*, 43(1-2):475–478, 2011.

[118] M. Utlaut. Focused ion beams. In J. Orloff, editor, *Handbook of Charged Particle Optics: Second Edition*, pages 523–600. CRC Press, 2009.

[119] G. Taylor. Disintegration of water drops in an electric field. *Proceedings of the Royal Society of London Series A: Mathematical and Physical Sciences*, 280(1382):383–397, 1964.

[120] L. Reimer. *Scanning Electron Microscopy: Physics of Image Formation and Microanalysis*. Springer, 1998.

[121] International Technology Roadmap for Semiconductors. "More-than-Moore" White Paper, 2009. Online; accessed 26 February, 2013.

[122] J. A. Van Vechten, R. Tsu, and F. W. Saris. Nonthermal pulsed laser annealing of Si; plasma annealing. *Physics Letters A*, 74(6):422–426, 1979.

[123] J. A. Van Vechten, R. Tsu, F. W. Saris, and D. Hoonhout. Reasons to believe pulsed laser annealing of Si does not involve simple thermal melting. *Physics Letters A*, 74(6):417–421, 1979.

[124] National Science and Technology Council, Committee on Technology. Materials genome initiative for global competitiveness, 2011. Online; accessed 26 February, 2013.

[125] J. Alkemper and P. W. Voorhees. Quantitative serial sectioning analysis. *Journal of Microscopy*, 201(3):388–394, 2001.

[126] J. E. Sipe, J. F. Young, J. S. Preston, and H. M. Van Driel. Laser-induced periodic surface structure. I. Theory. *Physical Review B*, 27(2):1141–1154, 1983.

[127] J. F. Young, J. S. Preston, H. M. Van Driel, and J. E. Sipe. Laser-induced periodic surface structure. II. Experiments on Ge, Si, Al, and brass. *Physical Review B*, 27(2):1155–1172, 1983.

[128] Q. Wu, Y. Ma, R. Fang, Y. Liao, Q. Yu, X. Chen, and K. Wang. Femtosecond laser-induced periodic surface structure on diamond film. *Applied Physics Letters*, 82(11):1703–1705, 2003.

[129] A. Borowiec and H. K. Haugen. Subwavelength ripple formation on the surfaces of compound semiconductors irradiated with femtosecond laser pulses. *Applied Physics Letters*, 82(25):4462–4464, 2003.

[130] Y. Shimotsuma, P. G. Kazansky, J. Qiu, and K. Hirao. Self-organized nanogratings in glass irradiated by ultrashort light pulses. *Physical Review Letters*, 91(24):247405/1–247405/4, 2003.

[131] J. Bonse, M. Munz, and H. Sturm. Structure formation on the surface of indium phosphide irradiated by femtosecond laser pulses. *Journal Of Applied Physics*, 97(1), 2005.

[132] O. Varlamova, F. Costache, M. Ratzke, and J. Reif. Control parameters in pattern formation upon femtosecond laser ablation. *Applied Surface Science*, 253(19):7932–7936, 2007.

[133] A. Y. Vorobyev, V. S. Makin, and C. Guo. Periodic ordering of random surface nanostructures induced by femtosecond laser pulses on metals. *Journal Of Applied Physics*, 101(3), 2007.

[134] J. Bonse, A. Rosenfeld, and J. Krger. On the role of surface plasmon polaritons in the formation of laser-induced periodic surface structures upon irradiation of silicon by femtosecond-laser pulses. *Journal Of Applied Physics*, 106(10), 2009.

[135] Min Huang, Fuli Zhao, Ya Cheng, Ningsheng Xu, and Zhizhan Xu. Origin of laser-induced near-subwavelength ripples: Interference between surface plasmons and incident laser. *ACS Nano*, 3(12):4062–4070, 2009.

[136] M. P. Echlin, A. Mottura, C. J. Torbet, and T.M. Pollock. A new TriBeam system for three-dimensional multimodal materials analysis. *Review Of Scientific Instruments*, 83(2):023701, 2012.

[137] C. J. Chen and R. M. Osgood. Direct observation of the local-field-enhanced surface photochemical reactions. *Physical Review Letters*, 50(21):1705–1708, 1983.

[138] M. Lax. Temperature rise induced by a laser beam. *Journal Of Applied Physics*, 48(9):3919–3924, 1977.

[139] T. Q. Qiu and C. L. Tien. Femtosecond laser heating of multi-layer metals: I. Analysis. *International Journal of Heat and Mass Transfer*, 37(17):2789–2797, 1994.

[140] J. K. Chen and J. E. Beraun. Numerical study of ultrashort laser pulse interactions with metal films. *Numerical Heat Transfer: Part A – Applications*, 40(1):1–20, 2001.

[141] J. K. Chen, J. E. Beraun, and C. L. Tham. Investigation of thermal response caused by pulse laser heating. *Numerical Heat Transfer: Part A – Applications*, 44(7):705, 2003.

[142] I. H. Chowdhury and X. Xianfan. Heat transfer in femtosecond laser processing of metal. *Numerical Heat Transfer: Part A – Applications*, 44(3):219, 2003.

[143] S. H. Lee, J. S. Lee, S. Park, and Y. K. Choi. Numerical analysis on heat transfer characteristics of a silicon film irradiated by pico- to femtosecond pulse lasers. *Numerical Heat Transfer: Part A – Applications*, 44(8):833–850, 2003.

[144] S. V. J. Narumanchi, J. Y. Murthy, and C. H. Amon. Submicron heat transport model in silicon accounting for phonon dispersion and polarization. *Journal of Heat Transfer*, 126(6):946–955, 2004.

[145] A. Banerjee, A. A. Ogale, C. Das, K. Mitra, and C. Subramanian. Temperature distribution in different materials due to short pulse laser irradiation. *Heat Transfer Engineering*, 26(8):41–49, 2005.

[146] L. Jiang and H. L. Tsai. Improved two-temperature model and its application in ultrashort laser heating of metal films. *Journal of Heat Transfer*, 127(10):1167–1173, 2005.

[147] H. Ki and J. Mazumder. Numerical simulation of femtosecond laser interaction with silicon. *Journal of Laser Applications*, 17(2):110–117, 2005.

[148] X. Qi and C. S. Suh. Generalized thermo-elastodynamics for semiconductor material subject to ultrafast laser heating. Part I: Model description and validation. *International Journal of Heat and Mass Transfer*, 53(1-3):41–47, 2010.

[149] J. I. Dadap, X. F. Hu, N. M. Russell, J. G. Ekerdt, J. K. Lowell, and M. C. Downer. Analysis of second-harmonic generation by unamplified, high-repetition-rate, ultrashort laser pulses at Si(001) interfaces. *IEEE Journal of Selected Topics in Quantum Electronics*, 1(4):1145–1155, 1995.

[150] S. R. J. Brueck and D. J. Ehrlich. Stimulated surface-plasma-wave scattering and growth of a periodic structure in laser-photodeposited metal films. *Physical Review Letters*, 48(24):1678–1681, 1982.

[151] M. A. Ordal, L. L. Long, R. J. Bell, S. E. Bell, R. R. Bell, Jr R. W. Alexander, and C. A. Ward. Optical properties of the metals Al, Co, Cu, Au, Fe, Pb, Ni, Pd, Pt, Ag, Ti, and W in the infrared and far infrared. *Applied Optics*, 22(7):1099–1119, 1983.

[152] P. A. Franken, A. E. Hill, C. W. Peters, and G. Weinreich. Generation of optical harmonics. *Physical Review Letters*, 7(4):118–119, 1961.

[153] J. A. Armstrong, N. Bloembergen, J. Ducuing, and P. S. Pershan. Interactions between light waves in a nonlinear dielectric. *Physical Review*, 127(6):1918–1939, 1962.

[154] N. Bloembergen and P. S. Pershan. Light waves at the boundary of nonlinear media. *Physical Review*, 128(2):606–622, 1962.

[155] Y. R. Shen. Surface properties probed by second-harmonic and sum-frequency generation. *Nature*, 337(6207):519–525, 1989.

[156] W. S. Kolthammer, D. Barnard, N. Carlson, A. D. Edens, N. A. Miller, and P. N. Saeta. Harmonic generation in thin films and multilayers. *Physical Review B: Condensed Matter and Materials Physics*, 72(4), 2005.

[157] L. Rotkina, J. F. Lin, and J. P. Bird. Nonlinear current-voltage characteristics of Pt nanowires and nanowire transistors fabricated by electron-beam deposition. *Applied Physics Letters*, 83(21):4426–4428, 2003.

[158] L. Rotkina, S. Oh, J. N. Eckstein, and S. V. Rotkin. Logarithmic behavior of the conductivity of electron-beam deposited granularPtC nanowires. *Physical Review B - Condensed Matter and Materials Physics*, 72(23), 2005.

[159] A.P.J.M. Botman. *Towards high purity nanostructures from electron beam induced deposition of platinum*. PhD thesis, TU Delft, 2009.

[160] D. A. Genov, A. K. Sarychev, V. M. Shalaev, and A. Wei. Resonant field enhancements from metal nanoparticle arrays. *Nano Letters*, 4(1):153–158, 2004.

[161] S. Zou and G. C. Schatz. Silver nanoparticle array structures that produce giant enhancements in electromagnetic fields. *Chemical Physics Letters*, 403(1-3):62–67, 2005.

[162] K. A. Willets and R. P. Van Duyne. Localized surface plasmon resonance spectroscopy and sensing. *Annual Review of Physical Chemistry*, 58:267–297, 2007.

[163] F. Le, N. Z. Lwin, J. M. Steele, M. Käll, N. J. Halas, and P. Nordlander. Plasmons in the metallic nanoparticle-film system as a tunable impurity problem. *Nano Letters*, 5(10):2009–2013, 2005.

[164] P. Nordlander and F. Le. Plasmonic structure and electromagnetic field enhancements in the metallic nanoparticle-film system. *Applied Physics B: Lasers & Optics*, 84(1/2):35–41, 2006.

[165] P. F. Moulton. Spectroscopic and laser characteristics of Ti:Al_2O_3. *Journal of the Optical Society Of America B*, 3(1):125–133, 1986.

[166] D. E. Spence, P. N. Kean, and W. Sibbett. 60-fsec pulse generation from a self-mode-locked Ti:Sapphire laser. *Optics Letters*, 16(1):42–44, 1991.